

Strangeness photoproduction via the reactions
 $\gamma p \rightarrow K^+ \Sigma^0$ and $\gamma p \rightarrow \phi p$ using CLAS at Jefferson
Lab: differential cross sections, polarizations, and a
partial-wave analysis

by

Biplab Dey
June 1, 2010

Contents

1	Event Selection	2
1.1	Reaction Topologies	2
1.1.1	$K^+\Sigma^0$: “Three-track” and “Two-track” Topologies	2
1.1.2	ϕp : “Charged-mode” and “Neutral-mode” Topologies	3
1.2	Excluded Runs	3
1.3	Kinematic Fitting	4
1.3.1	Introduction	4
1.3.2	Event Selection Scheme using Kinematic Fitting	5
1.3.3	Confidence Levels	5
1.4	Energy, Momentum and Tagger Corrections	6
1.4.1	Energy Loss Corrections	6
1.4.2	Vertex Corrections	6
1.4.3	Tagger Corrections	7
1.4.4	Momentum Corrections	7
1.4.5	Effectiveness of the Corrections	8
1.5	Photon Selection	8
1.6	Event Selection – $K^+\Sigma^0$ Three-track Topology	10
1.6.1	Kinematic Fitting of $\gamma p \rightarrow K^+ p \pi^-(\gamma)$	10
1.6.2	Effectiveness of the Confidence Level cut	10
1.6.3	Particle Identification – Timing Cuts	12
1.6.4	A subtlety	13
1.6.5	The “Iron-cross” Cut	15
1.6.6	PID uncertainty	16
1.6.7	$K^+\Lambda$ Background Removal	18
1.7	Event Selection – $K^+\Sigma^0$ two-track topology	19
1.7.1	“Dalitz” Cut	19
1.7.2	Initial Skim	19
1.7.3	Particle Identification – 2-D Calculated Mass and “Dalitz” Cut	21
1.8	Event Selection – ϕp Charged-mode Topology	21
1.8.1	Kinematic Fitting of $\gamma p \rightarrow K^+(K^-)p$	21
1.8.2	Particle Identification – Timing Cuts	25
1.8.3	$\Lambda(1520)$ Cut	25
1.9	Event Selection – ϕp Neutral-mode Topology	25
1.9.1	Kinematic Fitting of $\gamma p \rightarrow p\pi^+\pi^-(K_L^0)$	25
1.9.2	Timing Cuts	27
1.9.3	K_S^0 Selection Cut	27
1.9.4	$M(p, K_S^0)$ and $M(p, K_L^0)$ Dalitz Cut	27
1.10	Detector Performance Cuts	28
1.10.1	Minimum Proton Momentum Cut	28

CONTENTS	2
-----------------	----------

1.10.2 Fiducial Cuts	30
1.10.3 Problematic TOF Paddle Removal	32
1.11 Signal Background Separation	32
1.11.1 Q -values and Error Estimation	34
1.11.2 Application of the Procedure for $K^+\Sigma^0$	34
1.12 Systematic Study of the Background for ϕp	34
1.12.1 Charged-Mode Topology	37
1.12.2 Neutral-Mode Topology	38
1.13 Summary	38
2 Detector Acceptance and Normalization	41
2.1 Detector Simulation	41
2.1.1 “Raw” Monte Carlo	41
2.1.2 GSIM	42
2.1.3 GPP	43
2.2 Trigger Simulation	43
2.3 Start Counter Correction	44
2.4 Event Selection – $K^+\Sigma^0$ Three-track topology	45
2.5 Event Selection – $K^+\Sigma^0$ Two-track topology	47
2.6 Event Selection – ϕp Charged-mode topology	47
2.7 Event Selection – ϕp Neutral-mode topology	48
2.8 Systematic Uncertainties	48
2.9 Target Density	52
2.10 Photon Flux Normalization	52
2.10.1 gflux	52
2.10.2 Live Time Correction	53
2.10.3 Trigger Correction for Flux	53
2.10.4 Systematic Error	54
2.11 Summary	55
3 PWA Theoretical Formalism	56
3.1 Representation Theory of the Homogenous Lorentz Group	56
3.1.1 The HLG algebra	57
3.2 Spin Half Representation	58
3.3 Integral Spin Formalism	59
3.3.1 Massless Case	60
3.3.2 Spin-2 (and higher) Tensors	61
3.3.3 Orbital Angular Momentum	62
3.4 Tensor-Spinor Combinations	62
3.4.1 Spin-Polarization Connection for Photon	63
3.5 $\Sigma^0 \rightarrow \gamma\Lambda \rightarrow \gamma p\pi^-$ Amplitude	64
3.5.1 $\Sigma^0 \rightarrow \gamma\Lambda$	64
3.5.2 $\Lambda \rightarrow p\pi^-$	65
3.5.3 $\mathcal{A}_{\Sigma^0 \rightarrow \gamma\Lambda \rightarrow \gamma p\pi^-}$ normalization	66
3.6 $\phi \rightarrow K_1 K_2$ Amplitude	66
3.7 $K^+\Sigma^0$ Non-Resonant Amplitudes	67
3.7.1 t -channel 0^- Exchange	67
3.7.2 t -channel 1^- Exchange	68
3.7.3 t -channel 1^+ Exchange	69
3.7.4 u -channel Y Exchange	70
3.7.5 s -channel Proton Exchange	70

3.8	ϕp Non-Resonant Amplitudes	71
3.8.1	The P_1 Pomeron – VDM and DL theories	71
3.9	Resonant Amplitudes	71
3.9.1	Isospin Considerations	71
3.9.2	$J^P \rightarrow K^+ \Sigma^0$ Amplitudes	72
3.9.3	$\gamma p \rightarrow J^P$ Amplitudes	72
3.9.4	$\gamma p \rightarrow J^P \rightarrow K^+ \Sigma^0 \rightarrow K^+ \gamma \Lambda \rightarrow K^+ \gamma p \pi^-$ Amplitude	74
3.10	Gauge Invariance and Form Factors	74
3.10.1	Form Factors and Contact Terms	75
3.11	Summary	76
4	PWA Fit Formulae and $K^+ \Sigma^0$ Differential Cross Sections	77
4.1	The Maximum Likelihood Method	78
4.1.1	The Extended Maximum Likelihood Method (EMLM)	78
4.1.2	Amplitudes, Probabilities and Cross Sections	78
4.1.3	Log Likelihood Formula	80
4.1.4	Including Background	81
4.2	Least Squares Fitting	81
4.2.1	Calculation of $d\sigma/dt$	82
4.3	Multiple Dataset Fits	82
4.4	MINUIT	83
4.5	The Mother Fit	83
4.5.1	Setup	83
4.5.2	Quality Checks on Fit Results	84
4.6	Differential Cross Sections	86
4.6.1	Formula for Calculation	86
4.6.2	Uncertainties	87
4.7	Two- and Three-track Results	88
4.8	Final Differential Cross-Sections	88
4.8.1	A note on the errors	96
4.9	Comparision With Previous Experiments	97
4.10	Summary	100
5	$K^+ \Sigma^0$ Recoil Polarizations	103
5.1	Conventions	103
5.1.1	Helicity Frame	103
5.1.2	Axes Conventions	103
5.2	Polarization Transfer Between Σ^0 - Λ	105
5.3	Parity Argument for Hyperon Polarization	106
5.4	Final $\Sigma^0 \rightarrow \Lambda \gamma \rightarrow p \pi^- \gamma$ Angular Distribution	107
5.4.1	Approximate g_1 Expression	107
5.5	PWA Expression for Polarization	108
5.5.1	CGLN Amplitudes	108
5.5.2	Helicity Amplitudes	109
5.5.3	Polarization and Strong Phases	111
5.5.4	The 16 Observables	111
5.5.5	The PWA expressions	112
5.6	Preliminary Measurement Results and Discussion	117
5.7	Re-binned Polarizations	118
5.7.1	Statistical Error Estimation for the PWA method	118
5.8	“Traditional” Method Polarizations	118

5.9	Final Polarization Results and Statistical Errors	121
5.9.1	Three-track results	121
5.9.2	Including Two-track results	121
5.10	Systematic Error Estimation	124
5.11	Comparison With Previous Measurements	127
5.12	Summary	128
6	ϕ Differential Cross Sections	131
6.1	The Mother Fits	131
6.2	Cross section results	131
6.2.1	Comparison with previous world data	134
6.3	Summary	143
7	Spin Density Matrix Elements for ϕ	144
7.1	The Density Matrix of a Massive Vector Particle	144
7.2	Amplitude Level Construction of $\rho_{\lambda\lambda'}^V$	147
7.3	Reference Frames and Helicity Conservation	147
7.3.1	Conversion between the Adair, Helicity and GJ frames	148
7.4	Comparison of PWA and Schilling Methods	150
7.5	Systematic Uncertainties	150
7.6	Final SDME results	150
8	Systematic Studies of g_{11a}	158
8.1	Trigger Correction for Λ Decay	159
8.1.1	Simulated Λ Decay Start Counter Trigger	160
8.1.2	Comparison With Hard Cut	161
8.2	Background Subtraction Systematics Check	162
8.3	Acceptance Calculation	163
8.4	TOF Paddle Survey	163
8.5	A Few Other Checks	165
8.5.1	Re-entry of proton/ π^- Into Start Counter Region	165
8.5.2	Trigger Map For K^+	165
8.5.3	Additional $MM(K^+)$ Cuts (Three-track Topology)	165
8.5.4	Additional $MM(K^+)$ Cuts (Two-track Topology)	166
8.5.5	Additional Sector 5 Fiducial Cut	166
8.6	Summary	168

Chapter 1

Event Selection

The *g11a* dataset consists of about 20 billion event triggers and around 21 TB of data collected by the CLAS collaboration at Jefferson Lab between May 17th and July 29th, 2004. Next, the data underwent a step known as *cooking*, where raw signals recorded by the various detector subsystems were repackaged into a form suitable for physics analysis. This included recording of tracking information and assignment of particle kinematics for every event. Each detector component was also calibrated and checked for functionality at this point. The chef for *g11a* cooking was Maurizio Ungaro at INFN [1]. After cooking, the actual physics analysis began.

At the time of this writing, *g11a* was by far the largest strangeness photoproduction dataset in the world to have been fully analyzed. However, cross sections for strangeness photoproduction generally being much smaller compared to the non-strange sector, most of the data consisted of $N\pi$, $N\pi\pi$, $p\omega$, $p\rho$, ... production, which were “background” events for the $K^+\Sigma^0$ and ϕp channels. In this chapter, we describe all the steps involved in the extraction of good $K^+\Sigma^0$ and ϕp events from this very large dataset.

1.1 Reaction Topologies

1.1.1 $K^+\Sigma^0$: “Three-track” and “Two-track” Topologies

The Σ^0 is a neutral particle. Upon production, it decays \sim 100% of the time to $\gamma\Lambda$. This is an electromagnetic $M1$ transition and occurs almost instantaneously. The Λ subsequently undergoes a weak decay via both a charged ($p\pi^-$, 63.9%) and a neutral ($n\pi^0$, 35.8%) decay mode. Since CLAS was optimized for detecting charged tracks, in this analysis we will be concerned with the Λ charged decay mode only. Previous CLAS analyses often required detection of one greater than the minimum requisite number of charged tracks for the event trigger to fire. The *g11a* Level 1 trigger was a two-prong trigger. Thus, for a major portion of the $K^+\Sigma^0$ analysis, our selected events had tracks detected for all the three final state charged particles concerned, K^+ , p and π^- . The outgoing photon was reconstructed as the total missing 4-momentum. Henceforth, we will refer to $\gamma p \rightarrow K^+ p \pi^- (\gamma)$ as the “three-track” topology for this channel.

We also examined the full two-track dataset by detecting only the K^+ and the proton, and we will henceforth refer to $\gamma p \rightarrow K^+ p (\pi^- \gamma)$ as the “two-track” topology. Since the π^- tracks were negatively charged, they were bent *inwards* toward the beamline by the torus magnets and had a greater chance of escaping undetected through the beam-dump hole in the downstream region of the detector. Therefore, by not requiring the π^- to be detected, the two-track topology had a higher overall acceptance. However, the Σ^0 polarization measurements and our event-based partial

wave analysis setup requires knowledge of all four final-state particle momenta. Since the missing momentum for the two-track topology was the sum of the π^- and the outgoing photon momenta, the individual momenta of these tracks could be reconstructed. Hence, our two-track topology analysis was mostly limited to differential cross-section measurements only. As shown later, in regions where the kinematics overlapped and statistics was large enough, the two- and three-track $K^+\Sigma^0$ results were found to be in good agreement with each other, even though the two analyses were independent of each other with quite different event selection and analysis schemes. This in turn served as an good internal check for our understanding of the $g11a$ dataset and the detector acceptance.

1.1.2 ϕp : “Charged-mode” and “Neutral-mode” Topologies

The ϕ primarily decays into two kaons via charged- (K^+K^- , 49%) and neutral-mode ($K_S^0 K_L^0$, 34%) decays. For the charged-mode, both two-track $\gamma p \rightarrow \phi p \rightarrow K^+(K^-)p$ and three-track $\gamma p \rightarrow \phi p \rightarrow K^+K^-p$ topologies were possible. Since the ϕ cross-section is inherently small, the three-track topology had extremely limited statistics. Therefore, we only use the two-track dataset for the “charged-mode” topology in the analysis. This had the highest statistics and forms the primary source of results for this channel.

Along with the charged mode, we also analyzed the neutral-mode decay of the ϕ . Below $\sqrt{s} \sim 2.2$ GeV, the charged-mode topology overlaps in phase-space with the reaction $\gamma p \rightarrow K^+\Lambda(1520) \rightarrow K^+K^-p$, while the neutral-mode kinematics is impervious to the $\Lambda(1520)$. It is therefore crucial to compare results between the charged and the neutral modes to understand any effect the $\Lambda(1520)$ might have on ϕ photoproduction below 2.2 GeV. It is to be noted that all previous world data utilized only the charged decay mode by detecting the K^+ . The present results represent the first analysis of the neutral decay mode of the ϕ . Henceforth, we define the “neutral-mode” topology as $\gamma p \rightarrow \phi p \rightarrow K_S^0(K_L^0)p \rightarrow \pi^+\pi^-(K_L^0)p$ with the undetected K_L^0 being reconstructed as the missing 4-momentum. Being a three-track topology, statistics was again rather limited here. To bolster statistics, our energy bins were wider and our angular coverage was limited to the forward- and some of the mid-angles regions only.

1.2 Excluded Runs

Data acquisition (DAQ) in CLAS proceeds on a run-by-run basis, each “run” consisting of about 10 million events. This subdivision helps in diagnosing detector and DAQ problems that might creep in over time. The $g11a$ run period included CLAS runs 43490 to 44133. Runs 43490 to 44107 were taken with electron beam-energy 4.019 GeV, while for runs 44108 to 44133, the beam-energy was 5.021 GeV. Since the latter set of runs formed only a small fraction of the entire dataset and would not reduce our statistical uncertainties by any considerable amount if removed, but could lead to possible differences in systematics, we chose to use only the 4.019 GeV beam-energy runs in this analysis. We also excluded the very first few runs from 43490 to 43525. These were *commissioning* runs, taken for diagnostic reasons and were not meant to be used for any actual physics analysis.

There were several other runs which were later found to be unreliable and are excluded from this analysis. While $g11a$ was being recorded, a logbook was kept of all shift workers’ observations. The CLAS $g11a$ logbook entries for runs 43981-43982 show that there were problems with the drift chambers during these runs. Similarly, logbook entries for runs 43989-43991 show problems with the DAQ system. In order to study the $g11a$ trigger, runs 43675-6, 43777-8, 44013 were taken with different triggering configurations than the standard production trigger. Several runs showed systematic problems with the DC power supply to the TOF counters in sector 2 (runs 43989, 43990-1, 44000-2, 44007-8, 44010-2) and sector 3 (runs 43586-9, 43590-6). Lastly, run 43588 was found to have abnormalities in previous $g11a$ analyses and runs 43585, 43657, 44036 and 44101 exhibited

Excluded Run	Description
43490-43525	commissioning runs
44108-44133	5.021 GeV beam-energy
43675-43676, 43777-43778, 44013	alternate trigger
43989, 43990-43991, 44000-44002, 44007-44008, 44010-44012	TOF problem in sector 2
43586-43589, 43590-43596	TOF problem in sector 3
43588, 43585, 43657, 44036, 44101	abnormal data yields
43526, 43527, 43532, 43533, 43540, 43541, 43547-43553, 43561	Damaged magnetic tape during 2-track data transfer (only for two-track topologies)

Table 1.1: Table of $g11a$ runs excluded from this analysis

abnormal flux-normalized $K^+\Sigma^0$ yields (see Sec. 2.10). All of the runs listed above are excluded from our analysis. A summary of these is provided in Table 1.1.

For three-track analyses in both channels, all $g11a$ runs between 43525-44107 not mentioned as “excluded” in Table 1.1 were included in this analysis. During the full 2-track data transfer (this was done separately, at a later stage in the analysis), one particular magnetic tape containing about a hundred files was found to be physically damaged at the Jefferson Lab end. These hundred odd files spilled on to 15 runs (see Table 1.1), which were further excluded from the two-track analyses for both channels.

1.3 Kinematic Fitting

1.3.1 Introduction

Our particle identification methods (except for the $K^+\Sigma^0$ two-track dataset), as well as our tagger and momentum corrections made heavy use of a method called *kinematic fitting*. This powerful tool was developed by Mike Williams, a former CMU graduate student [2, 3]. In this section we sketch out very briefly how this method worked.

To start with, consider a set of n measured quantities, denoted by the n -vector $\vec{\eta}$. For example, these could be the momenta of different tracks as measured by CLAS. Each measurement had an associated error, given similarly by the n -vector $\vec{\epsilon}$. The *actual* values of the observables being measured were \vec{y} , with the relation

$$\vec{\eta} = \vec{y} + \vec{\epsilon}. \quad (1.1)$$

The idea was to estimate \vec{y} from $\vec{\eta}$ using a set of *kinematic* constraints, in our case, the conservation of energy and momentum. For example, in the $K^+\Sigma^0$ channel, we had an outgoing photon which we did not detect. The constraint equation would therefore be the requirement of a zero total missing mass and the fit would be a one constraint (1- C) fit. If we had detected *all* the final particles we would have required every component of the total missing 4-momenta to be zero and the fit would have been a 4- C fit. Note here that the fit parameters all went inside the constraint equations.

Then, consider the following n -vector, $\vec{\delta}$, given by

$$\vec{\delta}_i = \vec{y}_f - \vec{y}_i \quad (1.2)$$

where \vec{y}_f were the final required fit results, \vec{y}_i was the improved measurement at the i^{th} iteration step, the starting \vec{y}_0 been taken as the *measured* $\vec{\eta}$. If the covariance matrix for the measured quantities was C_η , then the quantity we wanted to minimize was $\vec{\delta}^T C_\eta^{-1} \vec{\delta}$. However, this minimization had to be in tandem with the aforementioned constraint equations. This was done by employing the standard procedure of Lagrange multipliers. Lastly, the actual fit was run by utilizing the method of least squares.

1.3.2 Event Selection Scheme using Kinematic Fitting

The way we used the above procedure to select good events was the following. First, we required every event to be of the form $(+, +)$, where at least two positively charged tracks had to be detected and ascribed to the particular event in question. For all three-track analyses, we also required an additional negatively charged track and the event topologies were of the form $(+, +, -)$. Note that the CLAS event reconstruction software typically assigned several tracks to the same event and incorrect particle track assignments could thereby be associated an event at this stage. However, as we show later, these would not escape our cuts. In the next step, we made a *physics hypothesis* of which particles these tracks referred to. For example, for the $K^+ \Sigma^0$ three-track analysis, this could be either (K^+, p, π^-) or (p, K^+, π^-) . That is, the negatively charged track was assumed to be a π^- and the positively charged tracks had to either be a proton and a K^+ , or vice versa. Similarly, for the ϕp charged-mode topology, our event hypotheses were of the forms (p, K^+) or (K^+, p) , with a missing K^+ . We reiterate upon the fact here that throughout this analysis, *all* possible particle hypothesis combinations were looped and each hypothesis was treated as an independent event hypothesis. This served to minimize any initial bias in our particle identification procedure.

1.3.3 Confidence Levels

The “goodness of fit” from our kinematic fitting was given by the *confidence level* for a given *physics hypothesis*. Note that the fit errors were contained in $\vec{\epsilon}$ vector. If all measurements were independent of each other so that the covariance matrix C_η was diagonal, the minimization quantity would have taken the familiar χ^2 form $\sum_{j=1}^n \epsilon_j^2 / \sigma_j^2$. However, for the general case, the covariance matrix would *not* be diagonal and the minimization quantity would follow a χ^2 distribution with $d = k - m$ degrees of freedom, where m was the number of fit parameters and k was the number of constraint equations. A measure of the “goodness of fit” for the least squares method would then given by the *confidence level*

$$CL = \int_{\chi^2}^{\infty} f(z; d) dz, \quad (1.3)$$

where $f(z; d)$ was the χ^2 probability density function with d degrees of freedom. The confidence level indicated how real and repeatable and not just random, a certain fit result was. It was the probability that another random event from the same distribution would have a χ^2 from the fit which was at least as large as the event in question. If the errors were normally distributed, the confidence levels from “good” events would populate the range $(0, 1]$ evenly. “Background” events which failed the hypotheses would have very small confidence levels.

The quality of error estimation from the above procedure were given by the *pull* distributions for each measured quantity. These were defined as $z_i = \epsilon_i / \sigma(\epsilon_i)$ with $\epsilon_i = \eta_i - y_i$ and standard

deviation $\sigma(\epsilon_i)$. Recasting this as

$$z_i = \frac{\eta_i - y_i}{\sqrt{\sigma^2(\eta_i) - \sigma^2(y_i)}}, \quad (1.4)$$

put them in a calculable form (the covariance matrix C_y for calculating $\sigma(y_i)$ was gotten here by standard error propagation techniques from C_η). If all the errors were being accounted for properly, the pull distribution should be a normal distribution, centered around zero with $\sigma = 1$.

The kinematic fitter for $g11a$ has undergone extensive testing and has been applied to several other channels with outstanding results [4, 5, 6]. The confidence level from kinematic fits were therefore one of the main handles for event selection and background reduction for this analysis. Since the confidence levels for good events was given by a flat distribution, by demanding that we accept events only with confidence level greater than a certain percentage, we would be throwing away a *known and well understood* fraction of actual good events, but as we show later, this effectively trimmed out most of the background.

1.4 Energy, Momentum and Tagger Corrections

1.4.1 Energy Loss Corrections

Energy loss by particles as they passed through various materials in the CLAS detector happened ubiquitously. Even before a particle hit any component of the tracking system, energy losses occurred in the target material (liquid Hydrogen) and walls, the beam pipe, the start counter, the air gap between the start counter and the inner regions of the drift chamber, and so on. The PDG [8] gives a comprehensive list of all such energy losses during the passage of high energy particles through matter. Thus these losses had to be properly corrected for. For CLAS, these corrections were handled by the `eloss` package written by Eugene Pasyuk at ASU [9].

1.4.2 Vertex Corrections

For the $K^+\Sigma^0$ three-track topology (as opposed to the two-track analysis, both in the present work and previous $K^+\Sigma^0$ analyses), we were able to reconstruct the Λ decay vertex. For the three-track case, since we detected the π^- along with the proton, we could use tracking information to find the point of closest approach between the π^- and the proton tracks, which was then assigned to as the Λ decay vertex position. We then set the π^- and proton vertices as the Λ decay vertex position. For both the two-track and the three-track analyses, the *event* vertex position was set as the point of closest approach between the K^+ track and an idealized beam along the z -axis. All vertex calculations were performed using *MVRT*, a vertexing package written by J. McNabb [10]. In earlier CLAS analyses and the early stages of the present analysis, the event vertex was being calculated by projecting back all the detected tracks to one single point and the energy loss for any particle was being calculated assuming it emanate from this point. Due to the multiple decays in the $K^+\Sigma^0$ channel and the fact that the Λ has a macroscopic pathlength of several centimeters, the p and the π^- tracks inevitably had “kinks” in the direction at each decay vertex. It was thus inappropriate to project all the tracks to a single point. Once we had reconstructed the more accurate event and Λ decay (for the three-track case) vertices, we could calculate the improved energy loss corrections accordingly.

For the ϕp charged-mode, all the final-state particles emanated from a single event vertex. This was reconstructed as the point of closest approach between the K^+ track and an idealized beam along the z -axis. For the neutral-mode, the K_S^0 had a finite path-length of $c\tau \sim 2.68$ cm. The

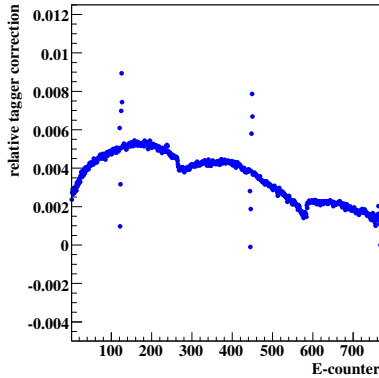


Figure 1.1: Shown above are the *relative* tagger corrections for each tagger E-counter for the *g11a* dataset as calculated in [3]. The four dips correspond to the sagging of the E-counter focal plane between its four support yokes. There are a couple of points off the general trend. These are due to wrong cable connections for the counters during data recording. Image source [3].

K_S^0 vertex was therefore different from the event vertex. The K_S^0 vertex was reconstructed as the point of closest approach between the π^+ and the π^- tracks. Energy loss corrections were employed accordingly after the improved vertex reconstructions.

1.4.3 Tagger Corrections

The photon energy (E_γ) for an event, came from the E-counters of the photon tagger in CLAS. However, physical distortions of the tagger's focal plane gave rise to inaccuracies in this measurement. This effect was examined by studying inclusive $(\gamma)p \rightarrow p\pi^+\pi^-$ events via a kinematic fit. This was an inclusive reaction in the sense that we ignored the measurements for the incoming photon but make a 1-C kinematic fit to zero total missing mass corresponding to a missing photon. Only events with a high enough confidence level were selected in this study (here one is concerned not about throwing away good events, but that the events selected *really* be good events). This was done for both the CLAS *g11a* [3] and *g1c* [11] datasets. Tagger corrections were then ascribed as the difference between the *measured* photon energy and the energy from the fit result. By taking the Gaussian mean over the entire \sqrt{s} range, a systematic correction was found for each tagger E-counter (see Fig. 1.1). These results have been interpreted as due to sagging of the focal plane between its four support yokes [12]. This sag displaced the narrow E-counters from their ideal locations, causing them to detect electrons with slightly different energies. In this analysis, we have applied the derived *g11a* tagger corrections to each event according to its associated tagger E-counter.

1.4.4 Momentum Corrections

Momenta for the various particles were measured in CLAS from tracking information as the particles bend during their flight though the toroidal magnetic field. Therefore, any discrepancy between the “ideal” field map from survey information and the “actual” field during the experiment would give rise to incorrectly reconstructed momenta. Similarly for misalignments and sagging in various parts of the drift chamber.

Momentum corrections for the *g11a* run period have been derived using the $\gamma p \rightarrow p\pi^+\pi^-$ channel [13]. Tagger and energy-loss corrections were applied to each $p\pi^+\pi^-$ event in which all final-state tracks were reconstructed by CLAS. Three separate kinematic fits were then performed, each treating one of the detected final-state particles as “missing”: $\gamma p \rightarrow p\pi^+(\pi^-)$, $\gamma p \rightarrow p(\pi^+)\pi^-$, and $\gamma p \rightarrow (p)\pi^+\pi^-$ hypotheses. Measured momenta for the “missing” particles were then compared to the missing momenta from the kinematic fits. Corrections were calculated for each CLAS sector and particle charge. Each sector was divided into twelve 5° bins in the azimuthal angle ϕ . Each ϕ bin was then divided into fifteen polar angle (θ) bins: nine 5° bins in the range $5^\circ \leq \theta < 50^\circ$, four 10° bins in $50^\circ \leq \theta < 90^\circ$, and two 25° bins in $90^\circ \leq \theta < 140^\circ$. Corrections to the magnitude of momentum for each track charge were calculated in each of the angular bins, and were typically found to be less than 10 MeV.

1.4.5 Effectiveness of the Corrections

To check the effectiveness of these corrections, we employed the $K^+\Sigma^0$ channel and looked at the missing mass off K^+ and the invariant ($p\pi^-$) mass distributions in the three-track dataset. The former corresponded to the Σ^0 mass (~ 1.1926 GeV) and the latter to the Λ mass (~ 1.1156 GeV). We chose events by kinematically fitting to $\gamma p \rightarrow K^+ p\pi^-(\gamma)$ and applying a 1% confidence level cut (the validity of this cut is described in detail in the next section) keeping only events with missing mass off K^+ between 1.14 GeV and 1.24 GeV. Fig. 1.2 shows the two distributions as they looked before and after the corrections were made (but before kinematic fitting). All events were taken from runs 43810-43819. There is a distinct shift in the peaks between the pre and post-correction distributions. The corrections pulled the mass peaks closer to their PDG values, demonstrating the effectiveness of our corrections.

1.5 Photon Selection

For photoproduction experiments, the interaction time for an event could be measured by two different ways. Each event had a number of tagged photons. The timing resolution of the tagging spectrometer in CLAS was 110 ps and this was good enough to identify the RF beam bucket the tagged photon is associated with. The next step was to temporally propagate the photon time from the radiator to the interaction vertex. This *tagger vertex time*, derived from the RF signal time was the most accurate timing information available in the entire experiment and *this the event vertex time that we used in this analysis*. For a given event, every tagged photon¹ was looped over independently, as “the” photon. Photons associated with the wrong RF bucket were removed by cuts later on. An alternative way of determining the event vertex time was to use timing information from the start counter. The start counter was the first detector system that a charged track triggered after it left the target. Timing information from the start counter was propagated backward temporally to the event vertex by using the track’s momentum and tracking information and a *start counter vertex time* was obtained from here. In some CLAS analyses (see Bob Bradford’s CLAS *g1c* analysis [51] for example), an initial ± 1 ns photon selection cut was placed between the tagger and start counter vertex times for every detected track. We examined the effect of this cut in the very initial stages of our analysis, and though we found it to be a loose enough cut, we *did not employ this cut in this analysis*.

¹For this analysis, this meant, having a “status word” 7 or 15 in the TAGR bank.

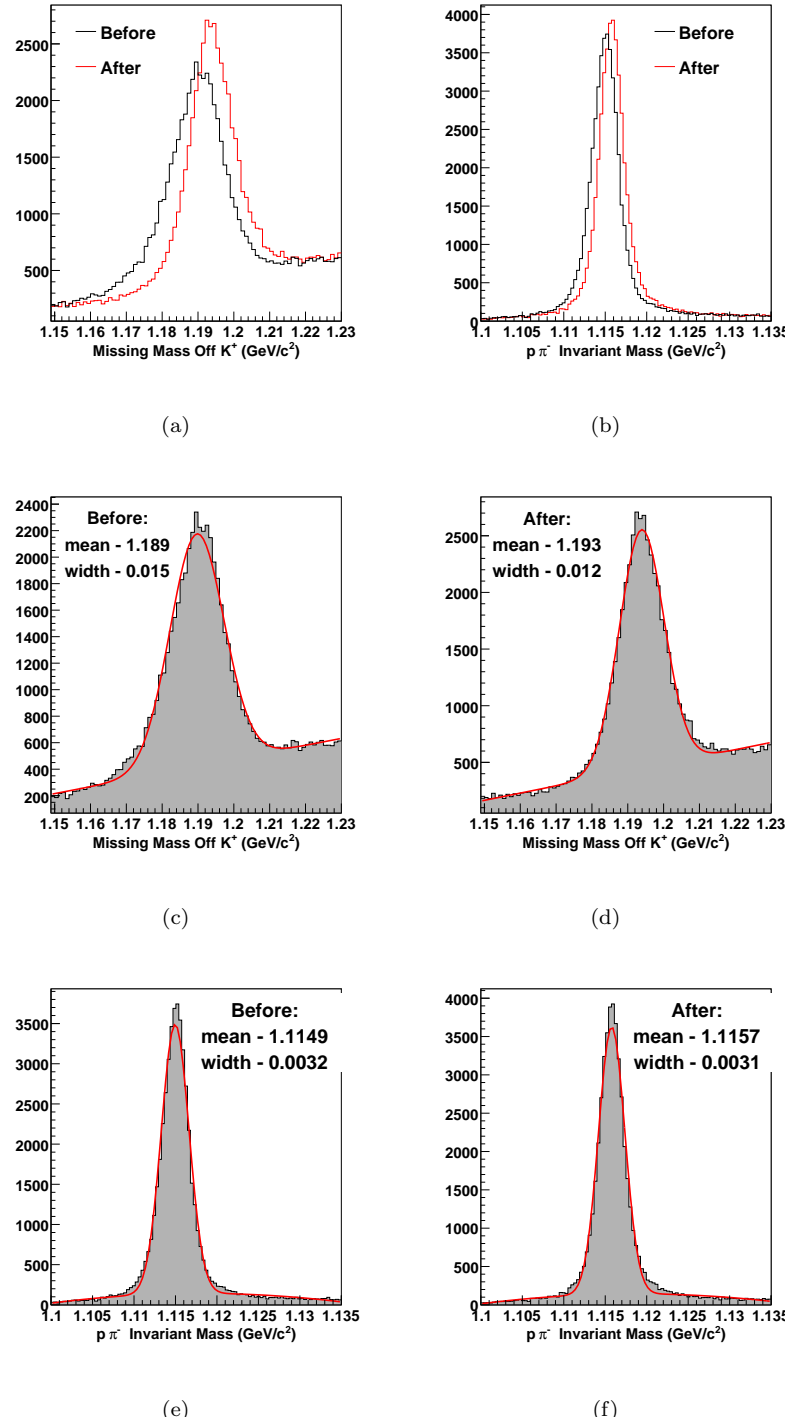


Figure 1.2: Effectiveness of energy, momentum and tagger corrections using the $K^+\Sigma^0$ channel: shifts in the (a) Σ^0 and (b) Λ mass peaks respectively, before and after the corrections. Fits to the distributions in (c) and (d) for Σ^0 , (e) and (f) for Λ show that the peaks are pulled closer to the masses listed in PDG after the corrections. Note that the events were *selected* using a kinematic fit cut, but the momenta used to compute the above variables used the corresponding pre-kinematic fit values.

1.6 Event Selection – $K^+\Sigma^0$ Three-track Topology

1.6.1 Kinematic Fitting of $\gamma p \rightarrow K^+ p \pi^- (\gamma)$

As we noted earlier, the $g11a$ dataset was swamped by events from the non-strange physics sector. For the $K^+\Sigma^0$ three-track topology, the first step towards cleaning up the data was to perform a very loose *skim* using the kinematic fitter, aimed at trimming out this large and all pervasive background.

As described in Sec. 1.3.2, we began by selecting $(+, +, -)$ events and making a physics hypothesis, where the tracks were assigned as (K^+, p, π^-) or (p, K^+, π^-) . To save computation time, we rejected events we could realistically assume to be background by placing the following two *extremely* loose cuts:

- require total missing mass to be less than 400 MeV, and,
- require missing mass off K^+ to be less than 1.45 GeV.

These cuts greatly reduced the number of ineligible background events that we kinematically fit. We then employed a 1- C kinematic fit to $\gamma p \rightarrow K^+ p \pi^- (\gamma)$ and placed a 1% confidence level cut.

Before proceeding to describe the results of this skim, we note that for any of the two combinatorial physics hypotheses we made, prior to applying kinematic fitting, we applied all the appropriate energy, momentum and tagger corrections. Also, post-skim, only events with missing mass off K^+ between 1.14 GeV and 1.3 GeV were retained. Clearly (from a simple fit as in Fig. 1.4a), the Σ^0 , for which the PDG [8] lists as mass of ~ 1.192 GeV, lies well within this range. The upper limit was intentionally kept higher to facilitate our background subtraction method.

The results of the fit are shown in Fig. 1.3. The confidence level distribution for all events is shown in Fig. 1.3(a). The distribution is almost flat above 0.5. Note that effectively (aside from the two *very* loose cuts mentioned above) we did not apply any cut at all and the $K^+\Sigma^0$ channel was completely swamped by background at this stage (Fig. 1.3(b)). Upon further requiring the total missing mass to be within ± 60 MeV, the Σ^0 peak finally showed up (this last cut is just for visualization purposes here and was not included in the actual skimming). There was still a large amount of background, most of which was removed by the 1% confidence level cut (shown in blue in Fig. 1.3(c)). Since we had not made any particle identification cuts at this stage and even our confidence level cut was pretty loose, expectedly, some amount of background leaked in, but the post-confidence-level dataset was reasonably clean (shown in red in Fig. 1.3(c)). The crucial point was that events rejected by the 1% confidence level cut (blue, Fig. 1.3(c)) hardly showed sign of any peak and we could fairly claim that we were throwing away very few “good” events.

1.6.2 Effectiveness of the Confidence Level cut

If the kinematic fitter was working perfectly and errors were Gaussian, we would expect to lose $\sim 1\%$ signal with a 1% confidence level cut. We checked this by comparing the estimated total signal from a Gaussian (signal) plus quartic (background) fit to the event distributions prior to and after making the confidence level cut. This is shown in Fig. 1.4. The cut hardly changed the signal Gaussian characteristics, the mean (~ 1.193 GeV) and the width (~ 0.011 GeV) of the signal Gaussians were almost equal in going from Fig. 1.4(a) to Fig. 1.4(b). The signal yield was then estimated by integrating the fit Gaussian function over $\mu \pm 2.5\sigma$. The estimated signal was found to be 34672 and 34335 before and after the cut, in excellent correspondence with a $\sim 1\%$ signal loss.

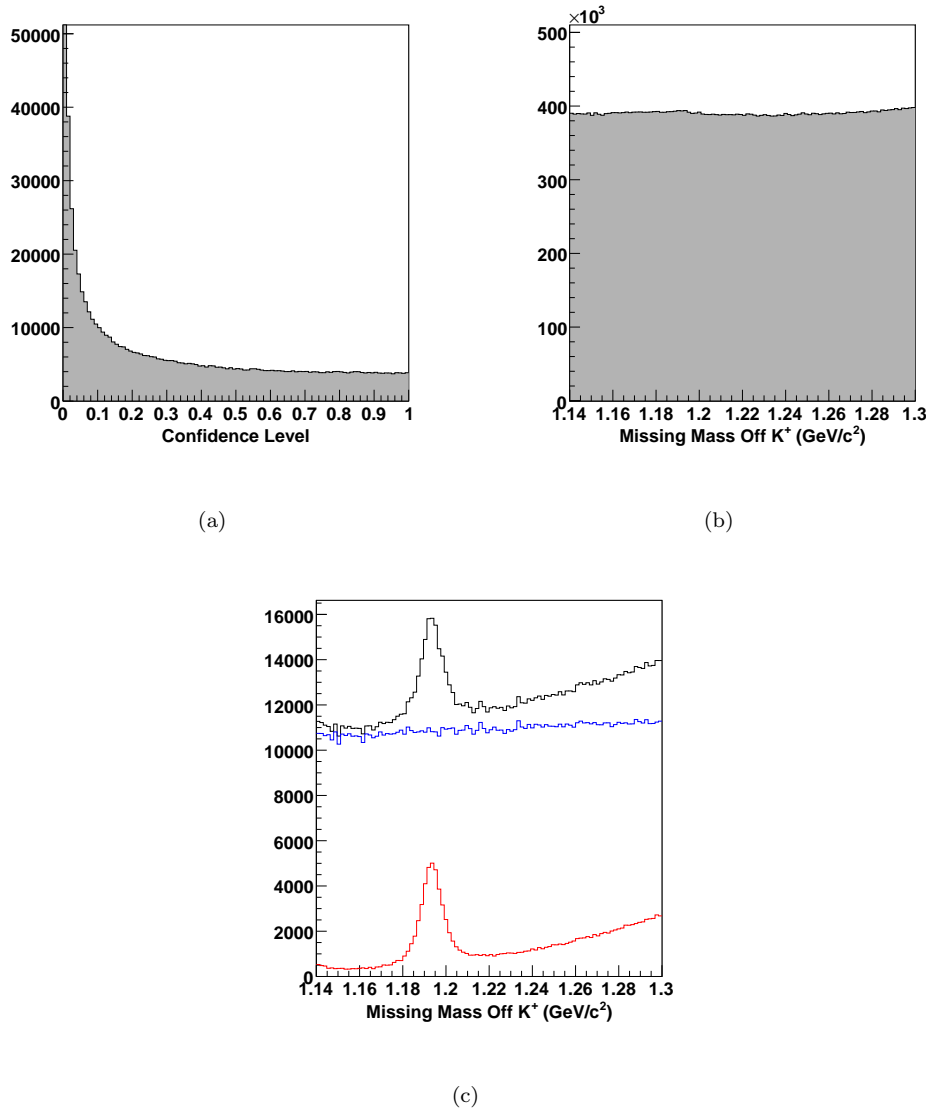


Figure 1.3: Kinematic fit to $\gamma p \rightarrow K^+ p \pi^- (\gamma)$ for the three-track topology analysis. Events are from runs 43810-43819: (a) confidence level from all the events – the distribution is fairly flat above 0.4. (b) Missing mass off K^+ distributions for all events (with the two loose skim cuts described in the text). Clearly $K^+\Sigma^0$ events are being completely swamped by background. (c) Includes now a total missing mass requirement between ± 60 MeV (see text). There is still a large amount of background, but the Σ^0 peak is visible. Shown are all the events (black), events rejected by a 1% confidence level cut (blue) and events passing the 1% confidence level cut (red).

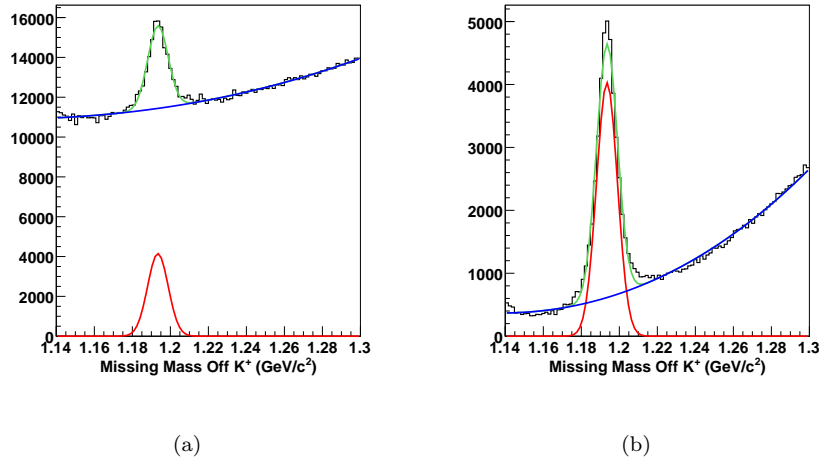


Figure 1.4: Effectiveness of the confidence level cut for the three-track dataset. Events were from runs 43810-43819 and included a $|MM| \leq 60$ MeV cut. The total fit function (in green) consisted of a Gaussian signal (in red) plus a quartic background (in blue). Fits were to the following event distributions: (a) all events, prior to confidence level cut. Estimated signal – 34672 events. (b) events surviving a 1% confidence level cut. Estimated signal – 34335 events.

1.6.3 Particle Identification – Timing Cuts

The main motivation behind the *skim* was to reduce the *g11a* dataset to a manageable size while losing as few good events as possible. We have seen that we were able to achieve this very efficiently using the kinematic fitter. To further our event selection process we had to decide upon, and fine tune the next level of cuts. Recall that the kinematic fitter used only kinematic information about the particle trajectories, the various momenta. A second source of information for particle identification (PID) was the *timing* information recorded by CLAS for the tracks. We will assume here that the negatively charged track was a π^- (positive and negative tracks bent differently in the magnetic field inside the detector and were distinguished quite easily). Then the main job of the PID method was to identify the positively charged tracks as either a proton or a K^+ and trim out the π^+ 's leaking in. By judiciously selecting timing based cuts, we were able to arrive upon a very clean dataset with minimal loss of good events.

Timing information for any particle was chiefly encoded in its *time-of-flight* (*tof*). This was the time difference between the event vertex time and time at which the particle hit the time-of-flight scintillator walls on the outer shell of the detector. Consider then the quantity

$$\Delta tof = tof_{meas} - tof_{calc}, \quad (1.5)$$

where tof_{meas} was the *measured* time-of-flight and tof_{calc} was the time-of-flight *calculated* for the mass hypothesis for the particle in question. The latter was given by

$$tof_{calc} = \frac{L}{c} \sqrt{1 + \left(\frac{m}{p}\right)^2}, \quad (1.6)$$

where L was the path length from the target to the scintillator, c was the speed of light, m was the hypothesized mass and p was the magnitude of the 3-momentum. Obviously, the closer to zero

Δtof was, the more confidence we had in our hypothesis. An equivalent way of looking at this was to look at the *calculated* mass (m_{calc}) for a particular track, given by

$$m_{calc} = \frac{p}{\gamma c} = \sqrt{\frac{p^2(1 - \beta^2)}{\beta^2 c^2}}, \quad (1.7)$$

where

$$\beta = \frac{1}{c} \times \frac{L}{tof_{meas}}. \quad (1.8)$$

For our analysis purposes, we will go back and forth between these two pictures to show the legitimacy and effectiveness of our cuts.

Note that the momenta used in Eqs. 1.5 to 1.8 were the track momenta as CLAS measured it, prior to our corrections and kinematic fitting. The other caveat to note is that the Δtof and the *calculated* mass plots that are to follow (which we based our cut selections on) included only events with missing mass off K^+ between 1.14 GeV and 1.24 GeV. That is, events with missing mass off K^+ between 1.24 GeV and 1.3 GeV, although included in the *skim*, were excluded for our PID studies. This was to ensure that events which we *apriori* knew to be background did not influence the selection of our cuts.

Fig. 1.5(a) and 1.5(b) show Δtof and m_{calc} respectively for the particle passing the kinematic fit under the K^+ hypothesis plotted against that for the particle passing under a proton hypothesis. There are a couple of things that are easy to see from the very outset:

- (1) in Fig. 1.5(a), the clusters of events around $(\pm 2, \pm 2)$, $(\pm 4, \pm 4)$, ..., were due to photons associated with the wrong *RF* bucket (recall from Chapter 2 that the accelerator delivered bunches of electrons to Hall B every 2 ns).
- (2) the band of events inside the boxed region “II” in Fig. 1.5(b) corresponded to events where our particle hypothesis called a particle a proton when it was actually a kaon, and vice versa. Likewise, in the same region one can also see $p\pi^+$ combinations which passed the kinematic cut under a K^+p hypothesis. Such incorrectly assigned events could pass the 1% confidence level cut if the tracks had a high enough momentum relative to the particle masses so that the kinematic fitter could not reliably distinguish between the two. This band actually continues vertically upwards till and beyond where the calculated mass distributions for the two combinations meet – which means also that we could not *reliably* separate signal from background in this region using timing information. To further clean the data we utilized our powerful signal-background separation method to be described in the next section.

1.6.4 A subtlety

Region “I” in Fig. 1.5(b) deserves special attention. The K^+ ’s seem to have been correctly identified here but the protons look more like K^+ ’s. One is first led to suspect that these events somehow resulted from the production of double strangeness cascade events. However, firstly, it is hard to imagine that such events would pass even a loose 1% confidence level cut from a kinematic fit to zero missing mass. Secondly, we have constrained the missing mass off K^+ to be less than 1.24 GeV and any double strangeness exotic particle itself would have a much higher mass. Thirdly, and most importantly, the missing mass off K^+ for these events contain a very clean peak around the Σ^0 mass (Fig. 1.6(a)).

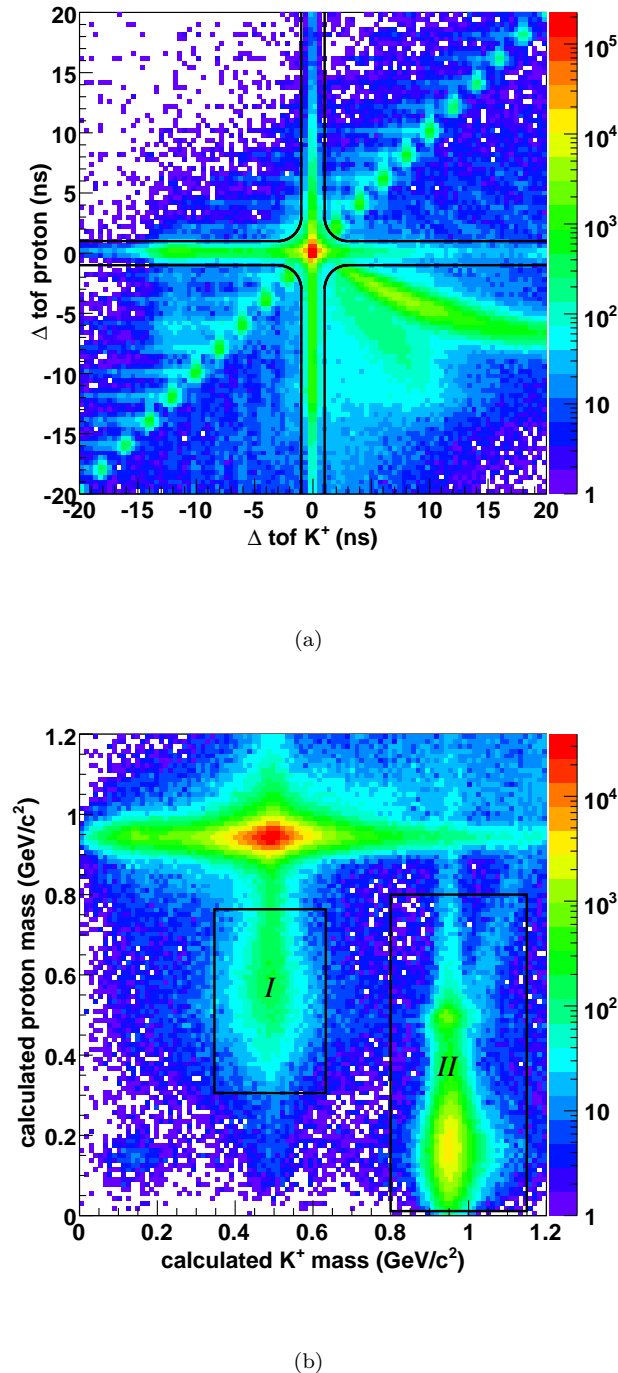


Figure 1.5: Cumulative skimmed three-track dataset: (a) Δtof and (b) calculated masses for p and K^+ (see text for regions marked “I” and “II”). The “iron cross” in (a) shows our PID timing cut. Only events with missing mass off K^+ between 1.14 GeV and 1.24 GeV were included for these plots.

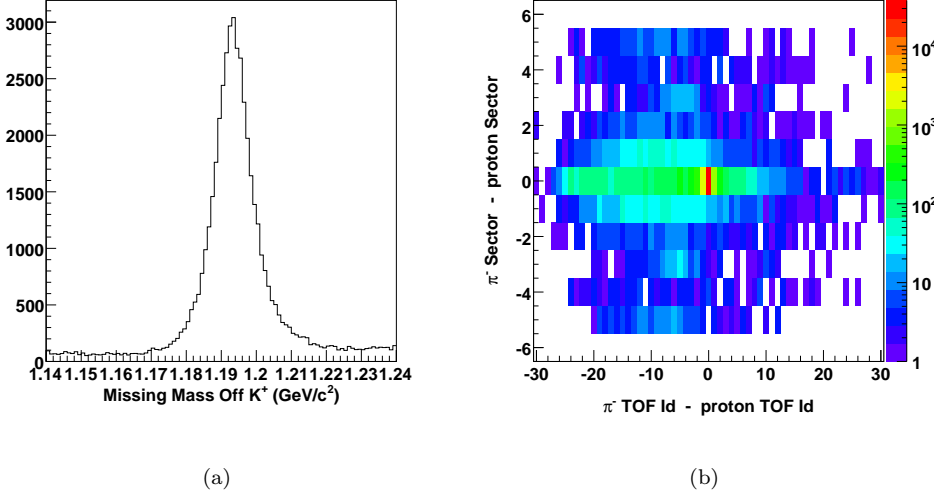


Figure 1.6: Incorrect Proton timing for region “I” of Fig. 1.5(b): (a) Missing Mass off K^+ for these events (b) sector Id difference vs TOF Paddle Id difference between π^- and proton – the blob at the center corresponds to both the tracks hitting the same physical TOF counter.

Upon further investigation it was found that these events *were* good $K^+\Sigma^0$ events after all, save that CLAS recorded the proton timing information incorrectly. Recall that the breakup momentum of the Λ particle is relatively small. This means that the breakup angle in the laboratory frame was also small. The proton and the π^- coming from the Λ decay would then be almost collinear, as seen in the laboratory/CLAS frame and could hit the same TOF scintillator paddle. This is indeed what happened for these particular events, as shown in Fig. 1.6(b). The big blob at $(0,0)$ is where CLAS recorded the same TOF paddle Id and the same sector Id, and thus the same physical TOF paddle, for the proton and the π^- tracks. TOF scintillators in CLAS are single-hit counters. CLAS would therefore assign the *same* one time-of-flight to both the proton and the π^- . The π^- being lighter, typically arrived first and was assigned the correct time-of-flight. The proton which follows was then assigned a shorter time-of-flight which reduced its calculated mass, bringing it closer to the kaon mass region. However, as long as we were careful not to use the proton timing information anywhere else in our analysis, we could still include these events. Note that the K^+ goes completely unaffected by this.

1.6.5 The “Iron-cross” Cut

The PID cut that we decided upon for the three-track analysis is shown by the quadruplet of black lines in Fig. 1.5(a) taking the shape of an “iron-cross”. That is, we rejected events lying outside the cross. The cut was essentially based on the idea of accepting tracks with $\Delta tof \leq 2\text{ns}$, executed in a 2-dimensional fashion. The cut was meant to be both loose enough to minimize signal loss but stringent enough to reduce the background substantially. The result of the cut is shown in Fig. 1.7. Fig. 1.8(a) shows the calculated mass distribution for events rejected by our cut while Fig. 1.8(b) shows that for events passing the cut. One could ask here whether our cut is too loose and we should also trim out region “I” (containing $\pi^+ p$ background) and region “II” (containing $p p$ background) in Fig. 1.8(a). However plotting the missing mass off K^+ for these regions (Fig. 1.9), we find that there is sufficient amount of signal in these regions to retain them. Furthermore we show in Sec. 2.4 that

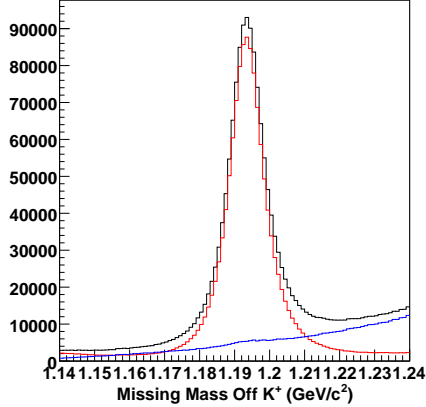


Figure 1.7: PID cut on the cumulative three-track skimmed dataset. In red are events that passed the cut and in blue are the events rejected by the cut.

for the Accepted Monte Carlo, which we know to have almost negligible $\pi^+ p$ and $p\bar{p}$ background, also have events populating these regions. The few events remaining in region “III” (Fig. 1.8(a)), though can reliably be claimed to have a wrong PID assignment, will be retained at this stage to give enough leverage to our background fitter for pulling out the background underneath region “II”.

This completes all our PID cuts for the three-track dataset. All remnant background will be removed by our signal-background separation method (Sec. 1.11).

1.6.6 PID uncertainty

As evident from Fig. 1.7, our PID cuts throw away very few good events. We can make an estimate of how much signal we are throwing away by fitting the missing mass off K^+ distribution before the cut and that for events rejected by the cut with a Gaussian plus a quartic. This is shown in Fig. 1.10. Fig. 1.10(a) shows the fit to the entire skimmed dataset. The total fit function seems to slightly fall short of the total histogram peak though the background function describes the background pretty well. We thus chose to estimate the total signal by subtracting the background integral from the total histogram in the range $[\mu - 2.5\sigma, \mu + 2.5\sigma]$, where μ ($= 1.1935$ GeV) and σ ($= 0.005$ GeV) are from the signal Gaussian fit. Our signal estimate is thereby found to be ~ 1.068 million events.

Next, we fit the distribution of events rejected by the cut. The small signal we are trying to pull out here made the fits sensitive to the starting values of the fit parameters as well as range that the fit was being run over. A good fit was found on running it between 1.175 GeV and 1.215 GeV and is shown in Fig. 1.10(b). For this range, the total fit function seems to match the event distribution very well in this case. The estimated signal content is thus found by a 2.5σ integral of the signal Gaussian ($\mu = 1.1934$ GeV, $\sigma = 0.004$ GeV) about the mean and amounts to ~ 6610 events. The percentage of signal lost by the PID cuts is therefore $\sim 0.62\%$. We will quote this as the uncertainty in our PID scheme for the three-track analysis.

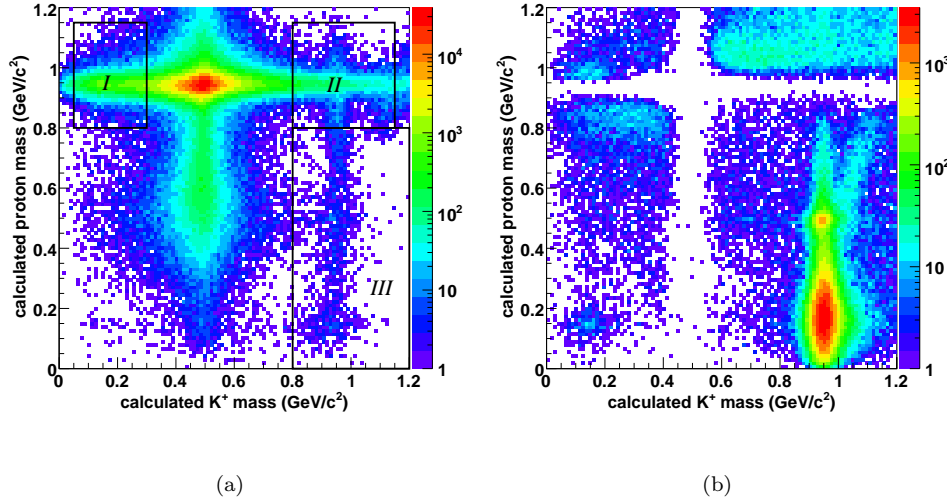


Figure 1.8: Calculated masses after the PID cut for the cumulative skimmed three-track dataset: (a) events passing the cut. Regions marked as “I” and “II” here contains possible $\pi^+ p$ and $p\bar{p}$ background respectively which survive the cut (see Fig. 1.9). Region “III” is also retained at this point (see text). (b) events rejected by the cut.

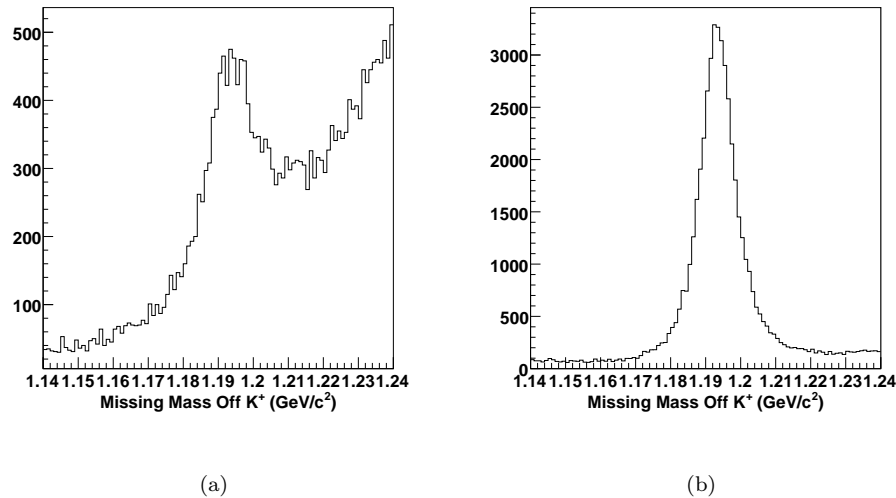


Figure 1.9: Missing Mass off K^+ for events in regions “I” and “II” from Fig. 1.8a: (a) Region “I” – $\pi^+ p$ background mostly (b) Region “II” – possible $p\bar{p}$ background. There is sufficient signal in both regions to not throw them away completely. The background remaining will instead be removed by our signal-background separation method.

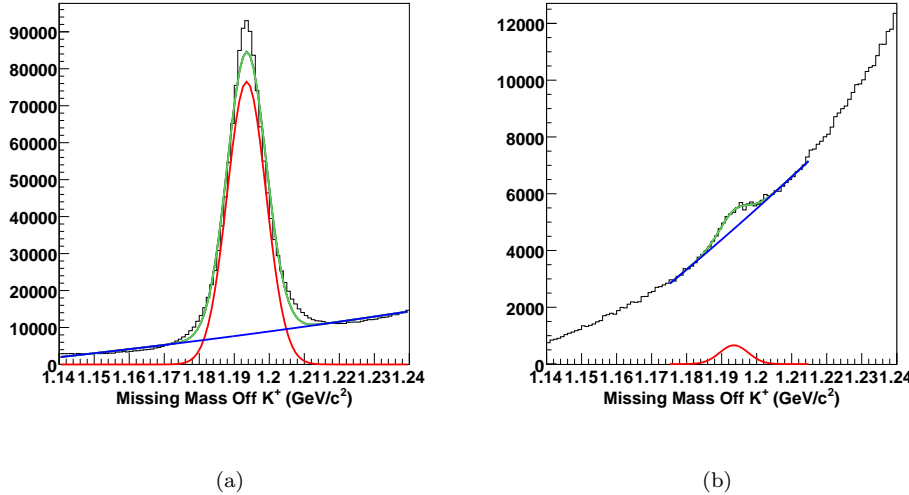


Figure 1.10: PID uncertainty for the three-track topology. Fits were to a Gaussian signal (red) plus quartic polynomial (blue). In green is the total fit function. (a) Cumulative skinned dataset before PID cuts. Estimated signal ~ 1.068 million (b) Events rejected by PID cuts. Estimated “signal” being lost due to PID cut ~ 6610 . The ratio $\sim 0.62\%$ is the estimated uncertainty in our PID scheme.

1.6.7 $K^+\Lambda$ Background Removal

Recall from Sec. 1.6.1 that during kinematic fitting, we fit each event to a $K^+p\pi^-$ hypothesis with zero total missing mass. While this was appropriate for $K^+p\pi^-$ events with a missing outgoing photon, events with the same topology but with *no* missing particle would also pass the kinematic fit cuts. In the present context, the latter set of events would originate from a long $K^+\Lambda$ tail. There are two kinematic regimes where this would occur more predominantly.

First, note that the higher one goes in \sqrt{s} , the higher the momenta of the various decay particles generally get. Momentum resolution in CLAS worsens with increasing particle momenta. Thus, the $K^+\Lambda$ signal peak (at ~ 1.115 GeV) widens as we go higher in \sqrt{s} and the $K^+\Lambda$ tail will encroach more and more under the $K^+\Sigma^0$ peak. This effect is clearly visible in going from Fig. 1.11a to 1.11b. Second, the breakup energy (and correspondingly, the breakup angle) of Σ^0 is small (~ 77 MeV). This means most of the time the Λ will continue to move in the same direction as the Σ^0 it originates from. When this opening angle is small enough, the kinematic fitter *can* end up wiggling the various momenta to make a Λ look like a Σ^0 . Fig. 1.11(c) demonstrates this effect. Note that given the information which is supplied to the fitter, this is not a pathology at all but a peculiarity of the kinematics.

Given the above considerations, we expect to see the Λ tail in higher \sqrt{s} and smaller Σ^0 breakup angle regions. Note that for the plots in Fig. 1.11, we have already applied our 1% confidence level (from a kinematic fit to $\gamma p \rightarrow K^+p\pi^-$, zero total missing mass) and PID cuts, which means that neither of these cuts removed the $K^+\Lambda$ background. This was actually a good sign, because the way we tuned these cuts, neither of them were *supposed* to remove $K^+\Lambda$ events in the first place.

The solution to the problem at hand again employed the kinematic fitter. To efficiently skim out the $K^+\Lambda$ events, we could fit every event which we included in our skim to $\gamma p \rightarrow K^+p\pi^-$ with *nothing missing* – that is, we fit to every component of the missing 4-momenta being zero. This

was a much tighter 4-*C* fit than fitting to a zero total missing mass (a 1-*C* fit). Real $K^+\Sigma^0$ events would have near zero confidence level to this fit while $K^+\Lambda$ events would have evenly distributed confidence levels over the range (0, 1]. Fig. 1.11(d) demonstrates this, where we have plotted the confidence level from $\gamma p \rightarrow K^+ p\pi^-$ (nothing missing) fit against missing mass off K^+ . The higher confidence level region corresponds to the $K^+\Lambda$ tail. We can thus effectively remove the $K^+\Lambda$ background by rejecting events with confidence level (from a kinematic fit to $\gamma p \rightarrow K^+ p\pi^-$, nothing missing) greater than 0.1% (Fig. 1.11(e)). The effect of the cut is shown in Fig. 1.11(f) – our cut is remarkably efficient in skimming out the $K^+\Lambda$ background with minimal signal loss (the blue histogram in 1.11f for events rejected by the cut, representing a long $K^+\Lambda$ tail, shows no sign of a Σ^0 peak).

Note that to accentuate the effect of the $K^+\Lambda$ background we have used events only with higher \sqrt{s} (between 2.7 and 2.84 GeV) for the plots shown in Fig. 1.11(b) through 1.11(f).

1.7 Event Selection – $K^+\Sigma^0$ two-track topology

1.7.1 “Dalitz” Cut

Consider the overall decay $\Sigma^0 \rightarrow \Lambda\gamma \rightarrow p\pi^-\gamma$, treating it as a three-body decay. In the standard “Dalitz” analysis of a three-body decay $M \rightarrow m_1 m_2 m_3$, for a given value of the invariant mass m_{12} , m_{23} is bound between

$$(m_{23}^2)_{max} = (E_2^* + E_3^*)^2 - \left(\sqrt{E_2^{*2} - m_2^2} - \sqrt{E_3^{*2} - m_3^2} \right)^2 \quad \text{and} \quad (1.9a)$$

$$(m_{23}^2)_{min} = (E_2^* + E_3^*)^2 - \left(\sqrt{E_2^{*2} - m_2^2} + \sqrt{E_3^{*2} - m_3^2} \right)^2, \quad (1.9b)$$

where

$$E_2^* = (m_{12}^2 - m_1^2 + m_2^2) / 2m_{12} \quad \text{and} \quad (1.10a)$$

$$E_3^* = (M^2 - m_{12}^2 - m_3^2) / 2m_{12}. \quad (1.10b)$$

In our case, if we assign M as Σ^0 , m_1 as p , m_2 as π^- , m_3 and γ , m_{12} is the ($p\pi^-$) mass corresponding to the Λ mass. Then m_{23} is the invariant ($\pi^-\gamma$) mass, which is also the total missing mass $MM(pK^+)$ for the two-track topology. Substituting the physical values of the masses, we find the condition:

$$0.176 \text{ GeV} \leq m_{23} \leq 0.251 \text{ GeV}. \quad (1.11)$$

We call a cut based on this requirement, a “Dalitz” cut.

1.7.2 Initial Skim

Event selection for the two-track topology followed the general itinerary set up earlier for the three-track case. We chose events of the type (+, +) having at least two positively charged tracks. We then made the *physics hypotheses* (p, K^+) and (K^+, p) for these two tracks, looping over all possible combinations. The event and the K^+ vertices were set as for the three-track case, but since information on the π^- track was unavailable, we were not able to locate the Λ decay vertex any longer. As our next best approximation, we set the p vertex as the event vertex. Energy, momentum and tagger corrections were then applied corresponding to each hypothesis.

Since both the outgoing photon and the π^- momenta remained unknown, we could not take advantage of the kinematic fitter. For our initial *skim*, we place the following four cuts:

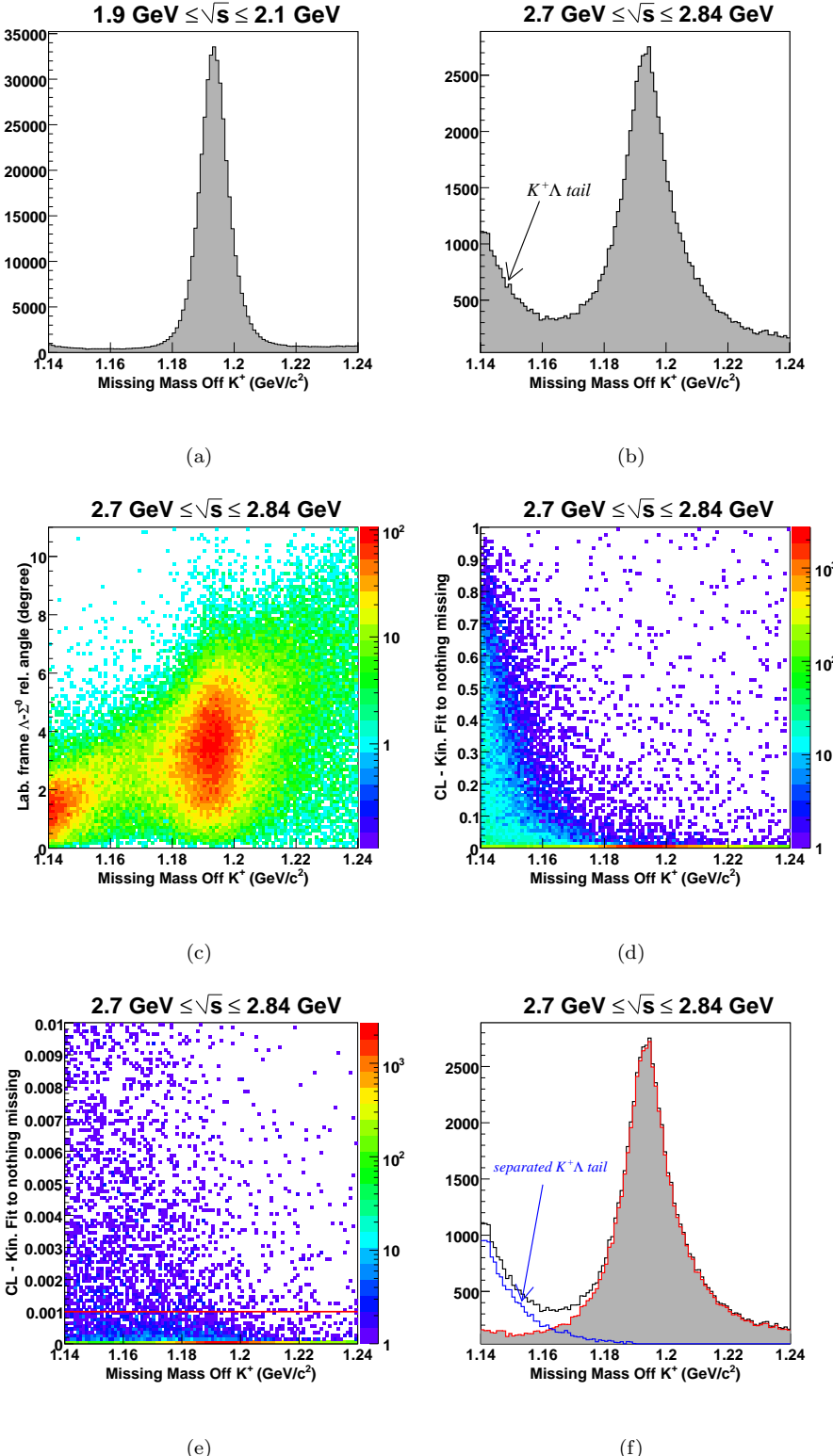


Figure 1.11: $K^+\Lambda$ background removal (three-track topology): $K^+\Lambda$ tail more prominent at higher \sqrt{s} (compare (a) and (b)) and smaller relative angle between Σ^0 and Λ (from (c)). (d) and (e) show the 0.1% CL cut we make (red horizontal line in (e)) and (f) shows the efficiency of the cut. See text for details.

- missing mass off K^+ between 1.14 GeV and 1.3 GeV,
- calculated mass of p between 0.3 GeV and 1.2 GeV,
- calculated mass of K^+ between 0.2 GeV and 0.85 GeV and
- total missing mass between 0.15 GeV and 0.28 GeV.

These cuts were been intentionally kept loose at this stage to minimize the loss of good events at a minimum. Cut (4) corresponded to the “Dalitz” cut after allowance for energy-momentum resolution. Fig. 1.13 shows the signal shape, calculated masses and total missing mass in the cumulative skimmed dataset. The total number of events which passed the skim was ~ 6.4 million.

1.7.3 Particle Identification – 2-D Calculated Mass and “Dalitz” Cut

Our first PID cut consists of a 2-D cut on the calculated masses of the hypothesized K^+ and p tracks. The cut is shown in Fig. 1.12a – events lying outside the quadruplet of black lines are removed. The second cut we employ is a “Dalitz” cut, accepting events only that satisfy the criterion:

$$0.16 \text{ GeV} \leq MM(pK^+) \leq 0.265 \text{ GeV}. \quad (1.12)$$

The two limits are marked by the two horizontal lines in Fig. 1.12c. Fig. 1.12b and 1.12d show the effect of the two cuts individually.

Fig. 1.13 shows the combined effect of both cuts (the histograms include around a third of the full 2-track dataset). The black histogram is the skimmed dataset. In green are events that pass the calculated mass cut. Events retained after a subsequent application of the Dalitz cut appears in red. The blue histogram shows the events that fail either cut. The estimated “signal” for the skimmed dataset and for events failing the PID cuts are ~ 2.28 million and $\sim 41,738$ respectively. Thus the upper limit on the signal loss due to the PID cuts is $\sim 1.8\%$. We quote this as our PID error for the two-track topology.

1.8 Event Selection – ϕp Charged-mode Topology

1.8.1 Kinematic Fitting of $\gamma p \rightarrow K^+(K^-)p$

For the charged-mode, the first step in the event selection process was a kinematic fit to $\gamma p \rightarrow K^+(K^-)p$. This was a 1-C fit to total missing mass $m_{K^-} = 0.493$ GeV with the K^- 4-momentum reconstructed as the total missing momentum. As always, both combination of proton and K^+ assignments to the two positively charged tracks were looped over. To save computation time, we placed an initial *extremely* loose constraint of $|MM(p) - 1.019| \leq 0.5$ GeV to select out possible ϕ events. Fig. 1.14a shows the confidence level distribution. To avoid an overwhelming amount of background, we have placed an additional $|MM - 0.493 \text{ GeV}| \leq 100 \text{ MeV}$ cut here (this is only for illustrative purposes and was not used during the actual kinematic fitting). Fig. 1.14b shows the effect of placing a 10% confidence level cut. The red histogram shows the $MM(p)$ distribution after the cut and the blue histogram shows the events rejected by the cut.

To facilitate further analysis, a “skimmed” ϕ dataset was formed by applying the 10% confidence level cut and two additional calculated mass cuts of $0.4 \text{ GeV} \leq m_{calc,p} \leq 1.2 \text{ GeV}$ and $0.2 \text{ GeV} \leq m_{calc,K^+} \leq 0.8 \text{ GeV}$. The dataset was binned in $\sqrt{s} = 10$ MeV-wide energy bins after this.

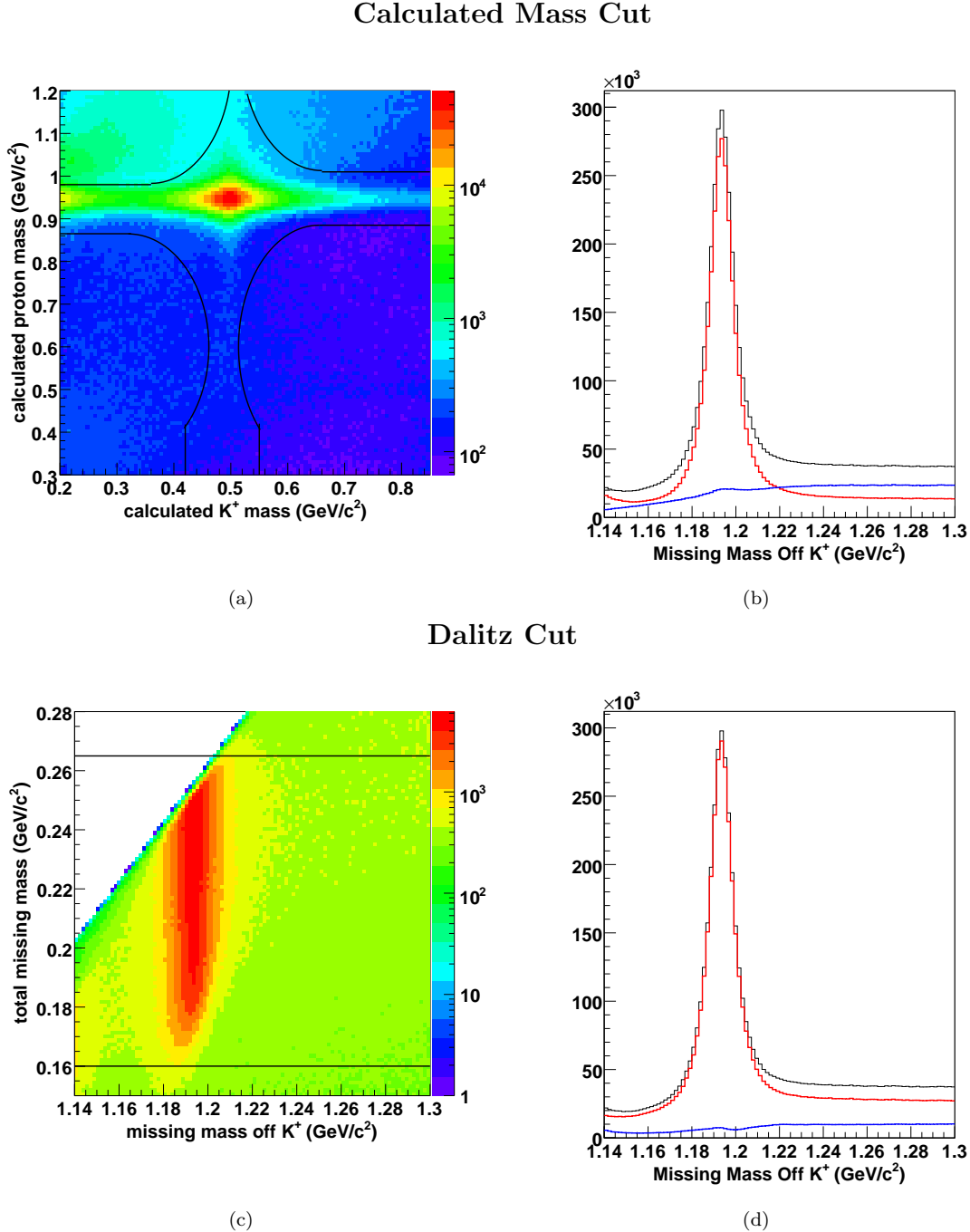


Figure 1.12: PID cuts on the skimmed two-track dataset: (a) Calculated masses for proton and the kaon. Events lying outside the quadruplet of black lines are rejected. (b) Effect of the calculated mass cut – the black histogram is the original skimmed dataset, in red are the accepted events and in blue are the rejected events. (c) Total missing mass (which, for real $K^+\Sigma^0$ events, should correspond to the invariant $(\pi^-\gamma)$ mass) plotted versus missing mass off K^+ . The two horizontal lines show the “Dalitz” cut – only events lying in between the two lines are kept. (d) Effect of the Dalitz cut – black histogram is the original skimmed dataset, in red are the accepted events and in blue are the rejected events.

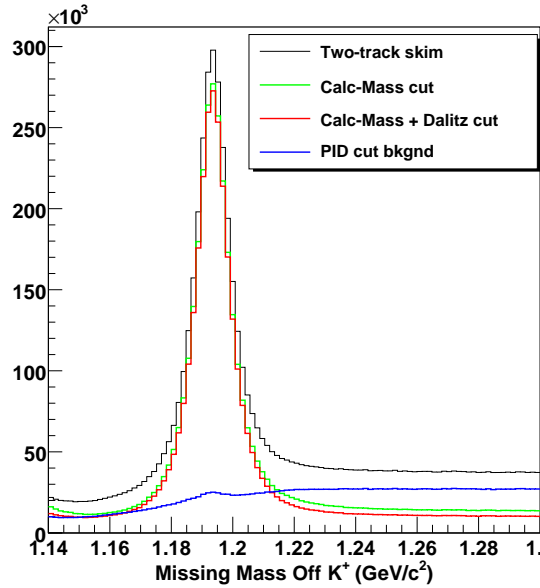


Figure 1.13: Two-track topology, PID cuts: green histogram shows just the calculated mass cut. Red histogram shows the effect of subsequently applying the Dalitz cut. The blue histogram is the background removed after both cuts are applied. Total signal loss is $\sim 1.8\%$.

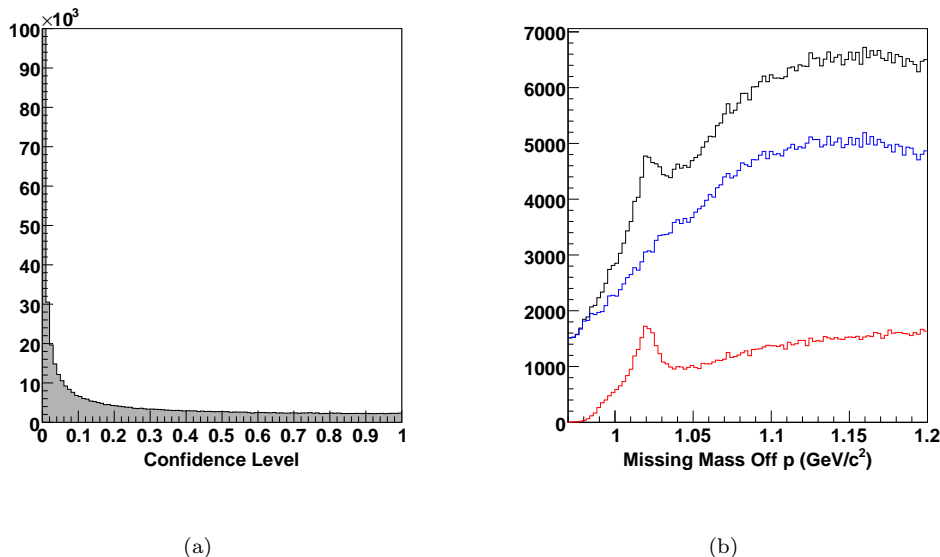


Figure 1.14: Kinematic fit to $\gamma p \rightarrow K^+(K^-)p$ for the ϕ charged-mode topology: (a) shows the confidence level distribution and (b) shows the effect of placing a 10% confidence level cut. In blue are the events rejected and in red are the events accepted by the cut.

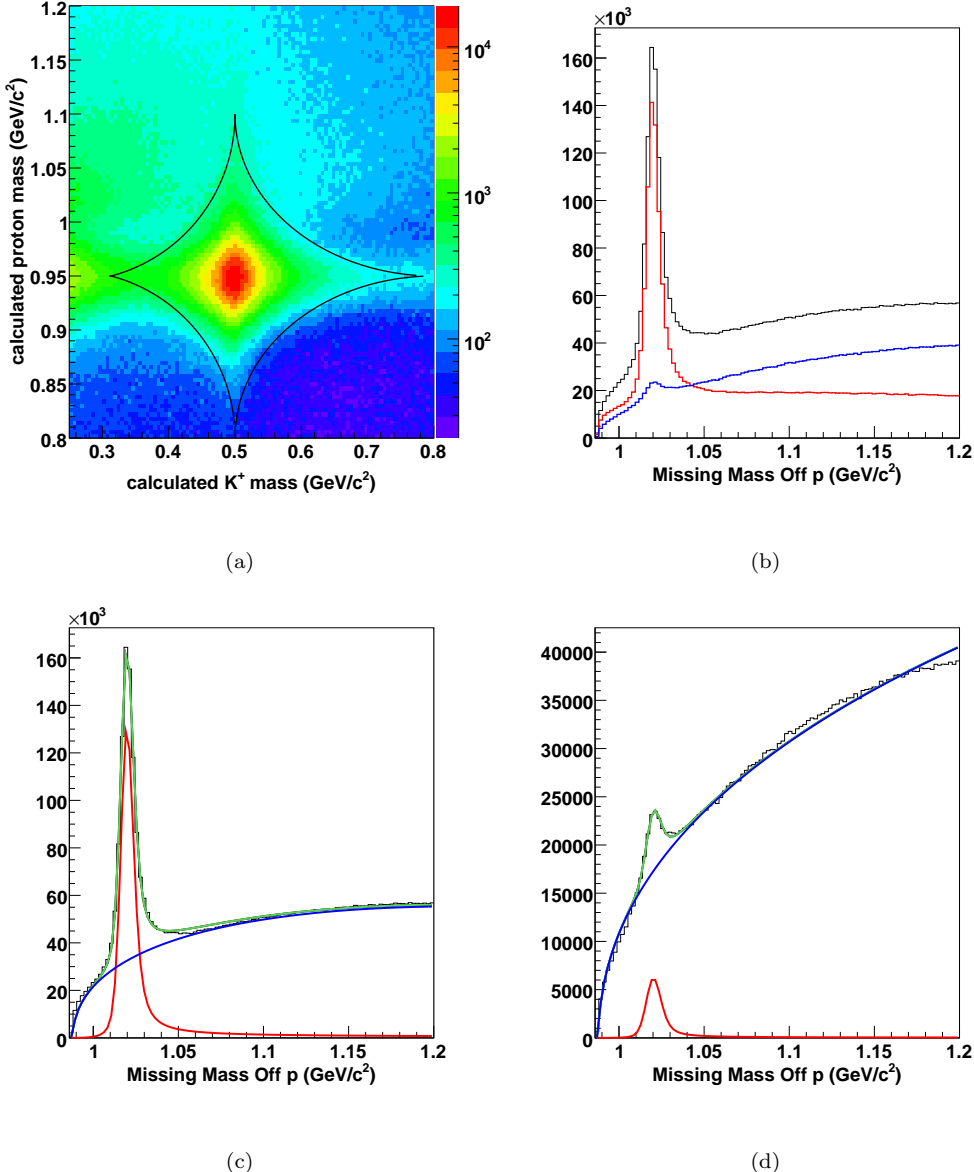


Figure 1.15: Timing cuts for the ϕ charged-mode topology: (a) shows the calculated mass distributions for the K^+ and proton. Events lying outside the quadruplet of black curves were rejected. (b) shows the effect of application of the timing cut on the entire skimmed dataset. In blue are the events rejected and in red are the events accepted by the cut. (c) shows a fit to the total distribution prior to the cut and (d) shows a fit to the set of rejected events (green shows the total fit function; red, the signal fit function; blue, the background fit function). The overall estimated signal loss due to the timing cut was $\sim 5\%$.

1.8.2 Particle Identification – Timing Cuts

Fig. 1.15a shows the calculated mass distribution of p and K^+ . Events lying outside the quadruplet of black curves in Fig. 1.15a were removed. Fig. 1.15b shows the effect of placing this cut. In red are the events accepted, while in blue are the events rejected by our timing cut. Note that in general, the ϕp channel had a larger amount of background than $K^+\Sigma^0$. Consequently our cuts for ϕp event selection were tighter than in the $K^+\Sigma^0$ case.

Fig. 1.15c shows a fit to the $MM(p)$ distribution prior to the application of the timing cut. The signal function (in red) was a modified Voigtian to incorporate the assymmetric ϕ lineshape while the background function (in blue) was taken to be of the form $f(x) = a\sqrt{x^2 - 4m_K^2} + b(x^2 - 4m_K^2)$. The estimate signal prior to the timing cut was ~ 0.561 million events. Fig. 1.15d shows similar fits to the set of rejected events. The estimated signal was $\sim 30,000$. The estimated signal loss due to the application of the timing cut was therefore $\sim 5\%$. We quote this as the upper limit of our PID systematic error for the ϕp charged-mode topology.

1.8.3 $\Lambda(1520)$ Cut

Consider the reaction chain $\gamma p \rightarrow K^+ \Lambda(1520) \rightarrow K^+ K^- p$. Since the final state particles in this reaction are the same as in the ϕp charged-mode topology, the two reactions can overlap in certain regions of phase space. For further insight, we look back at our $K^+\Sigma^0$ “Dalitz” cut discussion in Sec. 1.7.1. In Eq. 1.10b, if we put $M = \sqrt{s}$, $m_1 = m_{K^+}$, $m_2 = m_{K^-}$, $m_{12} = M(K^+, K^-) = m_\phi$ and $m_3 = m_p$, we obtain a \sqrt{s} dependent constraint on the minimum and maximum values of $m_{23} = M(K^-, p)$. Fig. 1.16a shows the variation of the $m_{23}(\sqrt{s})$ limits with \sqrt{s} , where $M(K^- p) = 1.52$ GeV is shown by a horizontal dashed line in red. Therefore, in the region roughly corresponding to $2.0 \text{ GeV} \leq \sqrt{s} \leq 2.2 \text{ GeV}$, the $K^+\Lambda(1520)$ and ϕp channels can kinematically overlap in phase space.

Now, in the region of overlap, if the $K^+\Lambda(1520)$ background does not interfere with ϕp production process, our background subtraction procedure (Sec. ??) should be able to remove the $K^+\Lambda(1520)$ events under the ϕ mass peak. If, however the $K^+\Lambda(1520)$ and the ϕp channels do interfere, then the situation becomes more complicated. To study this effect, we considered the following two cuts:

- \sqrt{s} dependent cut on $M(K^-, p)$ at the $m_{23}(\sqrt{s})$ limits described above (as shown in Fig. 1.16a), and/or
- hard cut around the $\Lambda(1520)$ mass: $|M(K^-, p) - 1.52 \text{ GeV}| \leq \delta$,

where δ was taken as 5, 10 or 15 MeV. At this point, we simply note that the current analysis did *not* find any appreciable effect from $K^+\Lambda(1520)$ interference. Our differential cross sections remained unchanged (within the limits of statistical precision) with or without the application of the $\Lambda(1520)$ removal cuts. However, it was important to study this in detail.

1.9 Event Selection – ϕp Neutral-mode Topology

1.9.1 Kinematic Fitting of $\gamma p \rightarrow p\pi^+\pi^-(K_L^0)$

For the neutral-mode topology, a kinematic fit to $\gamma p \rightarrow p\pi^+\pi^-(K_L^0)$ was first performed. This was a 1-C fit to total missing mass $m_{K^0} = 0.497$ GeV with the K_L^0 4-momentum reconstructed as the total missing momentum. The K_S^0 was reconstructed as the sum of the π^+ and π^- 4-momenta and both combination of proton and π^+ assignments to the two positively charged tracks were looped over. The confidence level distribution is shown in Fig. 1.17a. Fig. 1.17b shows the effect of a 10%

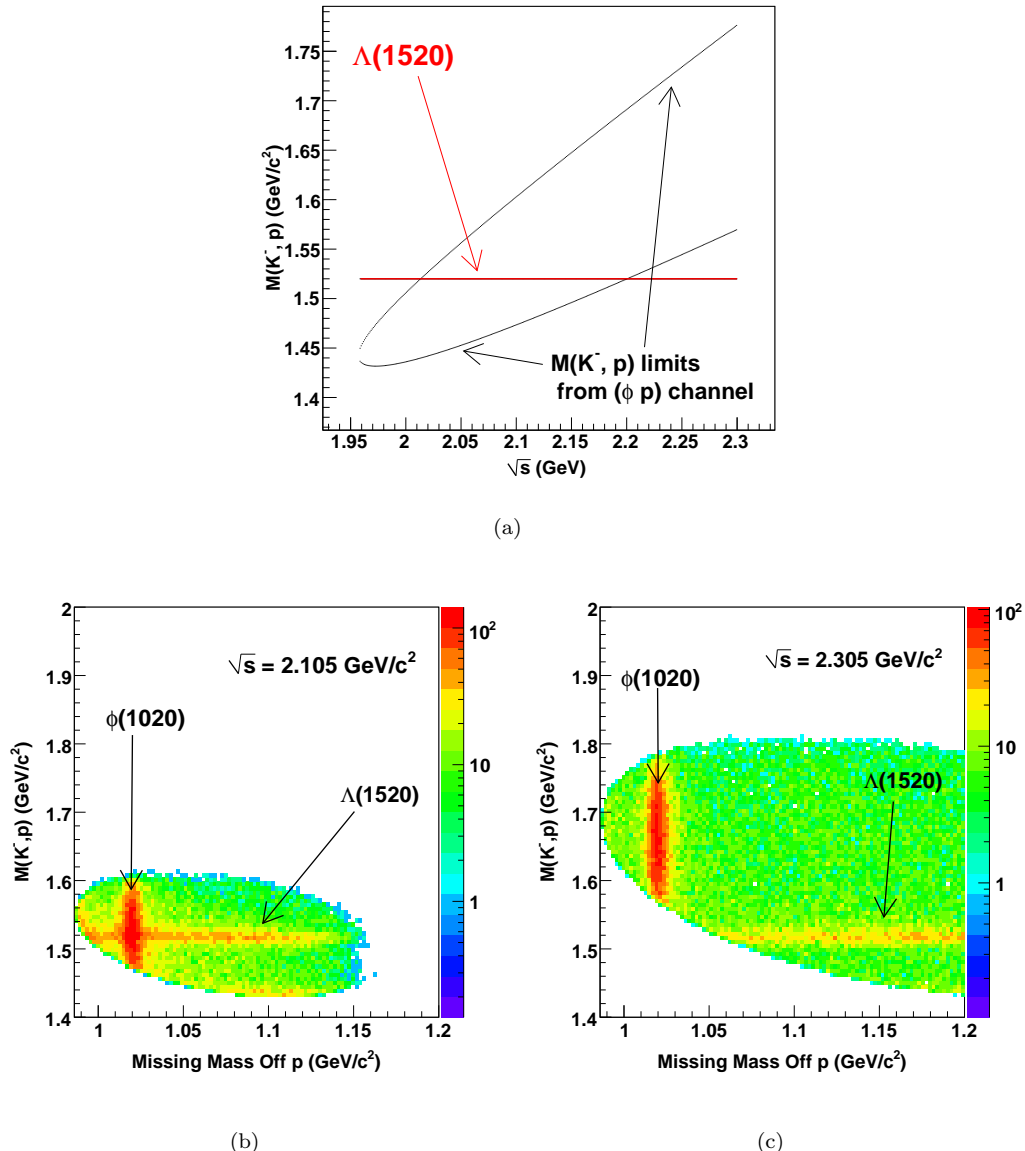


Figure 1.16: In the process $\gamma p \rightarrow \phi p \rightarrow K^+ K^- p$, the invariant mass $M(K^-, p)$ is constrained to lie between the two black curves as shown in (a), depending on \sqrt{s} . Between $2.0 \text{ GeV} \leq \sqrt{s} \leq 2.2 \text{ GeV}$, $M(K^-, p) = 1.52 \text{ GeV}$ falls within these limits and the ϕp and $K^+\Lambda(1520)$ channels are kinematically allowed to overlap in phase space. (b) shows $M(K^-, p)$ vs. $MM(p)$ in the overlap region, while (c) shows the same in a region where the $\Lambda(1520)$ and ϕ are separated.

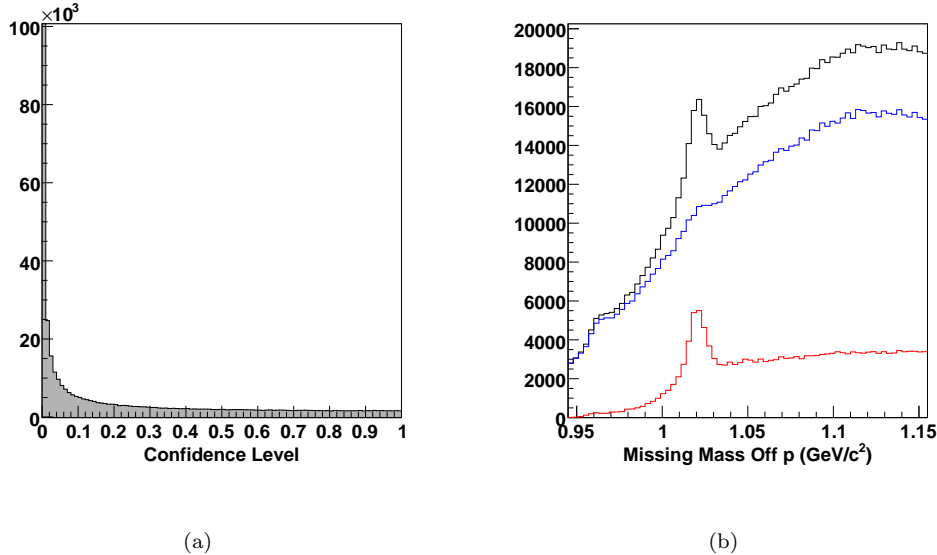


Figure 1.17: Kinematic fit to $\gamma p \rightarrow p\pi^+\pi^- (K_L^0)$ for the ϕ neutral-mode topology: (a) shows the confidence level distribution and (b) shows the effect of placing a 10% confidence level cut. In **blue** are the events rejected and in **red** are the events accepted by the cut.

confidence level cut. The **blue** histogram are the events rejected and in **red** are the events that passed the cut.

1.9.2 Timing Cuts

Given that the neutral-mode was a three-track topology, in conjunction with the inherently low statistics for the ϕp channel, we employed PID cuts that were as loose as possible. Fig. 1.18a shows the $\Delta\text{tof}_{\text{proton}}$ plotted against Δtof_{π^+} for the entire skimmed neutral-mode dataset along with the “iron-cross” cut described earlier in Sec. 1.6.5. The effect of applying this cut is shown in Fig. 1.18b. Events that passed the cut are in **red**, while those rejected are in **blue**. The latter shows no sign of a peak around $MM(p) = 1.019 \text{ GeV}$, depicting the fact that the cut was extremely loose.

1.9.3 K_S^0 Selection Cut

Fig.1.19a shows the invariant $M(\pi^+, \pi^-)$ mass of the skimmed ϕp neutral-mode dataset, after the application of the timing cuts. The peak around 0.5 GeV represents the K_S^0 mass. Fig.1.19b shows the distribution of $M(\pi^+, \pi^-)$ with $MM(p) \leq M(\pi^+, \pi^-) \leq 0.505 \text{ GeV}$. Fig.1.19c shows the effect of a $0.49 \text{ GeV} \leq M(\pi^+, \pi^-) \leq 0.505 \text{ GeV}$ K_S^0 selection cut. The **red** histogram are the events that passed the cut, while the **blue** histogram are the events failing the cut. It is clear from Fig.1.19b that the majority of the remnant background after the (timing + K_S^0 selection) cut corresponded to real $K_S^0 K_L^0 p$ events where the K_S^0 and K_L^0 did *not* come from a ϕ .

1.9.4 $M(p, K_S^0)$ and $M(p, K_L^0)$ Dalitz Cut

The last cut that we considered for the neutral-mode was a combined cut on $M(p, K_S^0)$ and $M(p, K_L^0)$ based on the same considerations as in Secs. 1.7.1 and 1.8.3. In Eq. 1.10b, if we put $M = \sqrt{s}$,

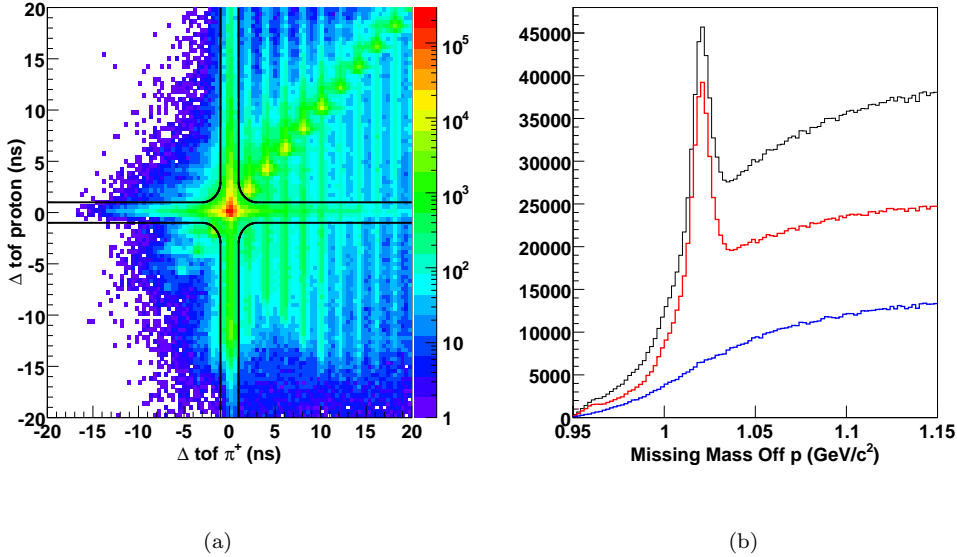


Figure 1.18: Timing cuts for the ϕp neutral-mode topology: (a) shows the “iron-cross” cut on proton- π^+ Δtof distribution. The effect of the cut is shown in (b). The rejected events in blue hardly show any sign of a peak at $MM(p) = 1.019 \text{ GeV}$, since the cut was very loose. The set of events that passed the cut is shown in red.

$m_{12} = M(K_L^0, K_S^0) = m_\phi$, $m_3 = m_p$ and $m_1 = m_2 = m_{K^0}$, we obtain a \sqrt{s} dependent constraint on the range of values for $m_{32} = M(p, K_S^0)$ or $m_{32} = M(p, K_L^0)$. The result of applying a cut based on these limits is shown in Fig. 1.20.

1.10 Detector Performance Cuts

A crucial part of our analysis depended on how well we understand the acceptance of the CLAS detector. Our acceptance calculations employed Monte Carlo $K^+\Sigma^0/\phi p$ events and GSIM, a GEANT based simulation of the CLAS detector, as described in the next chapter. At this point, we simply note that if there are regions, or particular elements, of the detector which were not well understood, to allow a reliable acceptance calculation, they had be removed from our analysis. This section deals with these types of cuts that went into our analysis.

1.10.1 Minimum Proton Momentum Cut

Slow moving protons, because of greater susceptibility to interactions with the detector material, were difficult to model accurately. Studies by Matt Bellis, a then post-doctoral researcher at CMU compared the acceptance of the data and Monte Carlo, both of which were calculated empirically using the $\gamma p \rightarrow p\pi^+\pi^-$ channel.

For example, one could require only a π^+ and a π^- to be detected and kinematically fit to a missing proton. For events passing this fit with a high enough confidence level, one could then cross check whether a proton was *actually* detected in the correct sector in CLAS or not. Using a large enough sample of events, the acceptance of each particle type could be calculated in each

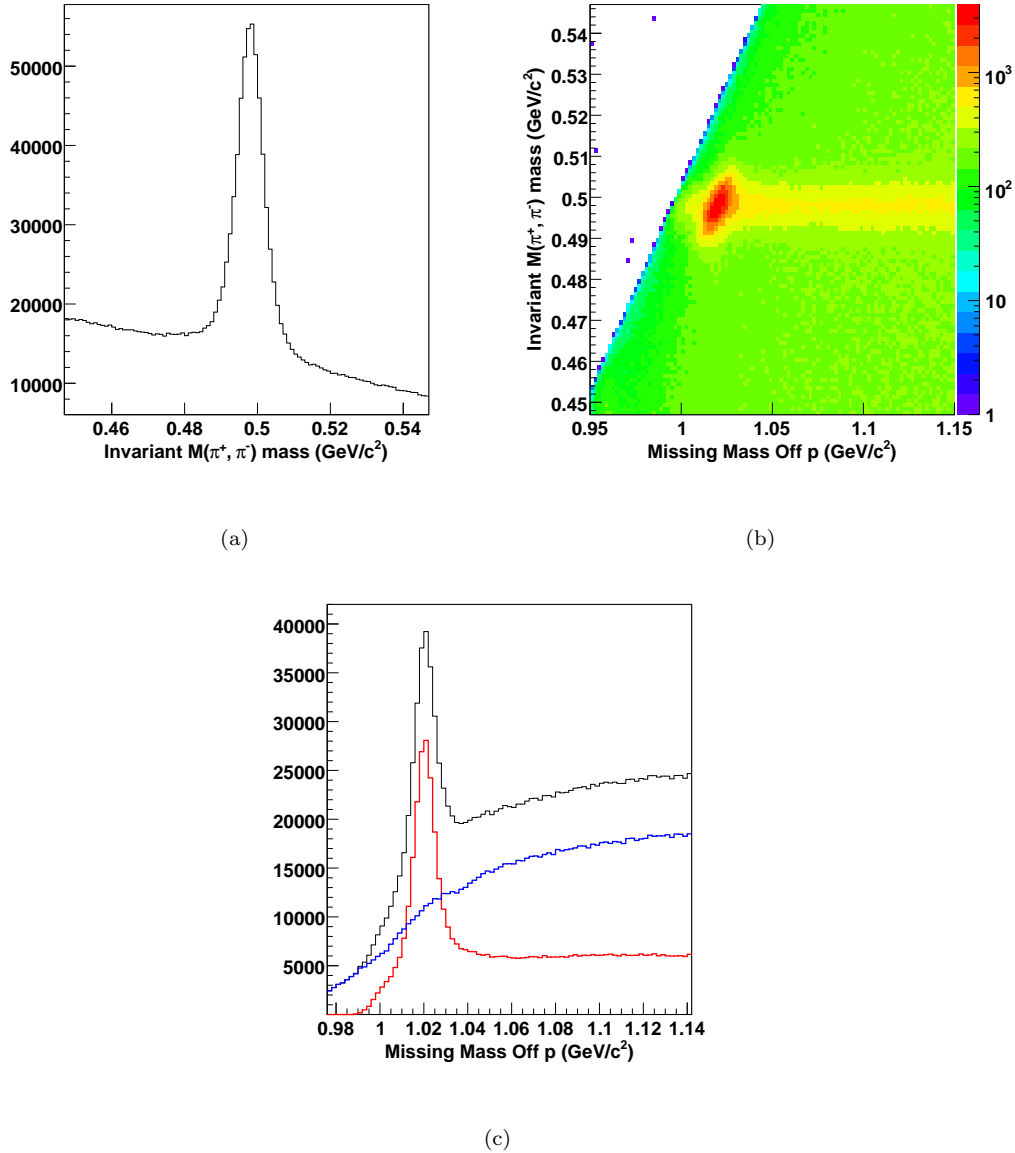


Figure 1.19: K_S^0 selection cut: (a) shows the K_S^0 peak and (b) shows the $m_{K_S^0}$ - m_ϕ distribution, after the timing cut. (c) shows the effect of a $0.49 \text{ GeV} \leq m_{K_S^0} \leq 0.505 \text{ GeV}$ K_S^0 cut, where the red histogram shows the events passing the cut and the blue histogram shows those that failed the cut.

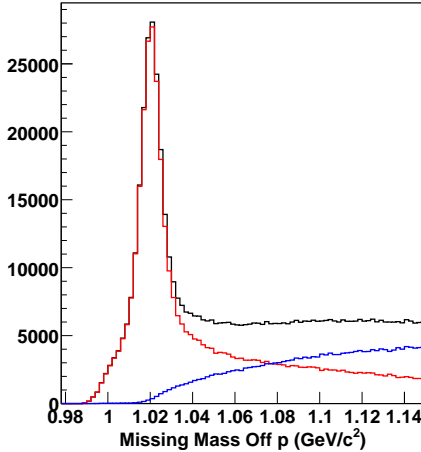


Figure 1.20: Effect of the $M(p, K_S^0)$ and $M(p, K_L^0)$ Dalitz cut on the neutral-mode ϕp dataset. The events surviving the cut are in red and those that failed the cut are in blue. See Sec. 1.9.4 for details.

kinematic region of the detector in this way. This was carried out both for the Data and the Monte Carlo, upon which we defined the *acceptance assymmetry* in the following manner

$$A = \frac{|\mathcal{A}_{data} - \mathcal{A}_{mc}|}{\mathcal{A}_{data} + \mathcal{A}_{mc}}, \quad (1.13)$$

where $\mathcal{A}_{data}, \mathcal{A}_{mc}$ were the acceptances of the data and Monte Carlo respectively. In regions where this was near zero, we could claim to have been reliably modeled the acceptance.

Fig. 1.21 shows A for protons, plotted as a function of the magnitude and direction of the track momentum. In most areas, A was found to be close to zero, signifying good agreement between the real data and the Monte Carlo. Two regions where problems are evident, are forward-angle track and low momentum track regions. The former region were to be removed by our Fiducial cuts as discussed below while the latter, we cut out by placing a minimum proton momentum cut at 375 MeV.

1.10.2 Fiducial Cuts

The acceptance study from the previous section also led to the need for removing events with tracks going into certain regions of the detector. For example, near the superconducting torus coils, the magnetic field varies too rapidly to be properly modeled by GSIM. Events with any track going into these regions will thus be removed from this analysis. This effect is most prominent in the forward direction where the coils occupy a greater amount of space. Similarly, CLAS has a hole in the very forward direction (the beam dump). We thus place a hard cut in the forward direction for tracks with $\cos \theta_{lab} \geq 0.985$. CLAS is also limited in detecting very backward angle tracks to accomodate space for the incoming beam. There is a sector-dependent backward angle cut to account for this. Finally, fiducial cuts remove events with any track having an unphysical sector or TOF paddle index assigned to it due to some glitch at the time of recording. The results of the fiducial cuts are shown in Fig. 1.22.

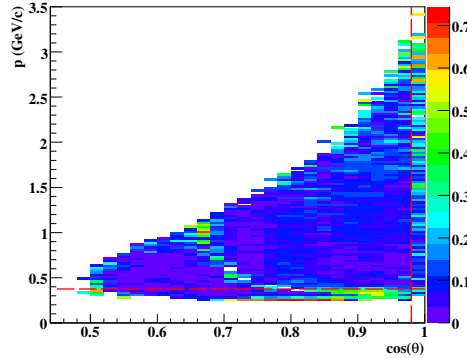


Figure 1.21: Acceptance asymmetry defined in Eq. 1.13 plotted as a function of 3-momentum magnitude p and $\cos \theta$ for protons in Matt Bellis' acceptance study. The curved band of large asymmetries was due a problematic 11th TOF counter in sector 3 which was removed from this analysis. The vertical dashed line at $\cos \theta = 0.985$ shows a hard fiducial cut placed on forward going tracks. The horizontal dashed line at $p = 375$ MeV indicates the minimum proton momentum cut that we employed.

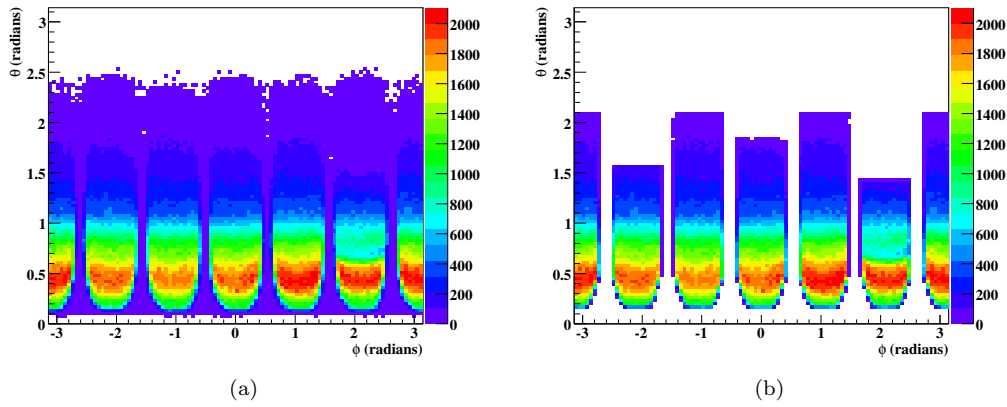


Figure 1.22: Fiducial cuts: (a) All tracks in run 43582 (three-track dataset). (b) Tracks which pass our fiducial cuts for the same run. Note that the effect of the cuts is most dramatic at the sector boundaries and the forward-angle regions where the torus coils occupy a large fraction of the available space.

Sector	Removed Paddles	
	configuration I	configuration II
1	18, 26, 27, 33	18,23,26,27,33
2	none	23
3	11, 24, 25	11,23
4	26	23,26
5	20, 23	20,23
6	25, 30, 34	23,25,30,34

Table 1.2: The two configurations of removed problematic TOF paddles used for this analysis. Configuration II has the 23rd paddle removed in all the sectors.

1.10.3 Problematic TOF Paddle Removal

There were also certain *specific* TOF paddles which we removed from our analysis. These problematic paddles caused discrepancies in the occupancy distribution between the Data and the Monte Carlo. Note that this was independent of the kind of particle track. For TOF paddles known to have problems, this would show up for protons, pions, kaons, *et al.* A sector wise list of these TOF paddles is given in Table 1.2. Two different configurations of the set of removed paddles were tried out for this analysis. These are given by configuration I and configuration II in Table 1.2. In configuration II, paddle 23 was removed in all six sectors. The 23rd paddle was located at the boundary between the first and second sections of the TOF wall which gave rise to an overlap in the logical output between paddle 23 and 24. For tracks that hit both paddles 23 and 24, tracking was sometimes inconsistent (assigned a default zero value). The overall difference in results from two configurations was found to negligible, but a comparative study was important for systematic checks.

1.11 Signal Background Separation

After the application of all our cuts (see Table 1.3 for a list), some amount of background still remained. A great deal of effort in the CMU PWA group had gone into devising a signal-background separation technique which suited our needs – both analytically/computationally and physics-wise. Traditionally, background separation has been performed using the side-band subtraction method. That is, one tries to estimate the background under the signal by looking at the side-band – regions where there is presumably no signal and only background. The problem with using such a method in our case was two-fold. First, for a reaction like $\gamma p \rightarrow K^+ \Sigma^0 \rightarrow K^+ \Lambda \gamma \rightarrow K^+ p \pi^- \gamma$ with multiple decays and thus multiple independent decay angles, the background would generally depend on the region of phase space was looking at, because the physics was different in the different phase space regions. One could bin in, say, $\cos \theta_{c.m.}^{K^+}$ and *then* apply the side-band technique individually for every bin. But again, given that there were multiple independent decay angles, such a process would not suffice. What one needed instead was a technique which somehow simultaneously incorporated *all* the relevant independent decay angles.

Secondly, our partial wave fits were event-based fits using unbinned likelihood fits. Normally for extracting yields for cross sections or asymmetries for polarization one employs a binned method where the collective background in a particular bin is what matters, as opposed to an event by event evaluation. Therefore, in our case it was required to have a signal-background separation method at individual event level for the kind of fits we wanted to run.

3-Track	2-Track
CL > 0.01 from Kinematic Fit to $MM_{tot} = 0$ (Sec. 1.6.1)	“Dalitz” cut on $MM(p, K^+)$ (Sec. 1.7.3)
–	$0.2 \text{ GeV} \leq m_{calc, K^+} \leq 0.85 \text{ GeV}$ (Sec. 1.7.2)
–	$0.3 \text{ GeV} \leq m_{calc, p} \leq 1.2 \text{ GeV}$ (Sec. 1.7.2)
2-dim (p, K^+) “iron-cross” Δtof cut (Sec. 1.6.5)	2-dim (p, K^+) m_{calc} cut (Sec. 1.7.3)
$K^+\Lambda$ background removal cut (Sec. 1.6.7)	–
\sqrt{s} dependent $MM(K^+)$ cut (Sec. 8.5.3)	\sqrt{s} dependent $MM(K^+)$ cut (Sec. 8.5.4)

Table 1.3: List of PID/event selection cuts applied for the two topologies in this analysis. Detector performance cuts (Sec. 1.10) like the Fiducial cuts, bad TOF paddle knockouts, *et al.*, remain the same for both topologies.

Inkeeping with the above two considerations, one would ideally want a binary 1 or 0 for every event to be a signal or a background. Whilst this was not possible, we could however assign a *signal probability* to every event by fitting a select group of events lying in the vicinity of the event in question in phase space to a signal plus a background fit function. By making this particular choice of events close lying together in phase space we were ensuring that that background shape remained similar between all of them. To make the definition of “closeness in phase space” more specific we defined the following metric between the i^{th} and j^{th} events

$$g_{ij}^2 = \sum_{k=1}^d \left[\frac{\xi_k^i - \xi_k^j}{r_k} \right]^2, \quad (1.14)$$

where $\vec{\xi}$ represented the d independent kinematic angles in phase space and \vec{r} were the corresponding ranges.

For the $K^+\Sigma^0$ three-track case, the angular variables were $\cos \theta_{c.m.}^{K^+}$, $\cos \theta_{\Sigma HF}^\Lambda$, $\phi_{\Sigma HF}^\Lambda$, $\cos \theta_{\Lambda HF}^p$ and $\phi_{\Lambda HF}^p$ (the superscript denotes the particular track in question and the subscript denotes the particular frame the angle is being measured in; *HF* refers to the Helicity Frame, which is loosely the same as the Rest Frame, but defined in Sec. 5.1.1). Thus, $d = 5$ and $\vec{r} = \{2, 2, 2\pi, 2, 2\pi\}$. For the two-track case, the variables were $\cos \theta_{c.m.}^{K^+}$ and $\cos \theta_{\Sigma HF}^p$. Then, $d = 2$ and $\vec{r} = \{2, 2\}$

Once we had defined a metric, we chose N_c events closest to the particular event in question and fit the missing mass off K^+ (hereonwards denoted simply by m) distribution for these $N_c + 1$ events to a gaussian signal $\mathcal{S}(m)$ and a suitably chosen background function $\mathcal{B}(m)$. The fits were unbinned likelihood fits ran using different choices of N_c (50, 100, 200) and the background function $\mathcal{B}(m)$. The latter consisted of two parts – a Gaussian centered at the Λ mass (the tail of the Gaussian encroaching into the Σ^0 mass region only matters) and another function which was test run as a linear, a quadratic, a quartic and finally as another Gaussian tail coming from above the Σ^0 mass peak from general pion background.

1.11.1 Q -values and Error Estimation

Once the fit functions $\mathcal{S}_i(m)$ and $\mathcal{B}_i(m)$ for the i^{th} event have been extracted, the event is assigned the following *quality factor* or Q -value as its signal probability

$$Q_i = \frac{\mathcal{S}_i(m_i)}{\mathcal{S}_i(m_i) + \mathcal{B}_i(m_i)}. \quad (1.15)$$

Furthermore, if the N_f fit parameters are denoted by the vector $\vec{\eta}$ and the Covariance matrix from the fit as C_η , we can extract the errors in the Q values as the following

$$\sigma_Q^2 = \sum_n^{N_f} \sum_m^{N_f} \frac{\partial Q}{\partial \eta_m} (C_\eta^{-1})_{mn} \frac{\partial Q}{\partial \eta_n}. \quad (1.16)$$

The use of these errors in yields calculation for differential cross section measurements is described in Sec. 4.6.2.

1.11.2 Application of the Procedure for $K^+\Sigma^0$

Fig. 1.23 shows the signal-background separation as a function of the missing mass off K^+ in three different \sqrt{s} regions for the two topologies. The shaded histograms have each event weighted by its Q -value and represent the extracted signal. The blue histograms use $(1 - Q)$ as the weight, representing the background. The fits were run with $N_c = 200$ and the background as a sum of two Gaussian tails – one $K^+\Lambda$ and the other from a general π^+ background coming from above the Σ^0 mass peak as mentioned earlier. The background estimation seems quite reasonable.

If we weigh each event by its Q -value, the cumulative yield after all our cuts and background separation is $\sim 655,500$ for the three-track topology and 4.64×10^6 for the two-track topology. We will quote these as the number of “good” events for this analysis. The Q -value weighted \sqrt{s} distributions is shown in Fig. 1.24. To check for systematic effects, fits with different N_c ’s and different background fit functions were run simultaneously. No significant shift in the fit results were observed. For example, with $N_c = 200$ and $\mathcal{B}(m)$ as a sum of a Gaussian (for the $K^+\Lambda$ background tail) and a quartic, the Q -value weighted cumulative yield for the three-track topology was found to be $\sim 653,200$, a less than 1% deviation from the earlier quoted value. A global fit to the same dataset with a Gaussian signal and quartic background also gave a very similar signal yield.

1.12 Systematic Study of the Background for ϕp

Since the ϕ lies very close to the edge of the KK production threshold, background subtraction for the ϕp channel had some unique issues that did not come up for the $K^+\Sigma^0$ channel. The main problem was that side-band subtraction was not always possible because the $MM(p)$ distribution on the lower side of the ϕ mass peak had very low occupancy. Additionally, the ϕ has a finite signal-width of ~ 4 MeV and strictly speaking, the ϕ line-shape is also not known exactly. Previous ϕ analyses have often employed a Gaussian signal line-shape, which is, at best, an approximation. Here, we have tried to employ a better approximation by taking the signal function as

$$S(m, \vec{\xi}) = F_s(\vec{\xi}) V(m, \mu, \sigma, \Gamma(m)), \quad (1.17)$$

where

$$V(m, \mu, \sigma, \Gamma(m)) = \frac{1}{\sqrt{2\pi}\sigma} \text{Real} \left[w \left(\frac{1}{2\sqrt{\sigma}}(m - \mu) + i \frac{\Gamma(m)}{2\sqrt{2}\sigma} \right) \right], \quad (1.18)$$

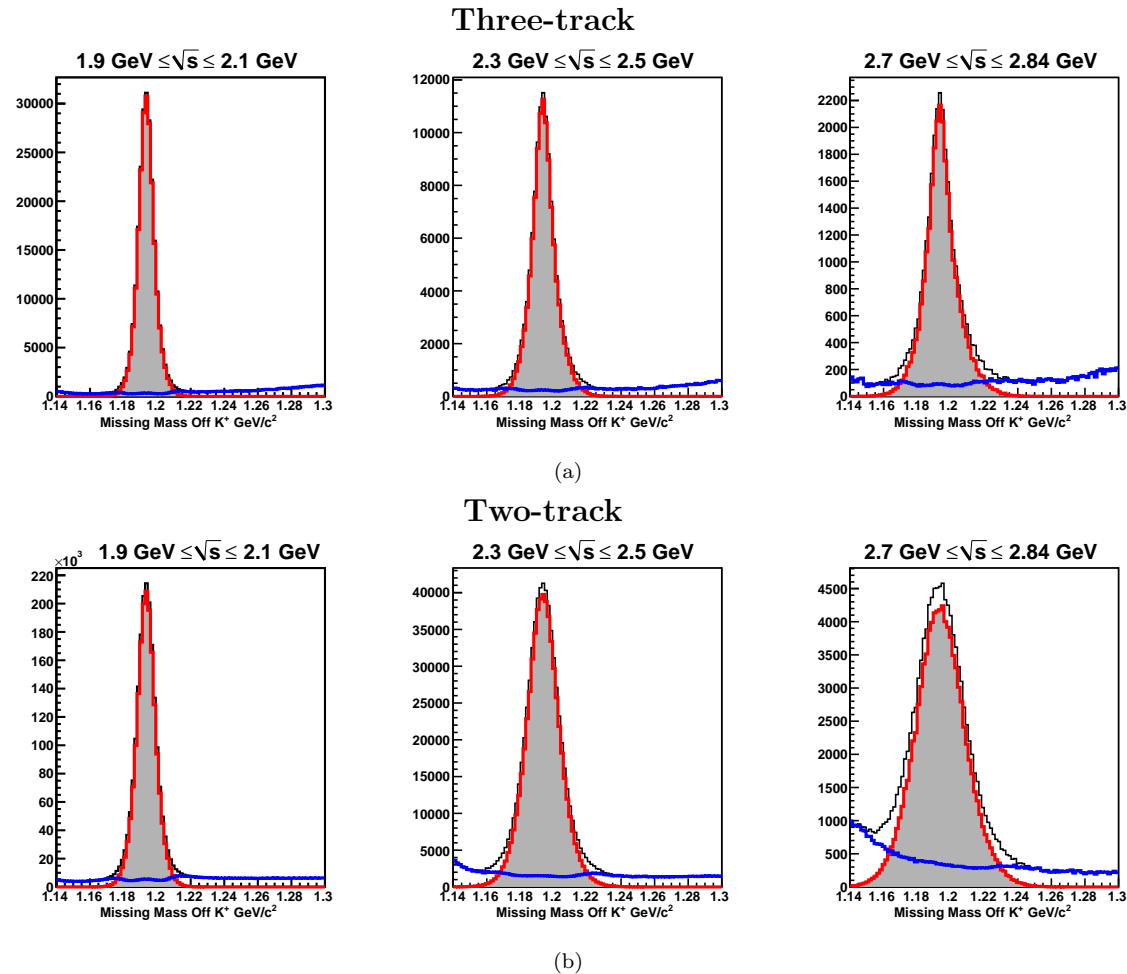


Figure 1.23: Signal Background Separation in three different \sqrt{s} ranges for the $K^+\Sigma^0$ (a) three-track and (b) two-track topologies. The black histograms are the unweighted distributions. The shaded histograms (bordered in red) are the Q -value weighted distributions representing the signal. The blue histograms are the same distributions but weighted by $(1-Q)$, representing the background.

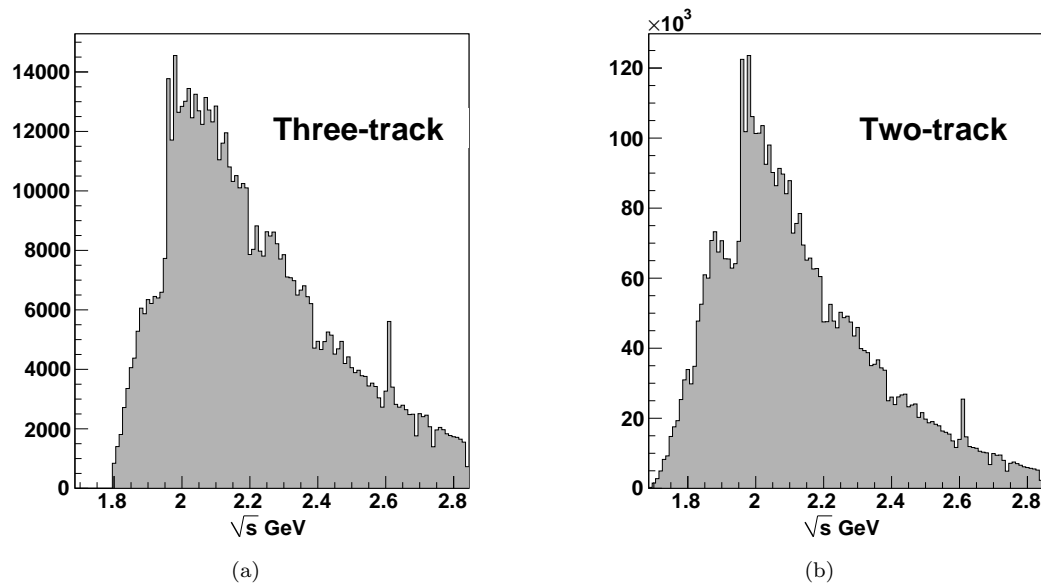


Figure 1.24: Q -value weighted occupancy as a function of \sqrt{s} for the two topologies. Each \sqrt{s} bin in the x-axes is 10 MeV wide so that the occupancies reflect the signal content in each \sqrt{s} bin where we will extract differential cross sections. The discontinuity near $\sqrt{s} \sim 1.95$ GeV is an artifact of the $g11a$ trigger (see Sec. 2.10.3) while the ‘‘hot’’ region at $\sqrt{s} \sim 2.61$ GeV is due to a discontinuity in the length of the T-counter scintillators. The total number of ‘‘good’’ events after all our cuts and background separation is ~ 0.655 million for the three-track and ~ 4.64 million for the two-track dataset.

was the convolution of a Gaussian of width σ and a non-relativistic Breit-Wigner of width $\Gamma(m)$ with mean μ , known as a Voigtian ($w(z)$ is the complex error function) and $F_s(\xi)$ was the unknown kinematic dependence of the signal distribution. The set of angular variables were chosen as $\vec{\xi} = \{\cos \theta_{c.m.}^\phi, \cos \theta_{hel}^\phi, \phi_{hel}^\phi\}$ where θ_{hel}^ϕ and ϕ_{hel}^ϕ described the $\phi \rightarrow KK$ decay in the helicity frame, and m was the ϕ mass variable, $MM(p)$.

Note that the Breit-Wigner width $\Gamma(m)$ was taken to be mass dependent. The $\phi \rightarrow KK$ decay is an $L = 1$ P -wave decay. In the ϕ rest frame, the maximum orbital angular momentum L of the KK system is limited by the break-up momentum $q(m) = \sqrt{m^2 - m_K^2}/2$ for a ϕ mass m . The daughter K particles moving slowly with an impact parameter (meson radius) d of the order of 1 fm ($d = 0.1973$ GeV) have difficulty in generating sufficient L to conserve the overall angular momentum. Each angular momentum amplitude therefore has to be weighted by the barrier factor given by the Blatt-Weisskopf function B_L [8]. For $L = 1$, $B_L = \sqrt{2z/(1+z)}$, where $z = q/d$. The mass dependent Breit-Wigner width is then given by

$$\Gamma(m) = \Gamma_0 \left(\frac{q}{q_0} \right)^{2L+1} \left(\frac{m_0}{m} \right) \left(\frac{B_0}{B} \right), \quad (1.19)$$

where the subscript 0 denotes evaluation at the ϕ mean mass $m_0 = 1.01946$ GeV, and $\Gamma_0 = 4$ MeV.

Three types of background functions were generally studied. The first one was a general quartic, the second was of the form $f(x) = a\sqrt{x^2 - 4m_K^2} + b(x^2 - 4m_K^2)$, $x > 2m_K$, and the third was $g(x) = a(x - 2m_K) + b(x - 2m_K)^2$, $x > 2m_K$. The set of angular variables were $\cos \theta_{c.m.}^\phi$, $\cos \theta_{HEL}^K$ and ϕ_{HEL}^K (the particular choice of reference frame for the $\phi \rightarrow KK$ decay did not matter here).

1.12.1 Charged-Mode Topology

Being a two-track topology, the charged-mode had higher statistics than the neutral-mode. Therefore a 10-MeV \sqrt{s} binning was preserved here. For each of the background function forms, we studied the quality of signal extraction with the number of closest points N_c as 50, 100, 200 and 300. The results we present here were with $N_c = 200$ and a quartic background. Initially, no hard cut was placed around the $\Lambda(1520)$ mass ($\delta = 0$ from Sec. 1.8.3). However the Q -values seemed to be unable to cleanly remove the $\Lambda(1520)$ background. This was true for all values of N_c and all types of background functions that were tried out. Fig. 1.25 shows $M(pK^-)$ plotted against $MM(p)$ in three angular regions for the energy range $2.08 \text{ GeV} \leq \sqrt{s} \leq 2.12 \text{ GeV}$. The $\Lambda(1520)$ background ($M(pK^-) \approx 1.52$ GeV) is especially prominent in the mid-angles.

At this point we clarify that our signal-background separation method assumes that the background does not interfere with the signal. It is possible however, that there is an interference between the charged-mode ϕp and $K^+\Lambda(1520)$ channels (due to the same final-states), in which case our method would fail. In this case, the separation has to be done at the amplitude level in a coupled-channel partial wave analysis. Our final signal-background separation method involved an additional cut of $|M(pK^-) - 1.52 \text{ GeV}| > 15 \text{ MeV}$. The results are shown in Fig. 1.26a where the Q -value weighted ϕ signal-distributions are in red and the $(1 - Q)$ weighted background distributions are in blue. Fig. 1.27a shows the weighted \sqrt{s} occupancies for the charged-mode, the dashed histogram corresponding to no hard cut around the $\Lambda(1520)$ mass, while the shaded histogram corresponds to a 15 MeV hard cut around the $\Lambda(1520)$. Our estimated signal yields are around 0.477 and 0.436 million events for the two cases, respectively.

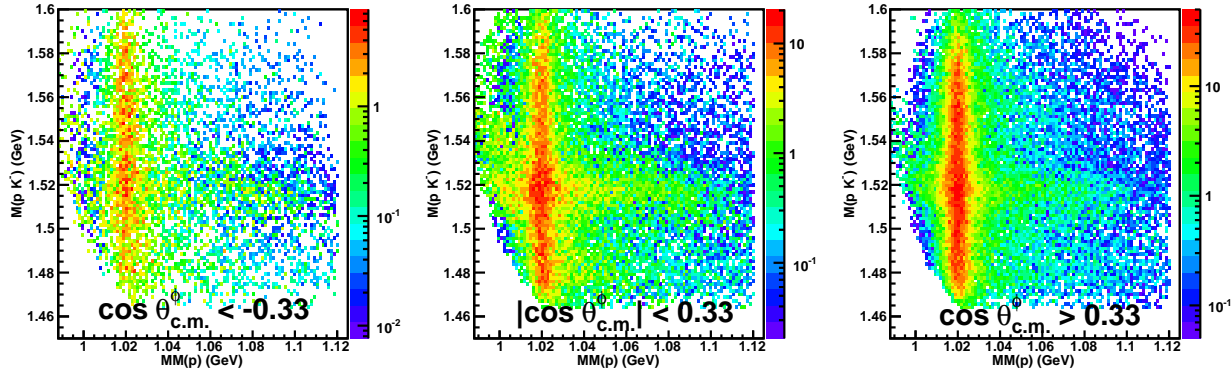


Figure 1.25: $\phi\text{-}\Lambda(1520)$ overlap for the charged-mode topology in the energy regime $2.08 \text{ GeV} \leq \sqrt{s} \leq 2.12 \text{ GeV}$. Q -value weighted $M(pK^-)$ vs. $MM(p)$ distribution after background removal. The $\Lambda(1520)$ “band” is clearly visible, with the most relative prominence in the mid-angles.

1.12.2 Neutral-Mode Topology

Being a three-track case this topology had a reduced detector acceptance. Additionally, the ϕ cross sections are inherently small. Therefore, this topology had an overall limited statistics. To bolster statistics, a wider energy binning was chosen (at least 30-MeV wide \sqrt{s} bins), though statistics was still quite limited in the backward-angles. All three background-functional forms mentioned earlier in this section were tried out and were found to give similar results. Our final Q -values with a general quartic background and $N_c = 200$ are shown in Fig. 1.26b. Fig. 1.27b shows the weighted \sqrt{s} occupancies for the neutral-mode topology, the estimated signal yield being around 0.097 million events, roughly a fifth that of the two-track charged-mode dataset.

1.13 Summary

To extract a clean sample of $\gamma p \rightarrow K^+ \Sigma^0$ events from the *g11a* dataset, we have selected events using two different final state topologies, a series of cuts and employment of a signal-background separation procedure. Some of the cuts employed pre-existing detector performance studies whilst others were specific to this channel. At every step we have detailed both the validity and utility of the cut we make. The result is a highly clean yield of $K^+ \Sigma^0$ events ready for further physics analyses.

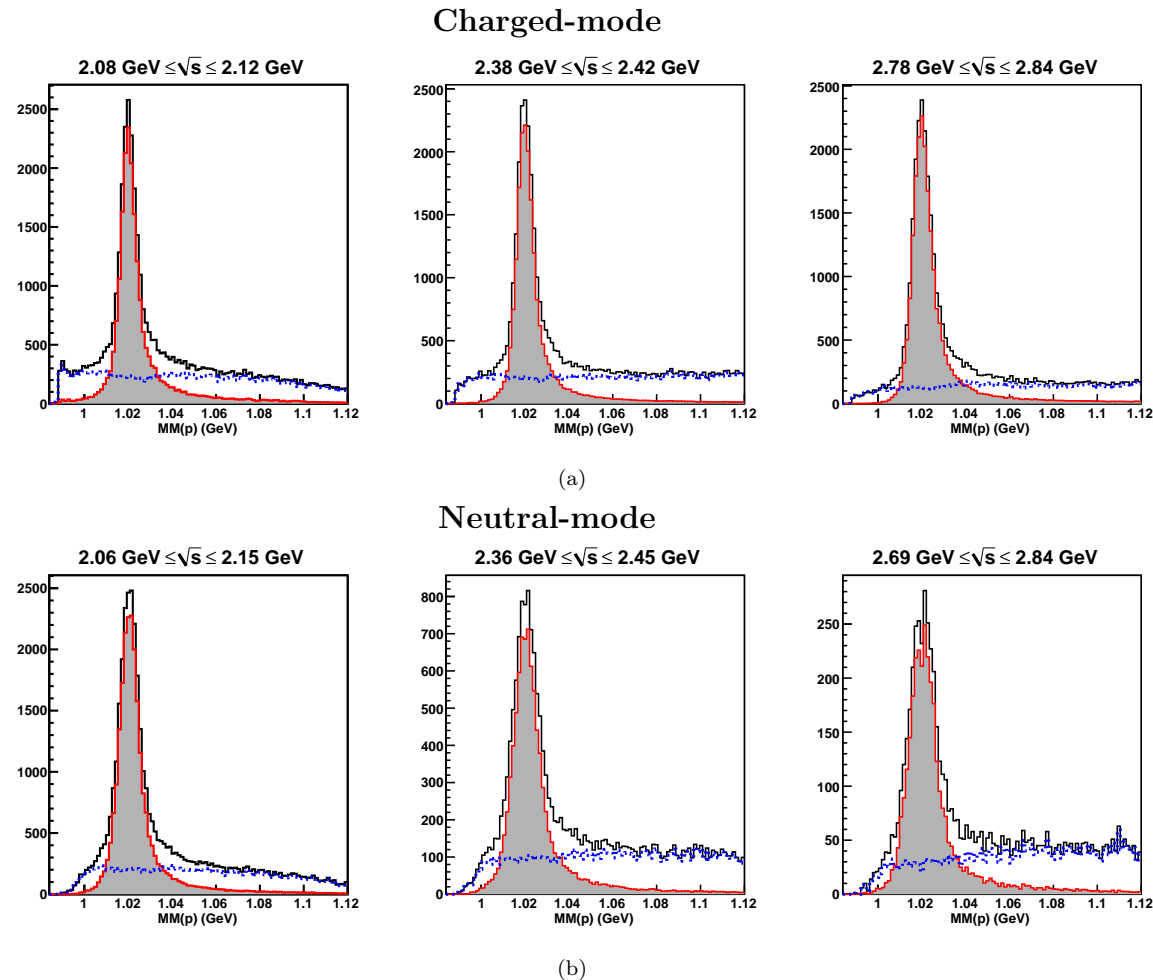


Figure 1.26: Signal Background Separation in three different \sqrt{s} ranges for ϕp (a) charged-mode and (b) neutral-mode topologies. The black histograms are the unweighted distributions. The shaded histograms (bordered in red) are the Q -value weighted distributions representing the signal. The blue histograms are the same distributions but weighted by $(1-Q)$, representing the background.

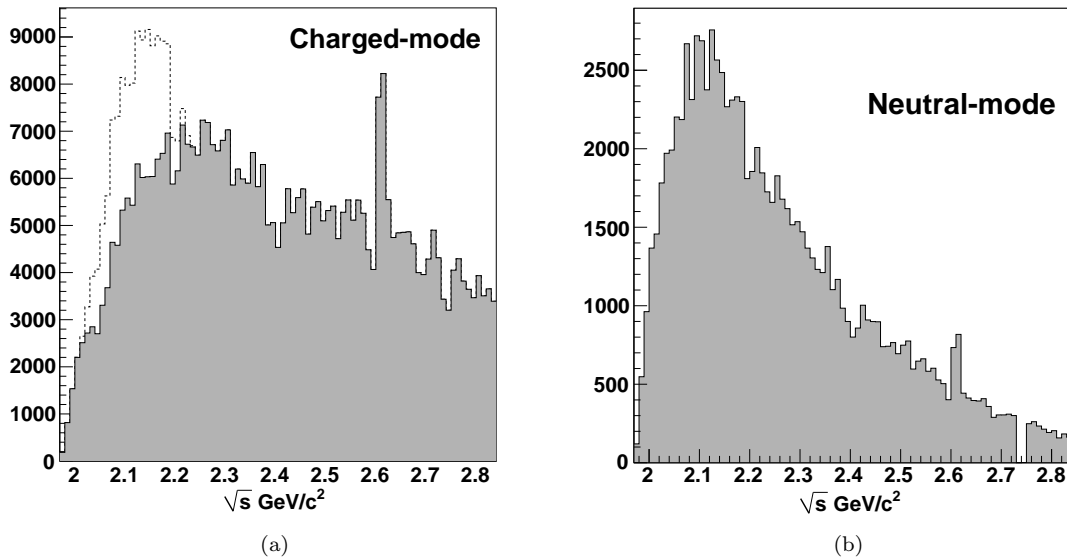


Figure 1.27: Q -value weighted occupancy for the ϕ channel as a function of \sqrt{s} for (a) charged- and (b) neutral-mode topologies. Each \sqrt{s} bin in the x-axes is 10 MeV wide. The dashed histogram in (a) represents the occupancies *without* the 15-MeV-wide cut around the $\Lambda(1520)$ mass for the charged-mode (≈ 0.477 million signal events) while the shaded histogram is *with* the $\Lambda(1520)$ hard cut (≈ 0.436 million signal events). Above $\sqrt{s} \approx 2.2$ GeV, this cut makes no difference any more. For the three-track neutral-mode dataset, the total estimated signal yield was ≈ 0.097 million, that is, around a fifth that of the two-track charged-mode dataset.

Chapter 2

Detector Acceptance and Normalization

Extraction of signal yields, which was covered in detail in the last chapter, was just one of the steps towards the measurement of differential cross sections, the other two being *detector acceptance* and *flux normalization*. The CLAS detector is a complex device. The mere production of an event with a particular kinematics does not mean that the event will actually be successfully detected and recorded by CLAS. The yields from the previous chapter will therefore have to be properly corrected for the *acceptance* of the detector. *Normalization* refers to the number of photons impinging on the target. If the photon flux is high, this will ratchet up the signal yields. The differential cross sections thus have to be normalized by the inverse of the flux factor. Additionally, the electronics of the detector have a finite dead time when it is not ready to record events because it is writing out previously recorded data, or for some other reasons. This fractional live time needs to be accounted for too in the normalization. All these calculations and corrections, we cover in the this chapter.

2.1 Detector Simulation

2.1.1 “Raw” Monte Carlo

To simulate detector acceptance, we first generated “raw” Monte Carlo events according to phase-space distributions. For the $K^+\Sigma^0$ channel, 300 million events were generated for the three-track and around 337 million for the two-track topology. For ϕp , around 100 million events were generated for both the charged- and neutral-mode topologies (the event-generator used the same ϕ lineshape as described in Sec. 1.12). The events were thrown such that after all cuts and background separation, the E_γ occupancy for the Monte Carlo was roughly three times that of the data. Ideally, one needs to throw Monte Carlo events based on some physics model. Except for the $K^+\Sigma^0$ two-track analysis, our acceptance calculation was obtained by weighing the Monte Carlo by a PWA fit to the actual data distribution, so that no *a priori* physics generator was needed.

For the $K^+\Sigma^0$ two-track case, this remained a concern, since a fit to the data could no longer be effected (our PWA setup required knowledge of all the final state particles). We were thus forced to use the unweighted Monte Carlo for this case. Fortunately, due to the break-up momenta being small in both Σ^0 and Λ decays, the difference between the weighted and unweighted acceptance calculations was found to be minimal (see Sec. 8.3). Were this not the case, it would have been considerably more difficult to use the two-track dataset for making measurements.

Parameter	Setting
AUTO	1
KINE	1
MAGTYPE	2
MAGSCALE	0.4974 0.0
FIELD	2
GEOM	ALL
NOSEC	OTHE
TARGET	g11a
TGPOS	0.0 0.0 0.0
STZOFF	-10.00
STTYPE	1
SAVE	'LEVL' 1 'HADR' 0.93
RUNG	43852 1
BEAM	4.023

Table 2.1: Some of the values used for input to the GSIM `ffread` card for this analysis. The items marked in blue were only used for the two-track topology.

2.1.2 GSIM

The “raw” events were next passed through GSIM, a GEANT based simulation software for the CLAS detector, and the collaboration’s standard simulation package [14]. GSIM’s main task was to simulate detector signals for each subsystem of CLAS based on the kinematics for each particle. To do so, GSIM took as input, the initial particle types, momenta, and positions for each raw MC (Monte Carlo) event and used spatial information regarding the CLAS detector materials and toroidal magnetic fields to “swim” particles through the detector. GSIM also knew how to decay the various unstable particles (K^0 , K^+ , Σ^0 , Λ , π^- , ...) so that we did not need to put in any branching fractions while calculating the cross-sections — these are already included in the acceptance. The only exception was the $\phi \rightarrow KK$ decay. This decay was effected by hand. That is, our thrown events already had the ϕ decayed either into K^+K^- or $K_S^0 K_L^0$ according to the corresponding branching fractions. Therefore the ϕ differential cross sections needed to be scaled up by the corresponding branching fractions.

GSIM accepts parameters in the form of an `ffread` “card”. Table 2.1 shows some of the typical values used for this analysis. One element that needs additional mention here is the set of parameters marked in blue. It is the peculiarity of the $K^+\Sigma^0$ and $K^+\Lambda$ channels in the *g11a* dataset (see Sec. 8.1 for explanations) that knowledge of the secondary vertex for the Λ decay was essential. At the time of this writing, no previous CLAS analysis at CMU required knowledge of secondary decay vertices. For the three-track topology, the vertex could be *re-constructed* from tracking information and the Λ momentum. Since the Λ momentum was unknown in the two-track case, even this approach failed. Since it was not required, the earlier existing local versions of GSIM at CMU was not set up to retrieve secondary decay vertex information directly from GEANT though the BOS banks which stored this information, namely, MCVX and MCTK, were already built in and compiled. One simply needed to instruct GSIM to correctly write out the information into these banks using the `SAVE` command in the `ffread` card. For our purposes, it sufficed to save the first decay vertex ('LEVL' 1) where the decay products include a "'HADR' 0.93", that is, a hadron with mass greater than 0.93 GeV (a proton, in our case) — this addition is shown in blue font in Table 2.1. We subsequently double checked our code using a small three-track topology test-run by fitting t_{rf} ,

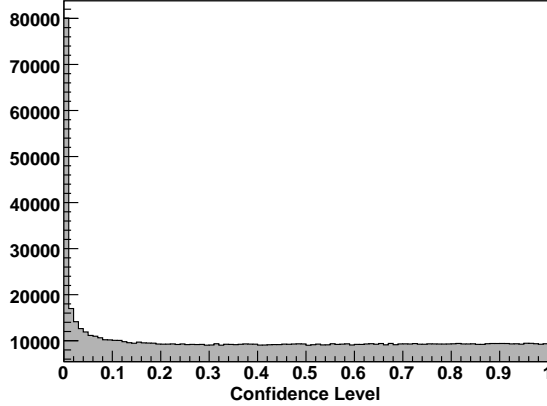


Figure 2.1: Confidence levels from kinematic fitting to $\gamma p \rightarrow K^+ p \pi^-(\gamma)$ after GPP and momentum smearing. The confidence level distribution is flat beyond 0.2 which suggests that the resolution of the accepted Monte Carlo is of the same order as the data.

the flight time of the Λ in its rest frame (this calculation requires knowledge of the Λ momentum and thus the necessity of the three-track topology) to an exponential and retrieved the value of $c\tau = 7.89$ cm, as quoted in PDG, to a fairly high precision.

2.1.3 GPP

The output from GSIM was next processed by GPP, a CLAS software package which smeared the detector signals to match the actual detector resolutions more accurately. Signals from the TOF scintillator paddles were smeared according to their lengths, a longer scintillator requiring a more diffused smearing function. Timing signals from the drift chambers were similarly diffused according to the distance of closest approach (DOCA) to set the momentum resolution in the Monte Carlo. After applying all these smearings, however, it was found that the Monte Carlo still had higher a resolution than the data [3]. Since GPP also allowed for user specified “degree of smearing”, a minimal smearing of 1.0 was applied to the drift chamber, and instead, an empirical smearing algorithm tuned to produce a more accurate resolution over all regions of the detector was applied.

The empirical algorithm took the reported values of the tracking angles as the mean and $1.85\sigma_{track}$ as the width of a Gaussian function and randomly sampled from this Gaussian distribution (σ_{track} was the resolution obtained from the tracking code). The momentum magnitudes were also smeared by ~ 2 MeV on the average. Fig. 2.1 shows the confidence level distribution from a subsequent $\gamma p \rightarrow K^+ p \pi^-(\gamma)$ kinematic fit for the accepted Monte Carlo. Since the covariance matrix of the kinematic fitter was tuned to give a globally flat confidence level for the $g11a$ data, the flatness for the accepted Monte Carlo distribution suggests a good resolution match between the two.

2.2 Trigger Simulation

The role of GSIM was to account for inefficiencies in the various detector components once a set of tracks triggers an “event” (see for the details on the $g11a$ triggering criteria). However the trigger-

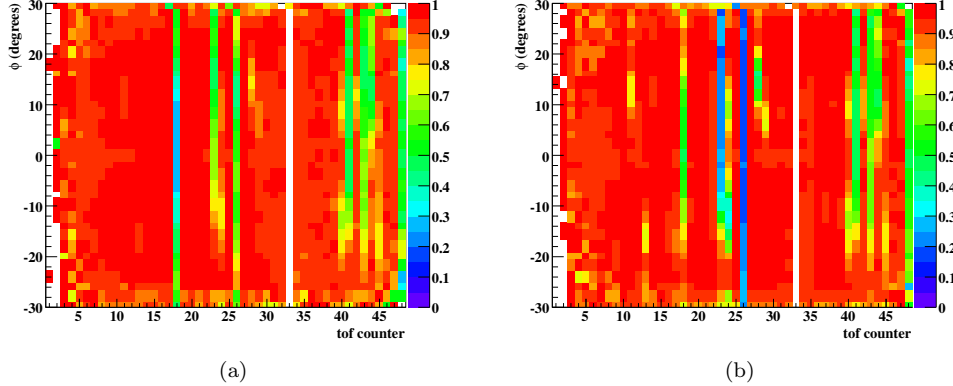


Figure 2.2: Trigger efficiency map as a function of ϕ (degrees) and TOF-counter for Sector 1: (a) proton (b) π^- (Source: [3]).

ing itself was not without inefficiencies, so the next step was to account for these in the Monte Carlo.

Trigger inefficiencies in $g11a$ were first noticed by the Genova group [15] through discrepancies in the $\gamma p \rightarrow p\omega$ differential cross-sections between the two topologies $\gamma p \rightarrow p\pi^+(\pi^-\pi^0)$ and $\gamma p \rightarrow p\pi^+\pi^-(\pi^0)$. This was investigated further in great detail by Krahn *et al* [13] by utilizing the *trigger word* written into the data stream when events were being recorded. The CLAS Level 1 trigger requires a coincidence between the start counter time and the TOF scintillator time within a time window for two charged tracks in two different sectors. The *trigger word* contains information on which sectors met this trigger condition. By using the kinematic fitter and a high enough confidence level cut to select good $\gamma p \rightarrow p\pi^+\pi^-$ events, one can look at the trigger word and see how many times one of the three final state particles did not meet the trigger condition (at least two of the tracks must have triggered for the event to have been recorded). In this manner Krahn *et al* built up a “trigger map” for each particle type (proton, π^+ and π^-) as a function of sector, TOF paddle and azimuthal angle ϕ . Fig. 2.2 shows this for the proton and π^- .

One can immediately make out the problematic TOF paddles from Fig. 2.2. For example paddle 33 in Sector 1 is non-functioning for both the proton and the π^- . Paddles 12 and 13 have localized regions of lower efficiencies, either due to defective scintillator materials in these regions or due to high threshold settings of the TDC’s in the PMT’s located at the ends of each paddle. Note that many of the problematic paddles are already excluded altogether, as mentioned in Sec. 1.10.3. To correct for the localized inefficiencies for the remaining paddles, we use the trigger map as follows. For every track, we generate a random number between 0 and 1. If this is lesser than the efficiency read out from the map, we set the trigger word as positive for that particular track. The event as a whole is accepted if two or more tracks are “triggered” in this way. For the K^+ , we utilized the π^+ trigger map (see also Sec. 8.5.2).

2.3 Start Counter Correction

Due to the peculiar simultaneity of certain nuances lying in the $g11a$ start counter, the $g11a$ trigger, and the kinematics involving the decay of a Λ , an additional trigger correction is required for the accepted Monte Carlo in this analysis. In a gist, events for which the Λ decays outside the geometrical boundary of the start counter fail to trigger in the data, but might be included in the Monte Carlo.

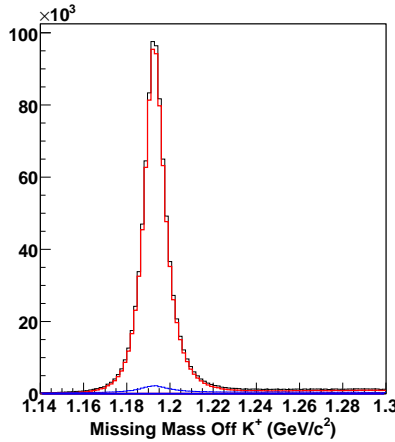


Figure 2.3: Accepted Monte Carlo from kinematic fit to $\gamma p \rightarrow K^+ p\pi^-(\gamma)$: in red are events after a 1% confidence level cut and in blue are events rejected by the cut. All histograms produced after a $|MM| < 60$ MeV cut to compare with data (Fig. 1.3c).

Thus, these events must be separately removed in the Monte Carlo by a cut. Both the effect and the cut are detailed in Sec. 8.1 and we direct the reader there to avoid repetition.

2.4 Event Selection – $K^+\Sigma^0$ Three-track topology

After passage through GSIM and GPP, the Monte Carlo is in the form of raw events as was obtained from the detector. Here on, it undergoes cooking and skimming using the same versions of the software that the data was processed with. This ensures any systematic inefficiencies to be reflected in the same way in the Monte Carlo as in the data.

Event selection follows suit along the same philosophy – kinematic fitting, particle identification and event selection are replicated on the Monte Carlo as was applied on the data. Fig. 2.3 shows the effect of a 1% confidence level cut after a kinematic fit to $\gamma p \rightarrow K^+ p\pi^-(\gamma)$. In red are events surviving the cut and in blue are events rejected by the cut. As for the data, we have applied a total missing mass between ± 60 MeV cut prior to making this plot. There is no “background” per se for the Monte Carlo, except for a proton- K^+ swap misidentification, which the latter cut removes. We have added this cut here for comparison with the corresponding plot for data – while skimming the Monte Carlo, as in the case of data, no such cut was applied. Fits to the black and red histograms (*i.e.*, before and after the cut) yield a signal loss of about 1.5%, in tune with what we had found for the data.

Fig. 2.4a shows the Δtof plot for the proton hypothesis vs. the K^+ hypothesis, inlayed with the “iron-cross”. As for the data, events outside the “cross” are rejected. Fig. 2.4b shows the calculated masses of the proton and the K^+ , while Fig. 2.4c (Fig. 2.4d) show the calculated mass distributions for events accepted(rejected) by the iron cross cut. It is to be noted that the feature in Region “I” of Fig. 1.5(b) due to incorrect timing information of the proton occurs for the Monte Carlo as well.

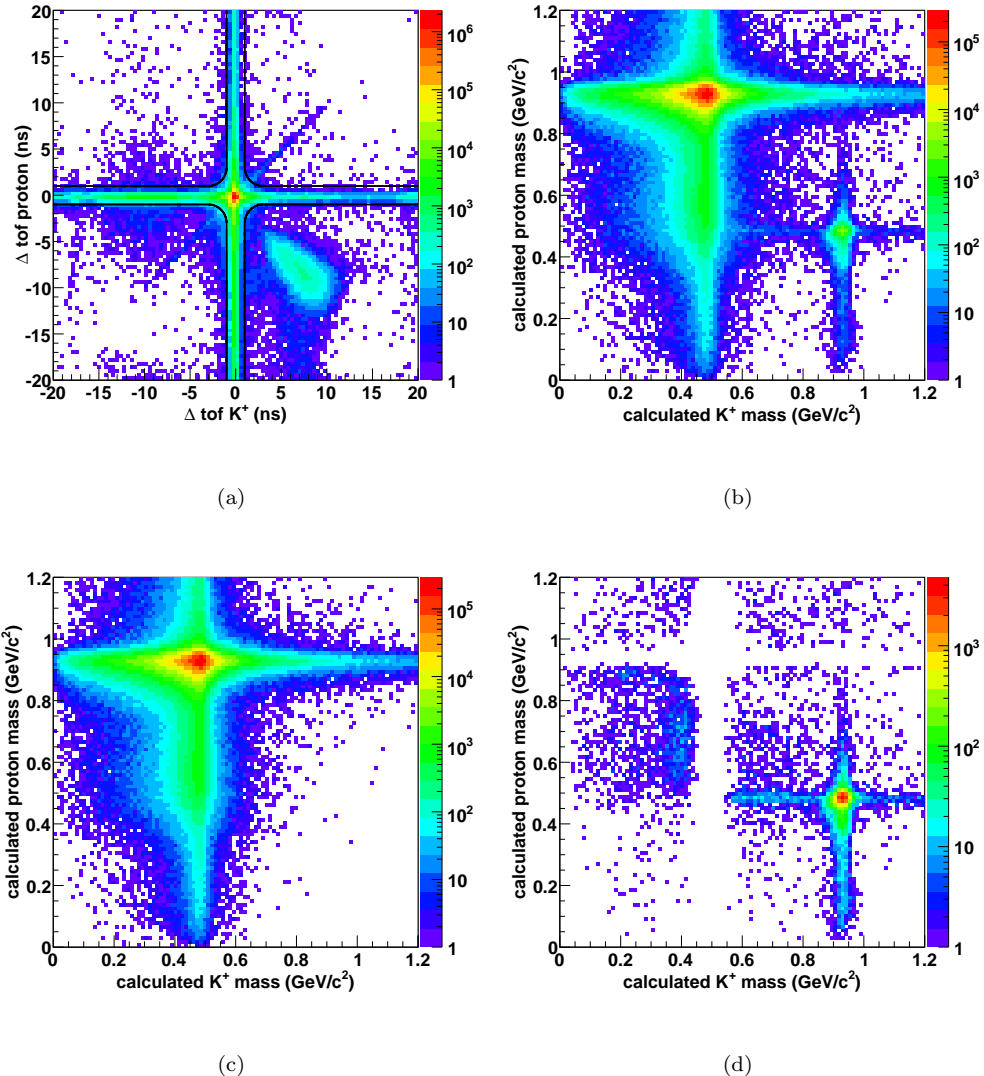


Figure 2.4: Accepted Monte Carlo PID for the $K^+\Sigma^0$ three-track topology: (a) Δtof – events outside the “iron-cross” are rejected. Calculated masses – (b) before cut, (c) events accepted by cut, and (d) rejected by cut. See text for details.

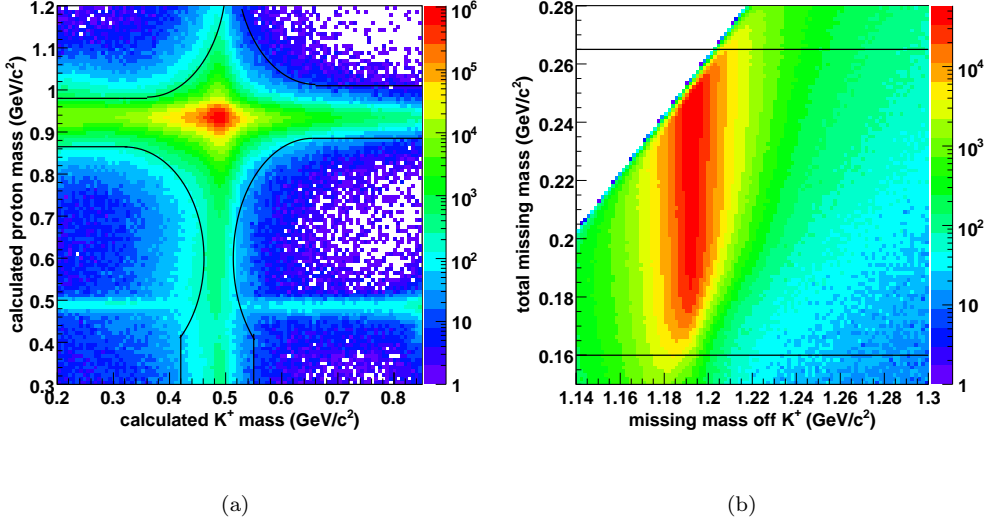


Figure 2.5: Accepted Monte Carlo PID for the $K^+\Sigma^0$ two-track topology: (a) calculated masses for the entire skinned dataset. The black lines denote our cut – events outside the “iron-cross” region are rejected. (b) Total missing mass, corresponding to the invariant ($\pi^-\gamma$) mass, plotted against missing mass off K^+ – only events lying between the two horizontal lines were accepted.

2.5 Event Selection – $K^+\Sigma^0$ Two-track topology

For the $K^+\Sigma^0$ two-track case, the only “background” is an identification-swap between the proton and K^+ , which is mostly removed during the initial skimming process (using the same calculated mass and Dalitz cuts as in the two-track data skim) itself. Thus the skinned dataset is very clean already. Fig. 2.5 shows the calculated masses and the total missing mass distributions for this. However, to avoid any systematic “bias” between data and Monte Carlo, the same PID cuts as applied on the data were applied on the Monte Carlo as well. The number of events rejected by these cuts were found to be nearly negligible. Energy, momentum and tagger corrections were also applied as was for the two-track data.

2.6 Event Selection – ϕp Charged-mode topology

Following the general norm for this analysis, as noted earlier, the accepted Monte Carlo for the ϕp channel was processed in exactly the same fashion as the real data. Fig. 2.6a shows a plot of the the proton and K^+ calculated mass for the accepted Monte Carlo ϕp charged-mode topology skinned dataset (after a 10% confidence level cut from kinematic fitting to $\gamma p \rightarrow K^+ p(K^-)$). The quadruplet of black curves shows the cut limits used for the ϕp charged-mode analysis and Fig. 2.6b shows the effect of this cut on the Monte Carlo data. Note that the cut boundaries appear somewhat tight on the lower side of the K^+ mass. We remind the reader that this is because the cut was designed keeping in mind the distribution for the real data and not the Monte Carlo data. The latter does not have any “real” background *per se* (apart from a combinatorial proton- K^+ identification background).

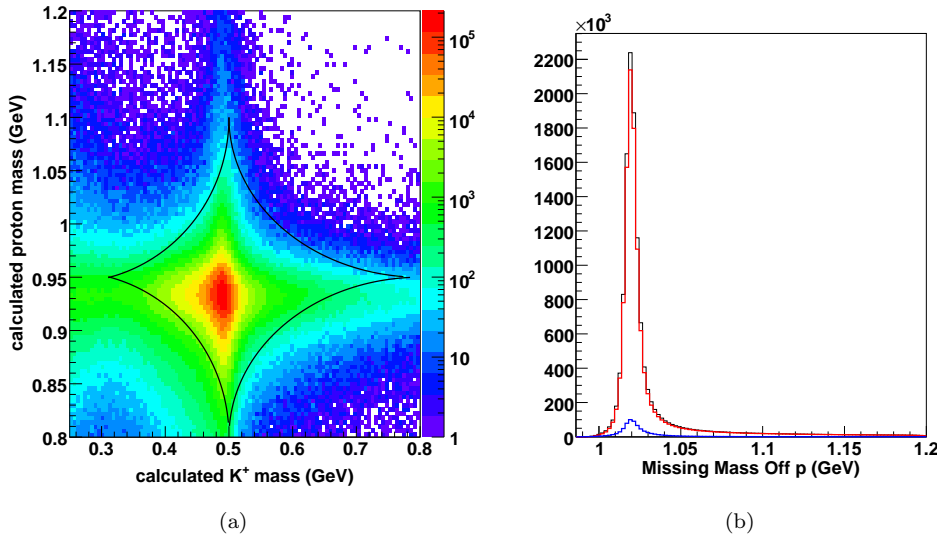


Figure 2.6: Accepted Monte Carlo timing cut for the ϕp charged-mode topology: (a) calculated masses for the entire skimmed dataset. The quadruplet of black lines denote our cut. (b) Shows the effect of the cut, the red and blue histograms represent the events accepted and rejected by the cut, respectively.

2.7 Event Selection – ϕp Neutral-mode topology

Figs. 2.7a and 2.7b show the timing and K_S^0 selection cuts for the ϕp neutral-mode topology on the accepted Monte Carlo skinned dataset (after a 10% confidence level cut from kinematic fitting to $\gamma p \rightarrow \pi^+ \pi^- (K_L^0)p$). The cut boundaries are shown by the black curves and lines.

2.8 Systematic Uncertainties

Since both the beam and target were unpolarized for $g11a$, the $K^+\Sigma^0$ photoproduction yields must be isotropic in the azimuthal production angle. To estimate systematic uncertainties in our acceptance calculation, we compare the acceptance normalized yields for each of the six (azimuthally symmetric) sectors the K^+ goes into. Tagging the sectors by the K^+ helps in mapping over the acceptance to useful quantities like $\cos\theta_{c.m.}^{K^+}$ and t . Since each sector has its own set of acceptance inefficiencies, if we have properly accounted for them in our acceptance calculation, we should get the same acceptance corrected yield for each sector. Fig. 2.8a and 2.8b show the yields before and after acceptance correction for $\sqrt{s} = 2.05$ GeV. The localized depletions in $\cos\theta_{c.m.}^{K^+}$ in Fig. 2.8a correspond to knocked out TOF paddles (for a given \sqrt{s} , each $\cos\theta_{c.m.}^{K^+}$ and $\phi_{c.m.}^{K^+}$ corresponds to a particular sector based TOF paddle). Since the same cuts that were applied on the data goes into the acceptance calculation, the acceptance correction removes these depletions and brings all the individual sector-wise yields into alignment, as evident from Fig. 2.8b.

Some discrepancies still exist between the sector-wise yields and the mean. Following [3], we next investigate whether these discrepancies can be accounted for by the statistical errors or whether one needs to assign supplementary uncertainties. If the errors were only statistical, then assuming a normal distribution, we expect that 68% of the time the deviation from the mean should be within

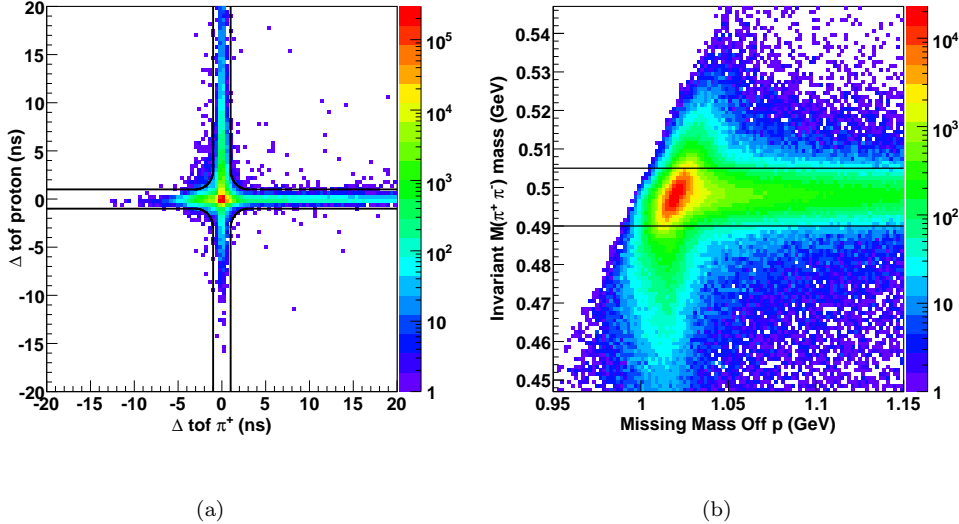


Figure 2.7: Accepted Monte Carlo PID cuts for the ϕp neutral-mode topology: (a) Δtof for the entire skinned dataset. The quadruplet of black lines denote our cut. (b) Shows the cut on the reconstructed K_S^0 mass as $M(\pi^+\pi^-)$. The cut limits are shown by the two horizontal lines.

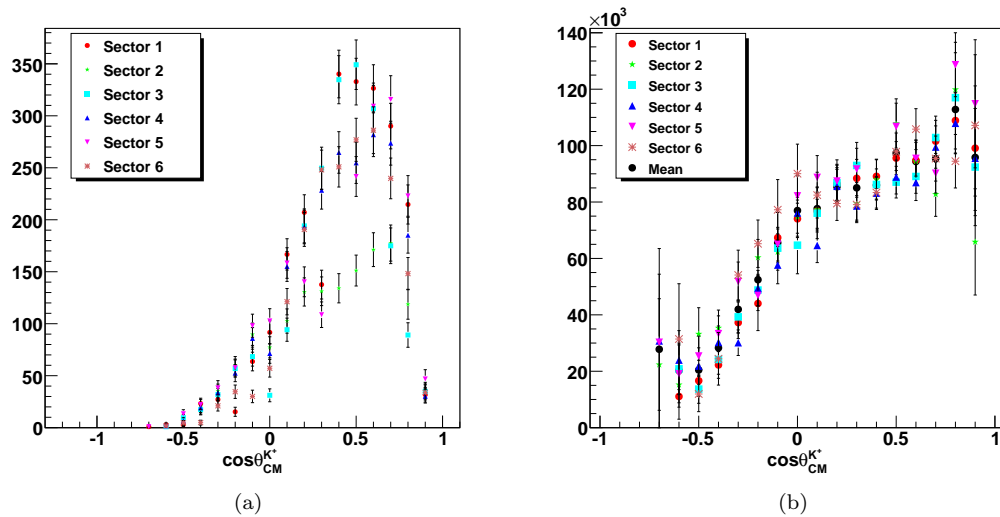


Figure 2.8: Acceptance normalization for $\sqrt{s} = 2.005$ GeV for the $K^+\Sigma^0$ channel: (a) sector-wise data yields before acceptance correction, and (b) normalized yields after acceptance correction. Post-correction, the occupancies are much more similar between the different sectors.

1σ , or,

$$\sum_{c,s} \Theta(\sigma_{c,s}^2 - (y_{c,s} - \mu_c)^2) \approx 0.68N, \quad (2.1)$$

where s denotes the sector, c is the $\cos \theta_{c.m.}^{K^+}$ bin, $\sigma_{c,s}$ is the statistical error for each point and Θ is the Heaviside step function. Before proceeding further, we pause to note that one of the differences between the $K^+\Sigma^0$ channel and the $p\omega$ channel analysis of [3] is that we have much lower statistics due to the inherent low cross-sections of strangeness production compared to non-strange channels. Thus, upon initial survey, it was found that the fraction within 1σ from Eq. 2.1 was more than 68%, indicating that $\sigma_{statistical}$ was being over-estimated. A check on the occupancies per sector based $\cos \theta_{c.m.}^{K^+}$ bin (see Fig. 5.3) revealed that due to TOF paddle knockouts, localized occupancy distribution could be as low as a single event per bin, which kicks up $\sigma_{statistical}$. However, the acceptance corrected yields are much closer to the mean ($|y_{c,s} - \mu_c| \sim 0$), since our acceptance was devised to correct for these deficiencies in the first place). So if acceptance correction is being handled properly, these bins on the average, will have $\sigma_{c,s}^2 > (y_{c,s} - \mu_c)^2$ more than 68% of the time, which is what we see. In other words, in a way, this confirms our faith in the acceptance calculation.

Similar issues with low statistics were encountered in the CLAS *g11a* $K^+\Lambda$ channel analysis [6]. Taking a cue from there, we first bolster our statistics by simply merging bins. For instance, bins were merged from $\sqrt{s} = 2.0$ GeV to 2.04 GeV. Now, since Eq. 2.1 is valid only in a statistical sense and we seem to be statistics limited here, we next arrive upon the following compromise – demand that the minimum occupancy (pre acceptance corrected yield) in every sector-wise $\cos \theta_{c.m.}^{K^+}$ bin is greater than 40 and that there are at least 40 such bins. Having enforced a higher statistics, we go back and check on Eq. 2.1 again. The percentage of points within 1σ is now reduced to $\sim 62\%$ which means that there Eq. 2.1 must be modified to

$$\sum_{c,s} \Theta(\sigma_{c,s}^2 + (\sigma_{acc} y_{c,s})^2 - (y_{c,s} - \mu_c)^2) \approx 0.68N \quad (2.2)$$

where σ_{acc} is the (relative) systematic error from our acceptance calculation. Note that since no particular dependence on $\cos \theta_{c.m.}^{K^+}$ can be noticed in the errors from Fig. 2.8, we will assume that σ_{acc} does not depend on this variable.

The discrete nature of Eq. 2.2 means that it cannot be solved analytically. In order to determine σ_{acc} we plot the percentage of points satisfying Eq. 2.2 versus incremental σ_{acc} as shown in Fig. 2.9. We see that 68% is hit at around $\sigma_{acc} = 0.04$ which is then our estimate for the systematic error in acceptance for a mean \sqrt{s} of 2.2 GeV.

Similar studies were undertaken for higher energies with wider bin summations. However, the higher in \sqrt{s} one goes the more forward peaked the yields become so that summing over \sqrt{s} bins often do not help too much. Since the study in [3] involved a much higher statistics channel but was on the same dataset (CLAS *g11a*) and the errors that are of concern here depend “mostly” on hardware/recording/cooking malfunctions independent of the particular reaction under analysis, we will use the σ_{acc} values for higher \sqrt{s} as quoted there. Namely,

$$\sigma_{acc}(\sqrt{s}) = 0.0217\sqrt{s} + 0.002791. \quad (2.3)$$

Fig. 2.10 shows the comparison between studies on the $p\omega$ and $K^+\Lambda$ channel. The errors are mostly within half a percent of each other for two completely different channels, easily within the limits of statistical fluctuations. Furthermore, in the region where there is enough statistics (the $\sqrt{s} \approx 2.2$ GeV region that we analysed above), our σ_{acc} estimate of 4% agrees well with [3]. This further bolsters our confidence in using Eq. 2.3.

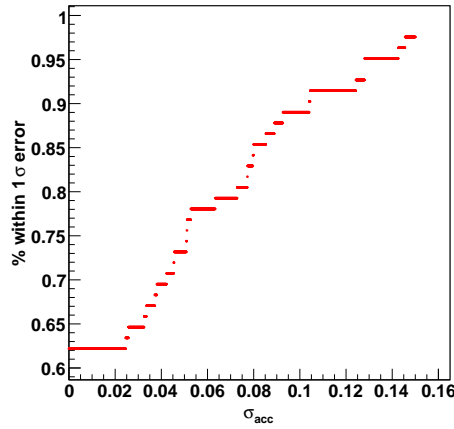


Figure 2.9: Percentage of points satisfying Eq. 2.2 plotted *vs.* incremental σ_{acc} . 68% is hit at around $\sigma_{acc} = 0.04$

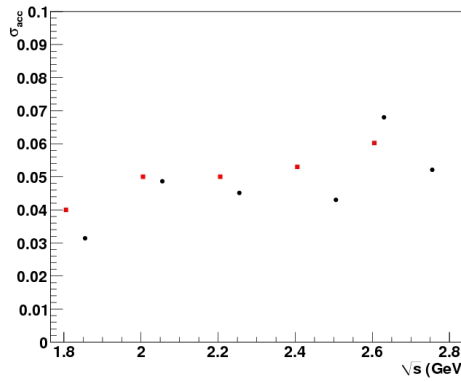


Figure 2.10: Variation of the acceptance uncertainty with center-of-mass energy (\sqrt{s}) for two different reactions, $p\omega$ (in red) [3] and $K^+\Lambda$ (in black) [6]. The agreement is mostly within sub-percent. Further, σ_{acc} goes from $\sim 4\%$ to $\sim 6\%$ over a \sqrt{s} range of ~ 1000 MeV so that *within* a \sqrt{s} bin (10 MeV wide) the variation in σ_{acc} due to $\cos \theta_{c.m.}^{K^+}$ dependence is conceivably quite small.

Since the ϕ (both charged- and neutral-mode topologies) has even lower statistics, it becomes even more difficult to conduct a similar sector-based study. Production-amplitude-wise, the ϕ channel is more akin to the ω . Particle-identification-wise, the difference between a kaon and a pion detection should not have too much of an effect on the acceptance uncertainty, as shown by the comparison between the ωp and $K^+ \Lambda$ channels in Fig. 2.10. We therefore adopt Eq. 2.3 for the ϕp channel as well.

2.9 Target Density

One of the factors going into the cross-section calculation is the density of the liquid hydrogen target. Like the rest of the assembly in CLAS, the density characteristics of the target changes with time and can be empirically written as a function of the pressure P , and temperature T of the target. CLAS records the latter quantities run by run and thus the density can be calculated on a run by run basis too. It was found in [3] that during the $g11a$ run period, the average target density was

$$\bar{\rho} = 0.07177 \frac{g}{cm^3}, \quad (2.4)$$

with a variance of

$$\sigma^2 = 6.776 \times 10^{-9} \frac{g^2}{cm^6}. \quad (2.5)$$

That is, the relative fluctuations are of the order of 0.11%.

2.10 Photon Flux Normalization

The final piece of information we require to calculate a physical cross-section from the quantum mechanical amplitudes is the total number of photons incident on the target. This quantity is called the *photon flux* and goes into the cross-section calculation as a factor in the denominator to give the *flux normalized* yields. The standard CLAS normalization utilizes the *gflux* package developed by Pasyuk *et al* [9]. We will give a brief description of the *gflux* next.

2.10.1 gflux

The basic idea is the following. Recall from that the Hall B tagging system converts a fraction of the electron beam provided by the CEBAF accelerator into a photon beam using bremsstrahlung. The remnant electron beam is thereafter bent by magnetic fields into the tagging system. However, only a fraction of these electrons are actually associated with any physical bremsstrahlung re-scattering, the rest of the electrons being the so called “out of time” electrons. Assuming Poissonian statistics for the “out of time” electron hits, one can estimate the total number of “good” (reliably detected) electrons entering the tagging system within a certain time window. One then defines the *tagging efficiency* as the number of “good” electrons relative to the number of photons impinging on the target. To calibrate the tagging efficiency, special *normalization* runs with lower beam intensity and thinner bremsstrahlung radiators were taken, the resultant lower photon flux being directly measured by a total absorption counter (TAC) placed directly in the photon beam. The efficiency was found to be around 85% and was generally dependent on the photon energy but independent of the flux. *gflux* also corrects for the detector *live time*, the fraction of the run time when the detector was “ready” to record data (CLAS experiences *dead time* when its data acquisition system is busy writing recorded information to the output stream). Finally, since the TAC was located some distance downstream from the target there were some additional corrections for the photon attenuation between the target location and the TAC [16].

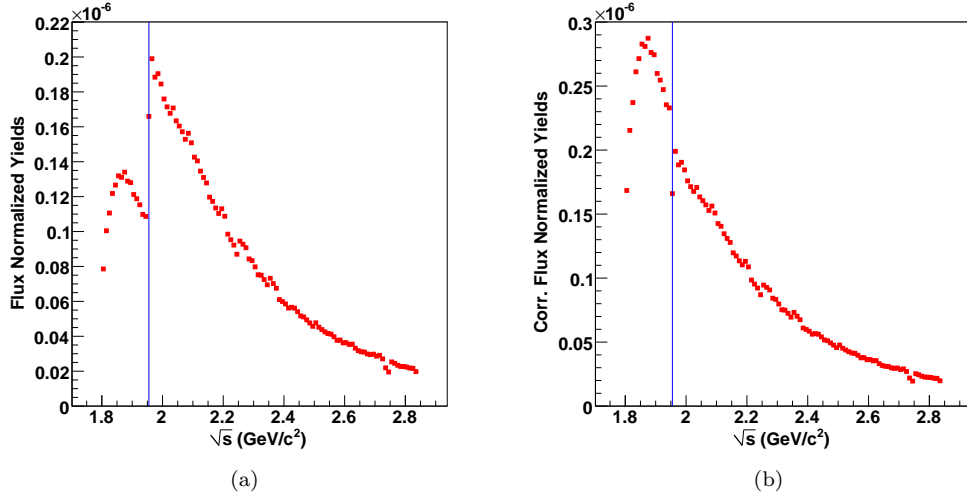


Figure 2.11: Flux normalized yields for the three-track topology: (a) Before and (b) After the correction for the $g11a$ trigger. The correction makes the yields look continuous across the cutoff bin $\sqrt{s} = 1.955$ GeV marked by the blue vertical line.

2.10.2 Live Time Correction

During preliminary analysis, inconsistencies in current dependence of flux-normalizations were found for the $g11a$ dataset, which was traced back to the live-time correction going into the $gflux$ calculation [3]. Generally, live time in CLAS is calculated by the scaler clocks in the DAQ system, but can also be measured by an additional component called the Faraday cup, a downstream device normally used for measuring the electron beam current, but which essentially measures electronic noise for a photon beam. Though the Faraday cup measurements are less precise for photons, no systematic discrepancies are expected with the clock measurements. However what was seen in practice was that the ratio LT_{FCUP}/LT_{CLOCK} showed a monotonic deviation from unity with an increasing beam current. Furthermore, the deviation went away with another factor of LT_{CLOCK} in the denominator, that is, LT_{FCUP}/LT_{CLOCK}^2 seemed to hold at a constant unity over a range of beam currents. Thus replacing LT_{CLOCK} by LT_{CLOCK}^2 in $gflux$ correspondingly removed the current dependence of the flux and here onwards LT_{CLOCK}^2 will be taken as the *corrected* time. For a more detailed account of this effect, see [3].

2.10.3 Trigger Correction for Flux

Recall from Sec. that the $g11a$ trigger required a signal from the first 40 T-counters in the Master OR (MOR). These T-counters correspond to the higher end of the photon energy spectrum. An event with a lower E_γ would have been recorded only if it fell within the time window of a separate electron hit on any of the first 40 T-counters. The exact cutoff E_γ whereon only the first 40 T-counters are hit varies from run to run, but the average is $E_\gamma \sim 1.57$ GeV or $\sqrt{s} \sim 1.956$ GeV as found in [3]. However, $gflux$ was programmed to accumulate photon flux over all the T-counters for any particular run. Thus for $\sqrt{s} \leq 1.956$ GeV, the photon flux is over-estimated by $gflux$. It was shown in [3] that the average probability over all runs that at least one photon hit any of the first 40 T-counters is ~ 0.47 . Thus if $gflux$ recorded N photons in all, only $\sim 0.47N$ would correspond to the first 40 T-counters. Correspondingly, below $\sqrt{s} \leq 1.956$ GeV, the photon flux has to be scaled down by a 0.47 multiplicative factor.

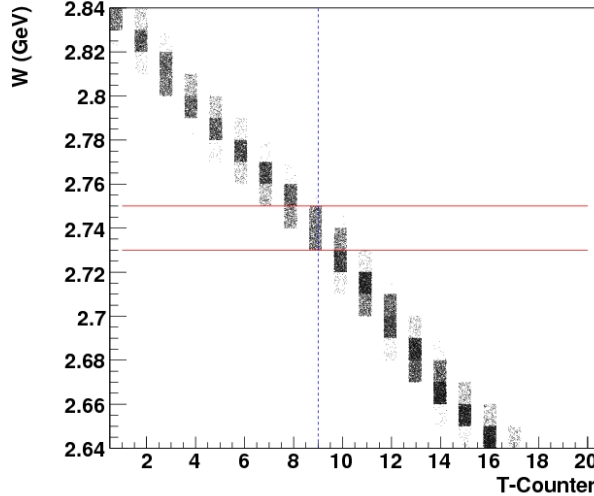


Figure 2.12: Photons corresponding to T-counter 9 spill on to the two W-bins (bin-centers 2.74 GeV and 2.75 GeV) where we see an abnormal photon flux.

Fig. 2.11 shows the flux normalized yield before and after the correction. Note that the correction brings continuity in the normalized yields across the cut-off energy 1.956 GeV though at the crossover bin itself, the yield seems abnormal. We shall henceforth exclude the $\sqrt{s} = 1.955$ GeV bin from this analysis. Also the two bins $\sqrt{s} = 2.735$ GeV and $\sqrt{s} = 2.745$ GeV show higher fluxes recorded than their surrounding bins. Fig. 2.12 shows a plot of W ($= \sqrt{s}$) vs. T-counter. Clearly photons from T-counter 9 are common to these two bins (and do not spill on to any other W-bin as well), so this effect is most probably due to a malfunction in T-9. Both these bins will thus also be excluded hereon.

2.10.4 Systematic Error

Fig. 2.13 shows the flux-normalized yields for the $K^+\Sigma^0$ three-track topology, as a function of the run number. The photon flux was recorded as a function of the photon beam energy E_γ , or equivalently, the center of mass energy \sqrt{s} . The flux normalized yield for a particular run was then obtained by

$$\mathcal{N}_r = \sum_s \frac{Y_s}{\mathcal{F}_s}, \quad (2.6)$$

where Y_s and \mathcal{F}_s are the $K^+\Sigma^0$ yield and corrected photon flux for each \sqrt{s} bin in the run r . A fit to the distribution gave a mean $\mu = 1.38192 \times 10^{-6}$ and standard deviation $\sigma = 4.44843 \times 10^{-8}$. Thus, $\sigma/\mu \sim 3.2\%$ which represents an *ad hoc* estimate of the systematic error for the flux normalization. Generally flux normalization systematics are studied by comparing cross-sections for different reactions between different experiments/datasets. A wider study encompassing the $p\omega$, $K^+\Lambda$ and $p\eta$ photo-production channels [4] gives a 7% systematic error for the flux. Combined in quadrature with the 3.2% run-by-run error (this number is 1.8 for the $p\omega$ case [4]) gives a 7.7% error for the flux.

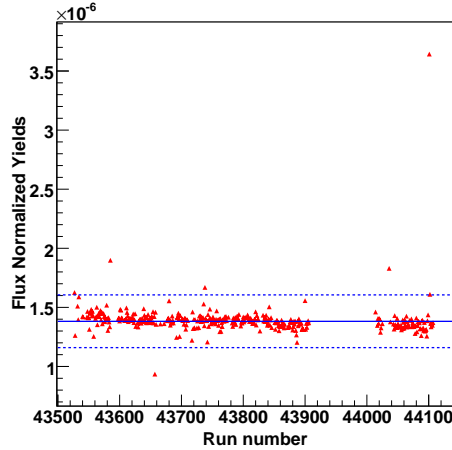


Figure 2.13: Flux normalized yields run by run for the $K^+\Sigma^0$ three-track topology. The mean $\mu = 1.38192 \times 10^{-6}$ and standard deviation $\sigma = 4.44843 \times 10^{-8}$ was found by fitting the distribution to a Gaussian. The continuous blue line shows the position of the mean and the dashed blue lines represent $\mu \pm 5\sigma$ limits.

Lastly, note that runs 43585, 43657, 44036 and 44101 seem to have abnormal flux-normalized yields. They were also found to have low statistics and will be removed from our analysis hereon.

2.11 Summary

To calculate the acceptance of the CLAS detector, we generated 300(200) million $\gamma p \rightarrow K^+\Sigma^0$ events for the three(two)-track topology, which were subsequently passed through GSIM, a GEANT based detector simulator. For the ϕp channel, similarly, 100 million $\gamma p \rightarrow \phi p$ events were generated for the charged- and neutral-mode topologies and processed by GSIM. Every particle identification and event selection cut that was applied on the data was repeated on the Monte Carlo using the same set of softwares. In addition the Monte Carlo required other corrections from triggering and resolution issues. The overall effort resulted in the Monte Carlo resembling the actual data as near as possible apart from the fact that the Monte Carlo contained no physics, being generated flat in phase space. We also calculated the photon flux and flux normalized yields for each run, with corrections for a live time detector error and an error arising from the *g11a* trigger. Our estimated systematic errors for each relevant factor were also calculated in this chapter.

Chapter 3

PWA Theoretical Formalism

In this chapter we discuss the construction of the amplitudes that we will be using in our partial wave analysis. Since our amplitudes will be written down in a manifestly covariant fashion, our language will be tensorial which is best equipped to deal with Lorentz covariance. We will first give a brief description of the representation theory of the Homogenous Lorentz Group (HLG). A particle of spin J and mass M is nothing but a member of a particular representation of the HLG. Furthermore, higher spin states are built up as tensor products of lower spin states, with supplementary conditions which are required to lower the number of independent components to that appropriate for a spin J state. The crucial point here is to do this while maintaining Lorentz covariance all the way. We describe this formalism, due to Rarita, Schwinger [17] and Zemach [18], in detail, following the setup of [3, 19]. Once we have constructed the spin states, we write out the amplitude for the entire decay chain. We also construct amplitudes for the non-resonant “background” processes and finally comment on how our formalism maintains the fundamental gauge invariance of QED all the way.

3.1 Representation Theory of the Homogenous Lorentz Group

The group of continuous space-time symmetries in special relativity consists of 4 space-time translations, 3 rotations and 3 boosts – a total of 10 generators. This group is called the Inhomogenous Lorentz Group or the Poincaré group [20, 21]. The group consisting of the 3 boosts and the 3 rotations, or 6 rotations in space-time, forms a sub-group called the Homogenous Lorentz Group or HLG. It is defined by the following group multiplication law

$$\Lambda^\mu_\rho \Lambda^\rho_\nu = g^\mu_\nu \tag{3.1}$$

where $g_{\mu\nu}$ is the metric tensor $\text{diag}(1, -1, -1, -1)$. This is nothing but the unitarity condition $\Lambda \Lambda^\dagger = 1$ written out with the proper indices attached. An infinitesimal element of the HLG can then be written as

$$\Lambda^\mu_\nu \sim g^\mu_\nu + \omega^\mu_\nu \tag{3.2}$$

where we have assumed that every element is path connected to the unit element g^μ_ν so that the discrete translations – space reflections and time inversion, are not included. It is easy to see then that $\omega_{\mu\nu} = -\omega_{\nu\mu}$ so that the HLG is isomorphic to the group of 4×4 anti-symmetric matrices (which also has ${}^4C_2 = 6$ generators).

A *representation* of the HLG is then defined as a group of operators $D(\Lambda)$ acting on a “state” space, with the following group multiplication law

$$D(\Lambda_1)D(\Lambda_2) = D(\Lambda_1 \Lambda_2), \tag{3.3}$$

with the generators $J^{\mu\nu}$ given by

$$D(\Lambda) = \exp\left(\frac{i}{2}\omega_{\mu\nu}J^{\nu\mu}\right) = 1 + \frac{i}{2}\omega_{\mu\nu}J^{\nu\mu} + \dots \quad (3.4)$$

The “state” space will contain all our usual particles – scalars, vectors, *et al.* But to see the connection between spin and representations, we need to further work out the algebra for the generators of the representations.

3.1.1 The HLG algebra

The easiest way to do is by invoking the group multiplication law for the infinitesimal element $\bar{\Lambda} = 1 + \bar{\omega}$:

$$D(\Lambda)D(\bar{\Lambda})D(\Lambda^{-1}) = D(\Lambda\bar{\Lambda}\Lambda^{-1}) \quad (3.5a)$$

$$= D(1 + \Lambda\bar{\omega}\Lambda^{-1}) \quad (3.5b)$$

$$= 1 + \frac{i}{2}(\Lambda\bar{\omega}\Lambda^{-1})_{\rho\sigma}J^{\rho\sigma} \quad (3.5c)$$

$$= 1 + \frac{i}{2}\bar{\omega}_{\mu\nu}\Lambda_{\rho}^{\mu}\Lambda_{\sigma}^{\nu}J^{\rho\sigma}. \quad (3.5d)$$

On the other hand,

$$D(\Lambda)D(\bar{\Lambda})D(\Lambda^{-1}) = 1 + D(\Lambda)\frac{i}{2}\bar{\omega}_{\mu\nu}J^{\mu\nu}D(\Lambda^{-1}). \quad (3.6)$$

Comparing Equations 3.5d and 3.6 we find that the generators $J^{\mu\nu}$ transform as second rank contravariant tensors:

$$D(\Lambda)J^{\mu\nu}D(\Lambda^{-1}) = \Lambda_{\rho}^{\mu}\Lambda_{\sigma}^{\nu}J^{\rho\sigma} \quad (3.7)$$

If we further take Λ be infinitesimal too, as $1 + \omega$, and keep all ω terms till the first order, Equation 3.7 gives the following algebra:

$$[J^{\mu\nu}, J^{\rho\sigma}] = i(g^{\mu\sigma}J^{\rho\nu} + g^{\nu\sigma}J^{\mu\rho} - g^{\rho\mu}J^{\sigma\nu} - g^{\rho\nu}J^{\mu\sigma}). \quad (3.8)$$

Until now we have not made assumptions about the dimensionality of space-time – Equation 3.8 will hold for $SO(1, d)$, the rotation group in $(d + 1)$ space-time dimensions. However $(n + 1)$ space-time has the special property ${}^nC_2 = n$ for $n = 3$, so that we can write the following:

$$J_1 \equiv J^{23} = J_{23} \quad (3.9a)$$

$$J_2 \equiv J^{31} = J_{31} \quad (3.9b)$$

$$J_3 \equiv J^{12} = J_{12} \quad (3.9c)$$

$$K_1 \equiv J^{10} \quad (3.9d)$$

$$K_2 \equiv J^{20} \quad (3.9e)$$

$$K_3 \equiv J^{30}, \quad (3.9f)$$

where the J_i 's are the three rotation generators and the K_i 's are the boosts. We can then recast Equation 3.8 into the more physically transparent following three commutators [21]:

$$[J_i, J_j] = i\epsilon_{ijk}J_k \quad (3.10a)$$

$$[J_i, K_j] = i\epsilon_{ijk}K_k \quad (3.10b)$$

$$[K_i, K_j] = -i\epsilon_{ijk}J_k \quad (3.10c)$$

Note that the K_i 's here are not Hermitian because the boost operator is not unitary (which is okay since the HLG is a non-compact group). Also, from Equations 3.10b and 3.10c, the rotations and boosts mix. This has consequences like the phenomenon of Thomas precession in relativity.

Next, consider the following linear combinations:

$$A_i \equiv \frac{1}{2}(J_i - iK_i) \quad (3.11a)$$

$$B_i \equiv \frac{1}{2}(J_i + iK_i), \quad (3.11b)$$

whereupon one finds,

$$[A_i, A_j] = i\epsilon_{ijk}A_k, \quad [B_i, B_j] = i\epsilon_{ijk}B_k \quad (3.12)$$

together with the decoupling

$$[A_i, B_j] = 0. \quad (3.13)$$

The structure of the HLG unfolds now – it is simply a direct product of two rotation groups! General representations of the HLG are to be labelled as (A, B) where A and B are integers or half-integers. Within a representation, a particular state is labelled as (a, b) where $a = -A, -A+1, \dots, A$ and $b = -B, -B+1, \dots, B$. Since the total angular momentum is $\vec{J} = \vec{A} + \vec{B}$, the “spin” j of any particle will come from Clebsch-Gordon decomposition of mixing two spins with j taking integral and half-integral values between $|A - B|$ and $|A + B|$.

3.2 Spin Half Representation

The simplest possible representations are fields transforming as $(0, \frac{1}{2})$ or $(\frac{1}{2}, 0)$. These 2-component spinors are called Weyl spinors. Now notice that the two discrete transformations – charge conjugation \mathcal{C} and parity reversal \mathcal{P} transforms (A, B) to (B, A) . This is easy to see from Equation 3.11 where A and B are evidently conjugate to each other. \mathcal{C} interchanges A and B explicitly, while \mathcal{P} reverses only \vec{K} keeping \vec{J} constant, whereby A and B are flipped again. Thus in theories like QED and QCD where both \mathcal{C} and \mathcal{P} are separately conserved, the fields must have both $(0, \frac{1}{2})$ and $(\frac{1}{2}, 0)$ components. These 4-component spinors transforming as $(\frac{1}{2}, 0) \oplus (0, \frac{1}{2})$ are called Dirac spinors. However, a spin half particle has only 2 independent components. To reduce the number of independent components from 4 to 2, we need a supplementary condition, which is nothing but the Dirac equation

$$(\gamma^\mu p_\mu - w)u(p, m) = 0, \quad (3.14)$$

where $u(p, m)$ is the Dirac spinor for a particle of mass w , 4-momentum p and spin projection $m (= \pm \frac{1}{2})$, while the 4×4 matrices γ^μ satisfy anti-commutation relations

$$\gamma^\mu \gamma^\nu + \gamma^\nu \gamma^\mu = 2g^{\mu\nu}. \quad (3.15)$$

In the *Dirac basis*, which we will use here, the γ matrices are defined as

$$\gamma^0 = \begin{pmatrix} 1 & 0 \\ 0 & -1 \end{pmatrix} \quad (3.16a)$$

$$\gamma^i = \begin{pmatrix} 0 & \sigma_i \\ -\sigma_i & 0 \end{pmatrix} \quad (3.16b)$$

where σ_i are the Pauli matrices. The “fifth” γ matrix, which anticommutes with all the other four is given by

$$\gamma^5 \equiv i\gamma^0\gamma^1\gamma^2\gamma^3 = \begin{pmatrix} 0 & 1 \\ 1 & 0 \end{pmatrix}. \quad (3.17)$$

The Dirac equation in the particle’s rest frame then becomes

$$\begin{pmatrix} 0 & 0 \\ 0 & -2w \end{pmatrix} u(p_{rf}, m) = 0. \quad (3.18)$$

Therefore, the lower two components of $u(p_{rf}, m)$ are zero and the 4-component spinor takes the form

$$u(p_{rf}, m) = 2w \begin{pmatrix} \chi(m) \\ 0 \end{pmatrix}, \quad (3.19)$$

where

$$\chi(+\frac{1}{2}) = \begin{pmatrix} 1 \\ 0 \end{pmatrix}, \quad \chi(-\frac{1}{2}) = \begin{pmatrix} 0 \\ 1 \end{pmatrix}, \quad (3.20)$$

are the 2-component spinors. To get the 4-component spinor in any arbitrary frame, we simply boost it from the rest frame yielding [20]

$$u(p, m) = \Lambda_{\frac{1}{2}}(p)u(p_{rf}, m) = \sqrt{E+w} \begin{pmatrix} \chi(m) \\ \frac{\vec{\sigma} \cdot \vec{p}}{E+w} \chi(m) \end{pmatrix}, \quad (3.21)$$

where $\Lambda_{\frac{1}{2}}(p)$ is the spinor boost operator under which the γ ’s transform like a 4-vector:

$$D(\Lambda_{\frac{1}{2}}^{-1}(p))\gamma^\mu D(\Lambda_{\frac{1}{2}}(p)) = \Lambda^\mu_\nu(p)\gamma^\nu. \quad (3.22)$$

An important property of the gamma matrices is that $(\gamma^i)^\dagger = -\gamma^i$ for i from 1 to 3, whilst $(\gamma^0)^\dagger = \gamma^0$. This stems from the fact that the HLG is isomorphic to $SO(1, 3)$ instead of $SO(4)$. Both these relations can be summed up as $(\gamma^\mu)^\dagger = \gamma^0\gamma^\mu\gamma^0$. An immediate consequence of this is that the adjoint of the Dirac spinor u is not u^\dagger but $\bar{u} \equiv u^\dagger\gamma^0$, for only then does the hadronic current $u^\dagger\gamma^\mu u$ come out to be Hermitian. With u and \bar{u} , we can now build Lorentz scalars $\bar{u}u$, pseudo-scalars $\bar{u}\gamma^5 u$, vectors $\bar{u}\gamma^\mu u$, pseudo-vectors $\bar{u}\gamma^5\gamma^\mu u$ and tensors $\bar{u}\sigma^{\mu\nu}u$ ($\sigma^{\mu\nu} = \frac{i}{2}[\gamma_\mu, \gamma_\nu]$). We also define the spin $\frac{1}{2}$ projection operator

$$P^{(\frac{1}{2})}(p) = \frac{1}{2w} \sum_m u(p, m)\bar{u}(p, m) = \frac{1}{2w}(\gamma^\mu p_\mu + w), \quad (3.23)$$

which, acting on an arbitrary spinor Π , projects out the piece that is a solution to the Dirac equation

$$(\gamma^\mu p_\mu - w)P^{(\frac{1}{2})}(p)\Pi = \frac{1}{2w}(p^2 - w^2)\Pi = 0. \quad (3.24)$$

3.3 Integral Spin Formalism

Moving on to integral spins now, the simplest case is for vectors – spin-1 massive particles (we will come back to the massless case in a bit). The transformation properties of these objects are

$$D(\Lambda_1^{-1})V^\mu D(\Lambda_1) = \Lambda^\mu_\nu V^\nu, \quad (3.25)$$

which leads to,

$$[J_i, V_j] = i\epsilon_{ijk}V_k, \quad [K_i, V_j] = 0, \quad (3.26)$$

or, in terms of A and B ,

$$[A_i, V_j] = \frac{i}{2} \epsilon_{ijk} V_k, \quad [B_i, V_j] = \frac{i}{2} \epsilon_{ijk} V_k. \quad (3.27)$$

That is, these come from the $(\frac{1}{2}, \frac{1}{2})$ representation or the direct product $(\frac{1}{2}, 0) \otimes (0, \frac{1}{2})$ (note however that the vector representation is an irreducible representation). A 4-vector has four independent components, but we know that there are only three polarization states for a spin-1 particle. Thus we need a constraint equation, which comes in the form

$$p_\mu \epsilon^\mu(p, m) = 0 \quad (3.28)$$

for momentum p_μ , mass w and spin projection m . In the particle's rest frame this correctly implies that the time-component of ϵ^μ is 0. The spatial components are then chosen as

$$\vec{\epsilon}(\pm 1) = \mp \frac{1}{\sqrt{2}}(1, \pm i, 0), \quad \vec{\epsilon}(0) = (0, 0, 1). \quad (3.29)$$

As earlier, the polarization vector in any general frame is gotten by making a boost on Equation 3.29 from the rest frame. The spin-1 projection operator is then defined as

$$P_{\mu\nu}^{(1)}(p) = \sum_m \epsilon_\mu(p, m) \epsilon_\nu^*(p, m) = -g_{\mu\nu} + \frac{p_\mu p_\nu}{w^2} \equiv -g_{\mu\nu}^\perp \quad (3.30)$$

so that $y_\mu^\perp = P_{\mu\nu}^{(1)}(p)y^\nu$ is orthogonal to p for any y^ν . Note that in the *CM* frame, $g_{\mu\nu}^\perp$ takes the simple form

$$g_{\mu\nu, CM}^\perp = \begin{pmatrix} 0 & 0 & 0 & 0 \\ 0 & -1 & 0 & 0 \\ 0 & 0 & -1 & 0 \\ 0 & 0 & 0 & -1 \end{pmatrix}, \quad (3.31)$$

so that it projects out the spatial part of any 4-vector in which the angular momentum states “live”.

3.3.1 Massless Case

For a massless particle like the photon, we cannot go to its rest frame. Equation 3.28 now does not uniquely specify ϵ^μ , for if ϵ^μ is a solution, so is $\epsilon^\mu + \alpha p^\mu$ for any α . This is quite common in gauge theories where the extra gauge symmetry renders certain degrees of freedom unphysical (here, the longitudinal polarization component). One needs to place extra conditions called gauge conditions to fix the gauge completely and the theory/final result is completely blind as to what this condition may be. In QED, this is called the Gupta-Bleuler formalism [22] where the only allowed physical states are those with ϵ^0 , or rather its expectation value, is equal to that of ϵ^3 . Following this, in this work we will choose the two states as the left and right circular polarization states for the particle momentum in the \hat{z} direction:

$$\epsilon^\mu(k\hat{z}, \pm 1) = \mp \frac{1}{\sqrt{2}}(0, 1, \pm i, 0). \quad (3.32)$$

Likewise, the massless spin projection operator cannot be written in the form of Equation 3.30 because the polarization now has only two independent components. Following [23], in photoproduction the photon projection operator is constructed for the γp system as a whole. Thus

$$g_{\mu\nu}^{\perp\perp} = \sum_{m_\gamma} \epsilon_\mu(m_\gamma) \epsilon_\nu^*(m_\gamma) = g_{\mu\nu} - \frac{P_\mu P_\nu}{P^2} - \frac{k_\mu^\perp k_\nu^\perp}{k_\perp^2}, \quad (3.33)$$

where P^μ is the total and k^μ is the relative momentum of the γp system and

$$k_\mu^\perp = k^\nu g_{\mu\nu}^\perp = k^\nu \left(g_{\mu\nu} - \frac{P_\mu P_\nu}{P^2} \right). \quad (3.34)$$

Then, in the CM frame, with the photon momentum parallel to the z -axis, $g_{\mu\nu}^{\perp\perp}$ takes the simple form

$$g_{\mu\nu,CM}^{\perp\perp} = \begin{pmatrix} 0 & 0 & 0 & 0 \\ 0 & -1 & 0 & 0 \\ 0 & 0 & -1 & 0 \\ 0 & 0 & 0 & 0 \end{pmatrix}. \quad (3.35)$$

3.3.2 Spin-2 (and higher) Tensors

Now that we have set up the formalism for spin-1 tensors, it is easy to couple them to form higher momentum tensors. A general spin- n tensor has n indices as $\epsilon_{\mu_1\mu_2\dots\mu_n}$. For massive states these will be representations of $SO(d-1)$ for d space-time dimensions. The massless case, as for example the graviton $g_{\mu\nu}$ which transforms as a massless spin-2 particle, will be in a $SO(d-2)$ representation because there being no rest frame and one has to go to the helicity frame $p_{hel} = (E, 0, \dots, E)$ to define the angular momentum states. Henceforth we will be concerned with massive higher spin states only.

The spin-2 polarization state is then formed as a direct product of two spin-1 states with the appropriate Clebsch-Gordon coefficients attached in the front:

$$\epsilon_{\mu\nu}(p, m) = \sum_{m_1, m_2} \langle 1m_1 1m_2 | 2m \rangle \epsilon_\mu(p, m_1) \epsilon_\nu(p, m_2). \quad (3.36)$$

Since these are representations of $SO(3)$, they are also traceless and symmetric and must satisfy the appropriate generalization of Equation 3.28. Or,

$$g^{\mu\nu} \epsilon_{\mu\nu}(p, m) = 0 \quad (3.37a)$$

$$\epsilon_{\mu\nu}(p, m) = \epsilon_{\nu\mu}(p, m) \quad (3.37b)$$

$$p^\mu \epsilon_{\mu\nu}(p, m) = 0. \quad (3.37c)$$

These supplementary conditions, known as Rarita-Schwinger conditions correctly reduce the number of independent components from 16 (for a general rank-2 tensor) to 5 (for a spin-2 state). The generalization of Equation 3.30 to spin-2 states is

$$P_{\mu_1\mu_2\nu_1\nu_2}^{(2)}(p) = \sum_m \epsilon_{\mu_1\mu_2}(p, m) \epsilon_{\nu_1\nu_2}^*(p, m) \quad (3.38a)$$

$$= \frac{1}{2} (g_{\mu_1\nu_1}^\perp g_{\mu_2\nu_2}^\perp + g_{\mu_1\nu_2}^\perp g_{\mu_2\nu_1}^\perp) - \frac{1}{3} g_{\mu_1\mu_2}^\perp g_{\nu_1\nu_2}^\perp, \quad (3.38b)$$

which projects out that part of a general rank-2 tensor $T_{\mu\nu}$ which satisfies the Rarita-Schwinger conditions.

Further generalization to spin- J states is easy to see now. One builds up the spin- J states by coupling together spin- $(J-1)$ and spin-1 states as follows

$$\epsilon_{\mu_1\mu_2\dots\mu_J}(p, m) = \sum_{m_{J-1}, m_1} \langle (J-1)m_{J-1} 1m_1 | Jm \rangle \epsilon_{\mu_1\mu_2\dots\mu_{J-1}}(p, m_{J-1}) \epsilon_{\mu_J}(p, m_1). \quad (3.39)$$

The Rarita-Schwinger conditions remain the same except that every summation in Equation 3.37 is done pairwise over all the indices now. And finally, the spin- J projection operator is defined as

$$P_{\mu_1 \mu_2 \dots \mu_J \nu_1 \nu_2 \dots \nu_J}^{(J)}(p) = \sum_m \epsilon_{\mu_1 \mu_2 \dots \mu_J}(p, m) \epsilon_{\nu_1 \nu_2 \dots \nu_J}^*(p, m). \quad (3.40)$$

The last object we need here is a projection operator for spin- J which is *not* of rank $2J$. In other words we want to project out the spin- J states of a rank r tensor when $J \neq r$ (we will need this during construction of amplitudes using the multipole basis). One of the ways in which this can be done is by coupling spin- $(r - 1)$ and spin-1 states and using Clebsch-Gordan coefficients to project out the spin- J part (note that J is constrained to be between $r - 2$ and r now, which will suffice for our multipole construction as we will see). Thus,

$$\epsilon_{\mu_1 \mu_2 \dots \mu_r}^J(p, m) = \sum_{m_{r-1}, m_1} \langle (r-1)m_{r-1} 1m_1 | Jm \rangle \epsilon_{\mu_1 \mu_2 \dots \mu_{r-1}}(p, m_{r-1}) \epsilon_{\mu_r}(p, m_1), \quad (3.41)$$

and

$$P_{\mu_1 \mu_2 \dots \mu_r \nu_1 \nu_2 \dots \nu_r}^{(J)}(p) = \sum_m \epsilon_{\mu_1 \mu_2 \dots \mu_r}^J(p, m) \epsilon_{\nu_1 \nu_2 \dots \nu_r}^{J*}(p, m). \quad (3.42)$$

3.3.3 Orbital Angular Momentum

Consider a general decay reaction $a \rightarrow b + c$. We know that the combined state bc has orbital angular momentum \vec{L} given by the spherical harmonics in the *CM* frame of the system. The trouble is that, with multiple decays, one cannot be in the *CM* frame for each individual decay all at the same time. Thus one needs to define orbital angular momentum in a covariant fashion, independent of any frame, but which boils down to the familiar spherical harmonics in the *CM* frame.

To proceed further, we first define $P = p_b + p_c$ and $p_{bc} = \frac{1}{2}(p_b - p_c)$ to be the total and relative momentum respectively. The angular momentum- ℓ state is formed by first building up a rank- ℓ tensor as the product of the relative momenta $p_{bc}^{\nu_1} p_{bc}^{\nu_2} \dots p_{bc}^{\nu_\ell}$ and then projecting out the spin- ℓ part with $P_{\mu_1 \mu_2 \dots \mu_J \nu_1 \nu_2 \dots \nu_J}^{(J)}(P)$ (*cf.* Equation 3.39). Thus,

$$L_{\mu_1 \mu_2 \dots \mu_\ell}^{(\ell)}(p_{bc}) = P_{\mu_1 \mu_2 \dots \mu_\ell \nu_1 \nu_2 \dots \nu_\ell}^{(\ell)}(P) p_{bc}^{\nu_1} p_{cb}^{\nu_2} \dots p_{bc}^{\nu_\ell}. \quad (3.43)$$

Note that the projection operator automatically enforces the Rarita-Schwinger conditions and ensures that there are $(2\ell + 1)$ independent components only. For $\ell = 0, 1, 2$ and 3 , these states are given as [23]

$$L^{(0)}(p_{bc}) = 1 \quad (3.44a)$$

$$L_\mu^{(1)}(p_{bc}) = p_\mu^{bc \perp} \quad (3.44b)$$

$$L_{\mu_1 \mu_2}^{(2)}(p_{bc}) = \frac{3}{2} \left(p_{\mu_1}^{bc \perp} p_{\mu_2}^{bc \perp} - \frac{1}{3} p_{bc \perp}^2 g_{\mu_1 \mu_2}^\perp \right) \quad (3.44c)$$

$$L_{\mu_1 \mu_2 \mu_3}^{(3)}(p_{bc}) = \frac{5}{2} \left(p_{\mu_1}^{bc \perp} p_{\mu_2}^{bc \perp} p_{\mu_3}^{bc \perp} - \frac{1}{5} p_{bc \perp}^2 (g_{\mu_1 \mu_2}^\perp p_{\mu_3}^{bc \perp} + g_{\mu_1 \mu_3}^\perp p_{\mu_2}^{bc \perp} + g_{\mu_2 \mu_3}^\perp p_{\mu_1}^{bc \perp}) \right) \quad (3.44d)$$

where $g_{\mu_1 \mu_2}^\perp = g_{\mu_1 \mu_2} - \frac{P_{\mu_1} P_{\mu_2}}{P^2}$ and $p_\mu^{bc \perp} = g_{\mu\nu}^\perp p_{bc}^\nu$.

3.4 Tensor-Spinor Combinations

Having covered Dirac spinors and tensors, we now want to combine them to form spin- J representations where $J = n + \frac{1}{2}$ for integral n . Consider for example the simplest case – spin- $\frac{3}{2}$. Note that a spin- $\frac{3}{2}$ particle can belong to any of the following representations $(\frac{3}{2}, 0)$, $(0, \frac{3}{2})$,

$(\frac{1}{2}, \frac{1}{2})$ or $(1, \frac{1}{2})$. This is a central feature of field theory – there is no unique correspondence between particles and fields. However, our aim here is to build up a spin- $\frac{3}{2}$ state out of a Dirac spinor and a vector, so we will look at the latter two, which are contained in the direct product $(\frac{1}{2}, \frac{1}{2}) \otimes ((\frac{1}{2}, 0) \oplus (0, \frac{1}{2})) = (1, \frac{1}{2}) \oplus (\frac{1}{2}, 1) \oplus (0, \frac{1}{2}) \oplus (\frac{1}{2}, 0)$. As usual, on adding spin-1 and spin- $\frac{1}{2}$, we get spin- $\frac{3}{2}$ and another spin- $\frac{1}{2}$. One can also count the degrees of freedom here. A Dirac spinor has $2+2$ (spin- $\frac{1}{2}$ and its antiparticle) and a spin-1 vector, 3 independent components – the product, 12. In the product, these 12 components are divided into 8 components for a spin- $\frac{3}{2}$ and its antiparticle, along with $2+2$ components for another pair of conjugate spin- $\frac{1}{2}$'s (which must be set to zero to project out the spin- $\frac{3}{2}$ part). If $\psi^\mu(p) = \epsilon^\mu(p)u(p, m_{\frac{1}{2}})$ then the latter two spinors are formed by the two possible ways of contracting ψ^μ , viz. $\psi_1 = p_\mu \psi^\mu$ and $\psi_2 = \gamma_\mu \psi^\mu$. If ψ^μ satisfies the Dirac equation, it is easy to see that ψ_1 too must.

The case for ψ_2 is slightly trickier. In fact ψ_2 does *not* satisfy the Dirac equation – the sign of the mass comes out with a wrong sign, i.e., $(\gamma^\lambda p_\lambda + w)\psi_2 = 0$. One needs an extra γ^5 here. Thus, $\psi'_2 = \gamma^5 \gamma^\mu \psi_\mu$ is the other Dirac spinor. Alternatively, ψ_2 satisfies the Dirac equation for an antiparticle (which has the sign of p_μ reversed). Since γ^5 is block diagonal (or *equivalent* to a block diagonal form in some basis) setting either ψ_2 or ψ'_2 to 0 will kill the extra 2 degrees of freedom floating around.

This formulation is easily generalizable to higher spins. The Rarita-Schwinger conditions for general spin- $(n + \frac{1}{2})$ tensor-spinor $\psi_{\mu_1 \mu_2 \dots \mu_n}(p, m)$ takes the form [17]

$$\psi_{\mu_1 \mu_2 \dots \mu_i \dots \mu_j \dots \mu_n}(p, m) = \psi_{\mu_1 \mu_2 \dots \mu_j \dots \mu_i \dots \mu_n}(p, m) \quad (3.45a)$$

$$g^{\mu_i \mu_j} \psi_{\mu_1 \mu_2 \dots \mu_i \dots \mu_j \dots \mu_n}(p, m) = 0 \quad (3.45b)$$

$$(\gamma^\mu p_\mu - w) \psi_{\mu_1 \mu_2 \dots \mu_n}(p, m) = 0 \quad (3.45c)$$

$$p^{\mu_i} \psi_{\mu_1 \mu_2 \dots \mu_i \dots \mu_n}(p, m) = 0 \quad (3.45d)$$

$$\gamma^{\mu_i} \psi_{\mu_1 \mu_2 \dots \mu_i \dots \mu_n}(p, m) = 0. \quad (3.45e)$$

Equations 3.45d and 3.45e are the generalized versions of setting ψ_1 and ψ_2 to zero, as explained above.

3.4.1 Spin-Polarization Connection for Photon

Before ending this section we want to clarify the connection between the “spin” of photon and its polarization, given by ϵ^μ . The photon, even though a spin-1 particle, has only two polarization states. As we have mentioned before, this comes from the fact that it is massless – the longitudinal polarization is unphysical and can be gauged away. Thus the “spin” of the photon can only take values ± 1 – there is no 0-spin state. Additionally, the “spin” quantization is along the longitudinal direction and these are called the helicity states, even though ϵ_z along the longitudinal direction is 0. This last part is slightly tricky to see, so we will demonstrate the connection here explicitly. Our proof follows Jackson [24] treating the problem semi-classically.

Classically, the angular momentum of the electromagnetic field is given by

$$\vec{J} = \int d^3x \vec{x} \times (\vec{E} \times \vec{B}) \quad (3.46)$$

where \vec{E} is the electric field and \vec{B} is the magnetic field given in terms of the vector potential \vec{A} as $\vec{B} = \vec{\nabla} \times \vec{A}$. In field theory, A^μ is the photon field, proportional to ϵ^μ . Expanding $\vec{E} \times (\vec{\nabla} \times \vec{A})$ we get

$$\vec{J} = \int d^3x \vec{x} \times (E_\ell \vec{\nabla} A_\ell - E_\ell \partial_\ell \vec{A}) \quad (3.47a)$$

$$= \int d^3x (E_\ell (\vec{x} \times \vec{\nabla}) A_\ell - E_\ell x_i \partial_\ell A_j \epsilon^{ijk} \hat{k}) \quad (3.47b)$$

$$= \int d^3x (E_\ell (\vec{x} \times \vec{\nabla}) A_\ell + \vec{E} \times \vec{A}), \quad (3.47c)$$

where ϵ^{ijk} is the completely anti-symmetric tensor and the last step uses an integration by parts. If we identify the orbital angular momentum operator by $-i(\vec{x} \times \vec{\nabla})$ then the expression for the total angular momentum breaks down into an orbital part $\vec{L} = E_\ell (\vec{x} \times \vec{\nabla}) A_\ell$ and a “spin” part $\vec{S} = \vec{E} \times \vec{A}$.

Now in the radiation gauge, \vec{A} is transverse to the propagation vector $\vec{k} = k\hat{z}$ with $\vec{E} = -\frac{\partial \vec{A}}{\partial t}$. This allows an expansion of \vec{A} in the helicity basis $\vec{\epsilon}_\pm = (1/\sqrt{2})(\vec{\epsilon}_x \pm i\vec{\epsilon}_y)$ as

$$\vec{A} = a_+(k)\vec{\epsilon}_+ + a_-(k)\vec{\epsilon}_-, \quad (3.48)$$

and using the property $\vec{\epsilon}_+ \times \vec{\epsilon}_- = -i\hat{z}$, one finds

$$\vec{S} \sim k(|a_+(k)|^2 - |a_-(k)|^2) \hat{z}. \quad (3.49)$$

Thus, semi-classically, the photon “spin” is always along \hat{k} with the amplitudes for “up” or “down” given by $a_+(k)$ and $a_-(k)$ respectively.

3.5 $\Sigma^0 \rightarrow \gamma\Lambda \rightarrow \gamma p\pi^-$ Amplitude

3.5.1 $\Sigma^0 \rightarrow \gamma\Lambda$

Since Σ^0 and Λ are both neutral, the $\Sigma^0 \rightarrow \gamma\Lambda$ transition can only be through a magnetic ($M1$) transition. The amplitude for this process is given by

$$\mathcal{A}_{\Sigma^0 \rightarrow \gamma\Lambda} = \epsilon_\mu^*(p_\gamma, m_\gamma) \langle \Lambda(p_\Lambda, m_\Lambda) | J^\mu | \Sigma^0(p_{\Sigma^0}, m_{\Sigma^0}) \rangle, \quad (3.50)$$

where $\epsilon_\mu^*(p_\gamma, m_\gamma)$ is the polarization of the outgoing photon and J^μ is the electromagnetic hadronic current. Due to the $M1$ transition, the matrix element for the electromagnetic hadronic current can be written as

$$\langle \Lambda(p_\Lambda, m_\Lambda) | J^\mu | \Sigma^0(p_{\Sigma^0}, m_{\Sigma^0}) \rangle = e g_{\Sigma^0\Lambda} \bar{u}_\Lambda(p_\Lambda, m_\Lambda) \sigma^{\mu\nu} p_\nu u_{\Sigma^0}(p_{\Sigma^0}, m_{\Sigma^0}), \quad (3.51)$$

where $p = p_\gamma = p_{\Sigma^0} - p_\Lambda$ and $g_{\Sigma^0\Lambda}$ is the effective coupling constant for the transition. In the Σ^0 rest frame, the amplitude expression then effectively boils down to

$$\mathcal{A}_{\Sigma^0 \rightarrow \gamma\Lambda} \sim \bar{u}_\Lambda(-p, m_\Lambda) \not{\epsilon}^*(p_\gamma, m_\gamma) \not{p} u_{\Sigma^0}(0, m_{\Sigma^0}), \quad (3.52)$$

where we have used the Feynman slash notation $\not{p} = p^\mu \gamma_\mu$.

To simplify this expression, from Equation 3.21,

$$\bar{u}_\Lambda = u^\dagger \gamma^0 = \sqrt{E_\Lambda + w_\Lambda} \left(\chi^\dagger(m_\Lambda), -\chi^\dagger(m_\Lambda) \frac{\vec{\sigma} \cdot \vec{p}_\Lambda}{E_\Lambda + w_\Lambda} \right) \sim \left(\chi^\dagger(m_\Lambda), \chi^\dagger(m_\Lambda) \frac{\vec{\sigma} \cdot \vec{p}}{E_\Lambda + w_\Lambda} \right) \quad (3.53)$$

in the Σ^0 rest frame. Similarly,

$$u_{\Sigma^0} \sim \begin{pmatrix} \chi(m_{\Sigma^0}) \\ 0 \end{pmatrix}. \quad (3.54)$$

Now,

$$\not{p} = \begin{pmatrix} p & -\vec{\sigma} \cdot \vec{p} \\ \vec{\sigma} \cdot \vec{p} & -p \end{pmatrix} \quad (3.55)$$

(from here on, $p = |\vec{p}|$) so that

$$\not{p} u_{\Sigma^0} \sim \begin{pmatrix} p \chi(m_{\Sigma^0}) \\ \vec{\sigma} \cdot \vec{p} \chi(m_{\Sigma^0}) \end{pmatrix}. \quad (3.56)$$

We also know that the time component of ϵ_μ^* is 0, so that

$$\not{\epsilon}^* = \begin{pmatrix} 0 & -\vec{\sigma} \cdot \vec{\epsilon}^* \\ \vec{\sigma} \cdot \vec{\epsilon}^* & 0 \end{pmatrix} \quad (3.57)$$

and thus

$$\not{\epsilon}^* \not{p} u_{\Sigma^0} \sim \begin{pmatrix} -(\vec{\sigma} \cdot \vec{\epsilon}^*)(\vec{\sigma} \cdot \vec{p}) \chi(m_{\Sigma^0}) \\ p(\vec{\sigma} \cdot \vec{\epsilon}^*) \chi(m_{\Sigma^0}) \end{pmatrix}. \quad (3.58)$$

Putting everything together, we arrive at the following expression for the decay amplitude, computed in the Σ^0 rest frame

$$\begin{aligned} \mathcal{A}_{\Sigma^0 \rightarrow \gamma \Lambda} &\sim \left(\chi^\dagger(m_\Lambda), \chi^\dagger(m_\Lambda) \frac{\vec{\sigma} \cdot \vec{p}}{E_\Lambda + w_\Lambda} \right) \begin{pmatrix} -(\vec{\sigma} \cdot \vec{\epsilon}^*)(\vec{\sigma} \cdot \vec{p}) \chi(m_{\Sigma^0}) \\ p(\vec{\sigma} \cdot \vec{\epsilon}^*) \chi(m_{\Sigma^0}) \end{pmatrix} \\ &= \left[-\chi^\dagger(m_\Lambda)(\vec{\sigma} \cdot \vec{\epsilon}^*)(\vec{\sigma} \cdot \vec{p}) \chi(m_{\Sigma^0}) + \frac{p}{E_\Lambda + w_\Lambda} \chi^\dagger(m_\Lambda)(\vec{\sigma} \cdot \vec{p})(\vec{\sigma} \cdot \vec{\epsilon}^*) \chi(m_{\Sigma^0}) \right]. \end{aligned} \quad (3.59)$$

The above expression can be further simplified as follows. First, note that since $p_\mu \epsilon^\mu = 0$ and we fixed the time component of ϵ^μ as 0 via our gauge choice, $\vec{p} \cdot \vec{\epsilon} = 0$, which means $\vec{p} \cdot \vec{\epsilon}^*$ is also 0. Thus $(\vec{\sigma} \cdot \vec{p})(\vec{\sigma} \cdot \vec{\epsilon}^*) = \vec{p} \cdot \vec{\epsilon}^* + (\vec{p} \times \vec{\epsilon}^*) \cdot \vec{\sigma} = (\vec{p} \times \vec{\epsilon}^*) \cdot \vec{\sigma} = -(\vec{\sigma} \cdot \vec{\epsilon}^*)(\vec{\sigma} \cdot \vec{p})$. Substituting this in the above expression, we get

$$\mathcal{A}_{\Sigma^0 \rightarrow \gamma \Lambda} \sim - \left(\frac{p}{E_\Lambda + w_\Lambda} + 1 \right) [\chi^\dagger(m_\Lambda)((\vec{p} \times \vec{\epsilon}^*) \cdot \vec{\sigma}) \chi(m_{\Sigma^0})]. \quad (3.60)$$

Let us now go to the helicity basis for the outgoing photon and expand $\vec{\epsilon}$ as $a_+ \vec{\epsilon}_+ + a_- \vec{\epsilon}_-$. Then $\vec{\epsilon}^* = a_- \vec{\epsilon}_+ + a_+ \vec{\epsilon}_-$ and $\vec{p} \times \vec{\epsilon}^* = -i(a_- \vec{\epsilon}_+ + a_+ \vec{\epsilon}_+) = -i\vec{\epsilon}^*$, whence we can write finally write the amplitude expression stripped of all pre-factors as

$$\mathcal{A}_{\Sigma^0 \rightarrow \gamma \Lambda} \sim \chi^\dagger(m_\Lambda) (\vec{\epsilon}^* \cdot \vec{\sigma}) \chi(m_{\Sigma^0}) \quad (3.61)$$

3.5.2 $\Lambda \rightarrow p \pi^-$

The $\Lambda \rightarrow p \pi^-$ decay is a weak decay. The most general form of the invariant amplitude for a spin- $\frac{1}{2}$ hyperon going into a spin- $\frac{1}{2}$ baryon and a spin-0 pseudo-scalar meson is given by [25]:

$$\mathcal{A}_{\Lambda \rightarrow p \pi^-} \sim \bar{u}_p (A - B \gamma^5) u_\Lambda. \quad (3.62)$$

To compute this in the Λ rest frame, from Equation 3.21,

$$\bar{u}_p \sim \left(\chi^\dagger(m_p), \chi^\dagger(m_p) \frac{-\vec{\sigma} \cdot \vec{p}}{E_p + w_p} \right) \quad (3.63a)$$

$$u_\Lambda \sim \begin{pmatrix} \chi(m_\Lambda) \\ 0 \end{pmatrix}, \quad (3.63b)$$

where \vec{p} is the proton momentum and E_p , the proton energy, in the Λ rest frame. Plugging these back, Equation 3.62 becomes

$$\mathcal{A}_{\Lambda \rightarrow p\pi^-} \sim \left(\chi^\dagger(m_p), \chi^\dagger(m_p) \frac{-\vec{\sigma} \cdot \vec{p}}{E_p + w_p} \right) \begin{pmatrix} A & -B \\ -B & A \end{pmatrix} \begin{pmatrix} \chi(m_\Lambda) \\ 0 \end{pmatrix} \quad (3.64a)$$

$$\sim \chi^\dagger(m_p) (s + p \vec{\sigma} \cdot \hat{n}) \chi(m_\Lambda) \quad (3.64b)$$

$$\sim \chi^\dagger(m_p) (1 + x \vec{\sigma} \cdot \hat{n}) \chi(m_\Lambda), \quad (3.64c)$$

where $s = A$, $p = |\vec{p}|B/(E_p + w_p)$, $x = p/s$, $\hat{n} = \vec{p}/|\vec{p}|$ and $\Delta = \delta_s - \delta_p$ is the phase between s and p (the s and p nomenclature here refers to the non-relativistic S and P wave decays respectively). To relate to experiments, we now define the following quantities

$$\alpha = 2Re(s^*p)/(|s|^2 + |p|^2) = 2|x| \cos \Delta / (1 + |x|^2) \quad (3.65a)$$

$$\beta = 2Im(s^*p)/(|s|^2 + |p|^2) = -2|x| \sin \Delta / (1 + |x|^2) \quad (3.65b)$$

$$\gamma = (|s|^2 - |p|^2)/(|s|^2 + |p|^2) = (1 - |x|^2)/(1 + |x|^2), \text{ so that} \quad (3.65c)$$

$$\alpha^2 + \beta^2 + \gamma^2 = 1. \quad (3.65d)$$

$$\text{Also, } \beta = (1 - \alpha^2)^{1/2} \sin \phi \quad (3.65e)$$

$$\gamma = (1 - \alpha^2)^{1/2} \cos \phi \quad (3.65f)$$

$$\tan \Delta = -\frac{1}{\alpha} (1 - \alpha^2)^{1/2} \sin \phi. \quad (3.65g)$$

The PDG [8] lists $\alpha = 0.642 \pm 0.013$ and $\Delta = 7.7^\circ \pm 4.0^\circ$, whence $x \simeq 2.71e^{-i\Delta}$ or $x \simeq 0.37e^{-i\Delta}$ from the quadratic equation 3.65a. The first value for x gives $\gamma = -0.76$ while the latter gives $\gamma = +0.76$. One can see the sign ambiguity arising from the square root in Equation 3.65f. However, PDG lists γ as 0.76, so we will take $|x| = 0.37$. Finally, for the two body decay of $\Lambda \rightarrow p\pi^-$, $|\vec{p}| \simeq 0.1005 \text{ GeV}/c$ and $E_p \simeq 0.9436 \text{ GeV}$ so that $B/A \simeq 6.88e^{-i\Delta}$ and the final form of the amplitude is

$$\mathcal{A}_{\Lambda \rightarrow p\pi^-} \sim \bar{u}_p (1 - 6.88e^{-i\Delta} \gamma^5) u_\Lambda. \quad (3.66)$$

As a passing note, for $|x| = 2.71$, $B/A \simeq 50.83e^{-i\Delta}$.

3.5.3 $\mathcal{A}_{\Sigma^0 \rightarrow \gamma\Lambda \rightarrow \gamma p\pi^-}$ normalization

The $\Sigma^0 \rightarrow \gamma\Lambda$ transition being an electromagnetic decay, occurs instantaneously before the Σ^0 can travel any significant macroscopic distance. The Λ pathlength is of the order $\sim 10 \text{ cm}$, which means that the probability of its decaying outside the CLAS detector (roughly around 5 m, till the outer regions of the Drift Chambers) is around $1/\exp(50)$. Negligible, that is. Thus, aside acceptance issues, all the final states should be detected by CLAS. Quantum mechanically, this translates to:

$$\int |A_{\Sigma^0 \rightarrow \gamma\Lambda \rightarrow \gamma p\pi^-}|^2 d\Phi_{\Sigma^0 \rightarrow \gamma\Lambda \rightarrow \gamma p\pi^-} = 1, \quad (3.67)$$

where $\Phi_{\Sigma^0 \rightarrow \gamma\Lambda \rightarrow \gamma p\pi^-}$ incorporates the phase space for the Σ^0 decay. This condition should thus be enforced by a normalization factor N . However, overall normalizations cancel out in our fitting procedure (see Section 4.1), so that N is not required to be included in our codes.

3.6 $\phi \rightarrow K_1 K_2$ Amplitude

The four kaons K^\pm , $K_{L,S}^0$ are all pseudo-scalars, while the ϕ is a vector, ϵ_ϕ . There is only one way to form a vector out of two pseudo-scalars, *viz.* $\partial_\mu K_1 - \partial_\mu K_2$, antisymmetric in the two kaons.

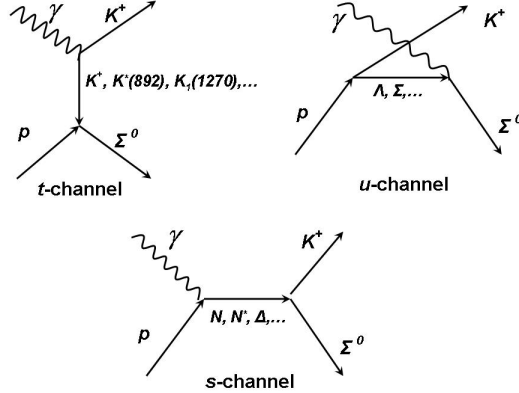


Figure 3.1: Shown are the diagrams characterizing the production mechanisms for the $\gamma p \rightarrow K^+ \Sigma^0$ process.

Therefore, the general $\phi \rightarrow K_1 K_2$ amplitude can be written as

$$\mathcal{A}_{\phi \rightarrow K_1 K_2} \sim (\epsilon_\phi)^\mu (p_{K_1} - p_{K_2})_\mu. \quad (3.68)$$

In other words, this is a simple P -wave decay.

3.7 $K^+ \Sigma^0$ Non-Resonant Amplitudes

Figure 3.1 shows the three production mechanisms for the $\gamma p \rightarrow K^+ \Sigma^0$ process. The Mandelstam variables are defined in the typical manner for two-to-two scattering [20]:

$$s = (p_p + p_\gamma)^2 = (p_{K^+} + p_{\Sigma^0})^2 \quad (3.69a)$$

$$t = (p_\gamma - p_{K^+})^2 = (p_p - p_{\Sigma^0})^2 \quad (3.69b)$$

$$u = (p_\gamma - p_{K^+})^2 = (p_p - p_{K^+})^2. \quad (3.69c)$$

The t and the u channels are referred to as non-resonant processes while the s channel proceeds through the various N, N^*, Δ intermediate resonances and is thus referred to as resonant processes.

3.7.1 t -channel 0^- Exchange

This is the simplest t -channel process – pseudo-scalar $K^+(493)$ exchange. To build the amplitude, we first write the necessary effective Lagrangians

$$\mathcal{L}_{\gamma K K} = -ie (K^\dagger \partial_\mu K - K \partial_\mu K^\dagger) A^\mu \quad (3.70a)$$

$$\mathcal{L}_{p K \Sigma}^{PS} = -ig_{p K \Sigma} K^\dagger \bar{\Sigma}^0 \gamma^5 p + H.c. \quad (3.70b)$$

$$\mathcal{L}_{p K \Sigma}^{PV} = \frac{f_{p K \Sigma}}{M} \partial^\mu K^\dagger \bar{\Sigma}^0 \gamma_\mu \gamma^5 p + H.c., \quad (3.70c)$$

where K , A_μ , p and Σ^0 are the K^+ meson, photon, proton and hyperon fields respectively and $H.c.$ denotes the Hermitian conjugate. $g_{p K \Sigma}$ and $f_{p K \Sigma}$ are coupling constants while M is an arbitrary mass scale (eg. proton or K^+ mass). Equation 3.70a can be understood to be arising from a kinetic term for the pseudo-scalar:

$$\mathcal{L}_{kinetic} \sim \frac{|D_\mu K|^2}{2}, \quad (3.71)$$

where D_μ is the covariant derivative $\partial_\mu - ieA_\mu$. For the $K\Sigma p$ hadronic vertex, both a pseudo-scalar (PS) and a pseudo-vector (PV) options are viable – for this analysis, we use the PS variant.

From these Lagrangians, we can write the K^+ pseudo-scalar meson exchange amplitude as

$$\mathcal{A}_{\gamma p \rightarrow K^+ \Sigma^0}^{K(bare)} = 2g_{K\Sigma p} e \bar{u}(p_{\Sigma^0}, m_{\Sigma^0}) \gamma^5 u(p_p, m_p) \frac{1}{t - w_{K^+}^2} (p_K)_\mu \epsilon^\mu(p_\gamma, m_\gamma), \quad (3.72)$$

where ϵ_μ is the photon polarization vector. We call this amplitude “bare” because it needs to be dressed by form factors to shield off short-distance hard processes to be described later on. The couplings are $e = \sqrt{4\pi/137}$, while the value of $g_{K\Sigma p}$ can be estimated from known πNN couplings using flavor $SU(3)$. Janssen, *et al* [26] reports this as

$$0.9 \leq \frac{g_{K\Sigma p}}{\sqrt{4\pi}} \leq 1.3, \quad (3.73)$$

but we will generally leave this as a free fit parameter.

3.7.2 t -channel 1^- Exchange

The necessary Lagrangians for the vector meson $K^*(892)$ exchange are

$$\begin{aligned} \mathcal{L}_{\gamma V K} &= \frac{e\kappa_{KV}}{4M} \epsilon^{\mu\nu\lambda\sigma} F_{\mu\nu} V_{\lambda\sigma} K + H.c. \\ &= \frac{e\kappa_{KV}}{M} \epsilon^{\mu\nu\lambda\sigma} \partial_\mu A_\nu \partial_\lambda V_\sigma K + H.c. \end{aligned} \quad (3.74a)$$

$$\mathcal{L}_{V\Sigma p} = -g_{V\Sigma p}^E \bar{\Sigma}^0 \gamma_\mu p V^\mu + \frac{g_{V\Sigma p}^M}{2(M_p + M_{\Sigma^0})} \bar{\Sigma}^0 \sigma_{\mu\nu} p V^{\mu\nu} + H.c. \quad (3.74b)$$

Here V^μ is the vector meson field and $V^{\mu\nu} = \partial^\mu V^\nu - \partial^\nu V^\mu$ is the anti-symmetric vector meson field tensor. κ_{KV} is the $K^+ K^*$ anomalous magnetic moment while $\epsilon^{\mu\nu\lambda\sigma}$ is the totally antisymmetric tensor with $\epsilon^{0123} = +1$. $F^{\mu\nu} = \partial^\mu A^\nu - \partial^\nu A^\mu$ is the electromagnetic field tensor while $\sigma_{\mu\nu} = \frac{i}{2}[\gamma_\mu, \gamma_\nu]$. Equation 3.74a can be understood as follows. First, the most basic gauge invariant interaction term for a massive vector boson can be written as $A_\nu \partial_\mu V^{\mu\nu}$ where the anti-symmetry of $V^{\mu\nu}$ is sufficient to show that this term is invariant under a gauge transformation of the kind $A_\nu \rightarrow A_\nu + \partial_\nu \Lambda$. An integration by parts renders this to the form $\partial_\mu A_\nu V^{\mu\nu}$. Now, since K^+ is a pseudo-scalar, one needs to include the $\epsilon^{\mu\nu\lambda\sigma}$ tensor from parity considerations. In the next step, noting that only the anti-symmetric part of $\partial_\mu A_\nu$ survives due to the anti-symmetry of $\epsilon^{\mu\nu\lambda\sigma}$, one can replace $\partial_\mu A_\nu$ by $F_{\mu\nu}$.

The hadronic vertex has two components – an electric part (coupling constant $g_{pV\Sigma}^E$) and a magnetic part (coupling constant $g_{pV\Sigma}^M$). The electric coupling amplitude thus becomes

$$\begin{aligned} \mathcal{A}_{\gamma p \rightarrow K^+ \Sigma^0}^{K_E^*(bare)} &= \sum_{m_{K^*}} (g_{K^*}^E) \bar{u}(p_{\Sigma^0}, m_{\Sigma^0}) \gamma^\mu u(p_p, m_p) \epsilon_\mu(p_{K^*}, m_{K^*}) \frac{1}{t - w_{K^*}^2} \\ &\quad \times \epsilon^{\nu\alpha\beta\lambda} \epsilon_\nu^*(p_{K^*}, m_{K^*}) (p_{K^*})_\alpha(p_\gamma)_\beta \epsilon_\lambda(p_\gamma, m_\gamma) \\ &= -(g_{K^*}^E) \bar{u}(p_{\Sigma^0}, m_{\Sigma^0}) \gamma_\nu u(p_p, m_p) \frac{1}{t - w_{K^*}^2} \epsilon^{\nu\alpha\beta\lambda} (p_{K^*})_\alpha(p_\gamma)_\beta \epsilon_\lambda(p_\gamma, m_\gamma) \end{aligned} \quad (3.75)$$

where we have replaced the sum over the vector meson polarizations by the metric tensor. Further replacing p_{K^*} by $p_\gamma - p_{K^+}$ and using the anti-symmetry of the Levi-Civita tensor, the above can be written as

$$\mathcal{A}_{\gamma p \rightarrow K^+ \Sigma^0}^{K_E^*(bare)} = (g_{K^*}^E) \bar{u}(p_{\Sigma^0}, m_{\Sigma^0}) \gamma_\nu u(p_p, m_p) \frac{1}{t - w_{K^*}^2} \epsilon^{\nu\alpha\beta\lambda} (p_{K^+})_\alpha(p_\gamma)_\beta \epsilon_\lambda(p_\gamma, m_\gamma). \quad (3.76)$$

Similarly, the magnetic part is given by

$$\begin{aligned} \mathcal{A}_{\gamma p \rightarrow K^+ \Sigma^0}^{K_M^*(bare)} &\sim \bar{u}(p_{\Sigma^0}, m_{\Sigma^0})(p_{K^*})^\mu \sigma_{\mu\nu} u(p_p, m_p) \frac{1}{t - w_{K^*}^2} \epsilon^{\nu\alpha\beta\lambda} (p_{K^*})_\alpha (p_\gamma)_\beta \epsilon_\lambda (p_\gamma, m_\gamma) \\ &= (g_{K^*}^M) \bar{u}(p_{\Sigma^0}, m_{\Sigma^0})(p_{K^*})^\mu \sigma_{\mu\nu} u(p_p, m_p) \frac{1}{t - w_{K^*}^2} \epsilon^{\nu\alpha\beta\lambda} (p_{K^+})_\alpha (p_\gamma)_\beta \epsilon_\lambda (p_\gamma, m_\gamma). \end{aligned} \quad (3.77)$$

3.7.3 t -channel 1^+ Exchange

For the pseudo-vector $K1(1270)$ exchange, the effective Lagrangians read

$$\begin{aligned} \mathcal{L}_{\gamma V_a K} &= i \frac{e \kappa_{KV_a}}{2M} F_{\mu\nu} V_a^{\mu\nu} K + H.c. \\ &= i \frac{e \kappa_{KV_a}}{M} \partial_\mu A_\nu (\partial^\mu V_a^\nu - \partial^\nu V_a^\mu) + H.c. \end{aligned} \quad (3.78a)$$

$$\mathcal{L}_{V_a \Sigma p} = -g_{V_a \Sigma p}^E \bar{\Sigma}^0 \gamma_\mu \gamma^5 p V_a^\mu + \frac{g_{pV_a \Sigma}^M}{2(M_p + M_{\Sigma^0})} \bar{\Sigma}^0 \sigma_{\mu\nu} \gamma^5 p V_a^{\mu\nu} + H.c., \quad (3.78b)$$

where V_a denotes the axial vector field. The structure of the two terms follows closely the reasoning given in the last subsection, except wherever the vector field needs to be replaced by the axial vector field and inclusion of a corresponding γ^5 wherever required for parity conservation.

The electric part of the amplitude is

$$\begin{aligned} \mathcal{A}_{\gamma p \rightarrow K^+ \Sigma^0}^{K1_E(bare)} &= \sum_{m_{K1}} \left[(g_{K1}^E) \bar{u}(p_{\Sigma^0}, m_{\Sigma^0}) \gamma^\mu \gamma^5 u(p_p, m_p) \epsilon_\mu (p_{K1}, m_{K1}) \frac{1}{t - w_{K1}^2} \right. \\ &\quad \times (p_\gamma)_\alpha \epsilon_\beta (p_\gamma, m_\gamma) ((p_{K1})^\alpha \epsilon^{*\beta} (p_{K1}, m_{K1}) - \alpha \leftrightarrow \beta) \Big] \\ &= (g_{K1}^E) \bar{u}(p_{\Sigma^0}, m_{\Sigma^0}) \gamma^\mu \gamma^5 u(p_p, m_p) \frac{1}{t - w_{K1}^2} \\ &\quad \times (p_\gamma)_\alpha \epsilon_\beta (p_\gamma, m_\gamma) \left((p_{K1})^\alpha \left(-g_\mu^\beta + \frac{(p_{K1})_\mu (p_{K1})^\beta}{w_{K1}^2} \right) - \alpha \leftrightarrow \beta \right) \\ &= (g_{K1}^E) \bar{u}_{\Sigma^0} \gamma^5 (k \cdot p_1 \not{e} - \epsilon \cdot p_1 \not{k}) u_p \frac{1}{t - w_{K1}^2}, \end{aligned} \quad (3.79)$$

where we have condensed our notation a bit in the last line to mean p_1 as the $K1$ momentum, ϵ as the photon polarization, k as the photon momentum and u_{Σ^0} and u_p as the Σ^0 and proton spinors.

The magnetic part is

$$\begin{aligned} \mathcal{A}_{\gamma p \rightarrow K^+ \Sigma^0}^{K1_M(bare)} &= \sum_{m_{K1}} \left[(g_{K1}^M) \bar{u}(p_{\Sigma^0}, m_{\Sigma^0}) \sigma^{\mu\nu} \gamma^5 u(p_p, m_p) (p_{K1})_\mu \epsilon_\nu (p_{K1}, m_{K1}) \frac{1}{t - w_{K1}^2} \right. \\ &\quad \times (p_\gamma)_\alpha \epsilon_\beta (p_\gamma, m_\gamma) ((p_{K1})^\alpha \epsilon^{*\beta} (p_{K1}, m_{K1}) - \alpha \leftrightarrow \beta) \Big], \end{aligned} \quad (3.80)$$

which after a few manipulations takes the form:

$$\mathcal{A}_{\gamma p \rightarrow K^+ \Sigma^0}^{K1_M(bare)} = (g_{K1}^M) \bar{u}_{\Sigma^0} \gamma^5 \left(k \cdot p_1 \not{e} \not{p}_1 - \epsilon \cdot p_1 \not{k} \not{p}_1 \right) u_p \frac{1}{t - w_{K1}^2}, \quad (3.81)$$

again in our condensed notation.

3.7.4 u -channel Y Exchange

The u -channel processes involve exchange of hyperons, the generic Lagrangians being

$$\begin{aligned}\mathcal{L}_{\gamma Y \Sigma} &= \frac{e\kappa_{\Sigma Y}}{4M_p} \bar{\Sigma}^0 \sigma_{\mu\nu} Y F^{\mu\nu} + H.c. \\ &= \frac{e\kappa_{\Sigma Y}}{2M_p} \bar{\Sigma}^0 \not{A} Y + H.c.\end{aligned}\quad (3.82a)$$

$$\mathcal{L}_{p Y K} = -ig_{K Y p} K^\dagger \bar{Y} \gamma^5 p + H.c. \quad (3.82b)$$

where Y is the hyperon spinor (assumed $\frac{1}{2}^+$). The amplitude is thus

$$\begin{aligned}\mathcal{A}_{\gamma p \rightarrow K^+ \Lambda}^{Y \frac{1}{2}^+ (bare)} &= \frac{ie\kappa_{Y \Sigma}}{2M_p} g_{K Y p} \bar{u}(p_\Sigma, m_\Sigma) \not{\psi}_\gamma \not{\epsilon}(m_\gamma, p_\gamma) \frac{i(\not{p}_Y + w_Y)}{u - w_Y^2} \gamma^5 u(p_p, m_p) \\ &= -\frac{e\kappa_{Y \Sigma}}{2M_p} g_{K Y p} \bar{u}(p_\Sigma, m_\Sigma) \not{\psi}_\gamma \not{\epsilon}(m_\gamma, p_\gamma) \frac{(\not{p}_Y + w_Y)}{u - w_Y^2} \gamma^5 u(p_p, m_p),\end{aligned}\quad (3.83)$$

where w_Y is the mass of the exchange hyperon and $\frac{i(\not{p}_Y + w_Y)}{u - w_Y^2}$ is the propagator.

The most natural candidate for the hyperon exchange is $\Lambda(1115)$. Though $\kappa_{\Sigma^0 \Lambda} \approx -1.61$ (we follow the sign convention from PDG based on $SU(3)$ calculations) is known, $g_{K \Lambda p}$ can only be estimated from flavor $SU(3)$. Assuming a 20% broken $SU(3)$, Janssen *et al* [26] reports this as

$$-4.5 \leq \frac{g_{K \Lambda p}}{\sqrt{4\pi}} \leq -3.0, \quad (3.84)$$

but we will leave this as a free parameter in our fits. In the same paper it is also mentioned that $\Lambda^*(1810)$ and $\Sigma^*(1880)$ could be included. Note that $\Lambda^*(1810)$ is a $\frac{1}{2}^-$ spinor, for which the amplitude is slightly different:

$$\mathcal{A}_{\gamma p \rightarrow K^+ \Lambda}^{Y \frac{1}{2}^- (bare)} = -\frac{e\kappa_{Y \Sigma}}{2M_p} g_{K Y p} \bar{u}(p_\Sigma, m_\Sigma) \not{\psi}_\gamma \not{\epsilon}(m_\gamma, p_\gamma) \gamma^5 \frac{(\not{p}_Y + w_Y)}{u - w_Y^2} u(p_p, m_p). \quad (3.85)$$

3.7.5 s -channel Proton Exchange

Even though this is an s -channel process, it is not a “resonance” term *per se* according to the nomenclature that we have set up. Though it is natural to include it, there is another reason for its inclusion in conjunction with the t -channel K^+ exchange. The argument comes from gauge principles and is explained in Section 3.10.

The $K\Sigma p$ vertex is the same as in t -channel K^+ exchange while the γpp vertex has both electric and magnetic terms. The amplitude reads

$$\mathcal{A}_{\gamma p \rightarrow K^+ \Lambda}^{proton\,exch.\,(bare)} = g_{K \Sigma p} e \bar{u}(p_{\Sigma^0}, m_{\Sigma^0}) \gamma^5 \frac{\not{p}_p + \not{p}_\gamma + m_p}{s - m_p^2} \left(\not{\epsilon}(p_\gamma, m_\gamma) - \frac{\kappa_p}{2M_p} \not{\epsilon}(p_\gamma, m_\gamma) \not{\psi}_\gamma \right) u(p_p, m_p), \quad (3.86)$$

where $\kappa_p = 2.793$ is the anomalous magnetic moment of the proton.

3.8 ϕp Non-Resonant Amplitudes

3.8.1 The P_1 Pomeron – VDM and DL theories

At high energies and forward scattering (\sqrt{s} large, $t \rightarrow t_0$), QCD cross-sections show the universal feature

$$\frac{d\sigma}{dt} = \left(\frac{d\sigma}{dt} \right)_{t=t_0} e^{B(t-t_0)}, \quad (3.87)$$

where $t_0 = |t|_{min}$. That is, the cross-sections are roughly independent of the energy and falls exponentially with $(t - t_0) \sim \cos \theta$. The exponential fall-off is reminiscent of the intensity formula in diffraction around a small circular object and therefore this is also called diffractive scattering. From a Regge theory perspective, $d\sigma/dt \sim s^{2(\alpha(t)-1)}$ and the near s -independence implies that the exchange Regge trajectory has an intercept of around 1. This is the well-known Pomeron which we will denote as P_1 . The experimentally known (from fits to high energy data) P_1 trajectory is

$$\alpha_1(t) = \alpha_1(0) + \alpha'_1 t \approx 1.08 + 0.25t. \quad (3.88)$$

For vector mesons V (ρ, ω, ϕ), forward angle photoproduction is known to be dominated by Pomeron exchange. In the vector meson dominance model (VDM), the photon first converts into a vector meson which then diffractively scatters off the nucleon as shown in Fig. It also seems that the Pomeron couples to quarks as a $C = +1$ isoscalar photon (the photon has both $I = 0$ and $I = 1$ components).

3.9 Resonant Amplitudes

3.9.1 Isospin Considerations

The Σ^0 is a iso-vector with $I_3 = 0$. As a result both N^* (iso-scalar) and Δ^* (iso-vector) exchange is possible in $K^+ \Sigma^0$ photoproduction with relative factors from Clebsch-Gordon coefficients between the two exchange amplitudes. The isospins of the different particles involved are listed in Table 3.1. Note that the photon is a mixture of $I = 0$ and $I = 1$ because it comes from mixing the $I = 0$, $I_3 = 0$ and $I = 1$, $I_3 = 0$ gauge bosons after spontaneous breaking of electroweak symmetry.

Thus, isospin-wise, we can write,

$$\begin{aligned} (\alpha|0,0\rangle + \beta|1,0\rangle)_\gamma |1/2,+1/2\rangle_p &= \alpha|0,0\rangle_\gamma |1/2,+1/2\rangle_p + \beta|1,0\rangle_\gamma |1/2,+1/2\rangle_p \\ &\rightarrow \alpha|1/2,+1/2\rangle_{N^*} + \beta(\sqrt{2/3}|3/2,+1/2\rangle_{\Delta^*} - \sqrt{1/3}|1/2,+1/2\rangle_{N^*}) \\ &= (\alpha - \beta\sqrt{1/3})|1/2,+1/2\rangle_{N^*} + \beta\sqrt{2/3}|3/2,+1/2\rangle_{\Delta^*} \\ &\rightarrow (\alpha - \beta\sqrt{1/3})(\sqrt{2/3}|1,+1\rangle|1/2,-1/2\rangle - \sqrt{1/3}|1,0\rangle_{\Sigma^0}|1/2,+1/2\rangle_{K^+}) \\ &\quad + \beta(\sqrt{1/3}|1,+1\rangle|1/2,-1/2\rangle + \sqrt{2/3}|1,0\rangle_{\Sigma^0}|1/2,+1/2\rangle_{K^+}) \\ &= \left(\alpha\sqrt{2/3} + \beta(\sqrt{1/3} - \sqrt{2/3}) \right) |1,+1\rangle|1/2,-1/2\rangle \\ &\quad + \left((\beta\sqrt{2/3} + 1/3) - \alpha\sqrt{1/3} \right) |1,0\rangle_{\Sigma^0}|1/2,+1/2\rangle_{K^+}. \end{aligned} \quad (3.89)$$

Thus, $K^+ \Sigma^0$ gets contributions from both the $I = 0$ and $I = 1$ parts of the photon. Also, in the $\gamma p \rightarrow J^P$ amplitude, as expected, there is a relative coefficient between $J^P = N^*$ and $J^P = \Delta^*$, but for our purposes since we will not be fitting to individual particles as such, this gets absorbed into the overall factor in the fit.

Particle	Isospin $ I, I_3\rangle$
K^+	$ 1/2, +1/2\rangle$
Σ^0	$ 1, 0\rangle$
p	$ 1/2, +1/2\rangle$
γ	$\alpha 0, 0\rangle + \beta 1, 0\rangle$

Table 3.1: Table of isospins for the particles involved in $\gamma p \rightarrow K^+ \Sigma^0$

3.9.2 $J^P \rightarrow K^+ \Sigma^0$ Amplitudes

Consider then a general J^P state (either N^* or Δ , Δ^*) with 4-momentum P and spin projection M decaying to $K^+ \Sigma^0$. As explained above we will ignore all prefactors and write down a single amplitude for both the N^* 's and the Δ 's.

J^P States with $P = (-)^{J-\frac{1}{2}} = (-)^{\ell-1}$, $\ell = J + \frac{1}{2} \left(\frac{1}{2}^+, \frac{3}{2}^-, \frac{5}{2}^+ \dots \right)$

Consider the state $J^P = \frac{1}{2}^+$ which decays to $K^+ \Sigma^0 \left(0^{-\frac{1}{2}}^+ \right)$ through a P-wave decay only. The amplitude can thus be written as

$$\mathcal{A}_{\frac{1}{2}^+ \rightarrow K^+ \Sigma^0} \sim \bar{u}(p_{\Sigma^0}, m_{\Sigma^0}) L_\mu^{(1)}(p_{K^+ \Sigma^0}) \gamma^\mu \gamma^5 u(P, M), \quad (3.90)$$

where $p_{K^+ \Sigma^0} = \frac{1}{2}(p_{K^+} - p_{\Sigma^0})$ is the relative momentum used to define $L^{(1)}$ and the inclusion of γ^5 ensures parity conservation (K^+ is a pseudo-scalar). The general case for J^P with $P = (-)^{J-\frac{1}{2}}$, going to $0^{-\frac{1}{2}}^+$ occurs in an ℓ -wave with the angular momentum selection rule $\ell = J \pm \frac{1}{2}$. Only $\ell = J + \frac{1}{2}$ survives from parity considerations and we can write the following amplitude

$$\mathcal{A}_{J^P \rightarrow K^+ \Sigma^0}^{P=(-)^{J-\frac{1}{2}}} \sim \bar{u}(p_{\Sigma^0}, m_{\Sigma^0}) L_{\mu_1 \dots \mu_\ell}^{(\ell)}(p_{K^+ \Sigma^0}) \gamma^{\mu_1} \gamma^5 u^{\mu_2 \dots \mu_\ell}(P, M), \quad (3.91)$$

where $\ell = J + \frac{1}{2}$.

J^P States with $P = (-)^{J+\frac{1}{2}} = (-)^{\ell+1}$, $\ell = J - \frac{1}{2} \left(\frac{1}{2}^-, \frac{3}{2}^+, \frac{5}{2}^- \dots \right)$

Now consider $J^P = \frac{1}{2}^-$, which can decay to $K^+ \Sigma^0$ only through an S-wave decay, the amplitude being simply

$$\mathcal{A}_{\frac{1}{2}^- \rightarrow K^+ \Sigma^0} \sim \bar{u}(p_{\Sigma^0}, m_{\Sigma^0}) \gamma^5 u(P, M). \quad (3.92)$$

For the general case, the decay occurs in an ℓ -wave, again with $\ell = J \pm \frac{1}{2}$, but this time parity dictates that only the $\ell = J - \frac{1}{2}$ survive and the general amplitude can be written down as

$$\mathcal{A}_{J^P \rightarrow K^+ \Sigma^0}^{P=(-)^{J+\frac{1}{2}}} \sim \bar{u}(p_{\Sigma^0}, m_{\Sigma^0}) L_{\mu_1 \dots \mu_\ell}^{(\ell)}(p_{K^+ \Sigma^0}) \gamma^5 u^{\mu_1 \dots \mu_\ell}(P, M), \quad (3.93)$$

where $\ell = J - \frac{1}{2}$.

3.9.3 $\gamma p \rightarrow J^P$ Amplitudes

J^P States with $P = (-)^{J+\frac{1}{2}} \left(\frac{1}{2}^-, \frac{3}{2}^+, \frac{5}{2}^- \dots \right)$

The crux of the discussion to follow is summarized in Table 3.2. We study the case J^P with $P = (-)^{J+\frac{1}{2}}$ with a few examples, but the trend should be obvious. First we couple the γp system $(1^- \otimes \frac{1}{2}^+)$ together to give a $\frac{3}{2}^-$ state and a $\frac{1}{2}^-$ state. Next, $\frac{3}{2}^-$ and $\frac{1}{2}^-$ are individually coupled

$j_{\gamma p}^P \otimes L$ (allowed) $\rightarrow J^P$	$1_{\gamma}^- \otimes L$ (allowed) \rightarrow Multipole
$\frac{3}{2}^- \otimes L = 2 \rightarrow \frac{1}{2}^-$	$1_{\gamma}^- \otimes L = 2 \rightarrow 1^-, 2^{\cancel{+}}, 3^{\cancel{+}}$
$\frac{1}{2}^- \otimes L = 0 \rightarrow \frac{1}{2}^-$	$1_{\gamma}^- \otimes L = 0 \rightarrow 1^-$
$\frac{3}{2}^- \otimes L = 1, 3 \rightarrow \frac{3}{2}^+$	$1_{\gamma}^- \otimes L = 3 \rightarrow 2^+, 3^{\cancel{+}}, 4^{\cancel{+}}$
$\frac{1}{2}^- \otimes L = 1 \rightarrow \frac{3}{2}^+$	$1_{\gamma}^- \otimes L = 1 \rightarrow 1^+, 2^+$
$\frac{3}{2}^- \otimes L = 2, 4 \rightarrow \frac{5}{2}^-$	$1_{\gamma}^- \otimes L = 4 \rightarrow 3^-, 4^{\cancel{+}}, 5^{\cancel{-}}$
$\frac{1}{2}^- \otimes L = 2 \rightarrow \frac{5}{2}^-$	$1_{\gamma}^- \otimes L = 4 \rightarrow 1^-, 2^-, 3^-$

Table 3.2: Evolution of multipole basis for a particular J^P resonance. In the left column, the photon and proton are first coupled together to give a $\frac{3}{2}^-$ and a $\frac{1}{2}^-$. These are subsequently coupled to those L states which can yield the final J^P state. The multipoles in the right column are formed by coupling the photon directly with these allowed L states. The crossed out multipoles are those which cannot combine with a $\frac{1}{2}^+$ proton to yield the final J^P .

to the appropriate angular momentum L states which can yield the final J^P state. In the second column we have first coupled the photon 1^- to the allowed L states to give spin-parity states called *multipoles*. These are next coupled with the proton $\frac{1}{2}^+$ to give the final J^P state where we have crossed out the multipoles which do not work (that is, cannot combine with the proton to give the final J^P state).

Until now we have not utilized the fact that even though the photon is a spin-1 particle, its L_z components are only ± 1 , there being no $L_z = 0$ state for a real massless photon. As a result, the amplitudes for a D-wave coupled with $\frac{3}{2}^- \gamma p$ and an S-wave coupled with $\frac{1}{2}^- \gamma p$ to produce the final $J^P = \frac{1}{2}^-$ state have the same angular distributions. Similarly, an F-wave coupled with $\frac{3}{2}^- \gamma p$ and a P-wave coupled with $\frac{1}{2}^- \gamma p$ to produce $J^P = \frac{3}{2}^+$ have the same angular distributions. And so on. We prove this for the $J^P = \frac{1}{2}^-$ case as follows. The two amplitudes are

$$\mathcal{A}_{\gamma p \rightarrow \frac{1}{2}^-}^{L=0} = \bar{u}(P, M)\gamma^\mu\gamma^5 u(p_i, m_i)\epsilon_\mu(k, m_\gamma), \quad \text{and} \quad (3.94a)$$

$$\mathcal{A}_{\gamma p \rightarrow \frac{1}{2}^-}^{L=2} = \bar{u}(P, M)L_{\mu\nu}^{(2)}(p_{p\gamma})\gamma^\mu\gamma^5 u(i_p, m_i)\epsilon^\nu(k, m_\gamma). \quad (3.94b)$$

However, $\mathcal{A}_{\gamma p \rightarrow \frac{1}{2}^-}^{L=2}$ can be written as

$$\begin{aligned} \bar{u}L_{\mu\nu}^{(2)}(p_{p\gamma})\gamma^\mu\gamma^5 u\epsilon^\nu &= \bar{u}(p_\mu^{p\gamma\perp}p_\nu^{p\gamma\perp} - \frac{1}{3}p_{p\gamma\perp}^2g_{\mu\nu}^\perp)\gamma^\mu\gamma^5 u\epsilon^\nu \\ &\sim \bar{u}p_{p\gamma\perp}^2\epsilon_\mu\gamma^\mu\gamma^5 u \\ &= |L^{(1)}|^2 A_{\gamma p \rightarrow \frac{1}{2}^-}^{L=0}, \end{aligned} \quad (3.95)$$

where we have used $p_{p\gamma\perp}^\mu\epsilon_\mu = 0$ and $g_{\mu\nu}^\perp\epsilon_\mu = \epsilon_\mu$ for a real photon (these relations are most easily proved in the *CM* frame of the γp system). Thus aside from the $|L^{(1)}|^2 \sim O(s)$ factor (which is just a multiplicative constant for us since we bin finely in \sqrt{s}), the two amplitudes are the same. The convenience of working in the multipole basis is that this fact it neatly separates independent angular amplitudes. Following standard nomenclature, we will then call the j^P multipole with $p = (-)^j$ as the *electric*, and with $p = (-)^{j+1}$, as the *magnetic* multipole. Thus, $1^-, 2^+, \dots$ are called $E1, E2, \dots$ while $1^+, 2^-, \dots$ are $M1, M2, \dots$

J^P	Multipole	J^P	Multipole
$\frac{1}{2}^-$	$E1$	$\frac{1}{2}^+$	$M1$
$\frac{3}{2}^-$	$E1, M2$	$\frac{3}{2}^+$	$M1, E2$
$\frac{5}{2}^-$	$M2, E3$	$\frac{5}{2}^+$	$E2, M3$
$\frac{7}{2}^-$	$E3, M4$	$\frac{7}{2}^+$	$M3, E4$
$\frac{9}{2}^-$	$M4, E5$	$\frac{9}{2}^+$	$E4, M5$
$\frac{11}{2}^-$	$E5, M6$	$\frac{11}{2}^+$	$M5, E6$

Table 3.3: Multipoles associated with J^P 's used in this analysis.

Getting back to the original problem at hand, we find that for J^P with $P = (-)^{J+\frac{1}{2}}$, there is an electric and an magnetic contribution, both of which can be built from an $\ell = J - 1/2$ wave. The difference is that we need to project out the j part where $j = J - 1/2$ is the magnetic part and $j = J + 1/2$ is the electric part. Thus

$$\mathcal{A}_{\gamma p \rightarrow J^P}^{P=(-)^{J+\frac{1}{2}}} = \bar{u}^{\mu_1 \mu_2 \dots \mu_\ell}(P, M) \gamma^\nu \gamma^5 P_{\mu_1 \mu_2 \dots \mu_\ell \nu \alpha_1 \alpha_2 \dots \alpha_\ell \beta}^{(j)}(P) L^{(\ell)\alpha_1 \alpha_2 \dots \alpha_\ell}(p_{p\gamma}) \epsilon^\beta(p_\gamma, m_\gamma) u(p_p, m_p). \quad (3.96)$$

Note that since there is no 0 multipole, $\frac{1}{2}^-$ has an $E1$ contribution only.

$$J^P \text{ States with } P = (-)^{J-\frac{1}{2}} \left(\frac{1}{2}^+, \frac{3}{2}^-, \frac{5}{2}^+ \dots \right)$$

The only thing which changes now is that $\ell = J + 1/2$. The electric part is now given by $j = J - 1/2$ while the magnetic part is from $j = J + 1/2$. Also, $\frac{1}{2}^+$ has an $M1$ contribution only. The amplitude is

$$\mathcal{A}_{\gamma p \rightarrow J^P}^{P=(-)^{J-\frac{1}{2}}} = \bar{u}^{\mu_1 \dots \mu_{\ell-1}}(P, M) \gamma^{\mu_\ell} \gamma^{\mu_{\ell+1}} P_{\mu_1 \dots \mu_{\ell+1} \nu_1 \dots \nu_{\ell+1}}^{(j)}(P) L^{(\ell)\nu_1 \dots \nu_\ell}(p_{p\gamma}) \epsilon^{\nu_{\ell+1}}(k, m_\gamma) u(p_i, m_i). \quad (3.97)$$

For ease of reference we have tabulated the relevant multipoles for the J^P waves used in this analysis in Table 3.3

3.9.4 $\gamma p \rightarrow J^P \rightarrow K^+ \Sigma^0 \rightarrow K^+ \gamma \Lambda \rightarrow K^+ \gamma p \pi^-$ Amplitude

The amplitude for the entire reaction chain is now easily formed by multiplying the individual components together. The only other thing we need to keep in mind is that all three J^P , Σ^0 and Λ are intermediate particles and thus their spins have to be summed over. Thus,

$$\mathcal{A}_{\gamma p \rightarrow J^P \rightarrow K^+ \Sigma^0 \rightarrow K^+ \gamma \Lambda \rightarrow K^+ \gamma p \pi^-} = \sum_{m_{J^P}} \sum_{m_{\Sigma^0}} \sum_{m_\Lambda} \mathcal{A}_{\gamma p \rightarrow J^P} \times \mathcal{A}_{J^P \rightarrow K^+ \Sigma^0} \times \mathcal{A}_{\Sigma^0 \rightarrow \gamma \Lambda} \times \mathcal{A}_{\Lambda \rightarrow p \pi^-}. \quad (3.98)$$

Note that, in the actual physics, there will be \sqrt{s} dependent Breit-Wigner and other factors in this amplitude, but for our purposes, since we will run fits on bunches of events finely binned in \sqrt{s} , this is just an additional factor floating around, to be absorbed in the overall scale during the fits.

3.10 Gauge Invariance and Form Factors

All the amplitudes constructed above have to satisfy one general condition – the Ward-Takahashi identity for gauge invariance in QED [20]. The total amplitude can be written as $\mathcal{A} = \epsilon_\mu \mathcal{A}^\mu$ where

ϵ_μ is the polarization of the incident external photon and \mathcal{A}^μ represents the hadronic current which the photon couples to. The Ward identity states that this current is conserved. That is, $\partial_\mu \mathcal{A}^\mu = 0$, or $k_\mu \mathcal{A}^\mu = 0$ for the photon momentum k_μ . Note that individual diagrams may not obey the Ward identity, but when summed up over all possible diagrams, the total amplitude has to be gauge invariant in this manner.

As an example, consider $\gamma p \rightarrow K^+ \Sigma^0$ occurring via the simplest s , t and u channels with the exchange of a proton, a K^+ and a Σ^0 respectively. The amplitude is given by

$$\begin{aligned}\epsilon_\mu \mathcal{A}^\mu &= g e \bar{u}_\Sigma \gamma^5 \frac{(p_p + k) \cdot \gamma + m_p}{s - m_p^2} \left[\epsilon \cdot \gamma - \frac{\kappa_p}{2m_p} \epsilon \cdot \gamma k \cdot \gamma \right] u_p \\ &\quad + 2g e \bar{u}_\Sigma \frac{p_K \cdot \epsilon}{t - m_K^2} \gamma^5 u_p \\ &\quad - g e \bar{u}_\Sigma \frac{\kappa_{\Sigma^0}}{2m_p} \epsilon \cdot \gamma k \cdot \gamma \frac{(p_\Sigma - k) \cdot \gamma + m_{\Sigma^0}}{u - m_{\Sigma^0}^2} \gamma^5 u_p,\end{aligned}\tag{3.99}$$

where k is the incoming photon momentum and p_Σ is the outgoing Σ^0 momentum. Now if we replace ϵ_μ with k_μ everywhere, we first see that the magnetic terms ($\sim \not{k} \not{k}$) go to zero (because $\not{k} \not{k} = k^2 = 0$ for a real photon). Thus the magnetic terms individually satisfy the Ward identity and it is only the electric terms that we need to be concerned about. The remnant electric terms are

$$\epsilon_\mu \mathcal{A}'^\mu = g e \bar{u}_\Sigma \left[\frac{2p_p \cdot \epsilon}{s - m_p^2} + \frac{2p_K \cdot \epsilon}{t - m_K^2} \right] \gamma^5 u_p,\tag{3.100}$$

where we have used the identity $\not{a} \not{b} = -\not{b} \not{a} + 2a \cdot b$ (from the γ^μ anti-commutation relations), the fact that γ^5 anticommutes with all the γ^μ 's and finally, $\not{p}_p u_p = m_p u_p$ from the Dirac equation. $k_\mu \mathcal{A}'^\mu$ is then easily seen to be zero after substituting $(k + p_p)^2$ for s and $(k - p_K)^2$ for t . Thus if we include the K^+ exchange t -channel process, we also have to include the proton exchange s -channel process to ensure that the Ward identity is satisfied.

The $K^*(892)$ exchange t -channel amplitude is gauge invariant by itself because of the $\epsilon^{\nu\alpha\beta\lambda} k_\beta \epsilon_\lambda$ term. The $K1(1270)$ exchange t -channel and the Y exchange u -channel terms too are manifestly gauge invariant, being built out of $F_{\mu\nu}$.

The PWA resonant amplitudes contain electric terms and are thus *not* gauge invariant in general. However, our setup ensures that we do run into gauge invariance violations using these. To understand why, note that if any amplitude is not gauge invariant as such, by multiplying it with $g^{\perp\perp}$ from Equation 3.33, we can project out the gauge invariant part. Indeed one should actually be doing this, but also note from Equation 3.32 that the way we have constructed our polarization vectors, $\epsilon^\nu(m_\gamma) g_{\nu\mu}^{\perp\perp} = \epsilon^\mu(m_\gamma)$. In other words, computationally, multiplying by $g^{\perp\perp}$ does not change anything, because of the particular choice of our polarization basis.

3.10.1 Form Factors and Contact Terms

Until now, we have assumed that the vertices have point particle interactions. In reality, the hadrons and mesons are extended particles and it is customary to put in phenomenological form factors to account for their finite sizes. These form factors involve a cutoff mass Λ which sets the short-range scale of our (effective) theory. However, it is well known that the addition of phenomenological form factors break gauge invariance even at the tree level. For example, if the s and t channels have different form factors F_s and F_t , Equation 3.100 becomes

$$\epsilon_\mu \mathcal{A}'^\mu_{FF} = g e \bar{u}_\Sigma \left[\frac{2p_p \cdot \epsilon}{s - m_p^2} F_s + \frac{2p_K \cdot \epsilon}{t - m_K^2} F_t \right] \gamma^5 u_p,\tag{3.101}$$

and thus the cancellation does not occur and gauge-invariance is violated.

There are various prescriptions in the literature for the addition of form factors and ways to tackle the ensuing violation of gauge invariance [27, 28, 26, 29]. It must be kept in mind here that *all* these prescriptions are phenomenological after all, so their correctness goes as far as the fits match the data. It is generally agreed upon however that some sort of form factor *is* required, because otherwise the bare tree level Born diagrams give too large a cross-section. A widely used form factor in the literature [30] is of the dipole form

$$F_x(\Lambda) = \frac{\Lambda^4}{\Lambda^4 + (x - M_x^2)^2} \quad (x \equiv s, t, u). \quad (3.102)$$

Since the problem lies in the s and t -channels getting different form factors in Equation 3.101, Haberzettl *et al* [27] applied a common form factor \hat{F} instead. That is, an $\epsilon_\mu \mathcal{A}'^\mu \hat{F}$ term is added to and subtracted from the total amplitude. After this, the electric terms which remain is what is called $-\epsilon_\mu \mathcal{A}'^\mu_{contact}$. To cancel this, one thus *adds* the term

$$\epsilon_\mu \mathcal{A}'^\mu_{contact} = ge\bar{u}_\Sigma \left[\frac{2p_p \cdot \epsilon}{s - m_p^2} (\hat{F} - F_s) + \frac{2p_K \cdot \epsilon}{t - m_K^2} (\hat{F} - F_t) \right] \gamma^5 u_p. \quad (3.103)$$

The contact terms represent 4-point interactions and thus cannot contain any pole. The original suggestion by Haberzettl [27] was

$$\hat{F}_H = a_s F_s(\Lambda) + a_t F_t(\Lambda) + a_u F_u(\Lambda), \quad a_s + a_t + a_u = 1, \quad (3.104)$$

which was shown to not be free of poles by Davidson and Workman [28] who subsequently suggested a different form,

$$\hat{F}_{DW} = F_s(\Lambda) + F_t(\Lambda) - F_s(\Lambda)F_t(\Lambda). \quad (3.105)$$

We will follow the DW model in this work.

To sum it up, the upshot of the above discussion is that the electric terms in the s and t -channels for the proton and the K^+ exchanges must get a common form factor \hat{F}_{DW} , while the magnetic terms can independently get (dipole) form factors based on whichever channel s , u or t they might be a part of.

3.11 Summary

We described the construction of our amplitudes in a fully covariant manner, following the Rarita-Schwinger formalism. Production amplitudes for both resonance and background processes were described. The problem of gauge invariance violation and a prescription for fixing it was also addressed.

Chapter 4

PWA Fit Formulae and $K^+\Sigma^0$ Differential Cross Sections

Having described in detail the construction of amplitudes in the previous chapter, we move on to describing the setup for using these amplitudes to run fits on the three-track dataset. We follow closely the works of Williams [3] and Chung [31]. Three points are to be noted at the outset. First, that we employ the powerful (but computationally intensive) technique of *unbinned event-based maximum likelihood fitting* for our purposes. A dedicated computer cluster for the Medium Energy group at Carnegie Mellon reduces concern for computation related limitations but the result is a highly stable fitting procedure where every event effectively becomes a separate degree of freedom. Compare this with binned χ^2 fits where information is lost due to binning.

Second, our resonance amplitudes are model independent, in the sense that for a given spin-parity J^P , we do not make *ab initio* assumptions about the masses and widths of the exchange resonances. We run individual fits on events which are finely binned in energy, so that \sqrt{s} is approximately a constant for every fit. Therefore, \sqrt{s} dependent propagators and Breit-Wigners (which depend on which particular resonances are being included in one's model) feature only as an overall pre-factor in our fits. It is to be noted that traditionally, one fits to the full expressions for the s -channel resonant amplitudes, including resonance-dependent propagators and Breit-Wigners. In our case, if a resonance of a particular spin-parity J^P and mass M contributes to our channel, its signature should lie in appreciable contributions from the same J^P amplitude *around* $\sqrt{s} \approx M$ (there are issues with overlapping resonances here which we will talk about later).

Finally, in this chapter we employ these fits to extract differential cross sections using s -channel J^P waves from $\frac{1}{2}^\pm$ up to $\frac{11}{2}^\pm$, for the three-track dataset. It is important to realize that in this particular fit (which we call the *mother fit*), we are not trying to interpret the fit results as *physics*. It is completely equivalent to using a (nearly) complete basis of sines and cosines to fit to a distribution, save that instead of harmonic functions, we use a (semi-)complete basis of J^P waves. As long as there are enough “wiggles” in these waves and as long as we use enough number of waves, we should be able to fit to any distribution.

The advantage of using the PWA procedure for cross-section extractions is that the accepted Monte Carlo events, weighted by our mother fit results, incorporates any *physics* dependency into our acceptance calculation. For the two-track dataset however, since the π^- and outgoing γ momenta are unknown, the amplitudes cannot be constructed any more. We thus have to fall back to the more conventional method of unweighted acceptance calculation to extract differential cross sections. Fortunately, the break-up angles for both the Σ^0 and Λ decays are small, so that the latter is a very

good approximation to the more correct physics incorporated acceptance (see Section 8.3).

4.1 The Maximum Likelihood Method

Suppose we have a set of n events, a set of variables \vec{x} whose values we want to estimate with the i^{th} event having the kinematics X_i . The probability of occurrence of the i^{th} event is given by the probability distribution function $\mathcal{P}(\vec{x}, X_i)$. The likelihood function is then defined as

$$\mathcal{L}(\vec{x}) = \prod_i^n \mathcal{P}(\vec{x}, X_i). \quad (4.1)$$

$\mathcal{L}(\vec{x}_0)$ is the *statistical inference* that, given the set of n observed events with the given kinematics, how likely it is that \vec{x}_0 were the *actual* values of the estimators. In reality one measures the intensities $\mathcal{I}(\vec{x}, X_i)$ and not the actual probabilities. The probabilities are obtained from dividing out the intensities by the normalization integral $\mathcal{N}(\vec{x})$:

$$\mathcal{N}(\vec{x}) = \sum_i^n \mathcal{I}(\vec{x}, X_i) \quad (4.2)$$

$$\mathcal{P}(\vec{x}, X_i) = \frac{\mathcal{I}(\vec{x}, X_i)}{\mathcal{N}(\vec{x})}. \quad (4.3)$$

The maximum likelihood method then says: *the best estimators are given by those which maximize the likelihood function.*

4.1.1 The Extended Maximum Likelihood Method (EMLM)

An important aspect of the above scheme is that it fits only to the *shape* of a particular distribution. The normalization integral always cancels out the overall normalization of the distribution. However, there are instances when one wants to fit not only to the shape but also to the overall number of events. For example, if one knows that events occur at a given rate \bar{n} , the probability of observing n events within a unit time interval is given by the Poisson distribution:

$$\mathcal{P}_n = \frac{\bar{n}^n}{n!} e^{-\bar{n}}, \quad (4.4)$$

so that the probability of observing n events with a particular shape per unit time is:

$$\mathcal{P}_{ext}(n, \vec{x}, X_i) = \left(\frac{\bar{n}^n}{n!} e^{-\bar{n}} \right) \mathcal{P}(\vec{x}, X_i), \quad (4.5)$$

where the subscript denotes that this is the *extended* maximum likelihood method. This is the probability distribution appropriate for differential cross section fits, where events are known to be occurring at a particular rate.

Note that the event rate is *not* known either. We will later write expressions for \bar{n} in terms of the amplitudes themselves.

4.1.2 Amplitudes, Probabilities and Cross Sections

In the previous chapter we wrote down the formulae for the PWA amplitudes $\mathcal{A}_{m_i, m_{gi}, m_{gf}, m_f}^a(X)$ for $\gamma p \rightarrow K^+ p \pi^- \gamma$ where m_i , m_{gi} , m_{gf} and m_f are the spin projections of the target proton, the incident photon, the outgoing final photon and the outgoing final proton respectively. The

superscript a denotes the particular type of amplitude concerned – it may be a background process or a J^P wave. The Lorentz invariant transition probability is given as:

$$|\mathcal{M}(\vec{x}, X)|^2 = \sum_{m_i, m_{gi}, m_{gf}, m_f} |\sum_a \alpha_a(\vec{x}, X) \mathcal{A}_{m_i, m_{gi}, m_{gf}, m_f}^a(X)|^2, \quad (4.6)$$

with α_a being (complex) coefficients built from the fit parameters (and possibly the kinematic variables X).

\mathcal{P} now become a probability density function and can be written as

$$\mathcal{P}(\vec{x}, X) = \frac{|\mathcal{M}(\vec{x}, X)|^2 \eta(X) \phi(X)}{\mathcal{N}(\vec{x})}, \quad (4.7)$$

where $\phi(X) = d\Phi(X)/dX$ is the differential phase space element and $\eta(X)$ is the detector acceptance.

The cross-section is now defined as the transition rate per unit incident flux per target particle, or in terms of measurable quantities,

$$\sigma = \frac{N}{\mathcal{F} \rho_{target} \ell_{target} N_A / A_{target}}, \quad (4.8)$$

where N is the number of scattering events, \mathcal{F} is the incident photon flux, ρ_{target} , ℓ_{target} and A_{target} are the target density, length and atomic weight and, N_A is Avogadro's number. Likewise, it can also be written in terms of the transition element as

$$\sigma = \frac{1}{4} \frac{(2\pi)^4}{2(s - w_p^2)} \int |\mathcal{M}(\vec{x}, X)|^2 d\Phi(X). \quad (4.9)$$

where the factor of 1/4 comes from averaging over the target proton and incident photon spins. Combining the two, one gets

$$N = (\mathcal{F} \rho_{target} \ell_{target} N_A / A_{target}) \frac{(2\pi)^4}{8(s - w_p^2)} \int |\mathcal{M}(\vec{x}, X)|^2 d\Phi(X), \quad (4.10)$$

and incorporating the detector acceptance $\eta(X)$ gives the following *expected* rate of events

$$\bar{n} = (\mathcal{F} \rho_{target} \ell_{target} N_A / A_{target}) \frac{(2\pi)^4}{8(s - w_p^2)} \int |\mathcal{M}(\vec{x}, X)|^2 \eta(X) d\Phi(X). \quad (4.11)$$

Since there is no analytical expression for $\eta(X)$, one has to resort to numerical computation using Monte Carlo techniques to calculate the last integral. We have already covered this in Chapter 2 where we described in detail how phase space “raw” $\gamma p \rightarrow K^+ \Sigma^0 \rightarrow K^+ \gamma \Lambda$ events are generated and passed through GSIM which simulates the CLAS detector and decays the various unstable particles as they “swim” through various detector components. In the end, $\eta(X_i)$ for the i^{th} event is either 1 or 0 according to whether the event was successfully “detected” or not. In this way, provided we have generated enough “raw” events everywhere in phase space, the numerical integral can be written as

$$\int |\mathcal{M}(\vec{x}, X)|^2 \eta(X) d\Phi(X) \approx \Phi(s) (|\mathcal{M}(\vec{x}, X)|^2 \eta(X))_{avg} \quad (4.12)$$

where $\Phi(s) = \int d\Phi(X)$ is the total phase space volume, while the average transition element is given by

$$\begin{aligned} (\langle |\mathcal{M}(\vec{x}, X)|^2 \eta(X) \rangle_{avg}) &\equiv \frac{\sum_i^{N_{raw}} |\mathcal{M}(\vec{x}, X_i)|^2 \eta(X_i)}{N_{raw}} \\ &= \frac{\sum_i^{N_{acc}} |\mathcal{M}(\vec{x}, X_i)|^2}{N_{raw}} \end{aligned} \quad (4.13)$$

with N_{raw} as the total number of “raw” Monte Carlo events generated and N_{acc} as the total number of “accepted” events after passage through GSIM.

The phase space volume can be broken down into three parts, the $\gamma p \rightarrow K^+\Sigma^0$ part, and the two subsequent decays. The latter was already assimilated by the amplitudes as explained in Section 3.5.3, while the former is the usual 2-body decay phase space factor, which, in our case is given by

$$\Phi(s)_{\gamma p \rightarrow K^+\Sigma^0} = \frac{[(s - (w_{K^+} + w_{\Sigma^0})^2)(s - (w_{K^+} - w_{\Sigma^0})^2)]^{1/2}}{4(2\pi)^5 s}, \quad (4.14)$$

which is also the total phase space factor $\Phi(s)$.

Combining Equations 4.11-4.14 we can then write

$$\bar{n} = \beta(s) \sum_i^{N_{acc}} |\mathcal{M}(\vec{x}, X_i)|^2, \quad (4.15)$$

where

$$\beta(s) = \frac{(2\pi)^4}{8(s - w_p^2)} \frac{\Phi(s)}{N_{raw}} \left(\frac{\mathcal{F} \rho_{target} \ell_{target} N_A}{A_{target}} \right). \quad (4.16)$$

Removing the detector acceptance now by summing over all of N_{raw} yields the total cross section

$$\sigma = \beta(s) \sum_i^{N_{raw}} |\mathcal{M}(\vec{x}, X_i)|^2. \quad (4.17)$$

4.1.3 Log Likelihood Formula

Instead of maximizing the likelihood function directly, most of the times, it is computationally simpler to maximize the the logarithm of the likelihood function. A heuristic argument is that near the maximum, the first derivative vanishes, so the the likelihood function looks like a Gaussian

$$\begin{aligned} \mathcal{L} &\sim \mathcal{L}_{max} + \frac{1}{2!} \mathcal{L}'' \delta x^2 + \dots \\ &\sim \mathcal{L}_{max} - \frac{1}{2c} \delta x^2 + \dots \sim \exp(-\frac{\delta x^2}{2c}), \end{aligned} \quad (4.18)$$

where $c = -1/\mathcal{L}''$ which has to be positive at a maximum. Since the logarithm is a monotonically increasing function in the range of the likelihood function, maximizing $\ln \mathcal{L}$ always ensures maximizing \mathcal{L} too. Also, instead of maximizing $\ln \mathcal{L}$, it is conventional to minimize the negative of the log

likelihood. From Equation 4.5 this is given by

$$\begin{aligned} -\ln \mathcal{L} &= -n \ln \bar{n} + \ln n! + \bar{n} - \sum_i^n \ln \mathcal{P}(\vec{x}, X_i) \\ &= -n \ln \bar{n} + \ln n! + \bar{n} - \sum_i^n \ln (|\mathcal{M}(\vec{x}, X_i)|^2 \eta(X_i) \phi(X_i)) + n \mathcal{N}(\vec{x}). \end{aligned} \quad (4.19)$$

Now, from Equations 4.7 and 4.11,

$$\mathcal{N}(\vec{x}) = \mathcal{C}(s) \bar{n}, \quad (4.20)$$

where

$$\mathcal{C}(s) = \frac{8(s - w_p^2)}{(2\pi)^4} \frac{A_{target}}{\mathcal{F} \rho_{target} \ell_{target} N_A}. \quad (4.21)$$

Thus we can rewrite Equation 4.19 as

$$\begin{aligned} -\ln \mathcal{L} &= -\sum_i^n \ln |\mathcal{M}(\vec{x}, X_i)|^2 + \bar{n} + C \\ &= -\sum_i^n \ln |\mathcal{M}(\vec{x}, X_i)|^2 + \beta(s) \sum_i^{N_{acc}} |\mathcal{M}(\vec{x}, X_i)|^2 + C, \end{aligned} \quad (4.22)$$

where we have accumulated all terms that are independent of the fit parameters in the term C .

Note that the pre-factor $\beta(s)$ is really superfluous here and can be absorbed into the amplitudes. If we scale the amplitudes by $1/\beta(s)$, $-\ln \mathcal{L}$ will still be minimized by the re-scaled amplitudes with the same fit parameters. If we want to estimate the yield \bar{n} , as long as we consistently use the same re-scaled amplitudes all over, we would get the same yield as earlier.

4.1.4 Including Background

In Section 1.11 we explained how we account for background for our analysis – every event gets a quality factor or Q between 0 and 1. Consider the hypothetically extreme case of Q being 0. This means that the event has rejected altogether and will not contribute to $-\ln \mathcal{L}$ at all. Likewise, if Q is 1 then the event fully contributes $-\ln |\mathcal{M}(\vec{x}, X_i)|^2$ for the i^{th} event. It is clear now that for the general case, we will have:

$$-\ln \mathcal{L} = -\sum_i^n Q_i \ln |\mathcal{M}(\vec{x}, X_i)|^2 + \beta(s) \sum_i^{N_{acc}} |\mathcal{M}(\vec{x}, X_i)|^2 + C. \quad (4.23)$$

4.2 Least Squares Fitting

We had earlier emphasized on the fact that the likelihood method is an *unbinned* method, every event being fitted to, all at once. While this lends stability to the fits, in some occasions, it becomes very computationally intensive. This is the case if our fit variable is a cutoff scale Λ in a form factor and value of the form factor has to be calculated event by event at every iteration from a complicated monopole or dipole expression (as opposed to, say, a simple multiplicative pre-factor like dependence). In such circumstances it is prudent to use the alternative method of least square fitting which fits to ~ 20 data points instead of $\sim 10,000$ events.

This is a *binned* method. As in the likelihood case, we are still trying to determine the estimators \vec{x} from a set of n data samples. However, the sample space is not the set of events themselves but

a set of *measured* observables $\mathcal{O}_i(X_i)$ from those events, with kinematics X_i at particular values of a subset of X'_i according to some binning in X'_i . For our purposes, these observables will be the measured differential cross sections or recoil polarizations or both. The fit function that we will try to minimize is

$$\chi^2 = \sum_i^n \frac{\mathcal{O}_i(X_i) - \hat{\mathcal{O}}_i(\vec{x}, X_i)}{\sigma_i^2}, \quad (4.24)$$

where $\mathcal{O}_i(X_i)$ are the *measured* values, $\hat{\mathcal{O}}_i(\vec{x}, X_i)$ are the *estimated* values from the functional form $\hat{\mathcal{O}}$ (to be built out of our amplitudes) and σ_i are the errors in the measurement. This definition of χ^2 is consistent with the fact that if the measurement errors are small, the estimated values will have to be even closer to the measured values for the same χ^2 .

4.2.1 Calculation of $d\sigma/dt$

For the differential cross sections $d\sigma/dt$, the functional form $\hat{\mathcal{O}}$ is obtained from

$$d\sigma(\vec{x}, X) = \frac{1}{4} \frac{(2\pi)^4}{2(s - w_p^2)} |\mathcal{M}(\vec{x}, X)|^2 d\Phi(X). \quad (4.25)$$

The phase space element is given by

$$\begin{aligned} d\Phi(X) &= \frac{1}{4(2\pi)^6} \frac{|\vec{p}_{\Sigma^0}| d\Omega}{\sqrt{s}} \\ &= \frac{1}{4(2\pi)^6} \frac{|\vec{p}_{\Sigma^0}| 2\pi d \cos \theta_{CM}^{K^+}}{\sqrt{s}}. \end{aligned} \quad (4.26)$$

To convert $d \cos \theta_{CM}^{K^+}$ to dt we need the following relations:

$$\begin{aligned} t &= w_p^2 + w_{\Sigma^0}^2 + 2E_i E_{\Sigma^0} + 2|\vec{p}_i| |\vec{p}_{\Sigma^0}| \cos \theta_{CM}^{K^+} \\ &= w_p^2 + w_{\Sigma^0}^2 + 2E_i E_{\Sigma^0} + \frac{s - w_p^2}{\sqrt{s}} |\vec{p}_{\Sigma^0}| \cos \theta_{CM}^{K^+}, \end{aligned} \quad (4.27)$$

where E_i and \vec{p}_i are the energy and momentum of the target proton. Thus,

$$d \cos \theta_{CM}^{K^+} = \frac{\sqrt{s}}{s - w_p^2} \frac{dt}{|\vec{p}_{\Sigma^0}|}. \quad (4.28)$$

Substitution of Equations 4.26 and 4.28 in Equation 4.25 yields

$$\begin{aligned} \frac{d\sigma(\vec{x}, X)}{dt} &= \frac{1}{4} \frac{(2\pi)^4}{2(s - w_p^2)} |\mathcal{M}(\vec{x}, X)|^2 \frac{1}{4(2\pi)^6} \frac{|\vec{p}_{\Sigma^0}|}{\sqrt{s}} \frac{\sqrt{s}}{s - w_p^2} \frac{2\pi}{|\vec{p}_{\Sigma^0}|} \\ &= \frac{1}{64\pi(s - w_p^2)^2} |\mathcal{M}(\vec{x}, X)|^2. \end{aligned} \quad (4.29)$$

4.3 Multiple Dataset Fits

To fit to several datasets at once, for example when a particular parameter is constrained to be the same over several datasets, is easily achieved here. The fit function, either χ^2 or $-\ln \mathcal{L}$, will simply be the sum of the fit functions of the two separate datasets.

4.4 MINUIT

To run all these fits, many degrees of freedom, significant hardware computing power and efficient minimization routines are needed. The software package we use for this purpose is MINUIT, an efficient and well-honed minimization routine widely used in the particle physics community [32].

The minimization algorithm we employ while running MINUIT is MIGRAD, which is based upon the Davidon-Fletcher-Powell (DFP) variable metric method. The DFP is an iterative process that assumes that the gradient $\vec{g}(\vec{x}) = \vec{\nabla}F(\vec{x})$ of the minimization function $F(\vec{x})$ with respect to the fit parameters \vec{x} can be calculated explicitly. In the majority of our fits, we supply MIGRAD with randomized initial values, \vec{x}_0 , of the fit parameters. MIGRAD then uses the gradient of $\vec{g}(\vec{x})$ to find another value of the fit parameters, \vec{x}_1 , for which $F(\vec{x}_1) < F(\vec{x}_0)$. The \vec{x}_0 are then replaced by the \vec{x}_1 , and a new set of fit parameters, \vec{x}_2 is found in the same manner. MIGRAD repeats this process until the difference in the minimization function between consecutive iterations, $\delta F \equiv F(\vec{x}_n) - F(\vec{x}_{n-1})$, is less than some user-defined tolerance.

Since MIGRAD requires the derivatives explicitly, to ease calculations, we also supply it the partial derivatives of the fit functions with respect to the fit parameters. For likelihood fits this is,

$$\frac{\partial(-\ln \mathcal{L})}{\partial x_j} = -\sum_i^n Q_i \left(\frac{1}{|\mathcal{M}(\vec{x}, X_i)|^2} \frac{\partial |\mathcal{M}(\vec{x}, X_i)|^2}{\partial x_j} \right) + \beta(s) \sum_i^{N_{\text{acc}}} \frac{\partial |\mathcal{M}(\vec{x}, X_i)|^2}{\partial x_j}, \quad (4.30)$$

while for least squares fits it is,

$$\frac{\partial \chi^2}{\partial x_j} = \left(\frac{1}{64\pi(s-w_p^2)^2} \frac{\partial |\mathcal{M}(\vec{x}, X_i)|^2}{\partial x_j} \right) \sum_i^n \frac{2}{\sigma_i^2} \left(\frac{d\sigma}{dt}(\vec{x}, X_i) - \frac{d\sigma}{dt} \right). \quad (4.31)$$

For both cases, we compute the partial derivatives of the $|\mathcal{M}(\vec{x}, X)|^2$ as

$$\frac{\partial |\mathcal{M}(\vec{x}, X_i)|^2}{\partial x_j} = \sum_{\text{all spins}} 2\Re \left(\sum_a \frac{\partial \alpha_a(\vec{x}, X_i)}{\partial x_j} \mathcal{A}_a \sum_{a'} \alpha_{a'}(\vec{x}, X_i) \mathcal{A}_{a'}^*(X_i) \right), \quad (4.32)$$

where the spin sum is over all the external particle spins.

4.5 The Mother Fit

As mentioned earlier, the first step towards extraction of differential cross sections constitutes running a likelihood fit to all events using a “sufficient” number of J^P waves. We call this fit the mother fit. What we mean by “sufficient” is a semi-complete basis of functions in $\cos \theta_{CM}^{K^+}$ which we will take as the PWA amplitudes $\gamma p \rightarrow J^P \rightarrow K^+\Sigma^0 \rightarrow K^+\gamma_{out} \Lambda \rightarrow K^+\gamma_{out} p\pi^-$ for J^P from $\frac{1}{2}^\pm$ till $\frac{11}{2}^\pm$. That is, we are not concerned with representing actual physics, but that the fit function has enough freedom to properly describe all the distributions in every independent kinematic variable, including correlations between them.

4.5.1 Setup

We parameterize the complex prefactor $\alpha_a(\vec{x}, X)$ in Equation (with “a” now consisting of J^P and electric/magnetic multipole specifications) in terms of three real fit parameters θ_{JP} , r_{JP} and ϕ_{JP} as

$$\alpha_a(\vec{x}, X) = f_{MP}(\theta_{JP}) r_{JP} \exp(i\phi_{JP}), \quad (4.33)$$

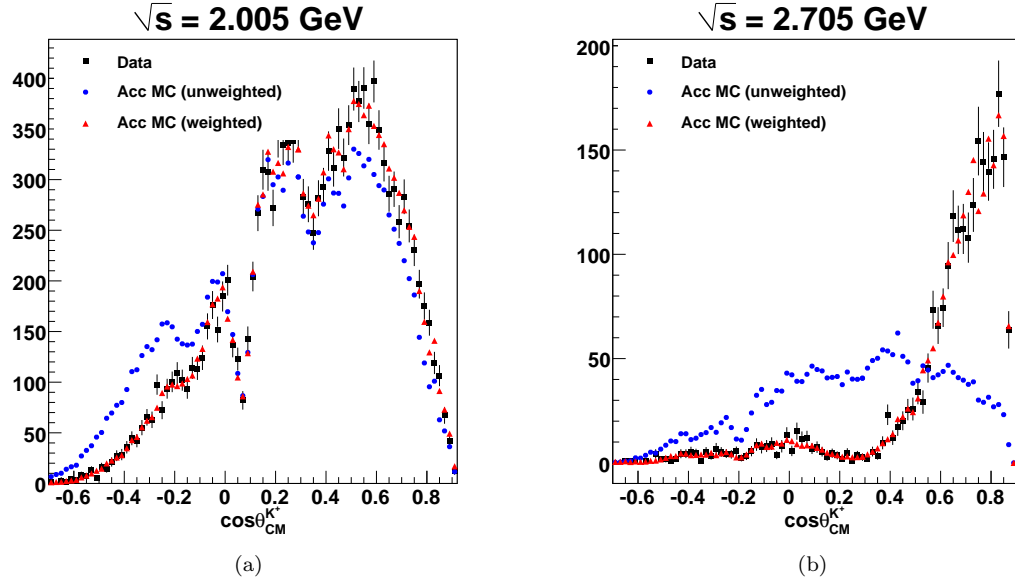


Figure 4.1: Mother fit results: weighing by the mother fit results brings the accepted Monte Carlo into excellent agreement with the data.

where

$$f_{MP}(\theta_{JP}) = \left\{ \begin{array}{ll} \cos \theta_{JP} & \text{for electric multipoles} \\ \sin \theta_{JP} & \text{for magnetic multipoles} \end{array} \right\} \text{ for } J^P \neq \frac{1}{2}^\pm. \quad (4.34)$$

Thus each J^P wave has an independent phase angle ϕ_{JP} and decay magnitude r_{JP} whilst between the two allowed monopole variants in each case we keep an extra factor which we parameterize by $\tan \theta_{JP}$. For $J^P \neq \frac{1}{2}^\pm$ there is only one allowed monopole, so that there is no f_{MP} for these two cases. In this way, $J^P \neq \frac{1}{2}^\pm$ has $2+2=4$ independent parameters while $\frac{3}{2}^\pm$ till $\frac{11}{2}^\pm$ has $3 \times 10 = 30$, resulting in 34 overall fit parameters and every fit was run for at least 4 iterations. For the results to follow, we used 10 iterations and present the result for the iteration with the least $-\ln \mathcal{L}$. All throughout, we bin events in 10 MeV wide \sqrt{s} bins and run individual fits for every \sqrt{s} bin.

4.5.2 Quality Checks on Fit Results

Figure 4.5.2 shows the results of our mother fit at two center-of-mass energies, in a particular kinematic variable ($\cos \theta_{CM}^{K^+}$). The black squares represent the data and the blue circles are the unweighted accepted Monte Carlo. The red triangles show the accepted Monte Carlo weighted by the fit results. The weighted accepted Monte Carlo matches very well with the data.

It is however not enough that the fit reproduce the data distribution in just one particular kinematic variable. Recall that the mother fit was designed to match the data in *every single independent kinematic variable*. To ensure that our fits satisfy this criterion, we must look how the results look in multiple kinematic variables simultaneously. Figure 4.5.2 shows $\phi_{\Sigma HF}^{\Lambda}$ plotted against $\cos \theta_{\Lambda HF}^p$ in eight different $\cos \theta_{CM}^{K^+}$ bins for $\sqrt{s} = 2.005$ GeV. The data and the weighted accepted Monte Carlo agree very well with each other.

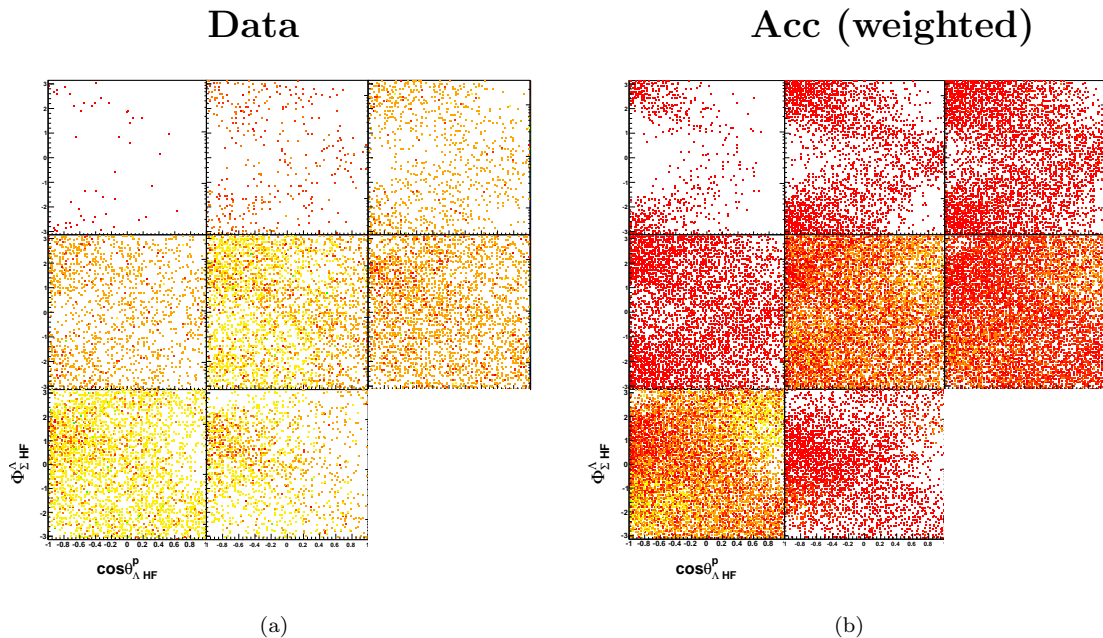


Figure 4.2: Quality check for the mother fit: (a) data and (b) accepted Monte Carlo (weighted by the fit) at $\sqrt{s} = 2.005$ GeV. The plots show $\phi_{\Sigma HF}^{\Lambda}$ plotted against $\cos\theta_{\Lambda HF}^P$ in eight $\cos\theta_{CM}^{K^+}$ bins. Each bin is of width 0.2 and the bin centers increase from -0.6 to 0.8, top-left to bottom-right, thus traversing from backward angles to forward angles. All correlations presented in the data are faithfully represented in the accepted Monte Carlo after being weighted by the fit results

Factor	Value	Description
ρ_{target}	0.7177 g/cm ³	Target density (see Section 2.9)
ℓ_{target}	40 cm	Target length [33]
N_A	6.022×10^{23}	Avogadro number
A_{target}	1.00794 g/mole	Target atomic weight

Table 4.1: Target factors used for $d\sigma/d\cos\theta_{CM}^{K^+}$ measurements.

4.6 Differential Cross Sections

We are in a position now to extract the differential cross section for $K^+\Sigma^0$ photoproduction. What is to follow is one of the central results from this thesis work. Though cross sections from previous experiments exist, our statistics and range in \sqrt{s} represent a significant improvement over them. We follow the customary norm in the literature and report $d\sigma/d\cos\theta_{CM}^{K^+}$ instead of $d\sigma/dt$ or $d\sigma/du$, for every \sqrt{s} bin, since this facilitates the study of the evolution of features in the cross sections with the *CM* energy (which is a monotonic function of \sqrt{s}).

4.6.1 Formula for Calculation

There are three parts to the formula for calculating differential cross sections. First comes the differential yield $\mathcal{Y}(\sqrt{s}, \cos\theta_{CM}^{K^+})$, next is the acceptance factor $\eta(\sqrt{s}, \cos\theta_{CM}^{K^+})$, and finally there is a *target factor*. In all, it reads,

$$\frac{d\sigma}{d\cos\theta_{CM}^{K^+}} = \left(\frac{A_{target}}{\mathcal{F}(\sqrt{s})\rho_{target}\ell_{target}N_A} \right) \frac{\mathcal{Y}(\sqrt{s}, \theta_{CM}^K)}{(\Delta \cos\theta_{CM}^{K^+})\eta(\sqrt{s}, \theta_{CM}^{K^+})}, \quad (4.35)$$

where A_{target} , ρ_{target} , and ℓ_{target} are the target atomic weight, density, and length respectively, N_A is the Avogadro number, $\mathcal{F}(\sqrt{s})$ is the corrected number of photons impinging on the target in each \sqrt{s} bin, and $\Delta \cos\theta_{CM}^{K^+} = 0.1$ is the width of our binning in $\cos\theta_{CM}^{K^+}$, kept same for all kinematic regions. The values used for the target factors are listed in Table 4.1.

The detected data yield in each $(\sqrt{s}, \theta_{CM}^{K^+})$ bin is obtained as

$$\mathcal{Y}(\sqrt{s}, \theta_{CM}^{K^+}) = \sum_i^N Q_i, \quad (4.36)$$

where N is the number of detected events in the bin and Q_i are the Q -values obtained in Section 1.11. In this analysis, we employ two expressions for calculating acceptance in any particular $(\sqrt{s}, \theta_{CM}^{K^+})$ bin:

$$\eta(\sqrt{s}, \theta_{CM}^{K^+})_{\text{weighted}} = \frac{\sum_i^{N_{acc}} |\mathcal{M}_i|^2}{\sum_j^{N_{raw}} |\mathcal{M}_j|^2} \quad (\text{three-track topology}) \quad (4.37a)$$

$$\eta(\sqrt{s}, \theta_{CM}^{K^+})_{\text{unweighted}} = \frac{N_{acc}}{N_{raw}} \quad (\text{two-track topology}), \quad (4.37b)$$

where N_{acc} (N_{raw}) is the number of accepted(raw) Monte Carlo events in the bin and the $|\mathcal{M}|^2$'s are the *physics weighted* transition elements obtained from the mother fit (for the three-track topology).

Source	Value	Description
Confidence Level	3%	Kinematic Fitter Uncertainty (three-track) [4]
Particle Identification	0.62%	Signal loss to PID cut (three-track) (Section 1.6.6)
Particle Identification	1.8%	Signal loss to PID cuts (two-track) (Section 1.7.3)
Acceptance	3-6%	Sector-wise acceptance study (Section 2.8)
$\Lambda \rightarrow p\pi^-$ Branching Fraction	0.5%	PDG listed uncertainty [8]
Target Density	0.11%	Std. dev. of target measurement per run [3]
Target Length	0.125%	Target survey precision [33]
Photon Normalization	7.7%	Based upon run-to-run normalized yields [4]
Photon Transmission Efficiency	0.5%	Propagation of photons to target along beamline [4]
Live-time	3%	DAQ live time [3]

Table 4.2: Table of Systematic Uncertainties

Note that the expression in Equation 4.37b ignores the *dynamics* of the reaction. This can be important in the present case since hyperons are known to be produced with a high degree of polarization. In Equation 4.37a, by weighing the Monte Carlo with results from the mother fit, we are properly accounting for the *physics*, in our acceptance calculation. However, for both Λ and Σ^0 decays, the breakup momenta/angles are small, so that in the laboratory/detector frame, the decays products keep travelling in almost the same direction as the decaying mother particle. Hence Equation 4.37b should be a very good approximation to the more correct expression appearing in Equation 4.37a. In Section 8.3 we will confirm this explicitly, when we compare the cross-sections for the three-track topology obtained by both expressions for acceptance and find them to agree very well.

4.6.2 Uncertainties

The statistical error in each $(\sqrt{s}, \theta_{CM}^{K^+})$ bin are given as

$$\sigma_y^2 = \mathcal{Y} + \left(\sum_i^{N_{data}} \sigma_{Q_i} \right)^2 \quad (4.38a)$$

$$\sigma_{acc}^2 = N_{acc} \quad (4.38b)$$

$$\sigma_{raw}^2 = N_{raw} \quad (4.38c)$$

where σ_{Q_i} is the error from our background fitting procedure in determining the quality factor Q_i for the i^{th} event (see Section 1.11.1). Note that by summing over the σ_{Q_i} 's, we are assuming that these errors are fully correlated with one another, which is an over-estimation. One could instead add the σ_{Q_i} 's in quadrature, but the difference is small. The total relative statistical error is:

$$\sigma_{rel}^2 = \frac{\sigma_y^2}{\mathcal{Y}^2} + \frac{1}{N_{acc}} - \frac{1}{N_{raw}}, \quad (4.39)$$

where the negative sign before the σ_{raw}^2 appears because N_{acc} is ultimately derived from N_{raw} . However, for all practical purposes, $\frac{1}{N_{raw}}$ is always negligibly small. The systematic uncertainties are summarized in Table 4.2. Due to the \sqrt{s} dependence in the acceptance uncertainty, we will present a point-to-point systematic error, but overall, this ranges from about 10 to 12%.

4.7 Two- and Three-track Results

We now present the $\gamma p \rightarrow K^+\Sigma^0$ differential cross-section results for the $g11a$ dataset. Figures 4.3 through 4.9 show the results from the two-track and the three-track analyses in red and blue respectively. There are 112 \sqrt{s} bins, each 10 MeV wide, from 1.695 to 2.835 GeV (bins $\sqrt{s} = 1.1955, 2.735$ and 2.745 GeV are skipped for reasons given in Section 2.10). Within each \sqrt{s} bin, the $\cos\theta_{CM}^{K^+}$ bins in the x -axis are 0.1 wide.

A number of features are immediately apparent from these results. First, where the kinematics overlap, the two- and three-track results are in very good agreement with each other. As the two analyses employed entirely different event selection and PID schemes, the internal consistency of $g11a$ results thus bolsters our confidence in this analysis.

Secondly, the two-track analysis provides cross-sections in the backward-angle regions where the three-track dataset has little, or almost zero statistics. There there is a prominent rise in the cross-sections in this region, signaling the possible presence of u -channel contributions. Thus, the two-track dataset adds vital information to our overall understanding of $K^+\Sigma^0$ photoproduction.

Figure 4.10 shows the the cumulative global difference between the two results. The quantity plotted here is:

$$\Delta(\sqrt{s}, \cos\theta_{CM}^{K^+}) = \frac{x_2 - x_3}{\sqrt{\sigma_2^2 + \sigma_3^2 + (\bar{x}\sigma_\eta(\sqrt{s}))^2}}, \quad (4.40)$$

where x_i and σ_i are the cross-section and its associated statistical error respectively, for the i -track topology, while \bar{x} is the weighted mean of the two and $\sigma_\eta(\sqrt{s})$ is the \sqrt{s} dependent systematic uncertainty provided by Equation 2.3. A Gaussian fit to the the distribution yields a mean $\mu_\Delta = 0.558$ and standard deviation $\sigma_\Delta = 1.017$. That the Δ distribution is roughly normal with unit width shows that estimated errors correctly reflect the uncertainties. The mean shows that the two-track cross-sections are on the average ~ 0.5 standard deviations higher than the three-track. A possible explanation for this might be the different acceptance calculation techniques (*c.f.* Equations 4.37a and 4.37b).

4.8 Final Differential Cross-Sections

The consistency between the results for the two topologies allow us to quote our final cross-sections as a weighted mean of the two in regions where results from both datasets exist. In any such “overlap bin”, let $\mu_{2,3}$ and $\sigma_{2,3}$ be the measured differential-cross section and its error from the 2- and 3-track datasets respectively. We then write the error matrix as

$$E = \begin{pmatrix} \sigma_2^2 & \rho\sigma_2\sigma_3 \\ \rho\sigma_3\sigma_2 & \sigma_3^2 \end{pmatrix}, \quad (4.41)$$

where the cross-terms denote the degree of correlation. Assuming $\rho = \rho_{23} = \rho_{32}$, we can invert this as

$$E^{-1} = \frac{1}{(1 - \rho^2)\sigma_2^2\sigma_3^2} \begin{pmatrix} \sigma_3^2 & -\rho\sigma_2\sigma_3 \\ -\rho\sigma_2\sigma_3 & \sigma_2^2 \end{pmatrix}, \quad (4.42)$$

and thereby, obtain the χ^2 function

$$\chi^2 = \sum (\bar{\mu} - \mu_i) (E^{-1})_{ij} (\bar{\mu} - \mu_j). \quad (4.43)$$

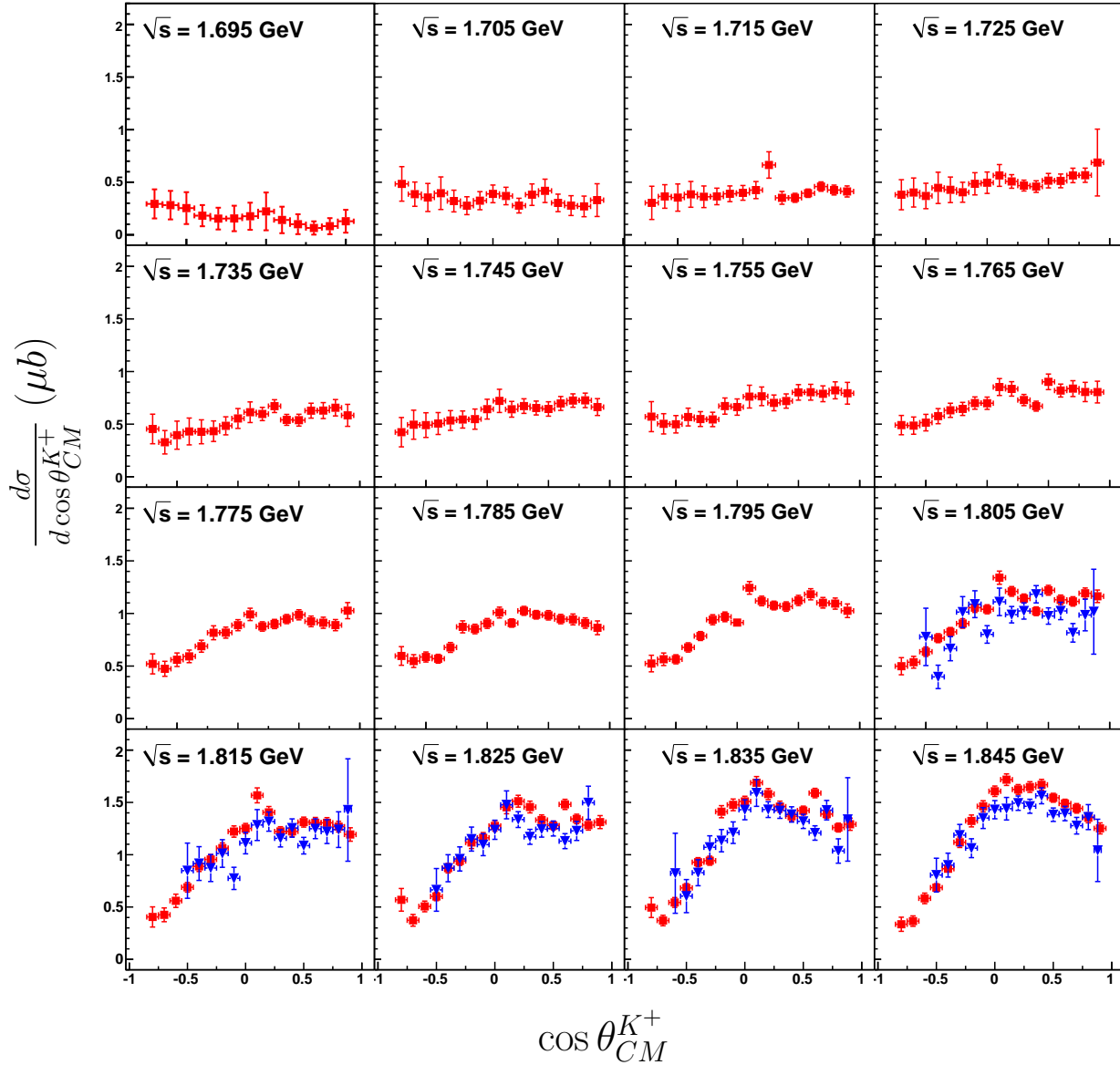


Figure 4.3: $\gamma p \rightarrow K^+\Sigma^0$ differential cross-sections for g11a: the **red** squares are the two-track results while the **blue** triangles are the three-track results. The vertical axis range is the same for all the plots in the canvas and is shown in the first column. All errors are statistical.

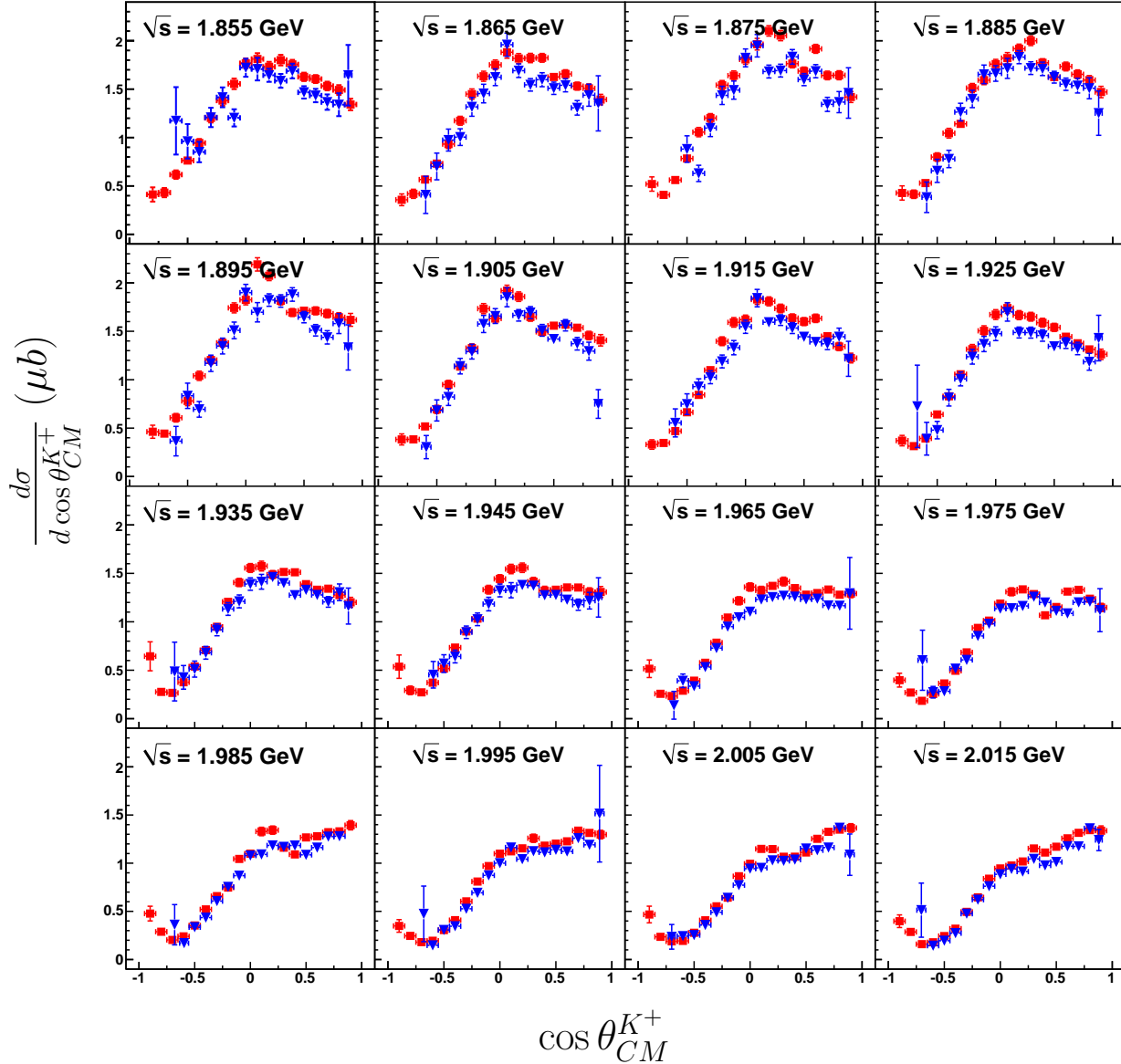


Figure 4.4: $\gamma p \rightarrow K^+\Sigma^0$ differential cross-sections for *g11a*: the **red** squares are the two-track results while the **blue** triangles are the three-track results. The vertical axis range is the same for all the plots in the canvas and is shown in the first column. All errors are statistical. No result is presented for the bin $\sqrt{s} = 1.955$ GeV due to reasons given in Section 2.10.

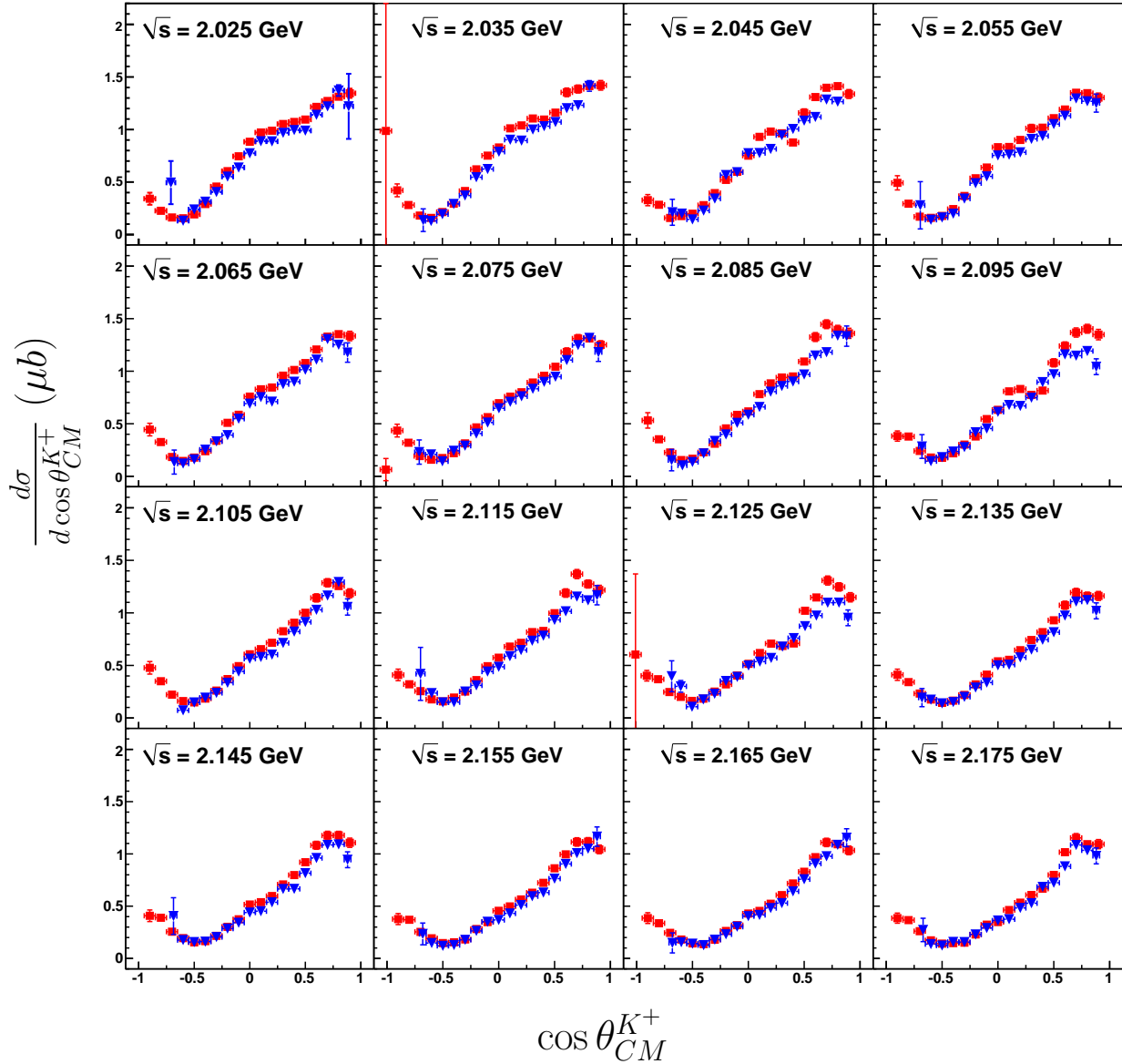


Figure 4.5: $\gamma p \rightarrow K^+\Sigma^0$ differential cross-sections for g11a: the **red** squares are the two-track results while the **blue** triangles are the three-track results. The vertical axis range is the same for all the plots in the canvas and is shown in the first column. All errors are statistical.

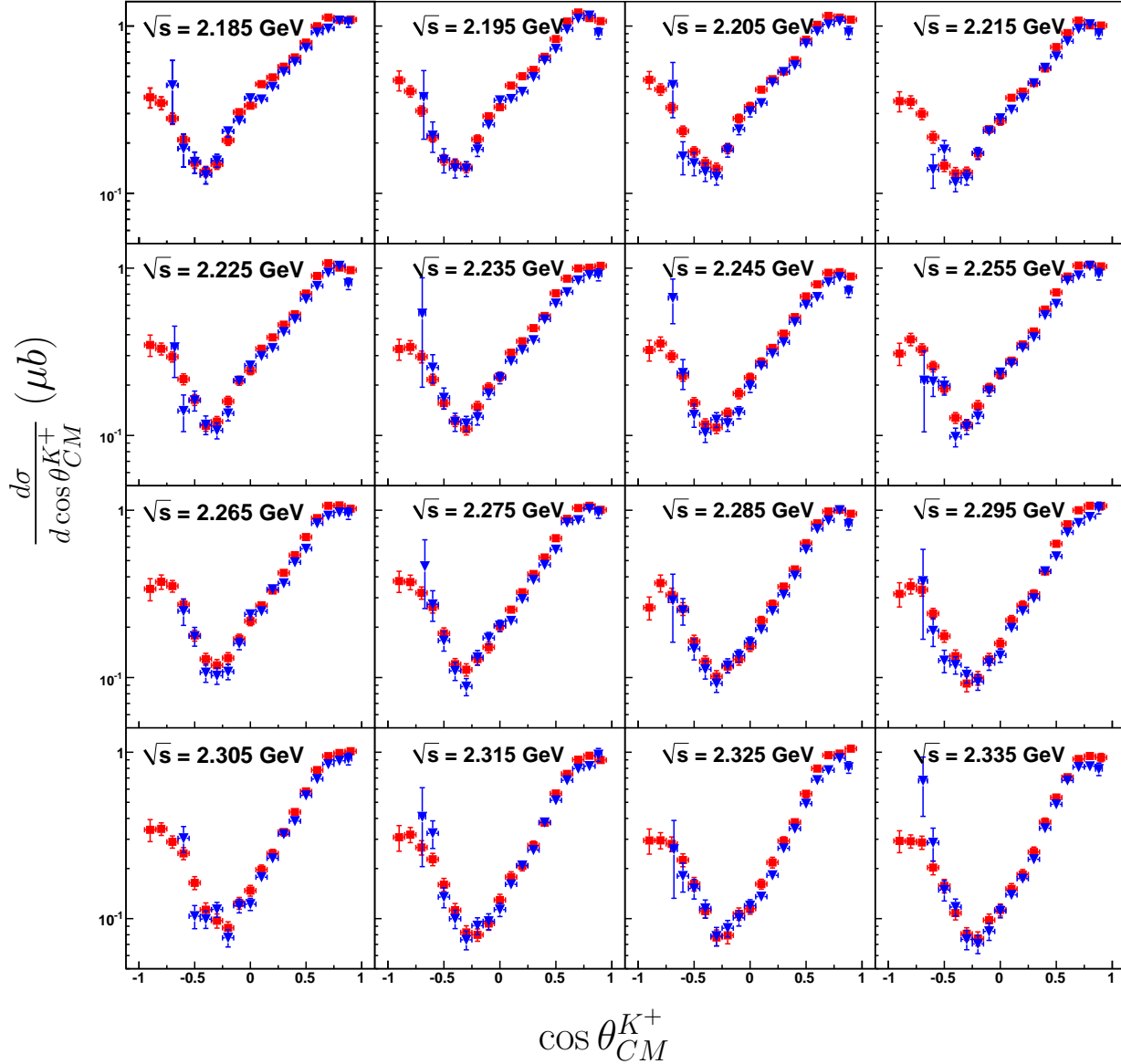


Figure 4.6: $\gamma p \rightarrow K^+\Sigma^0$ differential cross-sections for g11a: the red squares are the two-track results while the blue triangles are the three-track results. The vertical axis range (in logarithmic scale) is the same for all the plots in the canvas and is shown in the first column. All errors are statistical.

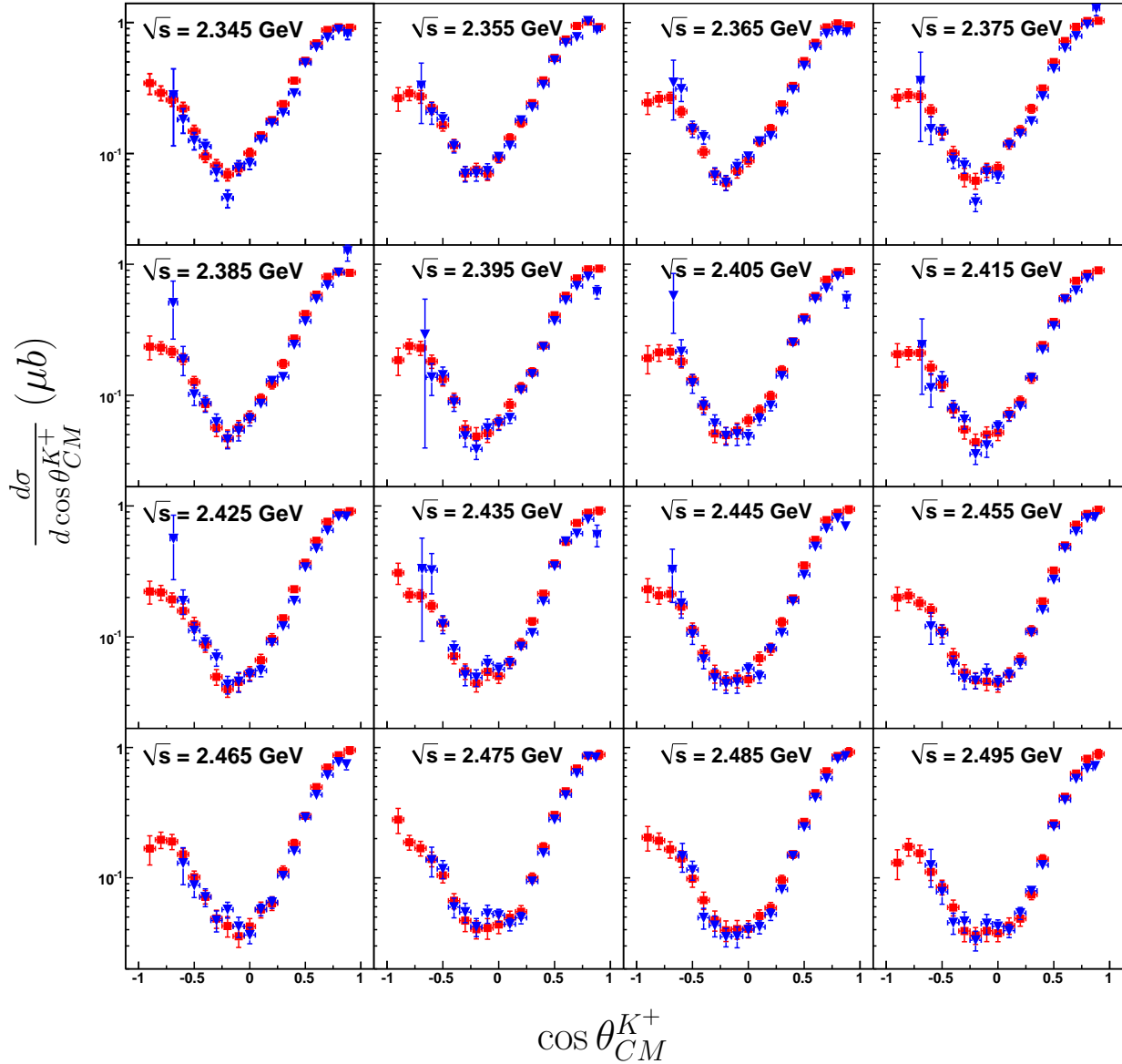


Figure 4.7: $\gamma p \rightarrow K^+\Sigma^0$ differential cross-sections for g11a: the red squares are the two-track results while the blue triangles are the three-track results. The vertical axis range (in logarithmic scale) is the same for all the plots in the canvas and is shown in the first column. All errors are statistical.

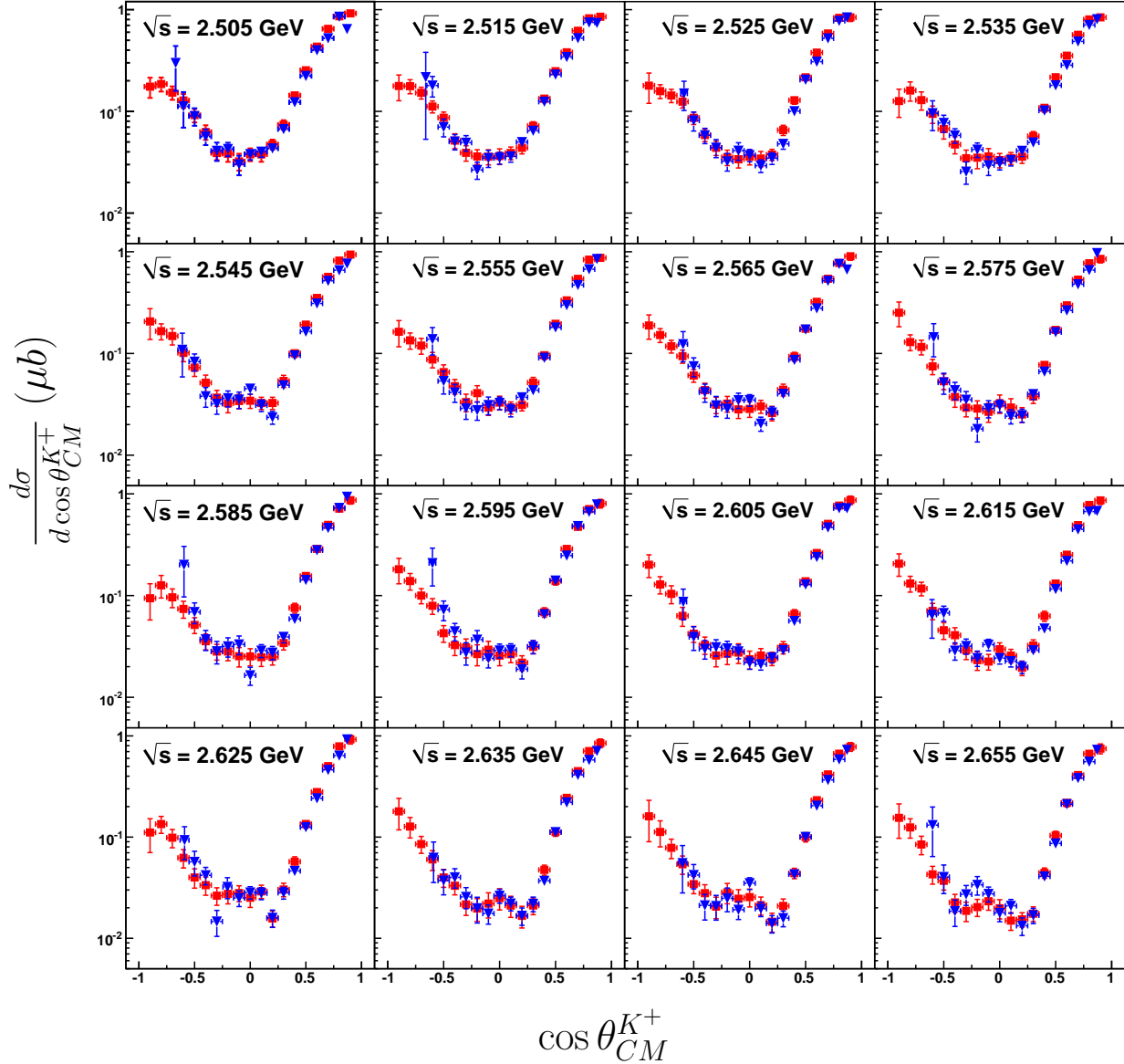


Figure 4.8: $\gamma p \rightarrow K^+\Sigma^0$ differential cross-sections for g11a: the red squares are the two-track results while the blue triangles are the three-track results. The vertical axis range (in logarithmic scale) is the same for all the plots in the canvas and is shown in the first column. All errors are statistical.

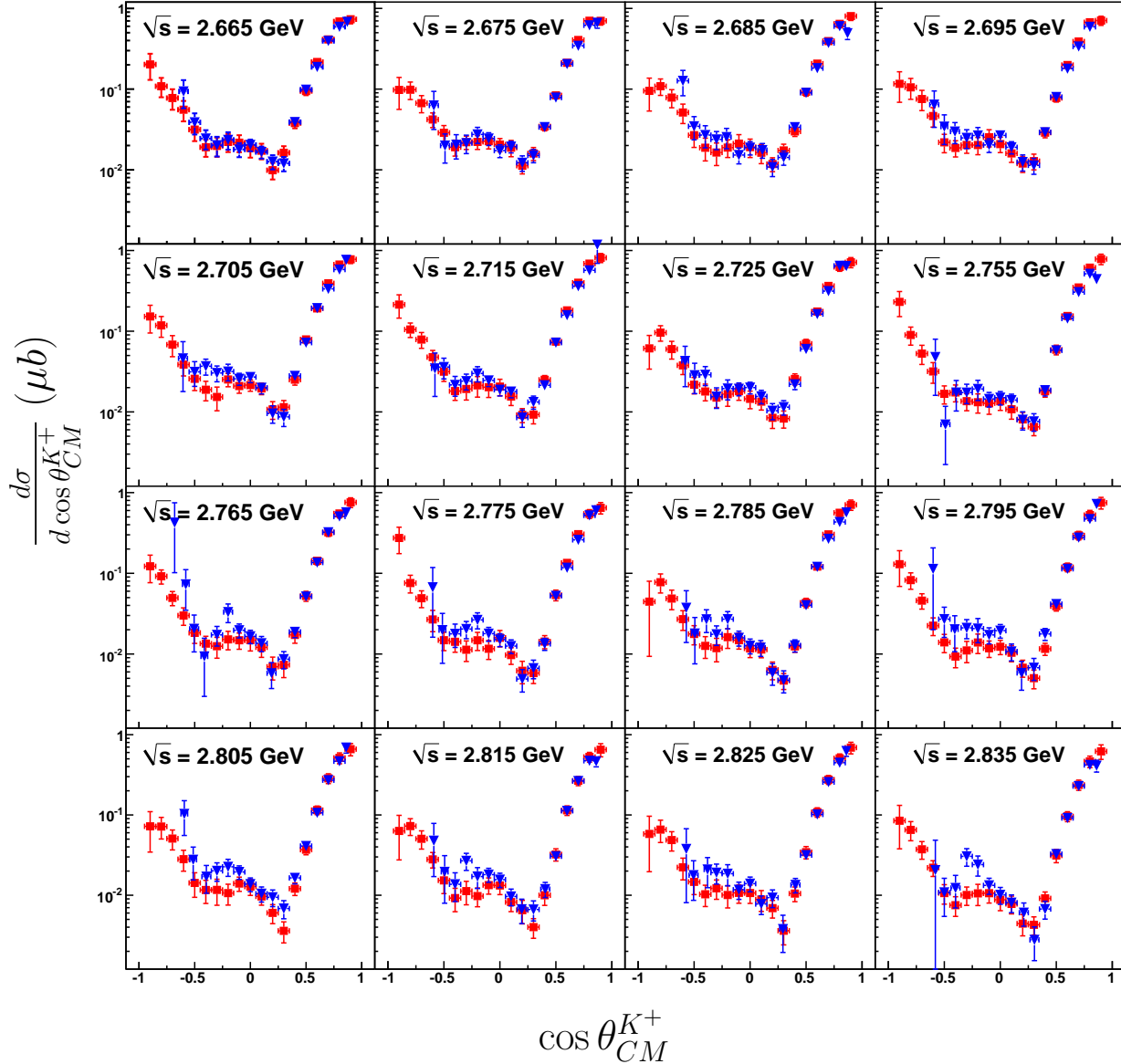


Figure 4.9: $\gamma p \rightarrow K^+\Sigma^0$ differential cross-sections for *g11a*: the red squares are the two-track results while the blue triangles are the three-track results. The vertical axis range (in logarithmic scale) is the same for all the plots in the canvas and is shown in the first column. All errors are statistical. No result is presented for the bins $\sqrt{s} = 2.735$ GeV and 2.745 GeV due to reasons given in Section 2.10.

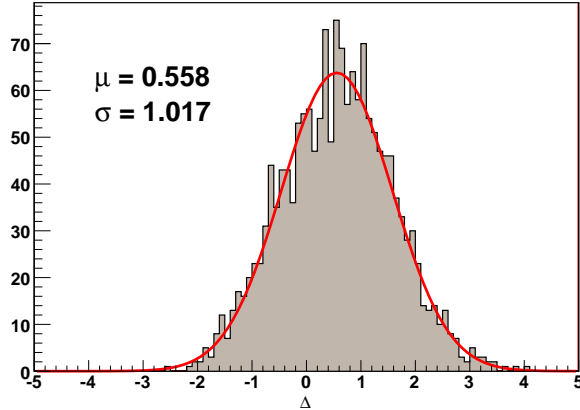


Figure 4.10: Δ (defined in Equation 4.40) depicting the relative spread between the two- and three-track differential cross sections for *g11a*.

Minimising the χ^2 yields the requisite mean $\bar{\mu}$

$$\bar{\mu} = \frac{\mu_2\sigma_3^2 - \rho(\mu_2 + \mu_3)\sigma_2\sigma_3 + \mu_3\sigma_2^2}{\sigma_2^2 - 2\rho\sigma_2\sigma_3 + \sigma_3^2}, \quad (4.44)$$

and the error on the combined measurement

$$\bar{\sigma} = \left(\frac{1}{2} \frac{\partial^2 \chi^2}{(\partial \bar{\mu})^2} \right)^{-1/2} = \left(\frac{1}{2} \sum_{i,j} (E^{-1})_{ij} \right)^{-1/2} = \sqrt{\frac{\sigma_2\sigma_3(1-\rho^2)}{\sigma_2/\sigma_3 - 2\rho + \sigma_3/\sigma_2}}. \quad (4.45)$$

This method is very similar to the so-called BLUE method [34, 35] employed elsewhere [36] and also boils down to the familiar expressions for uncorrelated measurements at $\rho = 0$. The only pathology of this method is the near $\rho \approx 1$ region where the error matrix becomes non-invertible, but as long as one is away from the high-correlation regime, the formula is pathology free (the $\rho \approx 1$ limit requires $\mu_2 \approx \mu_3$ and $\sigma_2 \approx \sigma_3$ and the formula becomes highly sensitive to small deviations from this behavior). Under the present circumstances, one can form *two* correlation factors. Since the entire 3-track dataset is (to a high approximation) present in the 2-track dataset, $\rho_{32} \approx 1.0$. However, from Section 1.11.1 the total occupancy after cuts and background separation is ~ 4.64 million for the 2-track and ~ 0.655 million for the 3-track dataset – hence $\rho_{23} \approx 0.14$. Taking the geometric mean of the two, one can get an *effective* correlation $\rho_{eff} \approx \sqrt{\rho_{23}\rho_{32}} \approx 0.37$.

Employing this method, our final differential cross-sections are shown in Figures 4.11 and 4.12 as a function of the center-of-mass energy in different production angle regions. In all we have made measurements at 2133 individual kinematic points covering almost the entire angular range, barring the extreme forward and backward angles (the CLAS detector has holes in these regions) and threshold upwards till 2.84 GeV in energy.

4.8.1 A note on the errors

Before ending this section we want to point out that several other related expressions were tried out before finalizing on formulas 4.45 and 4.44. While it is true that some events are *physically*

common between the two topologies, how we use the CLAS detector to *measure* these events are sufficiently different between the two topologies (event selection method, acceptance calculation, *et al*) that the degree of correlation might be less than 100% (that is, *all* 3-track events being included in the 2-track dataset). It is true however that certain segments of the measurements (the normalization, to be precise) which goes into the differential cross-section calculation is the same and thus highly correlated between the two measurements. The same might not apply for the apply to the acceptance calculation, however (see the discussion by Lyons [34]).

As a simple approximation, we tried a completely uncorrelated ($\rho = 0$) combination, both for μ and σ . Next, we tried keeping μ uncorrelated, but $\bar{\sigma} = \sqrt{\sigma_2\sigma_3}$. As an extreme, we also tried $\rho = 0.9$ – however, the errors seemed too small in this case, reflecting the near $\rho = 1$ pathology. The final correlation coefficient ρ_{eff} seemed the most plausible, both in terms of underlying justifiability and final results. However, we also found that to a large extent, as long as one stayed away from the $\rho = 1$ limit, the results (including taking the geometric mean of the errors) were very similar. This is probably due to the errors being small enough (as a reminder, we are *not* looking at the very backward angle regions here – which is where the largest statistical errors are) and also the fact that the agreement between the two datasets is generally very good.

4.9 Comparision With Previous Experiments

Figures 4.13 and 4.14 show our final differential cross sections for CLAS *g11a* in comparision with previously published high statistics measurements. The latter consists of results from the CLAS *g1c* dataset by Bradford *et al* (2005) [37], a SAPHIR analysis by Glander *et al* (2004) [38] and a set of two more recent forward angle measurements using the LEPS detector by Kohri *et al* (2006) [39]. Overall, there is good consistency among the different datasets, with an enhancement at $\sqrt{s} \sim 1.9$ GeV prominent over the entire angular range. Some structures are also visible around $\sqrt{s} \sim 2.1$ GeV in the forward angles. Some interesting localized discrepancies also occur between the different results. Chiefly, this pertains to the “hump” in the backward angles at ~ 2.2 GeV seen in the CLAS *g1c* results, but not prominent in the SAPHIR data. The present CLAS *g11a* analysis however clearly confirms this structure.

In the kinematic region around $0.4 \leq \cos\theta_{CM}^{K^+} \leq 0.7$, $2.0 \text{ GeV} \leq \sqrt{s} < 2.2 \text{ GeV}$, *g11a* seems to be slightly lower than *g1c*. The SAPHIR results seems to agree better with *g1c* in this region. The difference is small and can be attributed to the systematics involved in the different analyses. In Chapter 8, we make a detailed study of *g11a* to understand its systematics and find it to be self-consistent to a high degree. The particular kinematic region in question is neither statistics limited (see Figures 1.24 and 5.3), nor falls in a region of questionable understanding of the detector acceptance (see Section 1.10.2). For *g11a*, the energy and momentum corrections for the proton and π^- should also be better because of the usage of the kinematic fitter in deriving them (the kinematic fitter was especially honed for the *g11a* dataset [2]). This is especially true for the three-track topology where the secondary Λ decay vertex is reconstructed using tracking information on the proton and π^- trajectories and corrections for these two tracks subsequently derived using the Λ vertex as the source, instead of the event vertex, as used traditionally (see Section 1.4). Also note that only the three-track topology uses the more correct *physics-weighted* acceptance calculation, while we found in the previous section that the two-track results (which, like the previous *g1c* and SAPHIR measurements, used *unweighted* acceptances) to be higher than the three-track results by around 0.5σ . While none of these effects are large enough to cause a 5 – 10% difference, they do contribute to slight overall systematic shifts. Lastly, note that the more recent high statistics LEPS measurement roughly falls *between* the *g1c* and *g11a* results.

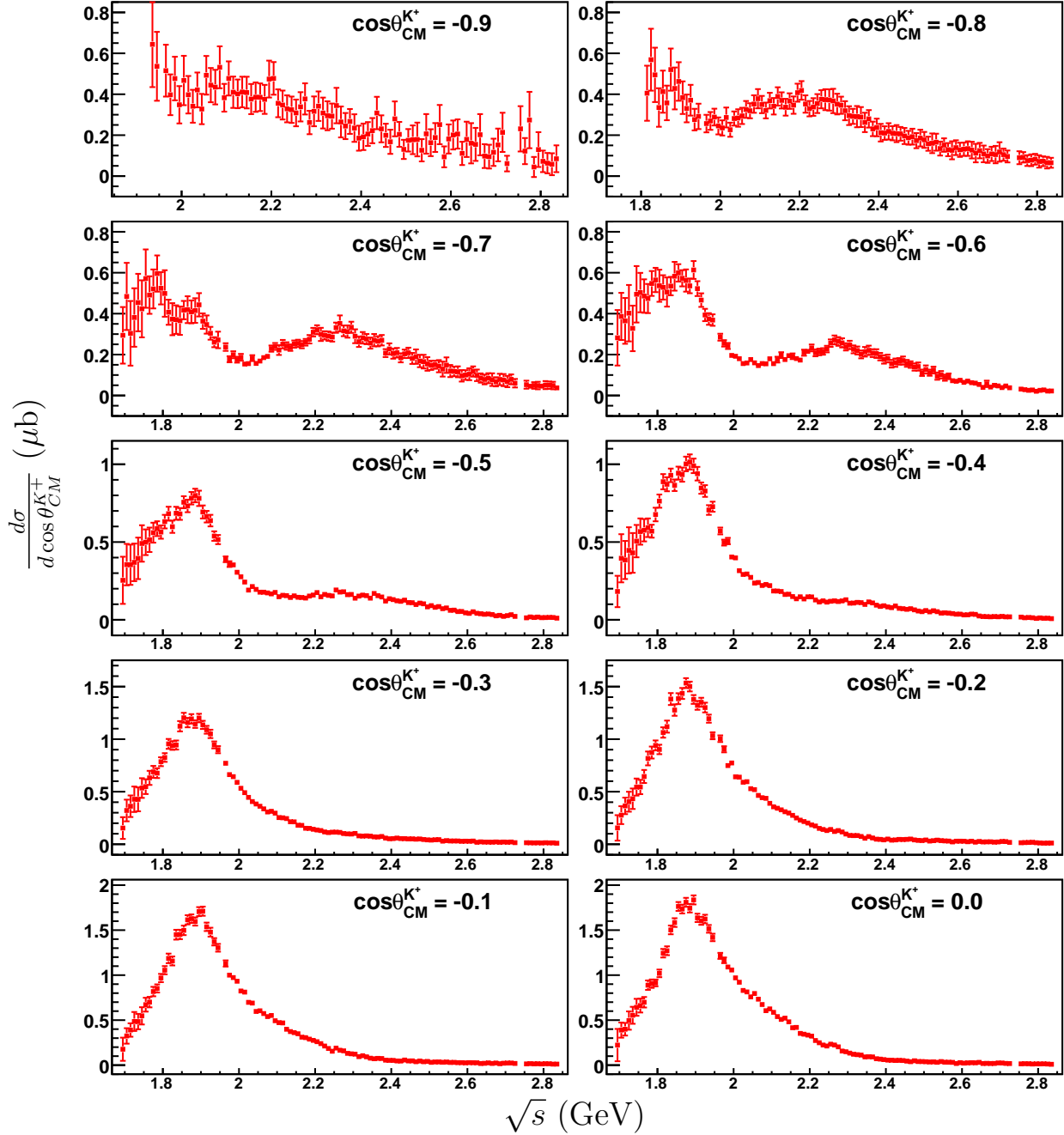


Figure 4.11: Final $\gamma p \rightarrow K^+\Sigma^0$ differential cross-sections for the $g11a$ dataset as a function of \sqrt{s} in the backward angles. The results shown are a weighted average between the two- and three-track topology cross-sections. All errors shown are statistical.

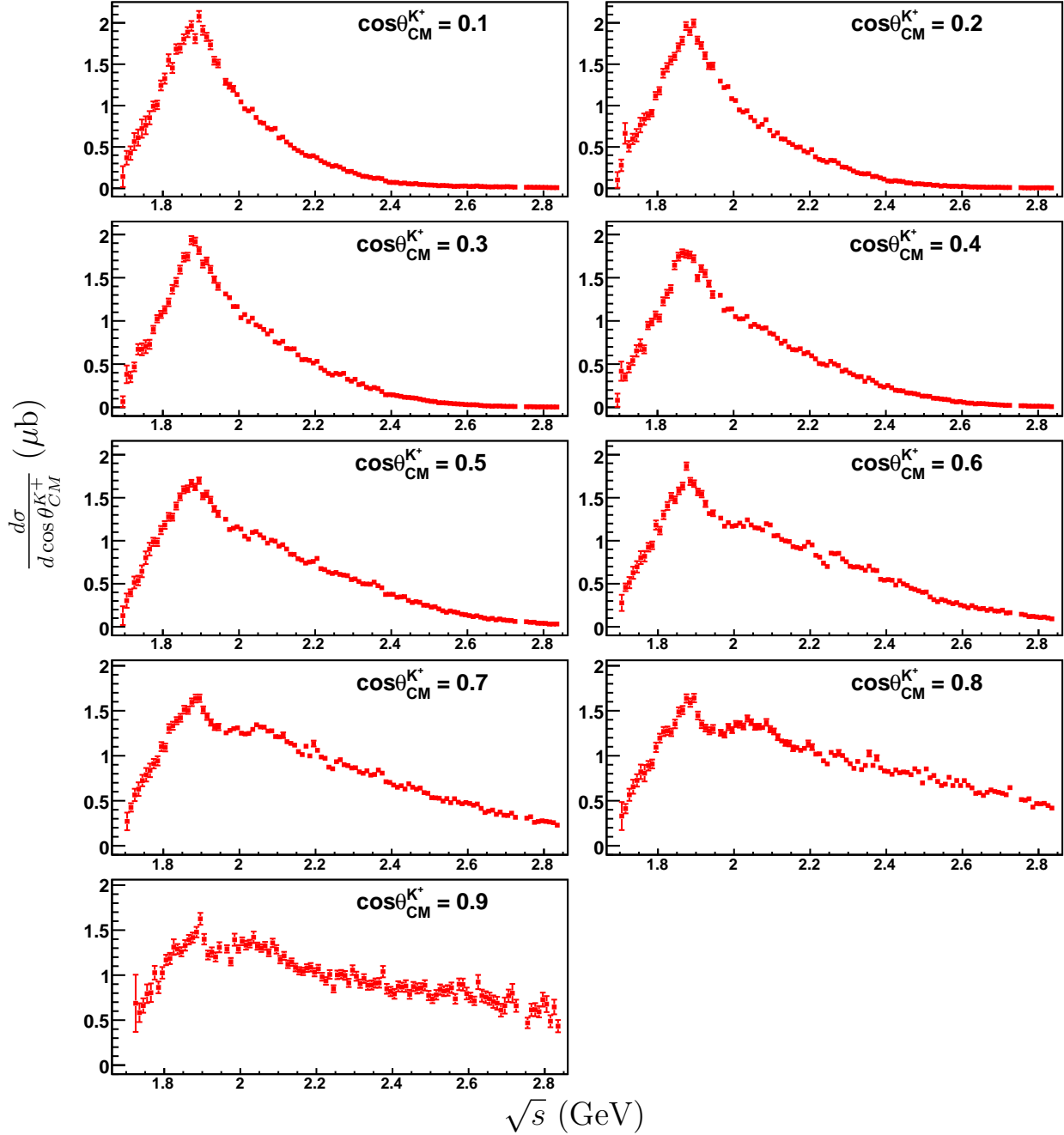


Figure 4.12: Final $\gamma p \rightarrow K^+\Sigma^0$ differential cross-sections for the $g11a$ dataset as a function of \sqrt{s} in the forward angles. The results shown are a weighted average between the two- and three-track topology cross-sections. All errors shown are statistical.

4.10 Summary

We extracted differential cross-sections for the $\gamma p \rightarrow K^+\Sigma^0$ for the CLAS *g11a* dataset separately for the two- and three-track topologies. The agreement between herein, despite the fact that the two topologies are almost independent, employing significantly different analysis techniques, strengthens our faith in the overall consistency of this analysis. We have also compared our results with previous world data. Mild localized differences remain between the CLAS *g11a* and *g1c* results, but on the whole, world data, including our results, for $K^+\Sigma^0$ photoproduction seems largely consistent amongst different measurements.

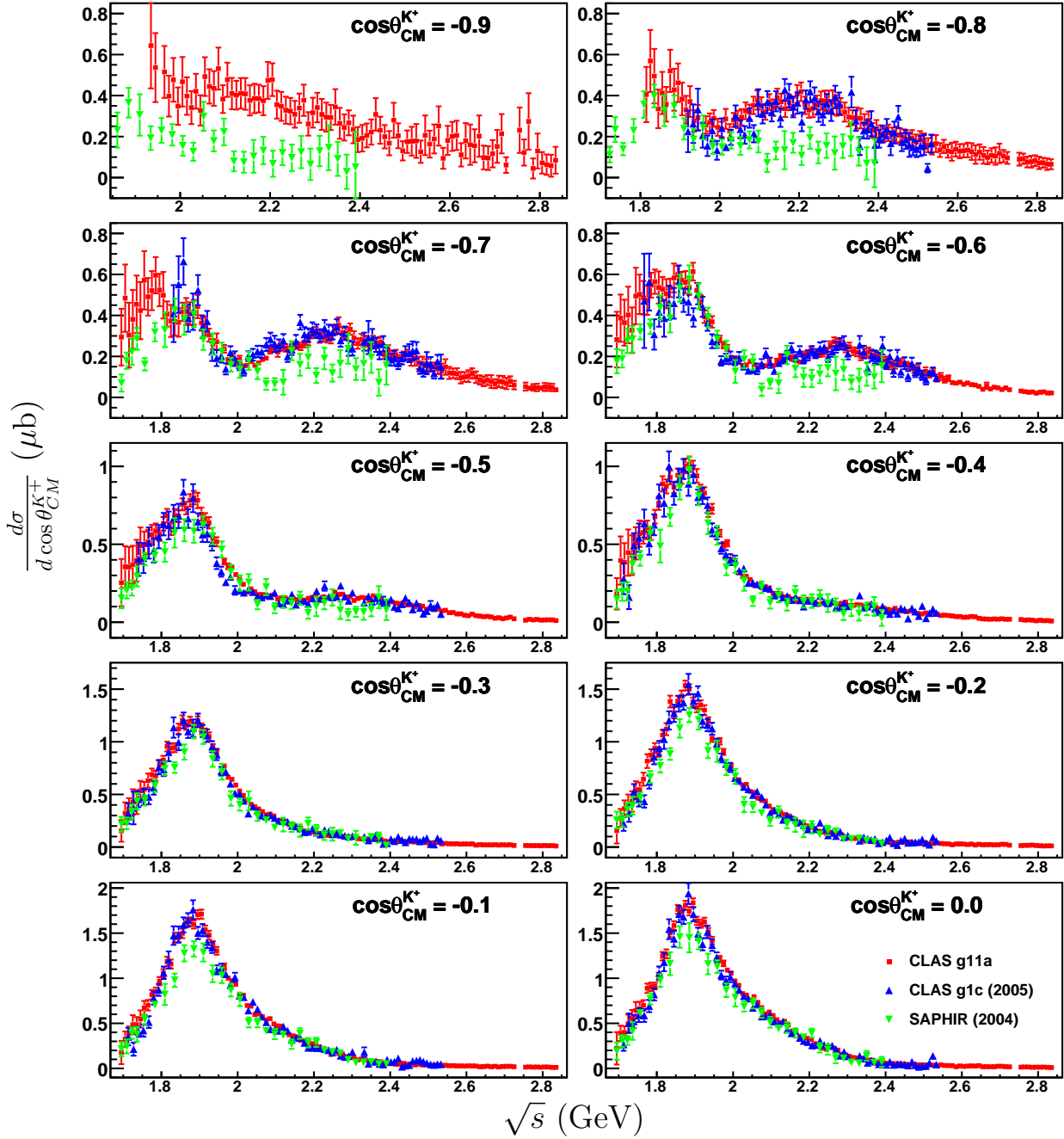


Figure 4.13: $\frac{d\sigma}{d \cos \theta_{CM}}$ (μb) vs \sqrt{s} in the backward angles: final CLAS $g11a$ (this analysis) differential cross section results as the weighted average of the topologies are in red squares. Previous CLAS $g1c$ results are in blue up-triangles while green down-triangles are results from SAPHIR.

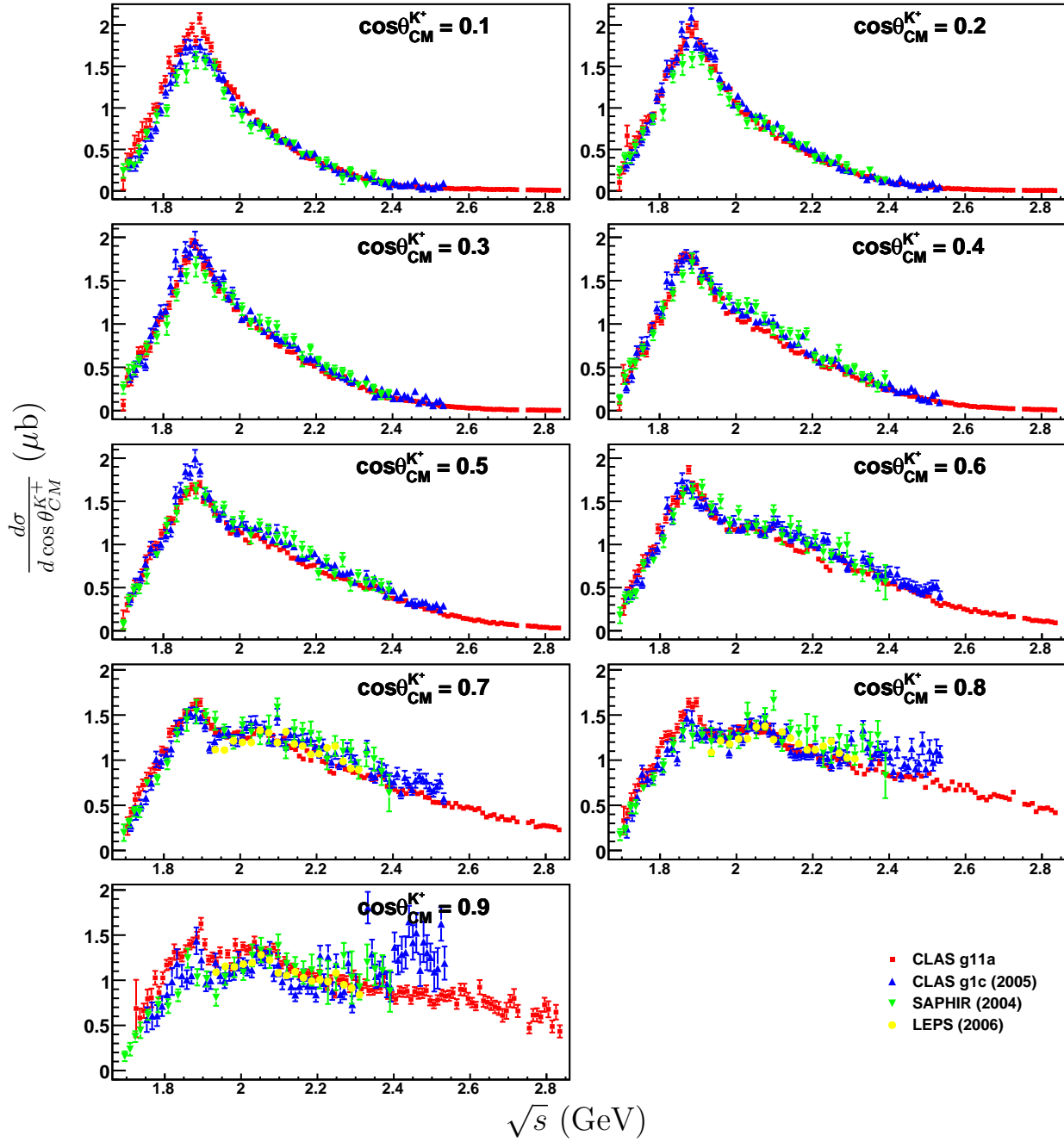


Figure 4.14: $\frac{d\sigma}{d \cos \theta_{CM}^{K^+}}$ (μb) vs \sqrt{s} in the forward angles: final CLAS g11a (this analysis) differential cross section results as the weighted average of the topologies are in red squares. Previous CLAS g1c results are in blue up-triangles while green down-triangles are results from SAPHIR. The yellow circles represent LEPS measurements in the forward-most angular bins.

Chapter 5

$K^+\Sigma^0$ Recoil Polarizations

A generic feature of hyperon physics is that over a large variety of production mechanisms, the hyperons come out (often strongly) polarized [41, 42]. The complete list of polarization observables for different beam and target configurations in hyperon photoproduction is described in detail in Reference [43]. The Hall B collaboration at Jefferson Laboratory has a broad program to study hyperons using these observables [50]. For the $g11a$ dataset, with an unpolarized beam and an unpolarized target, it follows from simple parity arguments (see Section 5.3) that the Σ^0 can have a net polarization only in the direction perpendicular to the production plane. This is called the “recoil” polarization P_Σ . In this chapter we first set up our axes conventions for polarization measurements in the $K^+\Sigma^0$ channel, describe the physics involved, and finally present our results. Since the tree-track topology has access to the Λ momentum, this topology *preserves the spin transfer information* between the Σ^0 and the intermediate Λ , unlike in the two-track topology case, where the Λ momentum is unknown and one needs to average over the intermediate Λ directions (Section 5.4.1). The latter represents an extra factor of “dilution” in our results (see Figures 5.7 and 5.8). Hence, the main bulk of the polarization results that we quote will be from the three-track dataset ($1.8 \text{ GeV} \leq \sqrt{s} \leq 2.84 \text{ GeV}$, $-0.55 \leq \cos \theta_{CM}^{K^+} \leq 0.95$). We quote results from the two-track dataset only in kinematic regions where the three-track dataset is severely limited by statistics (near-threshold and backward angle bins).

5.1 Conventions

There are multiple axes conventions for describing polarization variables in the literature. It is thus prudent to describe the one we will be using in this analysis.

5.1.1 Helicity Frame

Since the measured kinematic angles to follow will all be in what we call the “helicity frame” of some particle, we first describe what we mean by the helicity frame of a particle. To go to the helicity frame, we first rotate our system to align the velocity of the particle along \hat{z} , and then boost to its rest frame (see Figure 5.1). Thus, the only difference from the conventional “rest frame” is a rotation before the boost.

5.1.2 Axes Conventions

Our axes conventions follow those of Bradford [51]. First, we boost everything to the center-of-mass (CM) frame and set the \hat{z}_{CM} axis as the beam direction \hat{p}_{CM}^γ (our notation is as follows: the

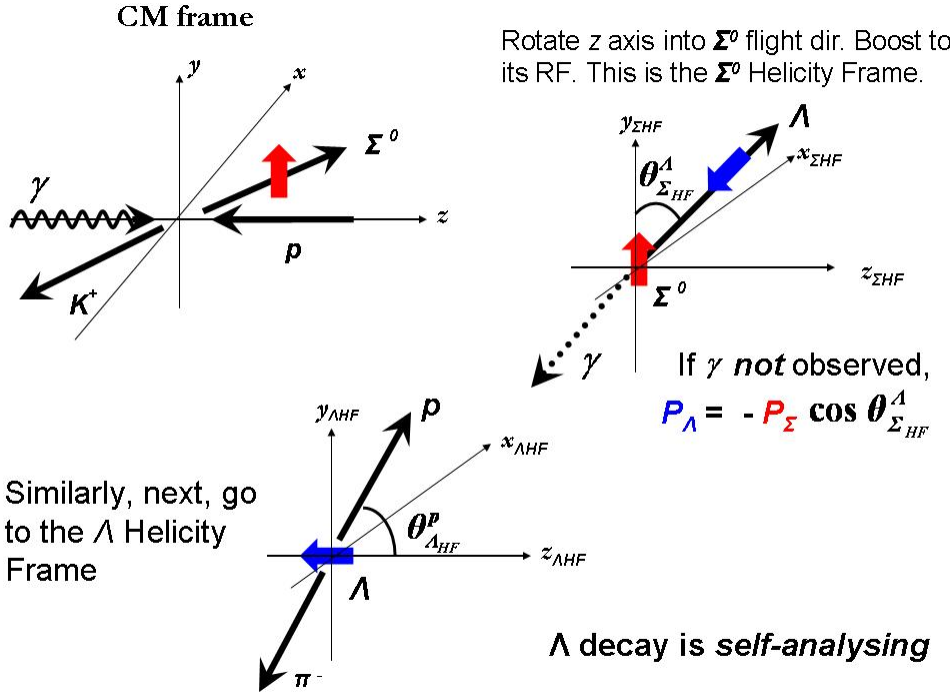


Figure 5.1: Shown is a pictorial depiction of the two angles going into the polarization dependent intensity profile, and how this expression is arrived at. The top-left figures assumes that $\hat{x}-\hat{z}$ is the reaction plane so that $\langle \vec{P}_\Sigma \rangle$ points along the perpendicular \hat{y} direction.

superscript denotes the particle and the subscript denotes the particular reference frame). We then define the $\gamma p \rightarrow K^+\Sigma^0$ reaction plane, or rather the normal to the plane, to be

$$\hat{n}_{CM} = \hat{p}_{CM}^\gamma \times \hat{p}_{CM}^{K^+}. \quad (5.1)$$

Note that since \hat{z}_{CM} and \hat{p}_{CM}^γ are the same, \hat{n}_{CM} is some unit vector in the $\hat{x}_{CM} \times \hat{y}_{CM}$ plane. Ultimately we want to align the normal vector \hat{n}_{CM} along \hat{y}_{CM} . To do this we form the auxiliary unit vector

$$\hat{u}_{aux} = \hat{n}_{CM} \times \hat{y}_{CM} \quad (5.2)$$

and rotate our system about \hat{u}_{aux} by the angle between \hat{n}_{CM} and \hat{y}_{CM} . Note that \hat{u}_{aux} is along the \hat{z}_{CM} (modulo a sign) so this rotation is simply the rotation of a vector (\hat{n}_{CM}) in the $\hat{x}_{CM} \times \hat{y}_{CM}$ plane about the \hat{z}_{CM} axis to bring it into alignment with the \hat{y}_{CM} axis. Once \hat{z}_{CM} and \hat{y}_{CM} (now pointing along \hat{n}_{CM}) have been set, \hat{x}_{CM} is simply $\hat{y}_{CM} \times \hat{z}_{CM}$.

We next perform a rotation followed by a boost as described in the last sub-section to go to the helicity frame (HF) of Σ^0 . The rotation in this case is about \hat{y}_{CM} (since \hat{p}_Σ is now in the $\hat{x}_{CM}-\hat{z}_{CM}$ plane) and the boost is in the \hat{z}_{CM} direction. Thus, $\hat{y}_{\Sigma_{HF}}$ is the same as \hat{y}_{CM} . Once in Σ_{HF} , we measure the following two variables (see Figure 5.1)

$$\cos \theta_{\Sigma_{HF}}^\Lambda = \hat{y}_{\Sigma_{HF}} \cdot \hat{p}_{\Sigma_{HF}}^\Lambda \quad (5.3a)$$

$$\cos \theta_{\Sigma_{HF}}^p = \hat{y}_{\Sigma_{HF}} \cdot \hat{p}_{\Sigma_{HF}}^p \quad (5.3b)$$

Going on to Λ_{HF} from here, we measure

$$\cos \theta_{\Lambda_{HF}}^p = \hat{y}_{\Lambda_{HF}} \cdot \hat{p}_{\Lambda_{HF}}^p \quad (5.4)$$

where $\theta_{\Lambda_{HF}}^p$ is interpreted as the angle between the proton and Λ flight directions, as measured in the rest frame of the Λ .

5.2 Polarization Transfer Between Σ^0 - Λ

The final result that we want to show is that in the electromagnetic decay $\Sigma^0 \rightarrow \Lambda\gamma$, if we do not measure the final photon polarization, then in the Σ^0 rest frame, the polarizations of the Λ and the Σ^0 are related as

$$\langle \vec{P}_\Lambda \rangle = - \left(\langle \vec{P}_\Sigma \rangle \cdot \hat{p}_\Lambda \right) \hat{p}_\Lambda, \quad (5.5)$$

where $\langle \vec{P}_\Lambda \rangle$ and \hat{p}_Λ are the polarization and direction respectively of the produced Λ and $\langle \vec{P}_\Sigma \rangle$ is the initial polarization of the decaying Σ^0 . The proof appears in several places [52, 53] and we will sketch the one given by Feldman and Fulton here.

The starting point is Equation 3.61. Since we are dealing with mixed states we need to take the density matrix approach to find expectation values. The initial density matrix for the Σ^0 with polarization \vec{P}_Σ is given by

$$\rho = \frac{1}{2} \left(1 + \langle \vec{P}_\Sigma \rangle \cdot \vec{\sigma} \right) \quad (5.6)$$

where the σ 's are the usual Pauli matrices and $\vec{\sigma} = (\sigma_x, \sigma_y, \sigma_z)$. The expectation value of the Λ polarization is then given as

$$\langle \vec{P}_\Lambda \rangle = \frac{\text{Tr} [T\rho T^\dagger \vec{\sigma}]}{\text{Tr} [T\rho T^\dagger]} = \frac{\text{Tr} \left[TT^\dagger \vec{\sigma} + T \langle \vec{P}_\Sigma \rangle T^\dagger \vec{\sigma} \right]}{\text{Tr} \left[TT^\dagger + T \langle \vec{P}_\Sigma \rangle T^\dagger \right]}. \quad (5.7)$$

where T is the transition matrix for $\Sigma^0 \rightarrow \Lambda\gamma$ and $T\rho T^\dagger$ is the final density matrix for the Σ^0 .

To evaluate this expression we will need the following properties of the Pauli matrices

$$\sigma^\dagger = \sigma \text{ (Hermitian)} \quad (5.8a)$$

$$\text{Tr}[\sigma_i] = 0 \text{ (traceless)} \quad (5.8b)$$

$$\text{Tr}[\sigma_i \sigma_j] = 2\delta_{ij}, \text{ from which it follows} \quad (5.8c)$$

$$\text{Tr}[(\vec{u} \cdot \vec{\sigma}) \vec{\sigma}] = 2\vec{u} \quad (5.8d)$$

$$(\vec{u} \cdot \vec{\sigma})(\vec{v} \cdot \vec{\sigma}) = (\vec{u} \cdot \vec{v}) I + i(\vec{u} \times \vec{v}) \cdot \vec{\sigma}, \text{ which leads to} \quad (5.8e)$$

$$\text{Tr}[(\vec{u} \cdot \vec{\sigma})(\vec{v} \cdot \vec{\sigma})] = 2(\vec{u} \cdot \vec{v}) \text{ and} \quad (5.8f)$$

$$\text{Tr}[(\vec{u} \cdot \vec{\sigma})(\vec{v} \cdot \vec{\sigma}) \vec{\sigma}] = 2i(\vec{u} \times \vec{v}) \quad (5.8g)$$

$$\text{Tr}[(\vec{u} \cdot \vec{\sigma})(\vec{v} \cdot \vec{\sigma})(\vec{w} \cdot \vec{\sigma})] = 2i\vec{w} \cdot (\vec{u} \times \vec{v}) \quad (5.8h)$$

$$\text{Tr}[(\vec{u} \cdot \vec{\sigma})(\vec{v} \cdot \vec{\sigma})(\vec{w} \cdot \vec{\sigma}) \vec{\sigma}] = 2[(\vec{u} \cdot \vec{v}) \vec{w} + (\vec{w} \cdot \vec{u}) \vec{v} - (\vec{w} \cdot \vec{u}) \vec{v}] \quad (5.8i)$$

Going back to Equation 3.61, we had chosen the polarization 3-vectors as the positive and negative helicity vectors $\vec{\epsilon}_\pm = (1/\sqrt{2})(\vec{\epsilon}_1 i \pm \vec{\epsilon}_2)$ where $\vec{\epsilon}_1$ and $\vec{\epsilon}_2$ are orthogonal unit vectors in the plane transverse to the photon momentum \vec{p}_γ such that $\vec{\epsilon}_1 \times \vec{\epsilon}_2 = \hat{p}_\gamma$. We then showed that the

photon "spin" is along its direction of motion and can be expressed in terms of the the $\vec{\epsilon}_\pm$ components of the photon field. The helicity vectors have the following properties

$$(\vec{\epsilon}_\pm)^* = \vec{\epsilon}_\mp \quad (5.9a)$$

$$\vec{\epsilon}_\pm \times \hat{p}_\gamma = \pm i \vec{\epsilon}_\pm \quad (5.9b)$$

$$\vec{\epsilon}_+ \cdot \vec{\epsilon}_- = \vec{\epsilon}_- \cdot \vec{\epsilon}_+ = 0 \quad (5.9c)$$

$$\vec{\epsilon}_+ \cdot \vec{\epsilon}_- = 1, \text{ so that} \quad (5.9d)$$

$$|\vec{\epsilon}_\pm| = (\vec{\epsilon}_\pm)^* \cdot \vec{\epsilon}_\mp = 1 \quad (5.9e)$$

$$\vec{\epsilon}_+ \times \vec{\epsilon}_- = -i \vec{p}_\gamma \quad (5.9f)$$

Then in Equation 3.61, we see that the transition matrix T goes like $(\vec{\epsilon} \times \vec{p}_\gamma) \cdot \vec{\sigma}$. So if $\vec{\epsilon}$ is one of $\vec{\epsilon}_{1,2}$ then $T_{1,2} \sim \vec{\epsilon}_{2,1} \cdot \vec{\sigma}$ and if it is one of $\vec{\epsilon}_\pm$ then $T_\pm \sim \vec{\epsilon}_\pm \cdot \vec{\sigma}$. Note that $\text{Tr}[TT^\dagger] = 2\vec{\epsilon} \cdot \vec{\epsilon}^* \sim 1$ for either case so that unitarity of the scattering matrix is maintained. For ease of computation, since they are real, we will use the $\vec{\epsilon}_{1,2}$ basis for the rest of the computation.

Then, putting it all together, the numerator of Equation 5.7 becomes

$$\text{Tr}[(\vec{\epsilon} \cdot \vec{\sigma})(\vec{\epsilon} \cdot \vec{\sigma})\vec{\sigma}] + \text{Tr}[(\vec{\epsilon} \cdot \vec{\sigma})(\langle \vec{P}_\Sigma \rangle \cdot \vec{\sigma})(\vec{\epsilon} \cdot \vec{\sigma})\vec{\sigma}] = 4(\vec{\epsilon} \cdot \hat{P}_\Sigma)\hat{\epsilon} - 2\langle \hat{P}_\Sigma \rangle, \quad (5.10)$$

while the denominator is

$$\text{Tr}[(\vec{\epsilon} \cdot \vec{\sigma})(\vec{\epsilon} \cdot \vec{\sigma})] + \text{Tr}[(\vec{\epsilon} \cdot \vec{\sigma})(\vec{P}_\Sigma \cdot \vec{\sigma})(\vec{\epsilon} \cdot \vec{\sigma})] = 2. \quad (5.11)$$

Thus for the two polarization states $\vec{\epsilon}_1$ and $\vec{\epsilon}_2$

$$\langle \vec{P}_{\Lambda, \vec{\epsilon}_{1,2}} \rangle = -\langle \vec{P}_\Sigma \rangle + 2(\vec{\epsilon}_{2,1} \cdot \vec{P}_\Sigma)\vec{\epsilon}_{2,1} \quad (5.12)$$

If we fix our coordinate axes as $\hat{x} = \vec{\epsilon}_1$, $\hat{y} = \vec{\epsilon}_2$ and $\hat{z} = \hat{p}_\Lambda$ the above two equations take the form

$$\langle \vec{P}_{\Lambda, \vec{\epsilon}_2} \rangle = -\vec{P}_\Sigma + 2(\vec{P}_\Sigma)_x \hat{x} \text{ and} \quad (5.13a)$$

$$\langle \vec{P}_{\Lambda, \vec{\epsilon}_1} \rangle = -\vec{P}_\Sigma + 2(\vec{P}_\Sigma)_y \hat{y}. \quad (5.13b)$$

Averaging over the two photon polarizations immediately gives

$$\langle \vec{P}_\Lambda \rangle = -\langle \vec{P}_\Sigma \rangle_z \hat{z} = -(\langle \vec{P}_\Sigma \rangle \cdot \hat{p}_\Lambda)\hat{p}_\Lambda. \quad (5.14)$$

5.3 Parity Argument for Hyperon Polarization

We now want to show that for unpolarized kaon-hyperon (KY) production via parity conserving interactions, the only component of the hyperon polarization which can survive is the component perpendicular to the reaction plane.

Without loss of generality, let us quantize all the spins along \hat{z} direction and orient our axes so that $\hat{x} - \hat{z}$ is the reaction plane and \hat{y} is the normal to the plane. Consider the amplitude for a particular set of spin configurations for the incoming photon, the target proton and the produced hyperon (Σ^0 in this case) as shown in Figure 5.2. A parity transform will flip all the momenta vectors but keep the spins intact (spin being a pseudo vector does not change sign under a parity flip). Next, if we rotate everything by 180° about the \hat{y} axis, both spins and momenta get reversed

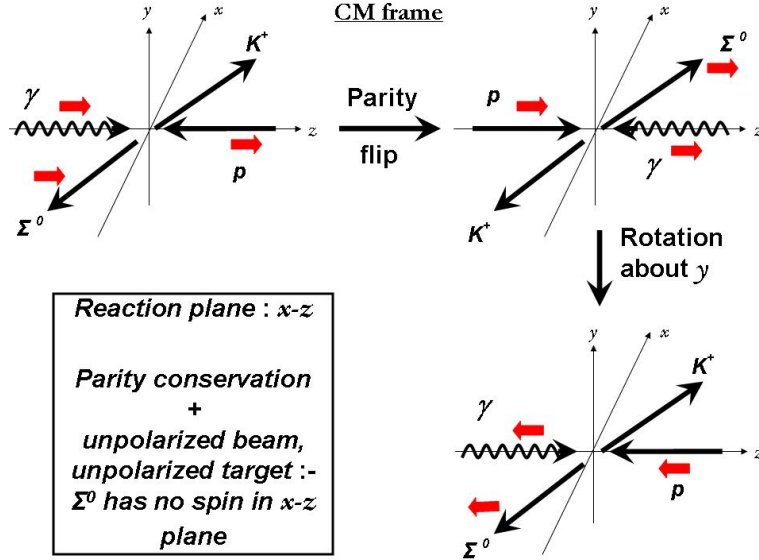


Figure 5.2: Amplitudes for two different sets of spin (red bold arrows) configuration are connected through a combined parity-rotation transformation. If the underlying interaction is invariant under this transformation, the two amplitudes will be physically indistinguishable.

and we go to a configuration where all the spins from the original configuration have been flipped.

Because the electromagnetic and strong interactions are invariant under this combined parity + rotation transform, the two configurations are indistinguishable and the two amplitudes will have the same probability of occurrence. Therefore the hyperon cannot have a net spin in the $\hat{x} - \hat{z}$ direction if we sum over the photon and target polarizations. The only component which will survive is the \hat{y} polarization because the \hat{y} rotation will not flip the hyperon spin in this case.

5.4 Final $\Sigma^0 \rightarrow \Lambda\gamma \rightarrow p\pi^- \gamma$ Angular Distribution

From Sect. 3.5.2, the weak decay of the Λ occurs by a combination of a parity-conserving S -wave decay and a parity-violating P -wave decay. Because of this, one says that the Λ decay is *self-analysing*, since the polarization information is contained in the intensity profile with respect to the proton angle. Combining the Λ and the Σ^0 decays, we get the final intensity angular distribution for the entire decay chain as

$$\begin{aligned} \mathcal{I}_{\gamma p \rightarrow K^+ \Sigma^0 \rightarrow K^+ \gamma p \pi^-} &\sim (1 + \alpha \langle \vec{P}_\Lambda \rangle \cos \theta_{\Lambda_{HF}}^p) \\ &= (1 - \alpha \langle \vec{P}_\Sigma \rangle \cos \theta_{\Lambda_{HF}}^p \cos \theta_{\Sigma_{HF}}^\Lambda), \end{aligned} \quad (5.15)$$

where $\alpha = 0.642 \pm 0.013$ is the Λ weak decay asymmetry. Figure 5.1 depicts pictorially, the two angles and the physics involved in this expression.

5.4.1 Approximate g_1 Expression

There is another (approximate) expression for this angular dependence for the case where the direction of the Λ is not measured explicitly. For example in the Σ^0 decay, if we detect only the

proton and have no information about both the π^- and the outgoing γ , then the only angle we can measure is $\theta_{\Sigma_{HF}}^p$ which is angle between the proton's flight direction and the normal to the $K^+\Sigma^0$ production plane, as measured in the Σ^0 helicity (rest) frame. This is the case in John McNabb's CLAS $g1$ [10, 54] and Bob Bradford's $g1c$ [51, 55] analyses, where only the kaons and the protons were identified. Bradford and Schumacher have shown [55] that averaging over the intermediate Λ flight directions, yields the intensity distribution

$$\mathcal{I} \propto (1 + \nu \alpha \langle \vec{P}_\Sigma \rangle \cos \theta_{\Sigma_{HF}}^p) \quad (5.16)$$

where ν is a *dilution factor* which they found to be approximately $-\frac{1}{3.90}$. For our three-track analysis, we detect all the charged tracks and reconstruct the missing photon, so we will be using the earlier (exact) expression only (Equation 5.15). However, extraction of P_Σ from the two-track dataset necessitates the use of the approximate expression (Equation 5.16) – in Section 5.9.2 we explicitly show the “dilution” effect arising from using the approximate expression.

5.5 PWA Expression for Polarization

Consider the general reaction $\gamma p \rightarrow \text{PS} + \text{B}$, where PS denotes $J^P = 0^-$ pseudo-scalar mesons (pion, kaon, η , η') and B denotes $J^P = \frac{1}{2}^+$ baryons (nucleons, hyperons). In the CM frame, let \vec{q} and \vec{k} be the outgoing meson and incoming photon momenta respectively. We will denote the three relevant spin projections as $m_\gamma = \pm 1$ (incoming photon), $m_i = \pm \frac{1}{2}$ (target proton) and $m_b = \pm \frac{1}{2}$ (outgoing baryon) and remind the reader that the spin quantization axis in all our partial wave amplitudes is always along the longitudinal beam direction \hat{z} . The expression for the unpolarized differential cross-section in terms of the PWA amplitudes $\mathcal{A}_{m_\gamma, m_i, m_b}$ was given in Equation ???. In this section we will express the rest of the physical observables, which are all polarization observables, in terms of these amplitudes. We will generally follow the discussion by Fasano, Tabakin and Saghai in Reference [44].

5.5.1 CGLN Amplitudes

The generic form of the scattering amplitude is

$$\mathcal{A}_{m_i m_\gamma m_b}(q, k) = \langle m_b | \vec{J} | m_i \rangle \cdot \vec{\epsilon}(m_\gamma, k), \quad (5.17)$$

where \vec{J} is the hadronic current operator, and $\vec{\epsilon}$ is the photon polarization vector. The current \vec{J} can be expressed in terms of four complex CGLN [45] amplitudes f_1, \dots, f_4 , where the quantization of the baryon spins is again along the \hat{z} direction:

$$\vec{J} = i f_1 \vec{\sigma} + f_2 (\vec{\sigma} \cdot \hat{q}) (\vec{\sigma} \times \hat{k}) + i f_3 (\vec{\sigma} \cdot \hat{k}) \hat{q} + i f_4 (\vec{\sigma} \cdot \hat{q}) \hat{q}. \quad (5.18)$$

This is in the 2-component Pauli basis. Equivalently, one can also write the most general invariant amplitude in the 4-component Dirac basis:

$$M_1 = -\gamma_5 \not{\epsilon} \not{k} \quad (5.19a)$$

$$M_2 = 2\gamma_5 (\not{\epsilon} \cdot \not{p}_i \not{k} \cdot \not{p}_b - \not{\epsilon} \cdot \not{p}_b \not{k} \cdot \not{p}_i) \quad (5.19b)$$

$$M_3 = \gamma_5 (\not{\epsilon} \not{k} \cdot \not{p}_i - \not{\epsilon} \cdot \not{p}_i \not{k}) \quad (5.19c)$$

$$M_4 = \gamma_5 (\not{\epsilon} \not{k} \cdot \not{p}_b - \not{\epsilon} \cdot \not{p}_b \not{k}), \text{ so that} \quad (5.19d)$$

$$\mathcal{A}_{m_i m_\gamma m_b} \sim \bar{u}_b(m_b) \sum_{j=1}^4 \alpha_j M_j(m_\gamma) u_i(m_i) \quad (5.19e)$$

$\mu \setminus \lambda$	$\lambda_\gamma = +1$		$\lambda_\gamma = -1$	
	$\frac{3}{2}$	$\frac{1}{2}$	$-\frac{1}{2}$	$-\frac{3}{2}$
$\frac{1}{2}$	H_1	H_2	H_4	$-H_3$
$-\frac{1}{2}$	H_3	H_4	$-H_2$	H_1

Table 5.1: Helicity amplitude nomenclature for pseudo-scalar meson photoproduction. The amplitudes for the two photon helicities $\lambda_\gamma = \pm 1$ are not independent. The rows and columns in the helicity matrix H_i correspond to initial- (λ) and final-state (μ) helicities.

where p_i and p_b are the target proton and final baryon 4-momenta and u_i and u_b are the corresponding Dirac spinors. Whichever way it is written out, the important point here is that there are *four* independent complex amplitudes. These CGLN amplitudes contain all the dynamics of the reaction and the basic problem in meson photoproduction is to determine all four of these complex numbers (or equivalently, eight real numbers). Note that photon and the two baryons each have two basis states, so that the full transition amplitude has $2^3 = 8$ independent parts. However, parity and rotational invariance reduces this number to four independent amplitudes.

5.5.2 Helicity Amplitudes

Here, we follow Walker's [46] notation who rewrites the four amplitudes in terms of spin-flip and non-spin-flip components, where the spin transfer is between the initial proton and the final baryon. For a given photon polarization, the spin dependence of the amplitude can thus be written as a 2×2 matrix whose columns and rows refer to the initial and final baryon spins:

$$\mathcal{A}_{\lambda_i \lambda_b} = \begin{pmatrix} A_{++} & A_{+-} \\ A_{-+} & A_{--} \end{pmatrix}, \quad (5.20)$$

where the spins of the two baryons are now chosen to be quantized in their *helicity basis*, that is, along their individual momentum directions (in the *CM* frame). The initial- and final-state helicities are then $\lambda = \lambda_\gamma - \lambda_i$ and $\mu = \lambda_{PS} - \lambda_b = -\lambda_b$ ¹.

For real transverse photons, $\lambda_\gamma = \pm 1$ and λ takes on the four values $\pm \frac{1}{2}$ and $\pm \frac{3}{2}$. Note that any of these four values for λ specifies both λ_γ and λ_i uniquely. Likewise μ is always $\pm \frac{1}{2}$. As mentioned before, these $4 \times 2 = 8$ helicity amplitudes are however connected by parity:

$$\mathcal{H}_{-\mu, -\lambda}(\theta, \phi) = -e^{i(\lambda - \mu)(\pi - 2\phi)} \mathcal{H}_{\lambda, \mu}(\theta, \phi), \quad (5.21)$$

so that there are only four independent amplitudes in the end. If we fix the azimuthal direction $\phi = 0$, so that $\hat{x} - \hat{z}$ is the scattering plane, then the four independent helicity amplitudes H_1, \dots, H_4 are given in Table 5.1.

Since, any given combination of λ and μ uniquely specifies λ_γ , λ_i and λ_b , in terms of H_i , we can write \mathcal{A} in Equation 5.20 as:

$$\mathcal{A}^{\lambda_\gamma=+1} = \begin{pmatrix} H_4 & H_2 \\ H_3 & H_1 \end{pmatrix} \quad (5.22a)$$

$$\mathcal{A}^{\lambda_\gamma=-1} = \begin{pmatrix} H_1 & -H_3 \\ -H_2 & H_4 \end{pmatrix}. \quad (5.22b)$$

¹In the language of Barker *et al* [47], $|\lambda - \mu|$ parameterizes the degree of "spin flip". Thus, $N = H_2$ is the non-spin-flip, $S_1 = H_1$ and $S_2 = H_4$ are the single spin-flip and $D = H_3$ is the double spin-flip amplitude.

Using the above relations and the expressions for plane and perpendicular polarizations

$$\epsilon_{\perp} = \vec{\epsilon}_y = (i/\sqrt{2})(\epsilon_+ + \epsilon_-) \quad (5.23a)$$

$$\epsilon_{\parallel} = \vec{\epsilon}_x = -(1/\sqrt{2})(\epsilon_+ - \epsilon_-), \quad (5.23b)$$

we can rewrite Table 5.1 for the linear polarizations as

$$\mathcal{A}^{\epsilon_{\perp}} = \begin{pmatrix} \frac{i}{\sqrt{2}}(H_1 + H_4) & \frac{i}{\sqrt{2}}(H_2 - H_3) \\ \frac{i}{\sqrt{2}}(H_3 - H_2) & \frac{i}{\sqrt{2}}(H_1 + H_4) \end{pmatrix} \quad (5.24a)$$

$$\mathcal{A}^{\epsilon_{\parallel}} = \begin{pmatrix} \frac{1}{\sqrt{2}}(H_1 - H_4) & -\frac{1}{\sqrt{2}}(H_2 + H_3) \\ -\frac{1}{\sqrt{2}}(H_2 + H_3) & \frac{1}{\sqrt{2}}(H_4 - H_1) \end{pmatrix}. \quad (5.24b)$$

From these expressions, the differential cross-section is given by

$$\sigma(\theta) = \frac{1}{2} \frac{q}{k} \text{Tr}(\mathcal{A}^\dagger \mathcal{A}) = \frac{1}{2} \frac{q}{k} \sum_{i=1}^4 |H_i|^2, \quad (5.25)$$

where the trace is over both the initial and final baryon spins. This expression is true for either $\lambda_\gamma = \pm 1$ (essentially from parity considerations) and is thus also the average unpolarized cross-section. Next, we look at the recoil polarization P_y , which is polarization in the direction $\frac{\hat{k} \times \hat{q}}{|\hat{k} \times \hat{q}|}$, or $-\frac{\hat{k} \times -\hat{q}}{|\hat{k} \times \hat{q}|}$, with \hat{k} being the beam direction and $-\hat{q}$, the outgoing baryon direction. From parity, the $\lambda_\gamma = \pm 1$ cases give the same result, so let us look at the $\lambda_\gamma = +1$ case only. Then,

$$P_y(\theta) = \frac{1}{2} \frac{1}{\sigma(\theta)} \frac{q}{k} \text{Tr}_i(\mathcal{A}^\dagger (-\sigma_y)^b \mathcal{A}) = \frac{1}{\sigma(\theta)} \frac{q}{k} \text{Im}(H_2^* H_4 + H_1^* H_3), \quad (5.26)$$

where the trace is in the initial proton spin space and the superscript in σ_y^b denotes the final baryon spin space. Since we will need such partial trace computations later, let us carry out this last computation in some detail.

If we suppress the photon and initial baryon spin indices, we can write the transition amplitude as $\mathcal{A} = \begin{pmatrix} \mathcal{A}_+ \\ \mathcal{A}_- \end{pmatrix}$ where the subscripts are in the outgoing baryon spin space. A simple computation then gives $\mathcal{A}^\dagger (-\sigma_y)^b \mathcal{A} = 2 \text{Im}(\mathcal{A}_-^* \mathcal{A}_+)$. The trace then simply means that we do an incoherent sum over all the initial baryon states $\sum_{i=+-} 2 \text{Im}(\mathcal{A}_{i-}^* \mathcal{A}_{i+})$, which yields the final result.

The cross-sections for linearly polarized photons are given by

$$\sigma_{\perp}(\theta) = \frac{1}{2} \frac{q}{k} \text{Tr}(\mathcal{A}^{\perp\dagger} \mathcal{A}^{\perp}) = \frac{1}{2} \frac{q}{k} (|H_1 + H_4|^2 + |H_2 - H_3|^2), \text{ and} \quad (5.27a)$$

$$\sigma_{\parallel}(\theta) = \frac{1}{2} \frac{q}{k} \text{Tr}(\mathcal{A}^{\parallel\dagger} \mathcal{A}^{\parallel}) = \frac{1}{2} \frac{q}{k} (|H_1 - H_4|^2 + |H_2 + H_3|^2), \quad (5.27b)$$

so that the beam asymmetry is

$$\Sigma(\theta) = \frac{\sigma_{\perp} - \sigma_{\parallel}}{\sigma_{\perp} + \sigma_{\parallel}} = \frac{q}{k} \frac{1}{\sigma(\theta)} \text{Re}(H_1 H_4^* - H_2 H_3^*). \quad (5.28)$$

Polarization	P_x^S	P_y^S	P_z^S
(c) Circular helicity +1 (r)	0	0	+1
(c) Circular helicity -1 (l)	0	0	-1
(\perp) Linear ($\phi_\gamma = \pi/2$)	+1	0	0
(\parallel) Linear ($\phi_\gamma = 0$)	-1	0	0
(t) Linear ($\phi_\gamma = -\pi/4$)	0	+1	0
(t) Linear ($\phi_\gamma = \pi/4$)	0	-1	0

Table 5.2: Stokes' vector \vec{P}^S for different photon polarization configurations. The right- (r) and left-handed (l) circular polarizations are our basis states. The different configurations for the linearly polarized states can be expressed in terms of these basis states. ϕ_γ is the angle the linear polarization direction makes with the x -axis, where the scattering plane is $\hat{x} - \hat{z}$.

The expression for the target assymmetry, which is the difference in the cross-sections between the target polarized along $+\hat{y}$ and $-\hat{y}$ is given by

$$T(\theta) = \frac{1}{2} \frac{1}{\sigma(\theta)} \frac{q}{k} \text{Tr}_b(\mathcal{A}^\dagger (-\sigma_y)^i \mathcal{A}) = \frac{1}{\sigma(\theta)} \frac{q}{k} \text{Im}(H_1 H_2^* + H_3 H_4^*), \quad (5.29)$$

where we have simply swapped the outgoing baryon helicity from Equation ?? with the initial target helicity. The extra minus sign before σ_y^i arises again, because the \hat{y} direction is given by $-\frac{(-\hat{k} \times \hat{q})}{|\hat{k} \times \hat{q}|}$ where $-\hat{k}$ is the target momentum direction in the CM frame.

5.5.3 Polarization and Strong Phases

Levy *et al* [48] casts the recoil and target polarization expressions in a particularly illustrative manner. The starting point is to write the helicity amplitudes as spin-flip (F) and non spin-flip (N) amplitudes:

$$h_\pm^N = \frac{1}{\sqrt{2}}(H_4 \pm H_1) \quad (5.30a)$$

$$h_\pm^F = \frac{1}{\sqrt{2}}(H_3 \mp H_2), \quad (5.30b)$$

where the subscripts \pm stand for linearly polarized photons perpendicular (+) and parallel (-) to the scattering plane. The expressions for P_y and T then become

$$P_y \sim \text{Im}(h_+^N h_+^{F*} - h_-^N h_-^{F*}), \text{ and} \quad (5.31a)$$

$$T \sim \text{Im}(h_+^N h_+^{F*} + h_-^N h_-^{F*}). \quad (5.31b)$$

This means that whatever dynamics is producing these polarizations need to have two components – one, that flips the baryon spins, and another that does not. In the final hadronization process, each of these two component will acquire strong phases and it is the relative strong phase which will give rise to the polarization. Notably, if there is only one mechanism for the reaction, there will be no relative strong phase and no polarization can be produced.

5.5.4 The 16 Observables

Since the beam (\mathcal{B}), the target (\mathcal{T}) and the recoiling (\mathcal{R}) baryon, can each be in two polarization states, besides the unpolarized differential cross-section (σ) and the three single polarization (P_γ, Σ

and T), one can define 12 other double polarization observables. These are correlations of the form $\mathcal{B}\mathcal{T}$, $\mathcal{B}\mathcal{R}$ and $\mathcal{R}\mathcal{T}$. All these 16 observables are expressible in terms of the fundamental CGLN or the helicity amplitudes [44, 49], and thus, only 8 of them are really independent variables. However, to fully determine the photomeson amplitude, one needs to measure the unpolarized cross-section, the three single-polarizations and four double-polarizations, provided all four are not from the same group. This is what constitutes a “complete set of measurements” [43].

Under actual experimental conditions, one deals with *ensembles* of \mathcal{B} , \mathcal{T} and \mathcal{R} . The correct description of these ensembles is the density matrix approach. For the two baryons, the density matrices are given by [49]

$$\rho_{i/b} = \frac{1}{2}(1 + \vec{P}_{i/b} \cdot \vec{\sigma}), \quad (5.32)$$

where $\vec{P}_{i/b}$ is the experimentally measurable *degree of polarization* for the initial target (i) and outgoing baryon (b), the quantization axis is the beam direction $+\hat{z}$. The photon case is slightly complicated by the fact that even though a real photon has two helicity states and should thus be describable in a 2-state Pauli basis, the actual polarizations are ± 1 instead of $\pm \frac{1}{2}$. The correct expression for the photon density matrix is

$$\rho_\gamma = \frac{1}{2}(1 + \vec{P}^S \cdot \vec{\sigma}) \quad (5.33a)$$

$$= \frac{1}{2} \begin{pmatrix} 1 + P_c & -P_t e^{-2i\phi_\gamma} \\ P_t e^{2i\phi_\gamma} & 1 - P_c \end{pmatrix}. \quad (5.33b)$$

where \vec{P}^S is the “Stokes’ vector”, $P_{c/t}$ are the measurable polarizations for circular and linear/transverse polarizations, and ϕ_γ is the azimuthal angle of the polarization vector. Table 5.2 (taken from Reference. [44]) lists the Stokes’ vectors for the various configurations. The definitions of the 16 observables are listed in References [44, 50].

5.5.5 The PWA expressions

We will use our PWA amplitudes $\mathcal{A}_{m_\gamma, m_i, m_b}$ with all spins quantized along the beam direction (\hat{z}) to write out all polarization observables. We will adapt the results appearing in Reference [44], Appendix A. The crucial point to keep in mind in these expressions is what space are the Pauli matrices residing in and what spins are the various traces taken over.

Single Polarization

I. Recoil Polarization P_y

Here the trace is over m_γ and m_i while σ_y is in m_b space:

$$P_y = \frac{\text{Tr}_{\gamma,i}[\sigma_y^b \mathcal{A} \mathcal{A}^\dagger]}{\text{Tr}_{\gamma,i}[\mathcal{A} \mathcal{A}^\dagger]} = \frac{\sum_{m_i m_\gamma} (i \mathcal{A}_{m_\gamma m_i+} \mathcal{A}_{m_\gamma m_i-}^* - i \mathcal{A}_{m_\gamma m_i-} \mathcal{A}_{m_\gamma m_i+}^*)}{\sum_{m_i m_\gamma} (\mathcal{A}_{m_\gamma m_i+} \mathcal{A}_{m_\gamma m_i+}^* + \mathcal{A}_{m_\gamma m_i-} \mathcal{A}_{m_\gamma m_i-}^*)}. \quad (5.34)$$

II. Target Polarization T

The only change from P_y is a swap between m_i and m_b :

$$T = \frac{\text{Tr}_{\gamma,b}[\sigma_y^i \mathcal{A} \mathcal{A}^\dagger]}{\text{Tr}_{\gamma,b}[\mathcal{A} \mathcal{A}^\dagger]} = \frac{\sum_{m_b m_\gamma} (i \mathcal{A}_{m_\gamma+m_b} \mathcal{A}_{m_\gamma-m_b}^* - i \mathcal{A}_{m_\gamma-m_b} \mathcal{A}_{m_\gamma+m_b}^*)}{\sum_{m_b m_\gamma} (\mathcal{A}_{m_\gamma+m_b} \mathcal{A}_{m_\gamma+m_b}^* + \mathcal{A}_{m_\gamma-m_b} \mathcal{A}_{m_\gamma-m_b}^*)}. \quad (5.35)$$

III. Beam Polarization Σ

The important point here is that the Pauli matrix is σ_x . The trace is over the target and recoil baryon spins:

$$\Sigma = \frac{\text{Tr}_{i,b}[\sigma_x^\gamma \mathcal{A}\mathcal{A}^\dagger]}{\text{Tr}_{i,b}[\mathcal{A}\mathcal{A}^\dagger]} = \frac{\sum_{m_b m_i} (\mathcal{A}_{+m_i m_b} \mathcal{A}_{-m_i m_b}^* + \mathcal{A}_{-m_i m_b} \mathcal{A}_{+m_i m_b}^*)}{\sum_{m_b m_i} (\mathcal{A}_{+m_i m_b} \mathcal{A}_{+m_i m_b}^* + \mathcal{A}_{-m_i m_b} \mathcal{A}_{-m_i m_b}^*)}. \quad (5.36)$$

For the double polarization observables, there are two sets of axis conventions in the literature, the primed and the unprimed axes, which are related by

$$\sigma_{x'} = c\sigma_x - s\sigma_z, \quad (5.37a)$$

$$\sigma_{z'} = s\sigma_x + c\sigma_z, \quad (5.37b)$$

$$\sigma_{y'} = \sigma_y, \quad (5.37c)$$

where we denote $\sin \theta$ as s and $\cos \theta$ as c . Thus, to go from the primed to the un-primed axes, one simply has to put $c = 1$ and $s = 0$. Also, we can transform $\sigma_{x'}$ into $\sigma_{z'}$ by changing c into s and s into $-c$.

Beam Recoil

IV. Double Polarization $O_{x'}$

This is the polarization transfer between a linearly polarized beam and the recoiling baryon. The trace is thus just on the target spin:

$$O_{x'} = \frac{\text{Tr}_i[\sigma_y^\gamma \sigma_{x'}^b \mathcal{A}\mathcal{A}^\dagger]}{\text{Tr}_i[\mathcal{A}\mathcal{A}^\dagger]}. \quad (5.38)$$

To work this out, we will first form the relevant density matrix, suppressing the target spin indices for the moment. Thus:

$$\begin{aligned} \rho_{m_\gamma m_b} = \mathcal{A}\mathcal{A}^\dagger &= \begin{pmatrix} \mathcal{A}_{++} \\ \mathcal{A}_{+-} \\ \mathcal{A}_{-+} \\ \mathcal{A}_{--} \end{pmatrix} \left(\begin{array}{cccc} \mathcal{A}_{++}^* & \mathcal{A}_{+-}^* & \mathcal{A}_{-+}^* & \mathcal{A}_{--}^* \end{array} \right) \\ &= \begin{pmatrix} \mathcal{A}_{++}\mathcal{A}_{++}^* & \mathcal{A}_{++}\mathcal{A}_{+-}^* & \mathcal{A}_{++}\mathcal{A}_{-+}^* & \mathcal{A}_{++}\mathcal{A}_{--}^* \\ \mathcal{A}_{+-}\mathcal{A}_{++}^* & \mathcal{A}_{+-}\mathcal{A}_{+-}^* & \mathcal{A}_{+-}\mathcal{A}_{-+}^* & \mathcal{A}_{+-}\mathcal{A}_{--}^* \\ \mathcal{A}_{-+}\mathcal{A}_{++}^* & \mathcal{A}_{-+}\mathcal{A}_{+-}^* & \mathcal{A}_{-+}\mathcal{A}_{-+}^* & \mathcal{A}_{-+}\mathcal{A}_{--}^* \\ \mathcal{A}_{--}\mathcal{A}_{++}^* & \mathcal{A}_{--}\mathcal{A}_{+-}^* & \mathcal{A}_{--}\mathcal{A}_{-+}^* & \mathcal{A}_{--}\mathcal{A}_{--}^* \end{pmatrix}, \end{aligned} \quad (5.39)$$

where the subscripts always carry the beam spin-projection first. Next we expand the operator

$$\begin{aligned} \sigma_y^\gamma \otimes \sigma_{x'}^b &= \begin{pmatrix} 0 & -i\sigma_{x'} \\ i\sigma_{x'} & 0 \end{pmatrix} \\ &= i \begin{pmatrix} 0 & 0 & s & -c \\ 0 & 0 & -c & -s \\ -s & c & 0 & 0 \\ c & s & 0 & 0 \end{pmatrix}. \end{aligned} \quad (5.40)$$

Completing the computation, we get:

$$O_{x'}(c, s) = i \frac{\sum_{m_i} \left(-s\mathcal{A}_{+m_i}\mathcal{A}_{-m_i+}^* + c\mathcal{A}_{+m_i}\mathcal{A}_{-m_i-}^* + c\mathcal{A}_{+m_i}\mathcal{A}_{-m_i+}^* + s\mathcal{A}_{+m_i}\mathcal{A}_{-m_i-}^* + s\mathcal{A}_{-m_i}\mathcal{A}_{+m_i+}^* - c\mathcal{A}_{-m_i}\mathcal{A}_{+m_i-}^* - c\mathcal{A}_{-m_i}\mathcal{A}_{+m_i+}^* - s\mathcal{A}_{-m_i}\mathcal{A}_{+m_i-}^* \right)}{\sum_{m_i} (\mathcal{A}_{+m_i}\mathcal{A}_{+m_i+}^* + \mathcal{A}_{+m_i}\mathcal{A}_{-m_i-}^* + \mathcal{A}_{-m_i}\mathcal{A}_{+m_i+}^* + \mathcal{A}_{-m_i}\mathcal{A}_{-m_i-}^*)}. \quad (5.41)$$

V. Double Polarization O_x

Computationally, this simply amounts to:

$$O_x = O_{x'}(1, 0). \quad (5.42)$$

VI. Double Polarization $O_{z'}$

This is given by:

$$O_{z'}(c, s) = O_{x'}(s, -c). \quad (5.43)$$

VII. Double Polarization O_z

Again, this is:

$$O_z = O_{x'}(0, -1). \quad (5.44)$$

IV. Double Polarization $C_{x'}$

This is the polarization transfer between a circularly polarized beam and the recoiling baryon. The trace is again the target spin:

$$C_{x'} = \frac{\text{Tr}_i[\sigma_z^\gamma \sigma_{x'}^b \mathcal{A} \mathcal{A}^\dagger]}{\text{Tr}_i[\mathcal{A} \mathcal{A}^\dagger]}. \quad (5.45)$$

Expanding the operator

$$\begin{aligned} \sigma_z^\gamma \otimes \sigma_{x'}^b &= \begin{pmatrix} \sigma_{x'} & 0 \\ 0 & -\sigma_{x'} \end{pmatrix} \\ &= \begin{pmatrix} -s & c & 0 & 0 \\ c & s & 0 & 0 \\ 0 & 0 & s & -c \\ 0 & 0 & -c & -s \end{pmatrix}, \end{aligned} \quad (5.46)$$

we get:

$$C_{x'}(c, s) = \frac{\sum_{m_i} \left(-s\mathcal{A}_{+m_i}\mathcal{A}_{+m_i+}^* + c\mathcal{A}_{+m_i}\mathcal{A}_{-m_i+}^* + c\mathcal{A}_{+m_i}\mathcal{A}_{+m_i-}^* + s\mathcal{A}_{+m_i}\mathcal{A}_{-m_i-}^* + s\mathcal{A}_{-m_i}\mathcal{A}_{+m_i+}^* - c\mathcal{A}_{-m_i}\mathcal{A}_{-m_i+}^* - c\mathcal{A}_{-m_i}\mathcal{A}_{-m_i-}^* - s\mathcal{A}_{-m_i}\mathcal{A}_{-m_i-}^* \right)}{\sum_{m_i} (\mathcal{A}_{+m_i}\mathcal{A}_{+m_i+}^* + \mathcal{A}_{+m_i}\mathcal{A}_{-m_i-}^* + \mathcal{A}_{-m_i}\mathcal{A}_{+m_i+}^* + \mathcal{A}_{-m_i}\mathcal{A}_{-m_i-}^*)}. \quad (5.47)$$

V. Double Polarization C_x

As before,

$$C_x = C_{x'}(1, 0). \quad (5.48)$$

VI. Double Polarization $C_{z'}$

Also,

$$C_{z'}(c, s) = C_{x'}(s, -c). \quad (5.49)$$

VII. Double Polarization C_z

And finally,

$$C_z = C_{x'}(0, -1). \quad (5.50)$$

Beam Target

For the $\mathcal{B}\mathcal{T}$ density matrix, we can still use Equation 5.39 if we swap m_b with m_i . The trace is over the recoiling baryon now.

VII. Double Polarization E

$$E = \frac{\text{Tr}_b[\sigma_z^\gamma \sigma_z^i \mathcal{A} \mathcal{A}^\dagger]}{\text{Tr}_b[\mathcal{A} \mathcal{A}^\dagger]}. \quad (5.51)$$

Since

$$\sigma_z^\gamma \otimes \sigma_z^i = \begin{pmatrix} \sigma_z & 0 \\ 0 & -\sigma_z \end{pmatrix} = \begin{pmatrix} 1 & 0 & 0 & 0 \\ 0 & -1 & 0 & 0 \\ 0 & 0 & -1 & 0 \\ 0 & 0 & 0 & 1 \end{pmatrix}, \quad (5.52)$$

$$E = \frac{\sum_{m_b} (\mathcal{A}_{++m_b} \mathcal{A}_{++m_b}^* - \mathcal{A}_{+-m_b} \mathcal{A}_{+-m_b}^* - \mathcal{A}_{-+m_b} \mathcal{A}_{-+m_b}^* + \mathcal{A}_{--m_b} \mathcal{A}_{--m_b}^*)}{\sum_{m_b} (\mathcal{A}_{++m_b} \mathcal{A}_{++m_b}^* + \mathcal{A}_{+-m_b} \mathcal{A}_{+-m_b}^* + \mathcal{A}_{-+m_b} \mathcal{A}_{-+m_b}^* + \mathcal{A}_{--m_b} \mathcal{A}_{--m_b}^*)}. \quad (5.53)$$

VII. Double Polarization F

$$E = \frac{\text{Tr}_b[\sigma_z^\gamma \sigma_x^i \mathcal{A} \mathcal{A}^\dagger]}{\text{Tr}_b[\mathcal{A} \mathcal{A}^\dagger]}. \quad (5.54)$$

$$\sigma_z^\gamma \otimes \sigma_x^i = \begin{pmatrix} \sigma_x & 0 \\ 0 & -\sigma_x \end{pmatrix} = \begin{pmatrix} 0 & 1 & 0 & 0 \\ 1 & 0 & 0 & 0 \\ 0 & 0 & 0 & -1 \\ 0 & 0 & -1 & 0 \end{pmatrix}, \quad (5.55)$$

$$F = \frac{\sum_{m_b} (\mathcal{A}_{++m_b} \mathcal{A}_{+-m_b}^* + \mathcal{A}_{+-m_b} \mathcal{A}_{++m_b}^* - \mathcal{A}_{-+m_b} \mathcal{A}_{--m_b}^* - \mathcal{A}_{--m_b} \mathcal{A}_{-+m_b}^*)}{\sum_{m_b} (\mathcal{A}_{++m_b} \mathcal{A}_{++m_b}^* + \mathcal{A}_{+-m_b} \mathcal{A}_{+-m_b}^* + \mathcal{A}_{-+m_b} \mathcal{A}_{-+m_b}^* + \mathcal{A}_{--m_b} \mathcal{A}_{--m_b}^*)}. \quad (5.56)$$

VII. Double Polarization G

$$G = \frac{\text{Tr}_b[\sigma_y^\gamma \sigma_z^i \mathcal{A} \mathcal{A}^\dagger]}{\text{Tr}_b[\mathcal{A} \mathcal{A}^\dagger]}. \quad (5.57)$$

$$\sigma_y^\gamma \otimes \sigma_z^i = \begin{pmatrix} 0 & -i\sigma_z \\ i\sigma_z & 0 \end{pmatrix} = \begin{pmatrix} 0 & 0 & -i & 0 \\ 0 & 0 & 0 & i \\ i & 0 & 0 & 0 \\ 0 & -i & 0 & 0 \end{pmatrix}, \quad (5.58)$$

$$G = i \frac{\sum_{m_b} (\mathcal{A}_{++m_b} \mathcal{A}_{+-m_b}^* + \mathcal{A}_{+-m_b} \mathcal{A}_{++m_b}^* - \mathcal{A}_{-+m_b} \mathcal{A}_{--m_b}^* - \mathcal{A}_{--m_b} \mathcal{A}_{-+m_b}^*)}{\sum_{m_b} (\mathcal{A}_{++m_b} \mathcal{A}_{++m_b}^* + \mathcal{A}_{+-m_b} \mathcal{A}_{+-m_b}^* + \mathcal{A}_{-+m_b} \mathcal{A}_{-+m_b}^* + \mathcal{A}_{--m_b} \mathcal{A}_{--m_b}^*)}. \quad (5.59)$$

VIII. Double Polarization H

$$H = \frac{\text{Tr}_b[\sigma_y^\gamma \sigma_x^i \mathcal{A} \mathcal{A}^\dagger]}{\text{Tr}_b[\mathcal{A} \mathcal{A}^\dagger]}. \quad (5.60)$$

$$\sigma_y^\gamma \otimes \sigma_x^i = \begin{pmatrix} 0 & -i\sigma_x \\ i\sigma_x & 0 \end{pmatrix} = i \begin{pmatrix} 0 & 0 & 0 & -1 \\ 0 & 0 & -1 & 0 \\ 0 & 1 & 0 & 0 \\ 1 & 0 & 0 & 0 \end{pmatrix}, \quad (5.61)$$

$$H = i \frac{\sum_{m_b} (-\mathcal{A}_{++m_b} \mathcal{A}_{--m_b}^* - \mathcal{A}_{+-m_b} \mathcal{A}_{-+m_b}^* + \mathcal{A}_{-+m_b} \mathcal{A}_{+-m_b}^* + \mathcal{A}_{--m_b} \mathcal{A}_{++m_b}^*)}{\sum_{m_b} (\mathcal{A}_{++m_b} \mathcal{A}_{++m_b}^* + \mathcal{A}_{+-m_b} \mathcal{A}_{-+m_b}^* + \mathcal{A}_{-+m_b} \mathcal{A}_{-+m_b}^* + \mathcal{A}_{--m_b} \mathcal{A}_{--m_b}^*)}. \quad (5.62)$$

Target Recoil

The \mathcal{TR} density matrix, can similarly be got from Equation 5.39 by swapping m_γ with m_i . The trace is over the beam polarizations now.

IX. Double Polarization $T_{x'}$

$$T_{x'} = \frac{\text{Tr}_b[\sigma_x^i \sigma_{x'}^b \mathcal{A} \mathcal{A}^\dagger]}{\text{Tr}_b[\mathcal{A} \mathcal{A}^\dagger]}, \quad (5.63)$$

where

$$\sigma_x^i \otimes \sigma_{x'}^b = \begin{pmatrix} 0 & \sigma_{x'}^b \\ \sigma_{x'}^b & 0 \end{pmatrix} = \begin{pmatrix} 0 & 0 & -s & c \\ 0 & 0 & c & s \\ -s & c & 0 & 0 \\ c & s & 0 & 0 \end{pmatrix}, \quad (5.64)$$

so that,

$$T_{x'}(c, s) = \frac{\sum_{m_\gamma} \left(-s\mathcal{A}_{m_\gamma++} \mathcal{A}_{m_\gamma-+}^* + c\mathcal{A}_{m_\gamma++} \mathcal{A}_{m_\gamma--}^* + c\mathcal{A}_{m_\gamma+-} \mathcal{A}_{m_\gamma-+}^* + s\mathcal{A}_{m_\gamma+-} \mathcal{A}_{m_\gamma--}^* \right)}{\sum_{m_\gamma} (\mathcal{A}_{m_\gamma++} \mathcal{A}_{m_\gamma++}^* + \mathcal{A}_{m_\gamma+-} \mathcal{A}_{m_\gamma-+}^* + \mathcal{A}_{m_\gamma-+} \mathcal{A}_{m_\gamma-+}^* + \mathcal{A}_{m_\gamma--} \mathcal{A}_{m_\gamma--}^*)}. \quad (5.65)$$

X. Double Polarization $T_{z'}$

As usual,

$$T_{z'}(c, s) = T_{x'}(s, -c). \quad (5.66)$$

XI. Double Polarization $L_{x'}$

$$L_{x'} = \frac{\text{Tr}_b[\sigma_z \sigma_{x'}^b \mathcal{A} \mathcal{A}^\dagger]}{\text{Tr}_b[\mathcal{A} \mathcal{A}^\dagger]}, \quad (5.67)$$

which is exactly the same as $C_{x'}$ if we swap m_γ and m_i

$$L_{x'}(c, s) = \frac{\sum_{m_\gamma} \left(-s\mathcal{A}_{m_\gamma++} \mathcal{A}_{m_\gamma++}^* + c\mathcal{A}_{m_\gamma+-} \mathcal{A}_{m_\gamma-+}^* + c\mathcal{A}_{m_\gamma-+} \mathcal{A}_{m_\gamma-+}^* + s\mathcal{A}_{m_\gamma+-} \mathcal{A}_{m_\gamma+-}^* \right.}{\sum_{m_\gamma} (\mathcal{A}_{m_\gamma++} \mathcal{A}_{m_\gamma++}^* + \mathcal{A}_{m_\gamma+-} \mathcal{A}_{m_\gamma-+}^* + \mathcal{A}_{m_\gamma-+} \mathcal{A}_{m_\gamma-+}^* + \mathcal{A}_{m_\gamma--} \mathcal{A}_{m_\gamma--}^*)} \left. + s\mathcal{A}_{m_\gamma-+} \mathcal{A}_{m_\gamma-+}^* - c\mathcal{A}_{m_\gamma--} \mathcal{A}_{m_\gamma--}^* - c\mathcal{A}_{m_\gamma+-} \mathcal{A}_{m_\gamma-+}^* - s\mathcal{A}_{m_\gamma--} \mathcal{A}_{m_\gamma--}^* \right). \quad (5.68)$$

XII. Double Polarization $L_{z'}$

Finally,

$$L_{z'}(c, s) = L_{x'}(s, -c). \quad (5.69)$$

5.6 Preliminary Measurement Results and Discussion

We have then at our disposal two equivalent ways of extracting the polarizations – the “traditional” way using Equation 5.15 and then the PWA method (Equation 5.34). However, before embarking on that, we need to reconsider our binning first to ensure that we have enough statistics for every polarization extraction point. Recall that earlier we binned the data very finely in 10 MeV \sqrt{s} bins. The final distribution of “good” (Q -value weighted) data events after this binning is shown in Figure 1.24a for the three-track dataset.

This is however not the complete story, because we are dealing with an essentially two dimensional problem here (in \sqrt{s} and $\cos\theta_{CM}^{K^+}$). In the higher \sqrt{s} bins, most of the events are very forward peaked, and thus, asymmetrically distributed in $\cos\theta_{CM}^{K^+}$ as apparent from Figure 5.3a.

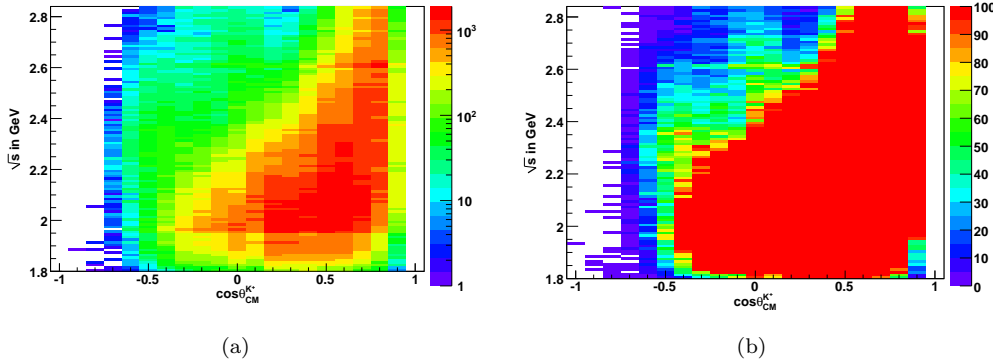


Figure 5.3: Q -value (from background subtraction fits) weighted data occupancies in both \sqrt{s} and $\cos\theta_{CM}^{K^+}$ for the three-track dataset: (a) log scale (b) normal scale with a cap at 100 events. Binning in both axes was set according to how we binned our data in \sqrt{s} and where we extracted differential cross sections in $\cos\theta_{CM}^{K^+}$. See text for details.

The y -axis bins in this plot are 10 MeV wide in \sqrt{s} with bin centers at 1.805 GeV, 1.815 GeV, ..., 2.835 GeV and the x -axis bins are 0.1 wide in $\cos\theta_{CM}^{K^+}$ with bin centers at -1.0, -0.9, ..., 1.0. That is, the binning is set according to where we measured our differential cross sections. If we now look at the same histogram but place an upper cap on the occupancy at 100 events (Figure 5.3b), we see that a lot of these bins have much fewer than 50 “good” events. If we tried to extract the polarizations in these regions with our present binning, we would be severely limited by statistics. We thus need to find a plausible way to merge our bins. To do this, we preserve the same 0.1 binning in $\cos\theta_{CM}^{K^+}$ but use wider bins in \sqrt{s} . Also, guided by Figure 5.3a, we will limit our $\cos\theta_{CM}^{K^+}$ bin center range from -0.5 to 0.9 for our polarization extractions.

Figure 5.4 shows the extracted polarizations with our initial 10 MeV wide \sqrt{s} binning. The errors (estimated from the scatter between adjacent \sqrt{s} bins) seem large, but the gross structures are clearly evident. It is to be noted here that we are limited not only by statistics but also by the

fact in the Σ^0 decay, with spin-1/2 going to spin-1/2 plus spin-1, we are not observing the spin-1 particle (the “missing” outgoing photon). Thus, the polarization information in Equation 5.15 is “diluted”. For example, for $\cos \theta_{CM}^{K^+} = 0.8$ in Figure 5.4, where we have excellent statistics for most \sqrt{s} , the polarizations are not as smooth as might have been expected.

5.7 Re-binned Polarizations

To choose an optimal binning such that we have reasonable statistics while retaining as fine a \sqrt{s} binning as possible, we tried setting a minimum \sqrt{s} bin-width of 20 and then 30 MeV, and required a minimum number of “good” events to be present per bin. The latter was gradually varied from 50, 75, …, to 500 events per bin. We found that a 30 MeV minimum \sqrt{s} bin-width and a minimum requirement of 200 events per bin was optimal. Figure 5.5 shows the polarizations after merging bins according to this criterion. The scatter in the points are much less now and the overall structures evolve quite smoothly.

5.7.1 Statistical Error Estimation for the PWA method

Unfortunately, there is no *a priori* way of estimating the statistical errors in the PWA method of polarization extraction. Ideally, in an asymmetry measurement, one needs to know N_{\pm} *separately* to estimate the statistical errors. In our case, we are extracting the polarization information by *fitting to a distribution*, without directly measuring N_{\pm} . The error bars in Figures 5.4 and 5.5 have been estimated by looking at the scatter between adjacent \sqrt{s} points inside a given $\cos \theta_{CM}^{K^+}$ bin. This method was also used in previous $g11a$ PWA analyses like $p\omega$, $K^+\Lambda$, *et al* [3, 6] and gave reasonable results. The statistics in those channels were high enough to maintain a 10 MeV \sqrt{s} binning. The scatter estimate, although *ad hoc*, appeared reasonable because the physics should remain essentially the same between two \sqrt{s} points just 10 MeV apart. Thus the scatter in the recoil polarization measurements should mainly arise out of statistical fluctuations.

In our case, even though the \sqrt{s} binning is not as fine after our re-binning, as we show below, this *ad hoc* method gives a good error estimate. The final statistical errors we will quote are from a more direct estimation, as explained in Section 5.9.

5.8 “Traditional” Method Polarizations

Figure 5.6 shows the polarizations extracted using the “traditional” way of fitting the data to the intensity profile appearing in Equation 5.15 (plotted in blue) and compared to the PWA results (in red). The fits were run using the unbinned maximum likelihood method and the errors are the errors that Minuit provides. The agreement between the two methods is remarkable (especially in regions of good statistics). This underscores the fact that the underlying physics is the same.

Note that, *by definition*, the polarizations from the PWA method are bound between ± 1 , while the “traditional” method involves a fit to a slope and can jump beyond the physical limits, as evident from some of the bins in Figure 5.6. If we constrain the fit to remain within ± 1 , we found the results to always cap off at ± 1 if the unconstrained result was already beyond ± 1 . Thus, no new information is gained by constraining the fits in this fashion.

The “traditional” method seems to be somewhat overestimating the polarizations in the forward-most angular bin. The reason is two-fold. Firstly, the statistics is not as good here as the next lower couple of angular bins. Secondly, note that the polarizations are typically very high in this region. In the PWA method, for a particular \sqrt{s} bin, we fit over the entire $\cos \theta_{CM}^{K^+}$ range as a whole. Thus,

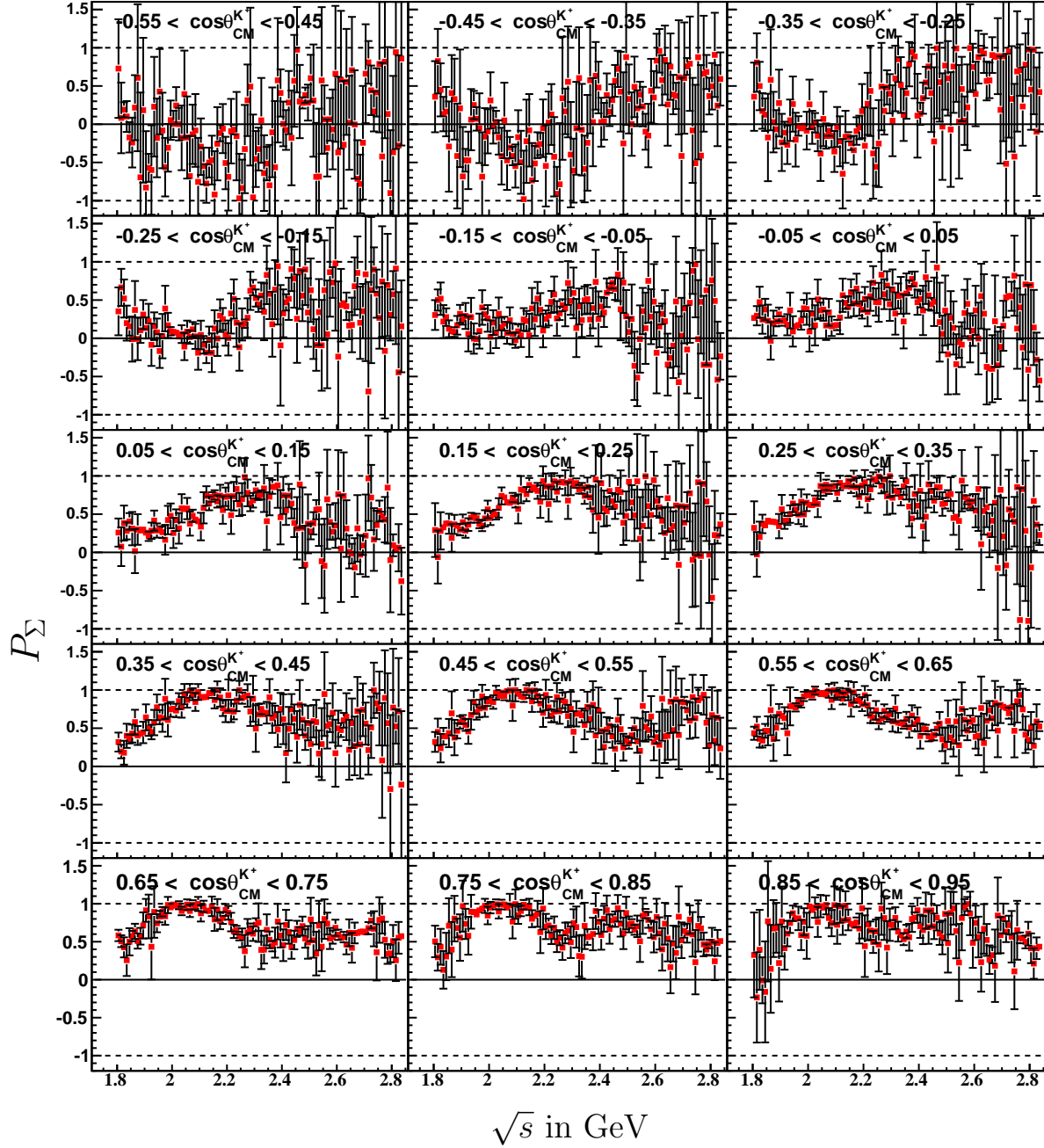


Figure 5.4: P_Σ from the PWA extraction method with 10 MeV wide \sqrt{s} binning. The error bars are derived from the scatter between adjacent \sqrt{s} bins. The large errors arise from the small statistics and mean that we need coarser binning in \sqrt{s} .

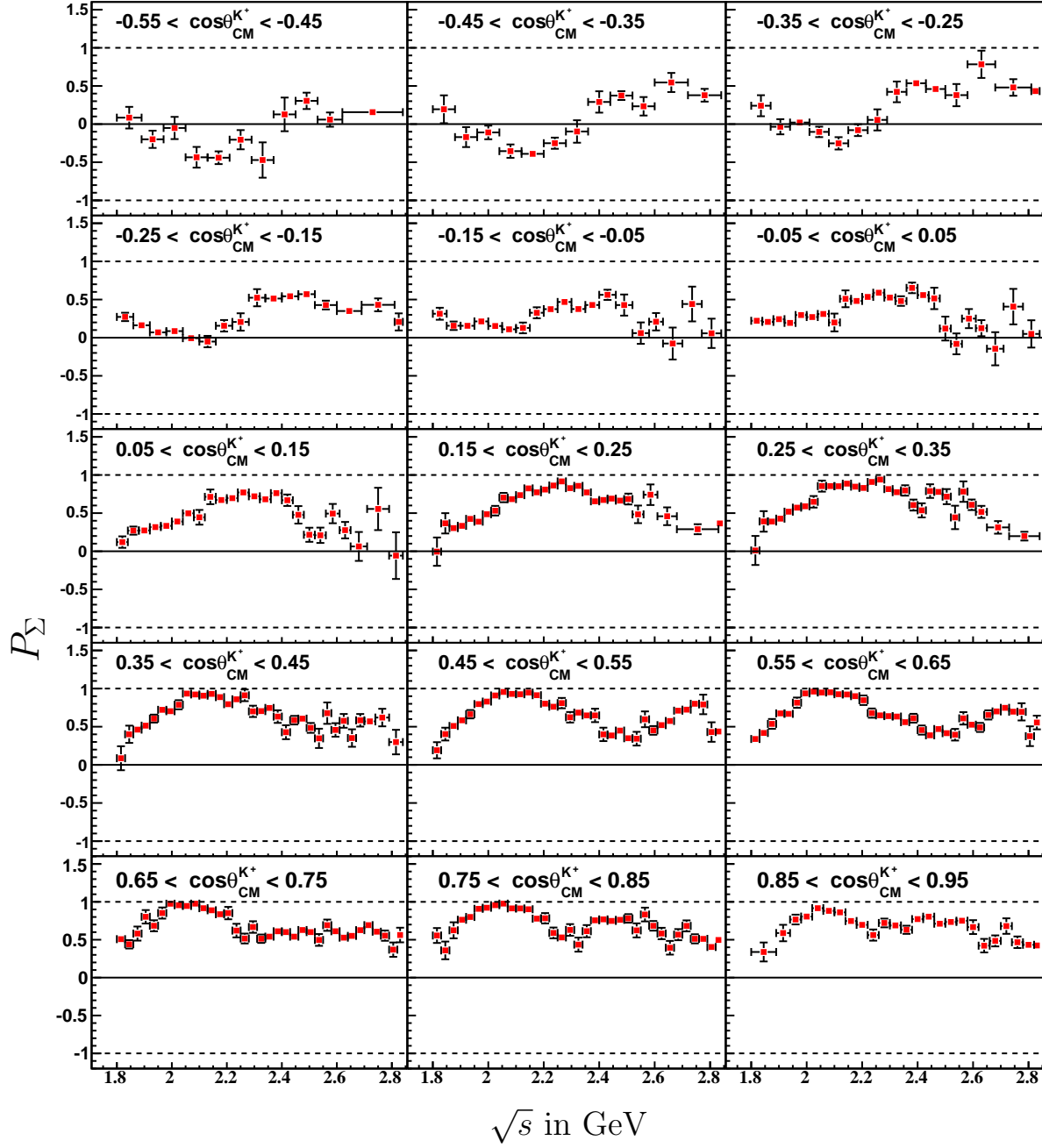


Figure 5.5: Re-binned P_Σ from the PWA extraction method. Every point is at least 30 MeV wide in \sqrt{s} and has a minimum of 200 events. Error estimates are from the scatter between adjacent \sqrt{s} bins.

the polarization results at a particular \sqrt{s} and $\cos\theta_{CM}^{K^+}$ is somewhat constrained by the PWA fit results in the neighbouring angular bins for the same \sqrt{s} . Since our angular binning is quite fine (0.1 in $\cos\theta_{CM}^{K^+}$), we expect the physics to be continuous between adjacent angular bins, which is exactly what the PWA method results show. For the traditional method, fits to the intensity profile are run independently in a particular \sqrt{s} and $\cos\theta_{CM}^{K^+}$ bin. Thus, these results are less constrained than the PWA results and for a high degree of polarization, tends to overestimate at the forward-most angles.

5.9 Final Polarization Results and Statistical Errors

5.9.1 Three-track results

It is clear from the previous sections that the two methods for polarization extraction agree very well with each other in regions of high statistics. The advantage of the PWA method lies in the polarizations being within the physical limits of ± 1 and also because of the reasons outlined in latter part of the last section. The disadvantage, however, is that there is no direct handle on the error estimates.

The polarizations from the “traditional” method, on the other hand, are less constrained, but here we have a direct access to the errors. Also, from Figure 5.6, these errors are quite comparable to the PWA errors obtained from the scatter in the measured polarizations. This shows that the errors from Minuit in the “traditional” method are a true reflection of the statistical uncertainties.

With these considerations in mind, we will present our final recoil polarization measurements for the three-track dataset in the following fashion – the *values* of the polarizations will be the ones from the PWA method, while the statistical *errors* will be the errors obtained from the “traditional” method. Our final P_Σ measurements and the final estimated errors are shown in Figure 5.13. A systematic account for differences between the two methods is given in Section 5.10.

5.9.2 Including Two-track results

We noted earlier that our P_Σ measurements from the intensity profile in Equation 5.15 are already diluted because the polarization of the outgoing photon is not being measured. Going from Equation 5.15 to Equation 5.16 represents a further step of dilution. To check this effect, for the three-track dataset, we measured P_Σ using the “approximate” expression (using Equation 5.16) and compared it to our previous measurements. The results are shown in Figure 5.7 – the effect of the dilution is clear. Quantitatively, we plot distribution of the ratio

$$r = \frac{\sigma_{approx}}{\sigma_{original}} \quad (5.70)$$

in Figure 5.8, where $\sigma_{original}$ (σ_{approx}) are the P_Σ errors from using Equation 5.15 (Equation 5.16). The peak at $r \approx 2.5$ indicates the degree of dilution introduced by averaging over the intermediate Λ directions.

Keeping in mind the above considerations, and the fact that the two-track dataset can use only the “approximate” expression for P_Σ extraction, we will quote results from the two-track analysis *only at those kinematic points where we do not have results from the three-track dataset* (recall that due to higher acceptance, the two-track dataset has a wider kinematic coverage than the three-track dataset). Though the two-track results have, in general, larger error bars than the three-track results, by including them, we are able to extend our \sqrt{s} coverage till the production threshold (~ 1.69 GeV) and our backward angle coverage all the way till $\cos\theta_{CM}^{K^+} = -0.85$.

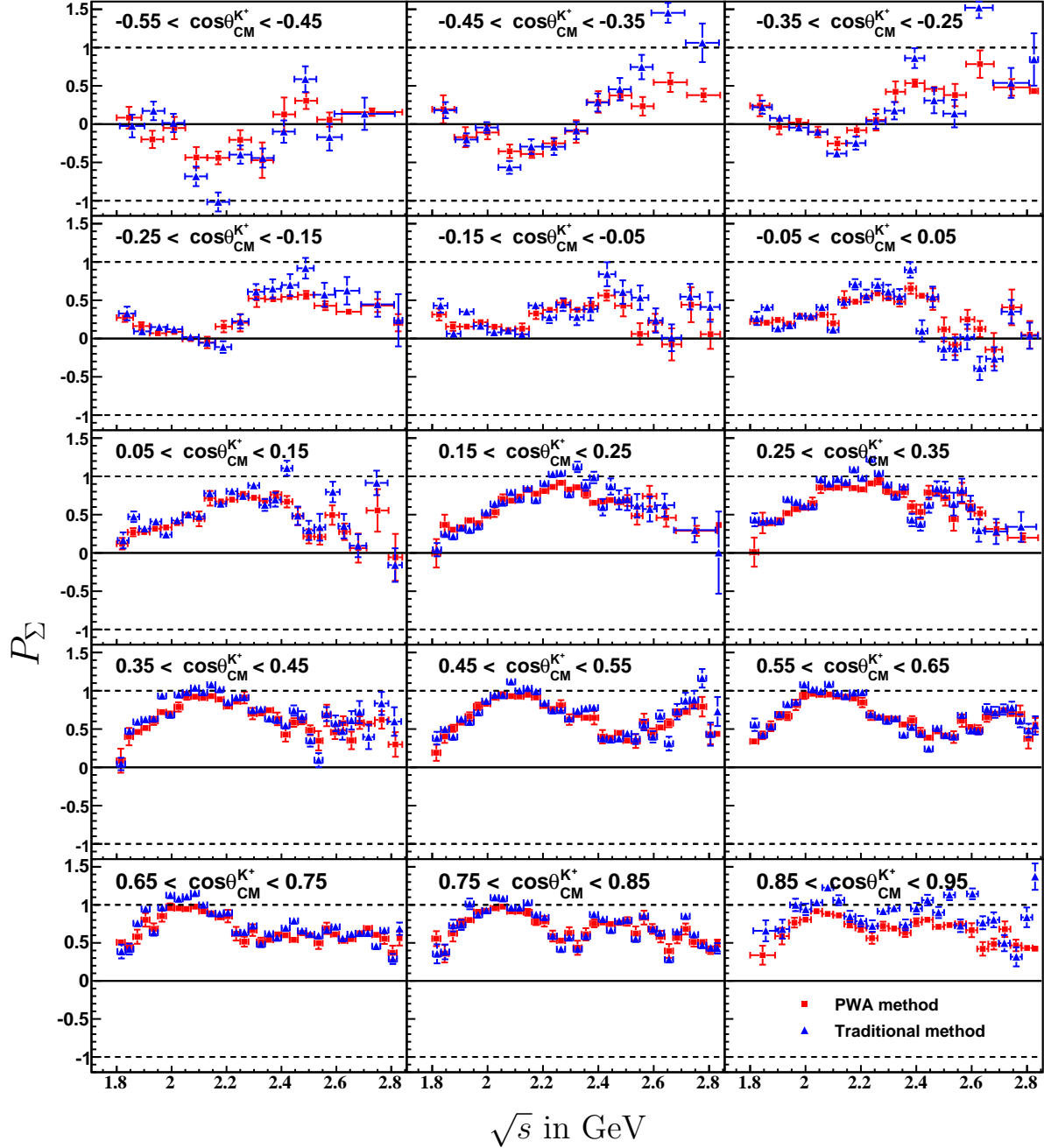


Figure 5.6: Compare P_Σ obtained from the PWA method (red squares) versus the “traditional” method (blue up-triangles). Within the statistical uncertainties, the agreement is excellent. The forward-most angle bin is both statistics limited and is highly polarized. The “traditional” method seems to be systematically overestimating the polarizations here. Errors for the PWA method are from the scatter between adjacent \sqrt{s} bins while for the “traditional” method, they are the Minuit errors.

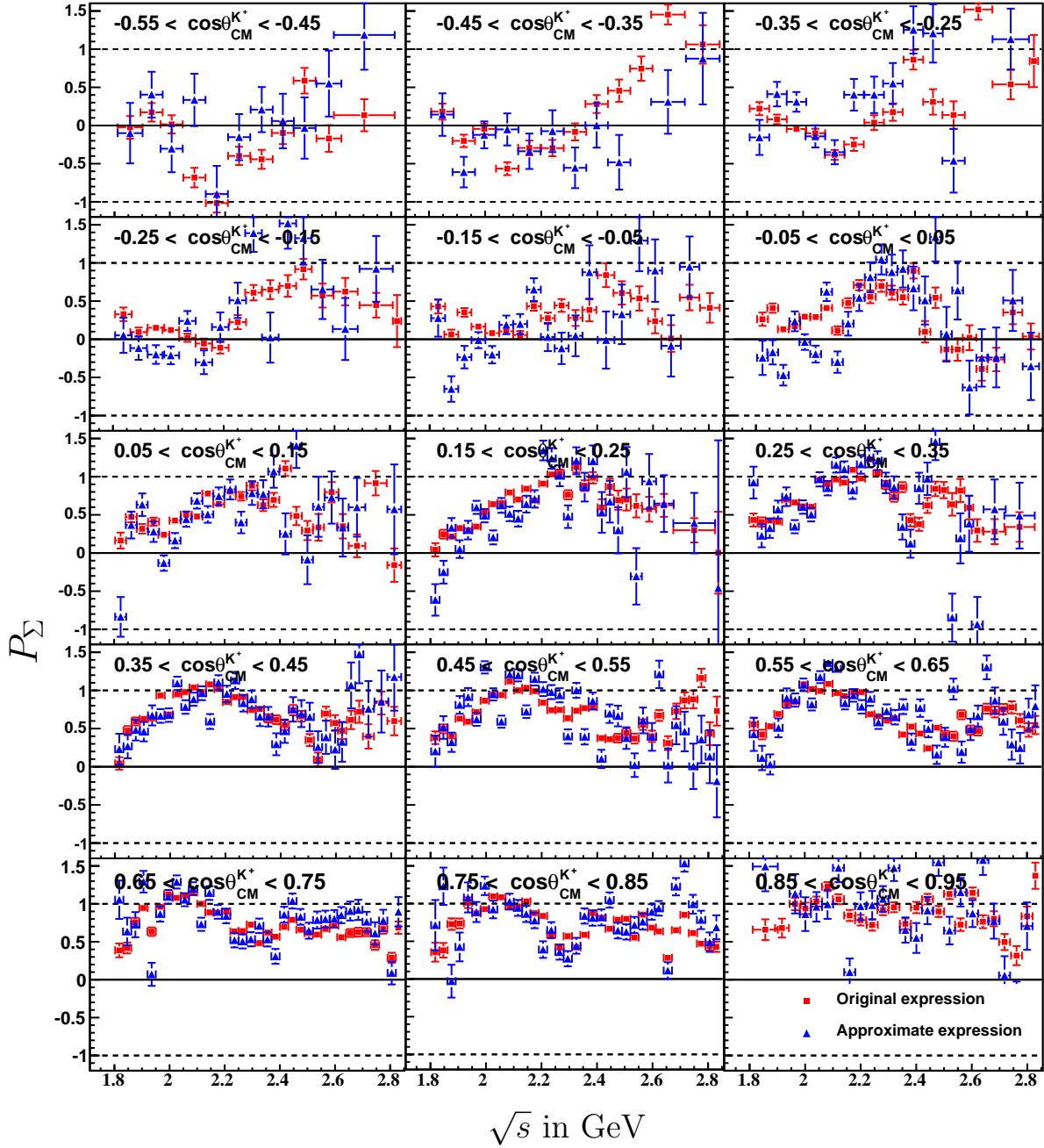


Figure 5.7: Compare P_Σ results for the three-track dataset: original expression using Equation 5.15 (red squares) versus the approximate expression using Equation 5.16 (blue up-triangles) for the three-track dataset. Both have the same binning in \sqrt{s} and $\cos\theta_{CM}^{K^+}$ and utilized unbinned maximum likelihood fits, but the latter is more scattered, reflecting the effect of the “dilution”.

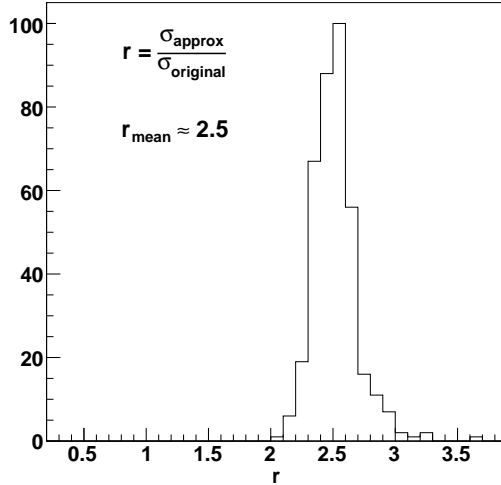


Figure 5.8: Distribution of the ratio between the errors in P_Σ measurements from the intensity profiles in Equations 5.15 and 5.16 (three-track dataset).

Our re-binning for the two-track dataset follows the method outlined in Section 5.7 for the three-track case. The only change is that instead of a minimum of 200 events, we now require at least 300 “good” events per kinematic point. While re-binning, we also ensure that the bin-edge around $\sqrt{s} \sim 1.8$ GeV is always *at* $\sqrt{s} = 1.8$ GeV for all values of $\cos \theta_{CM}^{K^+}$, so that there is no overlap with the three-track dataset (which extends from $\sqrt{s} \geq 1.8$ GeV onwards). The 2-track P_Σ results appeared to be unstable at the very backward angle bin, so we will not be presenting results for $\cos \theta_{CM}^{K^+} = -0.9$. Our final kinematic coverage for P_Σ extraction is as follows:

$$\begin{aligned} \text{Three-track} &: -0.55 \leq \cos \theta_{CM}^{K^+} \leq 0.95, \text{ AND, } 1.8 \text{ GeV} \leq \sqrt{s} \leq 2.84 \text{ GeV} \\ \text{Two-track} &: -0.85 \leq \cos \theta_{CM}^{K^+} < -0.55, \text{ OR, } 1.69 \text{ GeV} \leq \sqrt{s} < 1.8 \text{ GeV} \end{aligned}$$

In all, we present results at 472 independent kinematic points.

5.10 Systematic Error Estimation

The systematic errors for polarization measurements are of a different nature than those for the differential cross-sections. Since normalizations cancel out, the photon flux normalization does not contribute to the errors. We thus need only the systematic errors in our acceptance calculation. However, our acceptance calculation involved measuring the total yield N_{total} and not N_{\pm} (yields for opposite spin orientations of the Σ^0). Thus, there is no straight-forward (or rigorous) way to calculate the polarization systematic errors.

As a reasonable estimate, we chose to look at the difference between the polarization results obtained from the two methods of polarization extraction for the three-track results – the PWA method and the “traditional” method. Since the underlying physics is the same, within statistical fluctuations, both methods should yield the same results. Figure 5.11 shows the difference between the two measurements accumulated over the regions with reasonable statistics ($-0.05 \leq \cos \theta_{CM}^{K^+} \leq 0.85$). A Gaussian fit to the distribution gives a mean $\mu \sim -0.028$ and a width $\sigma \sim 0.1$. The

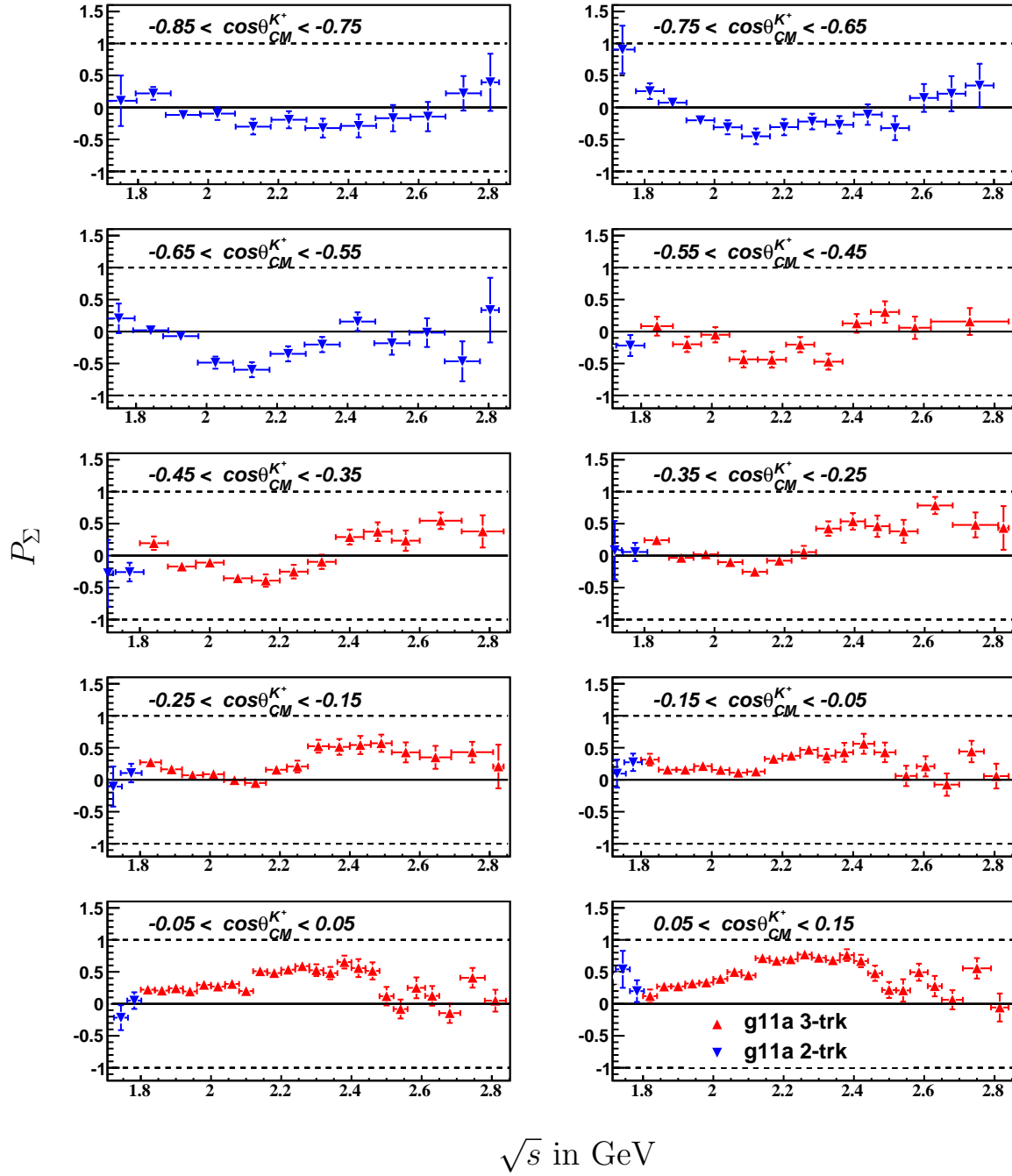


Figure 5.9: Final recoil polarization results from the CLAS $g11a$ dataset. Apart from the very backward angles and near-threshold regions, results are available from the 3-track dataset (in red). In the remaining kinematic regions, we present results from the 2-track topology (in blue), which involves an averaging over the Σ^0 - Λ spin transfer information.

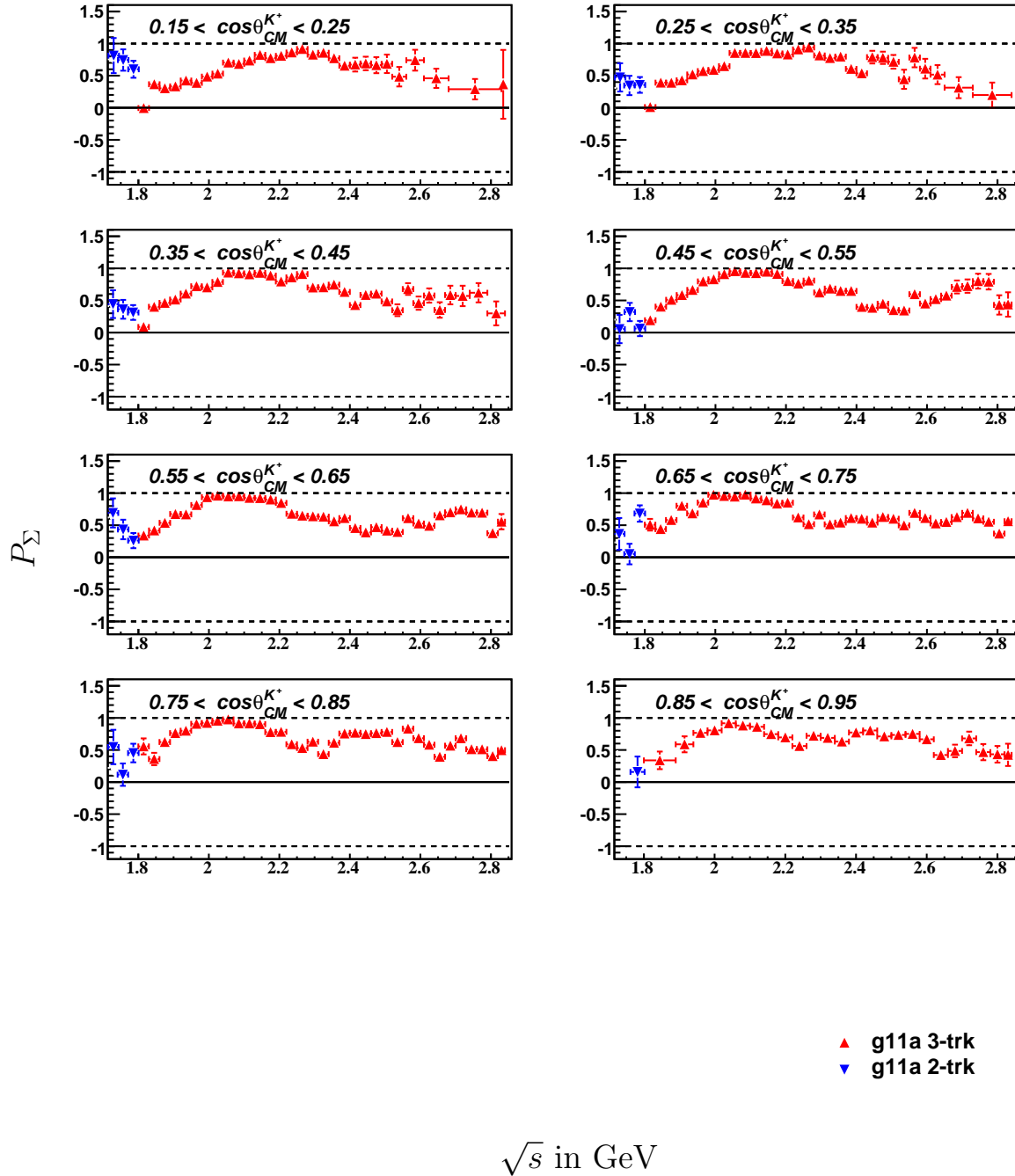


Figure 5.10: Final recoil polarization results from the CLAS g_{11a} dataset. Apart from the very backward angles and near-threshold regions, results are available from the 3-track dataset (in red). In the remaining kinematic regions, we present results from the 2-track topology (in blue), which involves an averaging over the Σ^0 - Λ spin transfer information.

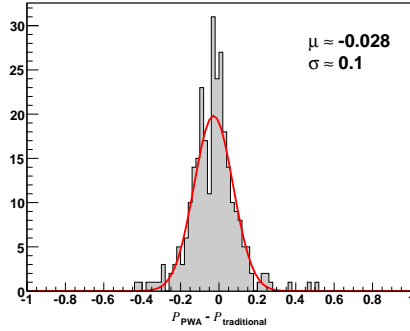


Figure 5.11: Systematic Error Calculation for P_Σ : difference in the extracted polarizations from two different but equivalent methods give an estimate of the systematic uncertainty in our P_Σ calculation.

width is due to statistical fluctuations, while the mean represents an overall *systematic* shift, and its absolute value will be quoted as our systematic error. As a check, we note that systematic errors in polarizations from previous CLAS analyses using the same dataset ($p\omega$ [3], $K^+\Lambda$ [6], *et al*) were in the same range. Since the systematic errors are ultimately dependent on the detector acceptance, 2.8% is reasonable estimate for the $K^+\Sigma^0$ channel as well. For the two-track results, to incorporate the dilution in averaging over the Λ directions, we include a $(1+r)$ multiplicative factor, where $r = 2.5$ from Figure 5.8.

5.11 Comparison With Previous Measurements

Previous world data on P_Σ is generally sparse. There are three other measurements – a Bonn measurement using the SAPHIR detector, published in 2004 (Glander *et al* [38]), an earlier CLAS analysis on the *g1* dataset in 2004 (McNabb *et al* [54]) and a more recent GRAAL analysis in 2007 (Lleres *et al* [56]).

SAPHIR published results at four $\cos \theta_{CM}^{K^+}$ (-0.75, -0.25, 0.25 and 0.75) points for each of three \sqrt{s} points – 1.847, 2.029 and 2.279 GeV. The CLAS *g1* results consisted of measurements at $\cos \theta_{CM}^{K^+} = -0.7, -0.5, \dots, 0.9$ with \sqrt{s} ranging from 1.79 to 2.29 GeV – a total of seventy data points. Finally, the GRAAL results were at two \sqrt{s} points – 1.762 and 1.85 GeV with two forward angle and two backward angle measurements at each \sqrt{s} ; a total of eight measurements. The present results cover 472 individual kinematic points, vastly increasing our overall knowledge of P_Σ , both in statistics and kinematic coverage.

Agreement between our results and previous world data is generally good. Even in the bins where the previous results seem to differ from ours, they either have large error bars or show a localized deviation from a smooth variation between angular bins. There are prominent structures present which the present results map out in much greater detail than before. In the $\cos \theta_{CM}^{K^+} = 0.7$ bin, the *g1* polarizations seem to get flatter than *g11a*. Note however, that *g11a* maintains its shape between the two neighbouring angular bins, while *g1* goes down and comes back up again. Our agreement with the latest GRAAL results is especially good. In the bin $\cos \theta_{CM}^{K^+} = -0.7$, there seemed to be considerable disparity between previous CLAS *g1* and SAPHIR results with both datasets having wide error bars. The new results smoothly varies between consecutive angular bins and seems to support the general trend of P_Σ tending towards negative values in the backward angle regions.

5.12 Summary

Recoil polarizations for $K^+\Sigma^0$ photoproduction in the CLAS *g11a* dataset were presented in this chapter. For the three-track dataset, two equivalent methods of polarization extraction along with their pros and cons were discussed. Our final results incorporate the best features of both methods. Systematic errors were extracted by looking at the difference between the two methods. For the two-track dataset, the polarization information is diluted because the Λ momentum is not accessible. We thus chose to present results from the two-track analysis only at kinematic points where the three-track dataset is limited by statistics. We also compared our results with previous world data and found good agreement. The present results however represent a many fold improvement in both statistics and kinematic coverage over previous world data and maps out in great detail, the structures only *hinted at* previously. The information gathered here will be of great use in our final PWA analysis as discussed in subsequent chapters.

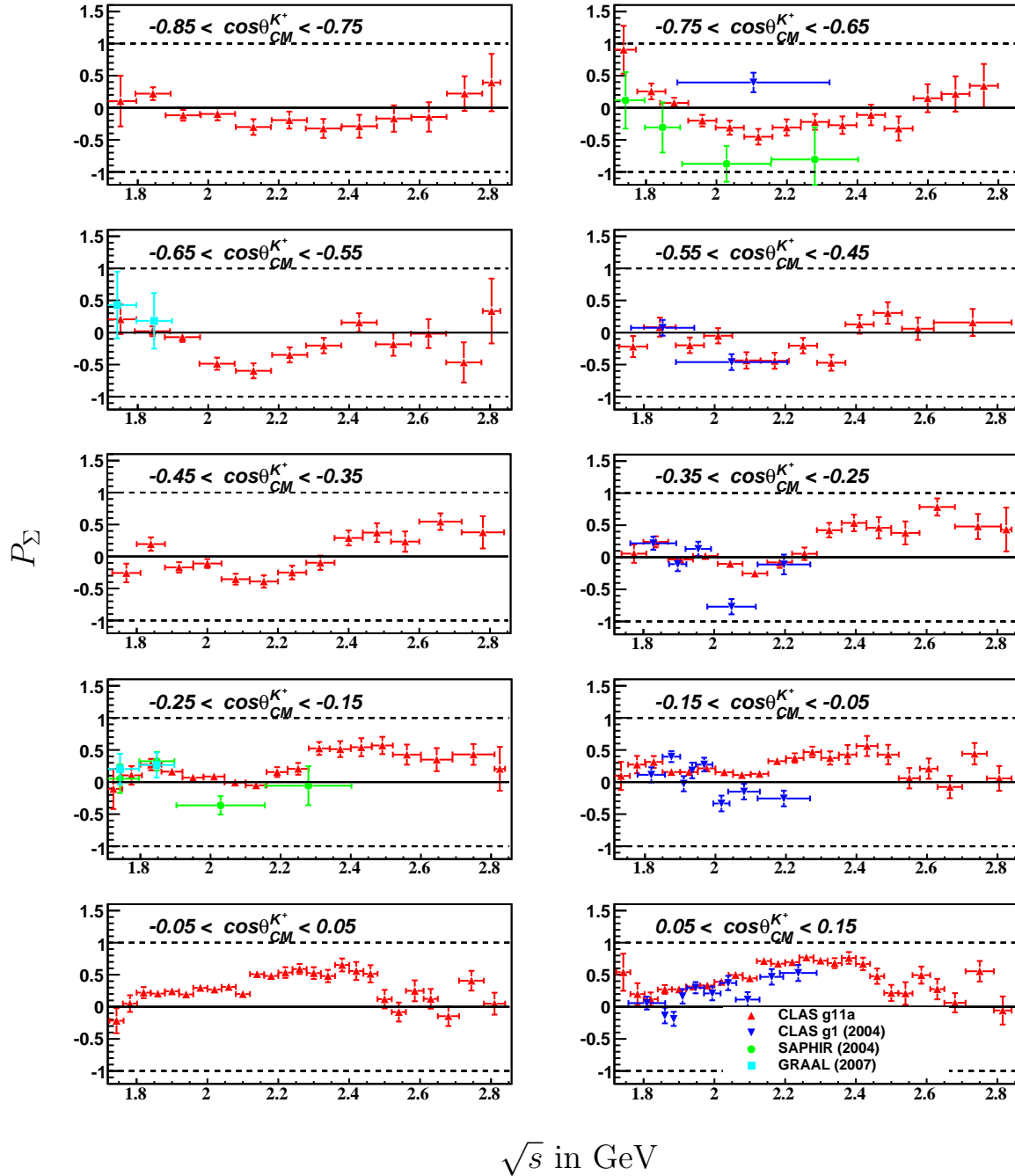


Figure 5.12: Compare P_Σ with previous world data in the backward angles: CLAS g_{11a} (this analysis, red squares), CLAS g_1 (McNabb [54], blue up-triangles), SAPHIR (Glander [38], green down-triangles) and GRAAL (Lleres [56], cyan circles). Within the statistical uncertainties, there is fair to good consistency with previous world data. All errors are statistical.

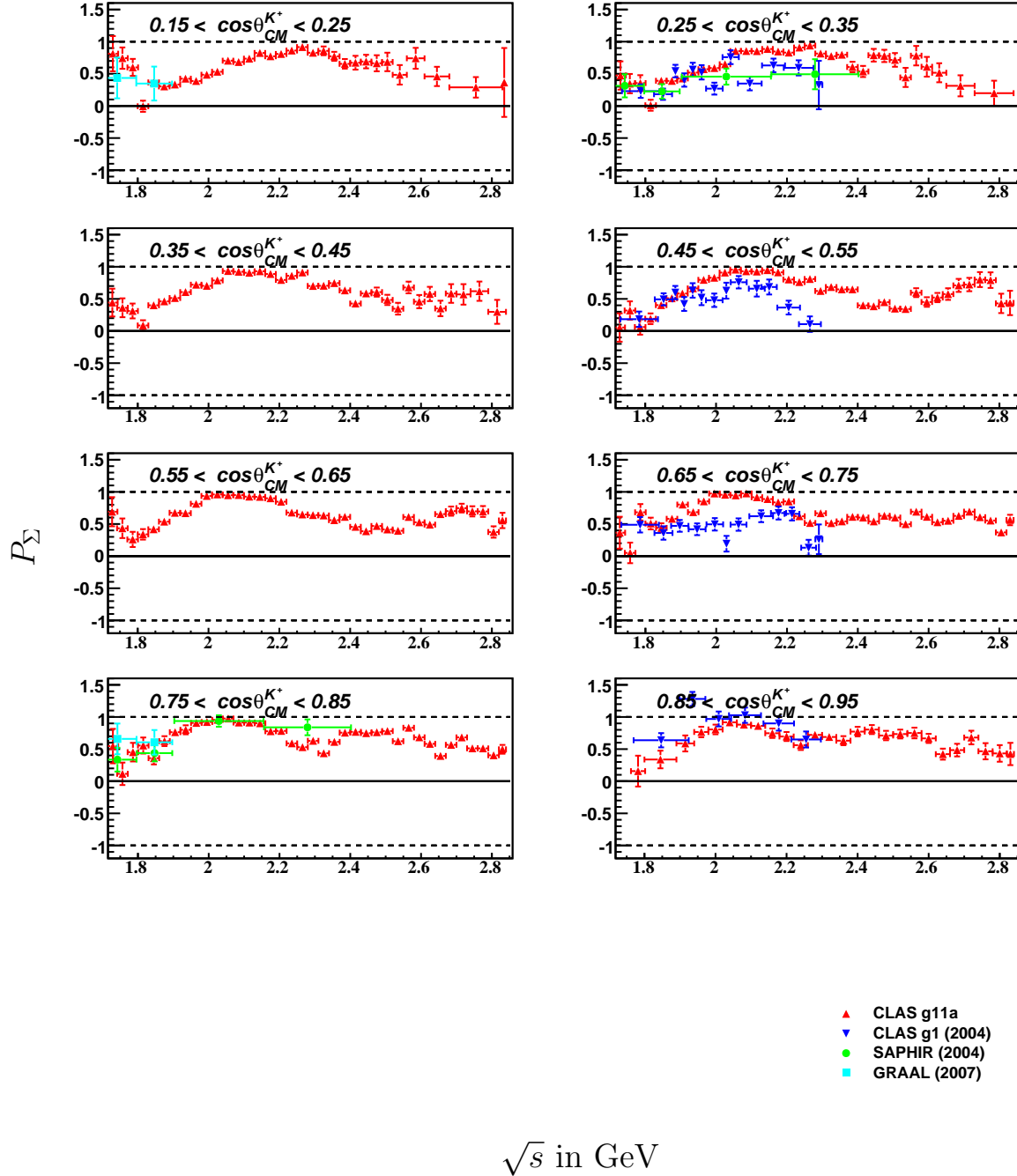


Figure 5.13: Compare P_Σ with previous world data in the forward angles: CLAS $g11a$ (this analysis, red squares), CLAS $g1$ (McNabb [54], blue up-triangles), SAPHIR (Glander [38], green down-triangles) and GRAAL (Lleres [56], cyan circles). Within the statistical uncertainties, there is fair to good consistency with previous world data. Between $\cos \theta_{CM}^{K^+} = 0.5$ and $\cos \theta_{CM}^{K^+} = 0.9$, $g1$ seems to drop down and come back up again, while $g11a$ maintains its shape throughout. All errors are statistical.

Chapter 6

ϕ Differential Cross Sections

In this chapter, the mother fit PWA formalism of Ch. 4 is applied to the $\gamma p \rightarrow \phi p$ channel. The only additional element here is the $\phi \rightarrow KK$ branching fraction, which was unity for the $\Sigma^0 \rightarrow \Lambda\gamma$ decay. The differential cross-section formula appearing in Eq. 4.35 had to be scaled up by $1/b.f.$, where $b.f.$ was the appropriate branching fraction – 34.0% for the neutral-mode and 49.1% for the charged-mode [8].

6.1 The Mother Fits

The basic set-up was exactly the same as in Sec. 4.5. We used J^P waves from $\frac{1}{2}^\pm, \dots, \frac{11}{2}^\pm$. Following Eq. ??, for each J^P wave, there was a phase angle ϕ_{JP} , a production angle θ_{JP} and three decay parameters $r_{JP,L \cdot S}$ corresponding to the triplet of spin-projections for a vector particle. However, $J^P = \frac{1}{2}^\pm$ were special cases again, where only a single $L \cdot S$ projection was possible. Therefore, the $J^P = \frac{1}{2}^\pm$ waves contributed three fit parameters, while $J^P \neq \frac{1}{2}^\pm$ waves had five fit parameters each. For J^P from $\frac{1}{2}^\pm$ till $\frac{11}{2}^\pm$, there were 56 independent fit parameters in all.

Figs. 6.1 and 6.2 show the mother fit results for the charged-mode topology at the energy bin-centers $\sqrt{s} = 2.155, 2.455$ and 2.755 GeV (10-MeV bins) and for the charged-mode topology at the energy bin-centers $\sqrt{s} = 2.135$ and 2.455 GeV (30-MeV-wide bins), respectively. For each energy bin, comparisons are shown in the angular variables $\cos\theta_{Adair}^K$, ϕ_{Adair}^K and $\cos\theta_{c.m.}^\phi$. The real data is shown in black, the unweighted accepted monte carlo in blue, and the monte carlo weighted by the fit results, in red. The weighted monte carlo matches the real data very well in all three kinematically independent variables.

6.2 Cross section results

Figs. 6.3, 6.3 and 6.5 show the differential cross section results for the charged-mode topology. Our energy coverage is from near production threshold, $\sqrt{s} = 1.97$ GeV, to 2.84 GeV in 10-MeV-wide \sqrt{s} bins. The angular binning is 0.1 in $\cos\theta_{c.m.}^\phi$ and our angular coverage is $-0.85 \leq \cos\theta_{c.m.}^\phi \leq 0.95$ at most energy bins. Also, no cross section result is presented at the bins $\sqrt{s} = 2.735$ and 2.745 GeV due to the normalization issues described in Sec. 2.10.3.

Fig. 6.6 shows the differential cross sections for the neutral-mode topology. The energy bins are at least 30-MeV-wide \sqrt{s} , with some 40-MeV bins at the higher energies. The angular binning remains 0.1 in $\cos\theta_{c.m.}^\phi$, as for the charged-mode, but the angular coverage at backward-angles is

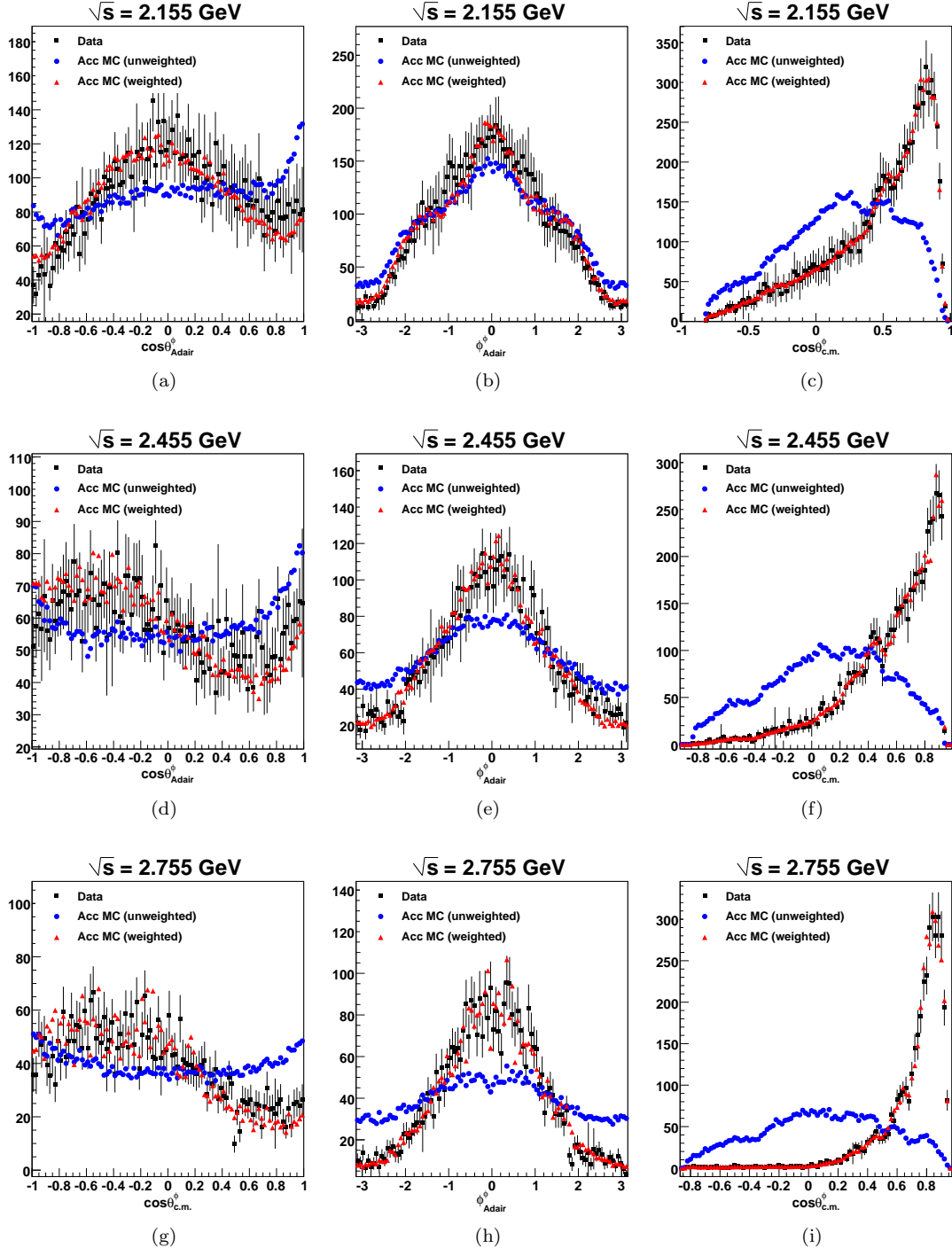


Figure 6.1: Mother fit results for the ϕp charged-mode topology using J^P waves from $\frac{1}{2}^\pm$ till $\frac{11}{2}^\pm$. The rows correspond to three different energy bins. The first, second and third columns show the $\cos\theta_{Adair}^{K^+}$, $\phi_{Adair}^{K^+}$ and $\cos\theta_{c.m.}^\phi$ distributions respectively. For each plot, the black points are the actual data, the blue points are the initial unweighted accepted monte carlo data while the red points are the accepted monte carlo weighted by the mother fit results. As evident from the plots, the weighted monte carlo follows the real data quite well.

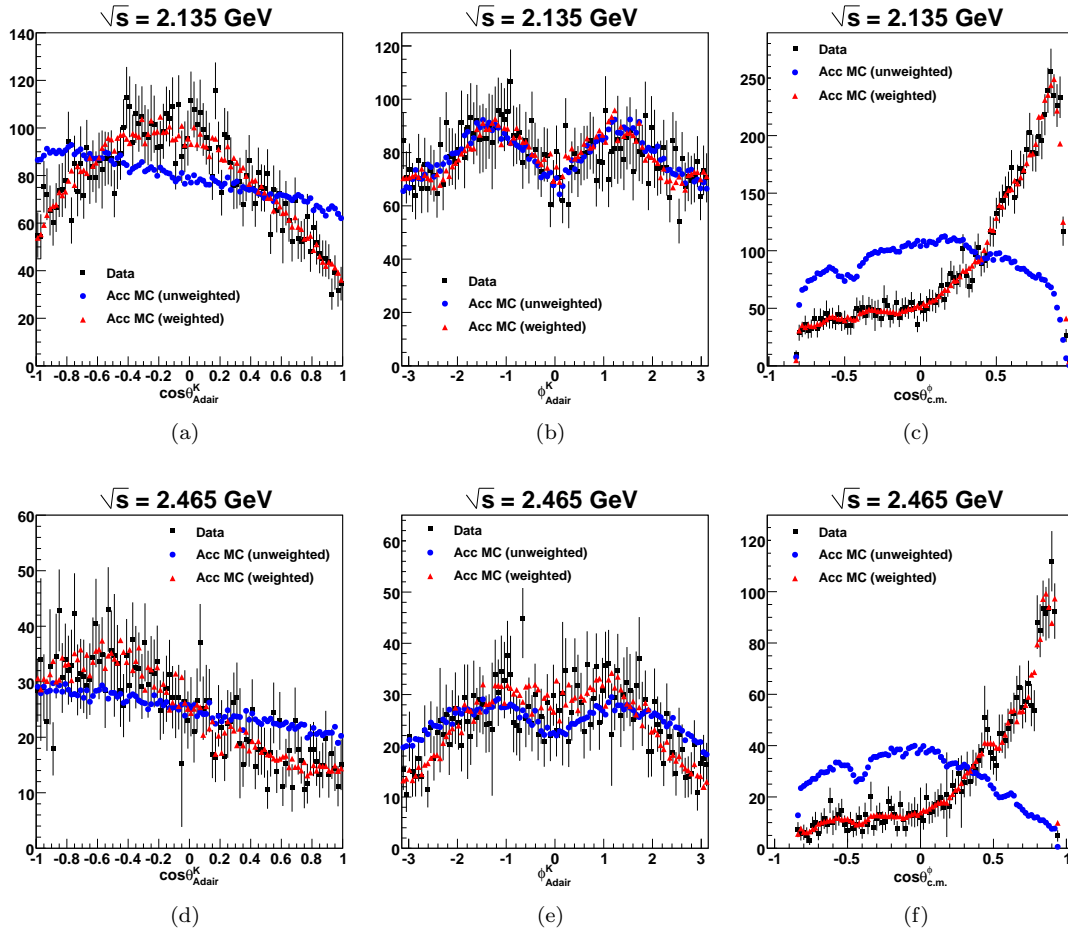


Figure 6.2: Mother fit results for the ϕp neutral-mode topology using J^P waves from $\frac{1}{2}^\pm$ till $\frac{11}{2}^\pm$. The rows correspond to two different energy bins. The first, second and third columns show the $\cos\theta_{\text{Adair}}^{K^0}$, $\phi_{\text{Adair}}^{K^0}$ and $\cos\theta_{c.m.}^\phi$ distributions respectively. For each plot, the black points are the actual data, the blue points are the initial unweighted accepted monte carlo data while the red points are the accepted monte carlo weighted by the mother fit results. As evident from the plots, the weighted monte carlo follows the real data quite well.

more restricted, especially at higher energies, due to very low available statistics for these kinematics.

Figs. 6.7 and 6.8 show the comparison between the charged- and neutral-mode differential cross section results. In keeping with the diffractive nature of vector meson photoproduction, we have chosen to present our results as $d\sigma/dt$ here, with the conversion being

$$\frac{d\sigma}{dt} = \frac{1}{2} \left(\frac{1}{E_\gamma |\vec{p}_\phi|} \right)_{c.m.} \left(\frac{d\sigma}{d \cos \theta_{c.m.}^\phi} \right). \quad (6.1)$$

The diffractive Pomeron exchange mechanism is clearly borne out in the very forward-most angular bin ($t \rightarrow 0$), where $d\sigma/dt$ remains almost constant above $\sqrt{s} > 2.3$ GeV. The structure around $\sqrt{s} \approx 2.1$ GeV is clearly present in both topologies. Above $\sqrt{s} > 2.3$ GeV, the two topologies are in very good agreement, except in the $\cos \theta_{c.m.}^\phi = 0.7$ and 0.8 bins, where the neutral-mode cross sections tend to be slightly lower.

6.2.1 Comparison with previous world data

Previous world data for ϕ photoproduction cross sections are generally scarce and no world data exists for the neutral-mode topology at all. We therefore restrict our discussion to the charged-mode topology only. For low energy and forward-angle kinematics, there are two previous results from the SAPHIR (2003, Barth *et al.* [65]) and LEPS (2004, Mibe *et al* [66]) Collaborations. Both data sets have wide energy binnings, $E_\gamma \approx 200$ -MeV-wide and 100-MeV-wide bins for SAPHIR and LEPS, respectively. However, the common feature in both results is of a prominent enhancement around $E_\gamma \approx 2$ GeV ($\sqrt{s} \approx 2.2$ GeV) in the forward-angle $d\sigma/dt$, in agreement with our current results.

Since the SAPHIR and LEPS kinematics was mostly at forward-angles, these results were presented as $d\sigma/dt$ vs. $|t - t_0|$, where t_0 was the value of t at $\theta_{c.m.}^\phi = 0$. From the phenomenology of diffractive production, $d\sigma/dt$ was expected to show a simple exponential fall off with $|t - t_0|$. The conversion of $\cos \theta_{c.m.}^\phi$ to t or $|t - t_0|$ depends on \sqrt{s} . With a wide energy bins, it is not immediately clear which \sqrt{s} should be chosen for this conversion. Therefore, we convert our results in to the units chosen by SAPHIR and LEPS and make independent comparisons with both of them. Since our energy binning is much finer (10-MeV-wide in \sqrt{s}), we overlay our results at the energy bin-center of the SAPHIR or LEPS results. Figs. 6.9 and 6.10 show the comparison between our results with SAPHIR and LEPS, respectively.

The only existing world data for large $|t|$ are the CLAS (2000, Anciant *et al* [68]) results for a bin-center at $E_\gamma = 3.6$ GeV (tagged photon energy range 3.3 to 3.9 GeV). The chief motivation of the previous CLAS experiment was to investigate whether u -channel processes (at small u or large t) contribute to the ϕ channel. Assuming that the ϕ is almost pure $s\bar{s}$ and the strangeness content in ordinary nucleons is small, the coupling constant $g_{\phi NN}$ is expected to be small and therefore nucleon exchanges in the u -channel are supposed to be suppressed. However, as shown in Fig. 6.11, both the CLAS 2000 and the current CLAS 2010 results show a small but distinct rise in the backward-angles, suggestive of a non-negligible value for $g_{\phi NN}$.

Lastly, we compare our results with the $E_\gamma = 3.3$ GeV bin-center results from Daresbury (1982, Barber *et al.* [62]). The Daresbury binning was 1-GeV in E_γ and away from the $t \rightarrow 0$ region, the error bars are large. Overall, within the limitations of statistical uncertainties, agreement between the two results is fair.

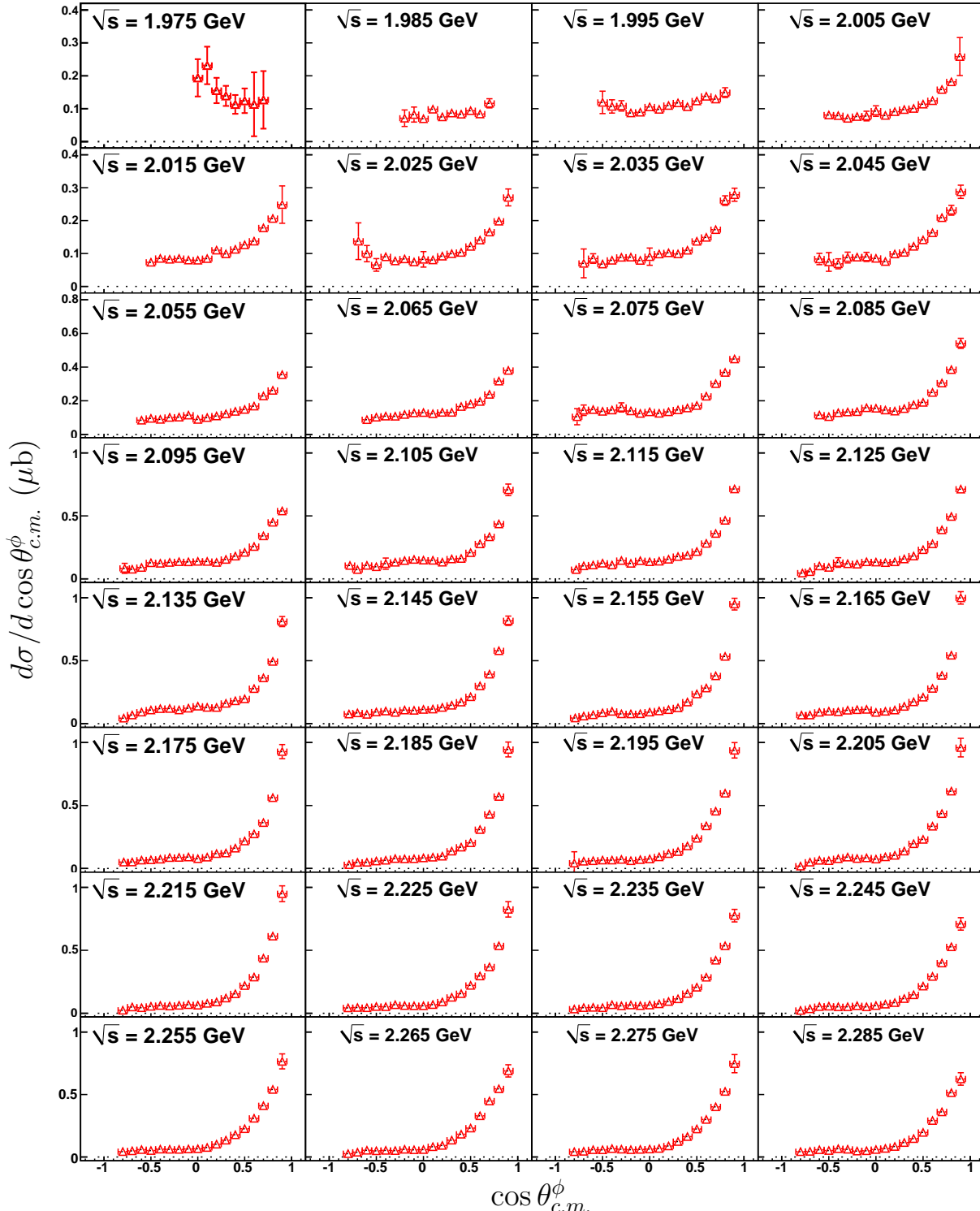


Figure 6.3: (Color On-line) $\frac{d\sigma}{d \cos \theta_{c.m.}^\phi}$ (μb) vs. \sqrt{s} : Differential cross section results for the charged-mode topology in the energy range $1.97 \text{ GeV} \leq \sqrt{s} < 2.29 \text{ GeV}$. The centroid of each 10-MeV-wide bin is printed on the plots. The y-axis range is constant over each horizontal row and is shown in the left-most column for every row. All error bars represent statistical uncertainties only.

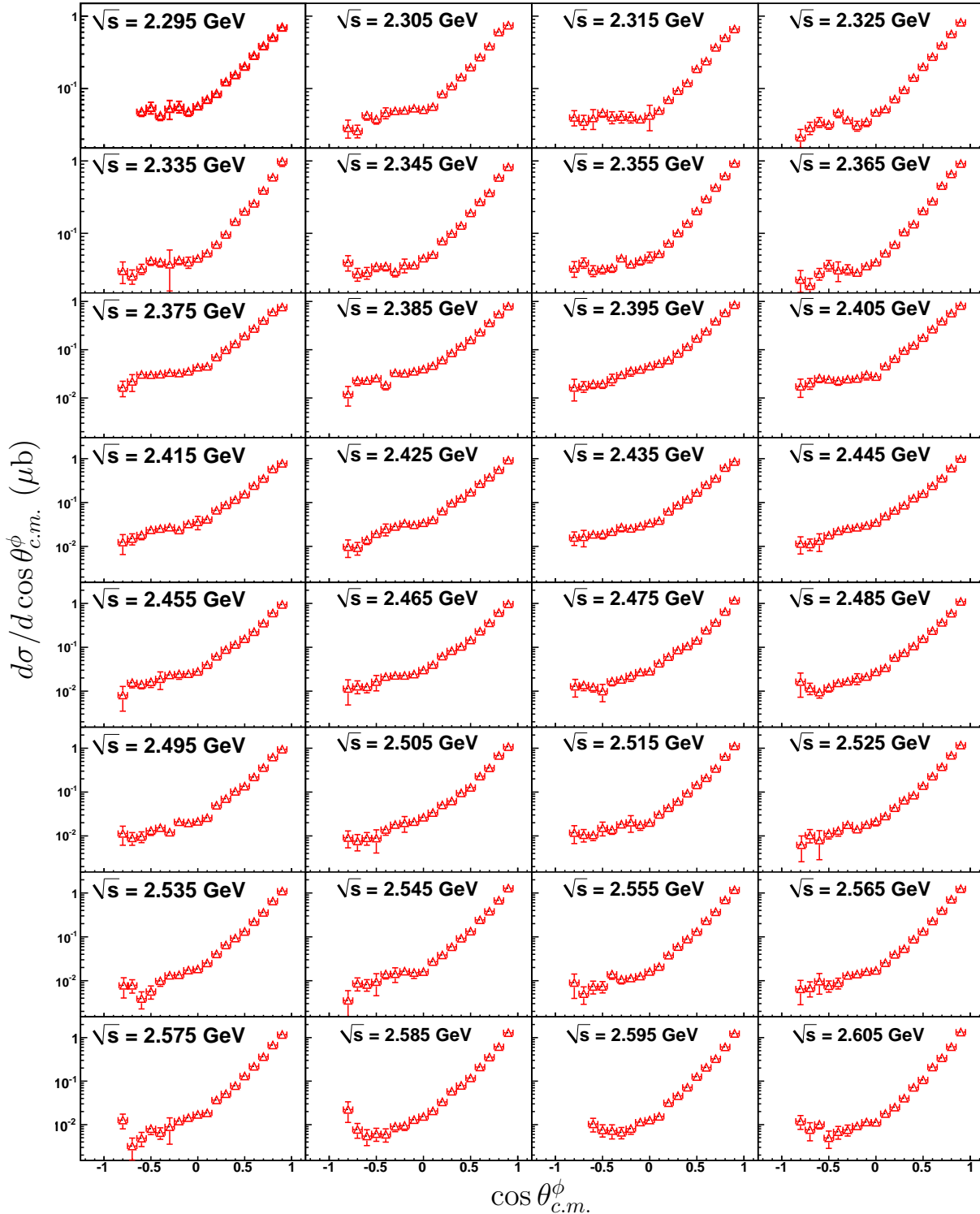


Figure 6.4: (Color On-line) $\frac{d\sigma}{d \cos \theta_{c.m.}^\phi} (\mu b)$ vs. \sqrt{s} : Differential cross section results for the charged-mode topology in the energy range $2.29 \text{ GeV} \leq \sqrt{s} < 2.61 \text{ GeV}$. The centroid of each 10-MeV-wide bin is printed on the plots. The y-axis range is constant over each horizontal row and is shown in the left-most column for every row. All error bars represent statistical uncertainties only.

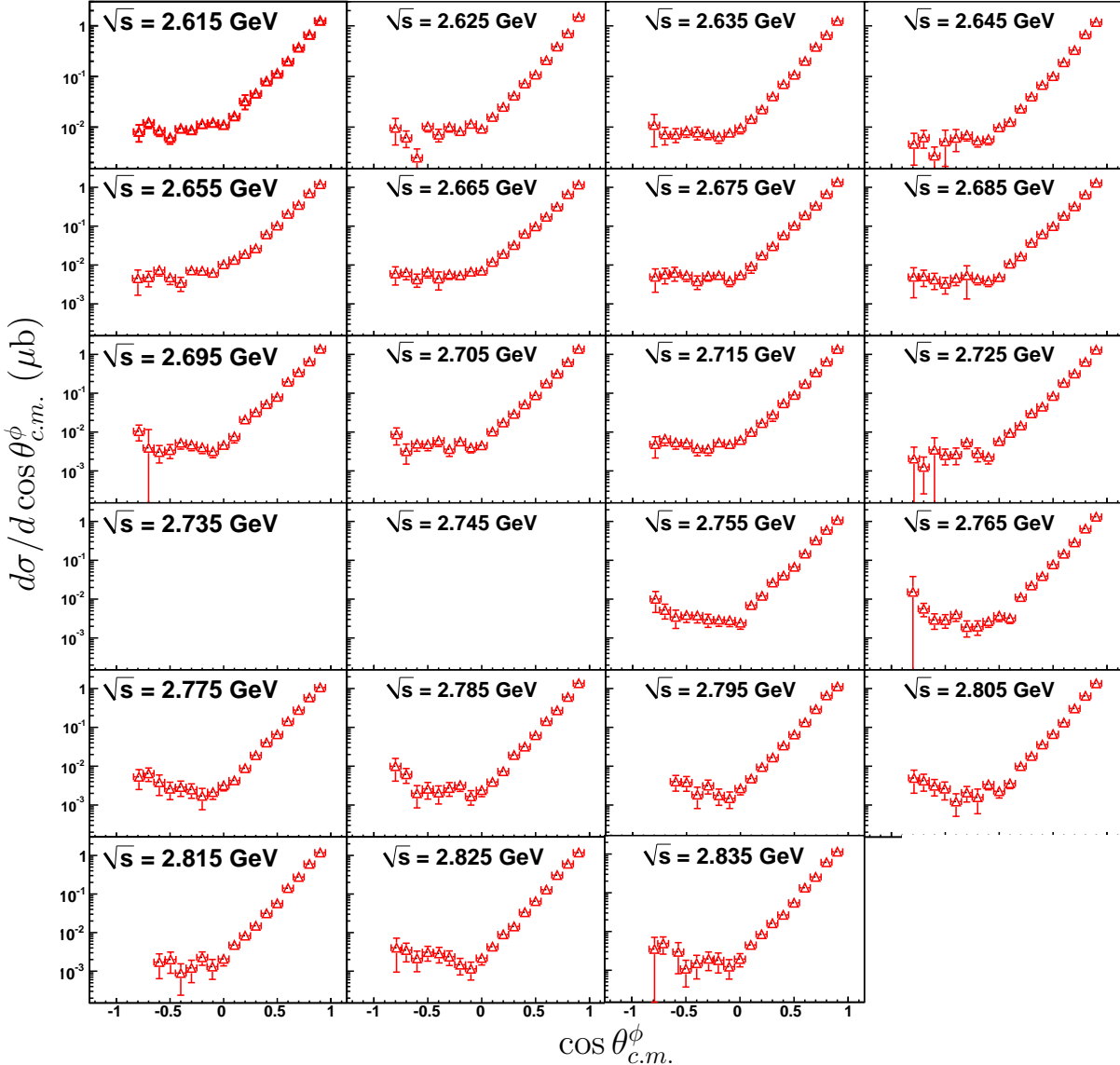


Figure 6.5: (Color On-line) $\frac{d\sigma}{d \cos \theta_{c.m.}^\phi}$ (μb) vs. \sqrt{s} : Differential cross section results for the charged-mode topology in the energy range $2.61 \text{ GeV} \leq \sqrt{s} < 2.84 \text{ GeV}$. The centroid of each 10-MeV-wide bin is printed on the plots. The y-axis range is constant over each horizontal row and is shown in the left-most column for every row. No results are presented for the bins $\sqrt{s} = 2.735$ and 2.745 GeV due to the normalization issues, as described in Sec. All error bars represent statistical uncertainties only.

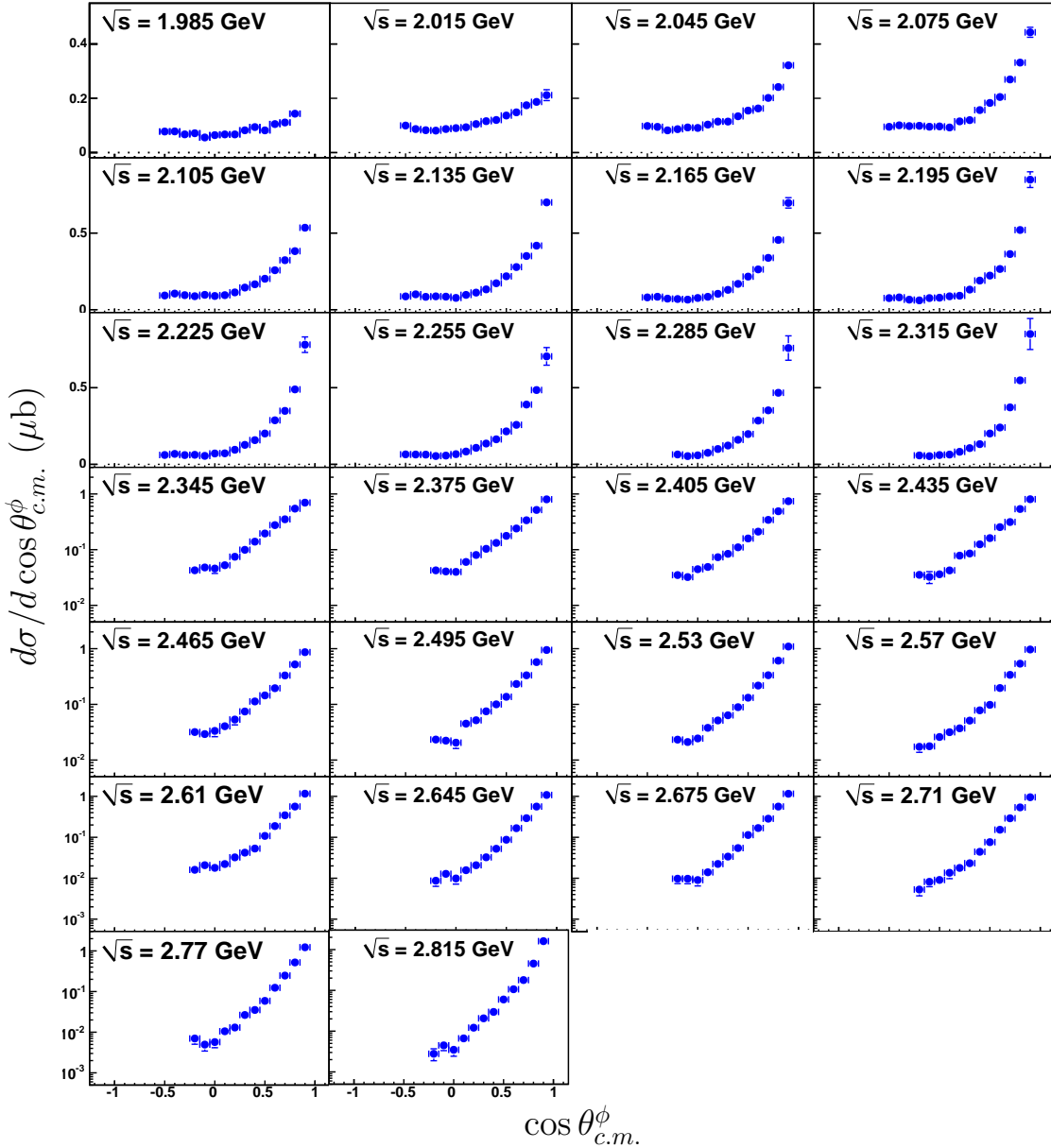


Figure 6.6: (Color On-line) $\frac{d\sigma}{d \cos \theta_{c.m.}^\phi}$ (μb) vs. \sqrt{s} : Differential cross section results for the neutral-mode topology. The minimum bin-width is 30-MeV and the bin-centroid is printed on the plots. The y-axis range is constant over each horizontal row and is shown in the left-most column for every row. All error bars represent statistical uncertainties only.

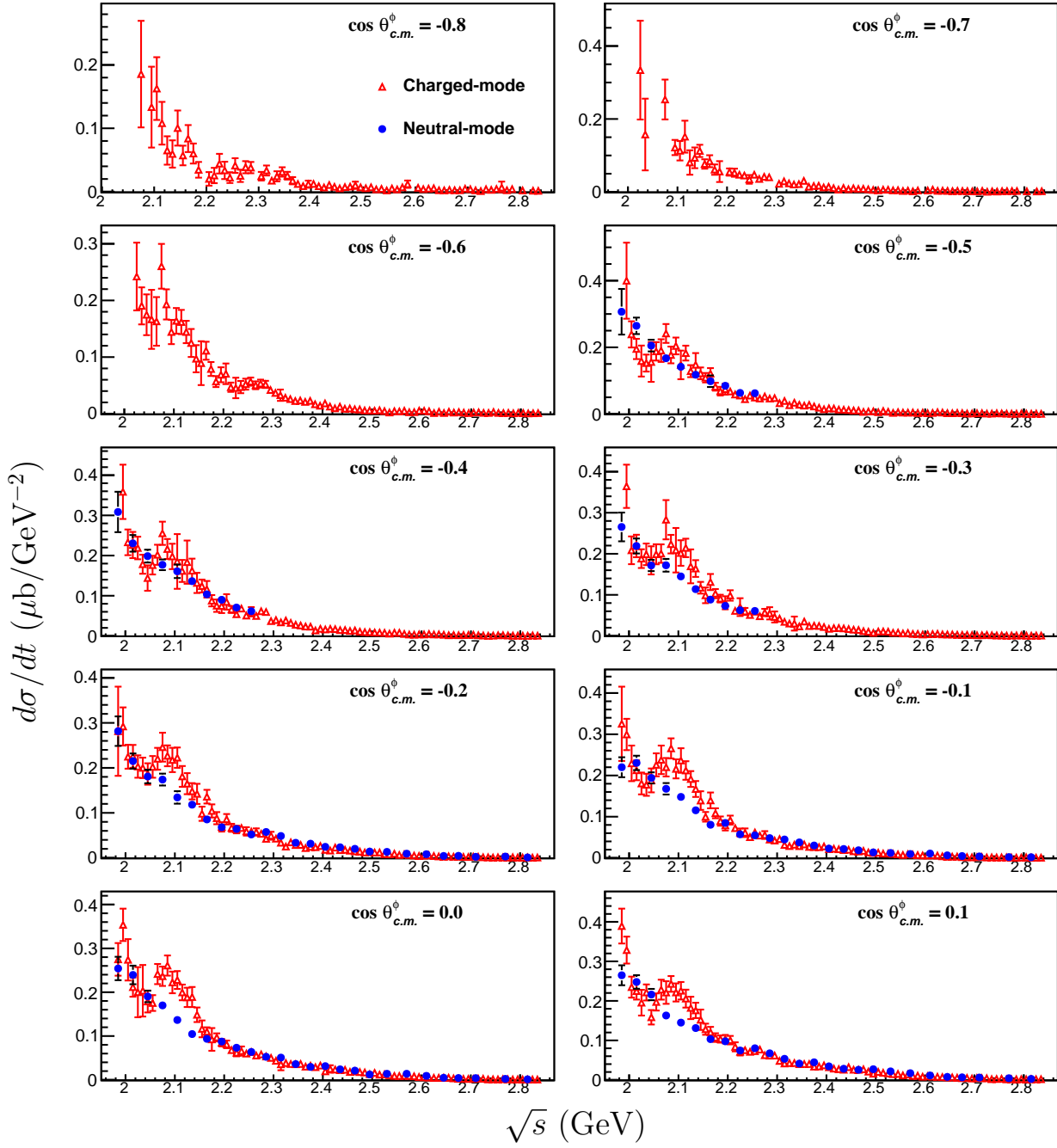


Figure 6.7: (Color On-line) Comparison of the charged- and neutral-mode $d\sigma/dt$ results in the mid- and backward-angle bins. There is a prominent difference between the two results around $\sqrt{s} \approx 2.1$ GeV, especially in the mid-angle regions. All error bars represent statistical uncertainties only.

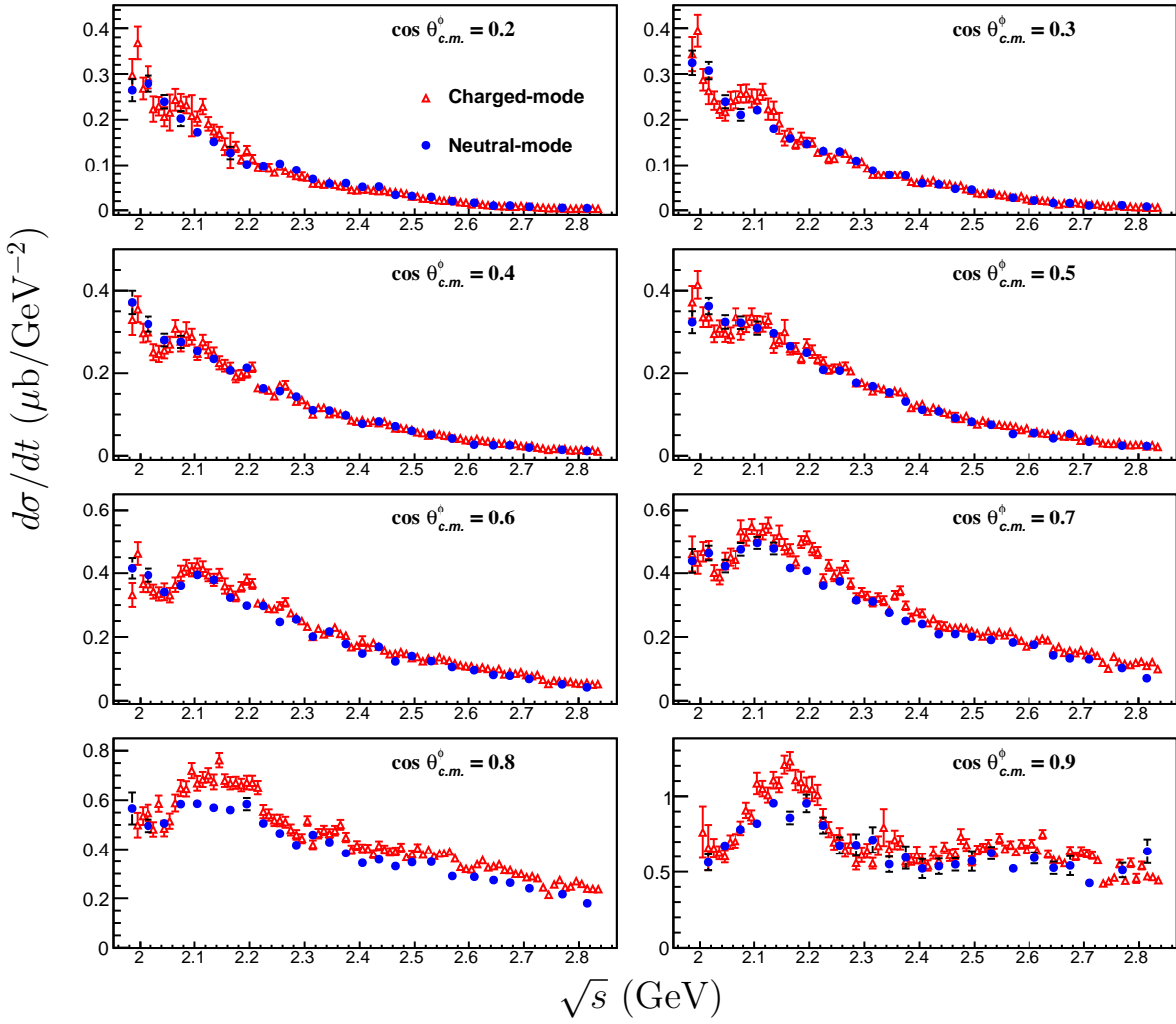


Figure 6.8: (Color On-line) Comparison of the charged- and neutral-mode $d\sigma/dt$ results in the mid- and forward-angle bins. There is a prominent difference between the two results around $\sqrt{s} \approx 2.1$ GeV, especially in the mid-angle regions. Both topologies show the $\sqrt{s} \approx 2.1$ GeV structure in the forward-most angular bins. $d\sigma/dt$ appears almost constant above $\sqrt{s} \approx 2.3$ GeV for $\cos \theta_{c.m.}^\phi = 0.9$ ($t \rightarrow 0$), as expected for diffractive photoproduction. All error bars represent statistical uncertainties only.

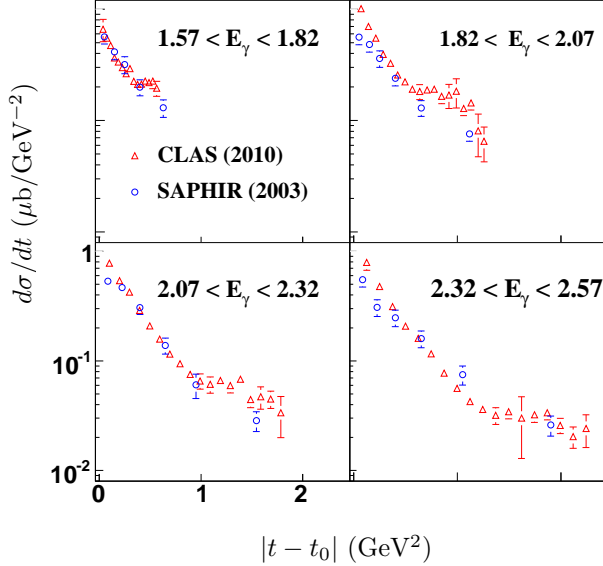


Figure 6.9: (Color On-line) Comparison between the present CLAS 2010 (red triangles) and 2003 SAPHIR 2003 [65] (blue circles) results. The SAPHIR binning in E_γ (GeV) is printed on each pad and the CLAS results are at the bin-centers for each SAPHIR energy bin. The CLAS results are taken from the charged-mode topology (including the $\Lambda(1520)$ hard cut). All error bars represent statistical uncertainties only.

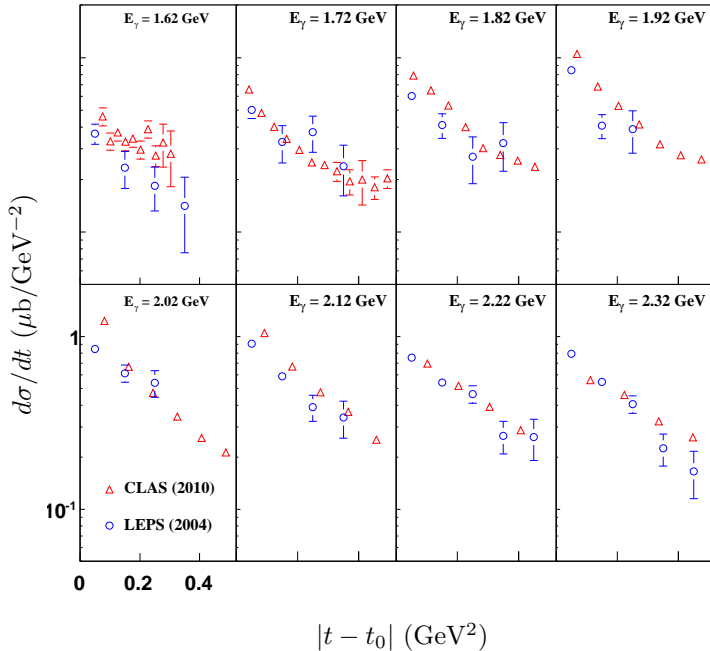


Figure 6.10: (Color On-line) Comparison between the present CLAS 2010 (red triangles) and LEPS 2004 [66] (blue circles) results. The LEPS data had $E_\gamma = 200$ MeV wide bins (the bin-center is printed on each pad). The present CLAS results are taken from the charged-mode topology (including the $\Lambda(1520)$ hard cut). All error bars represent statistical uncertainties only.

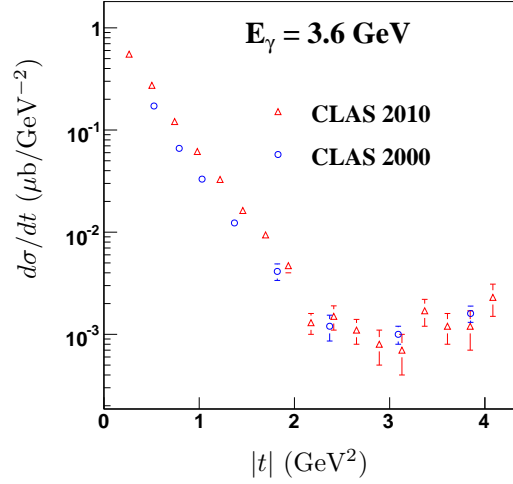


Figure 6.11: (Color On-line) Comparison between the current CLAS (red triangles) and 2000 CLAS [68] (blue circles) results at the energy bin-center $E_\gamma = 3.6 \text{ GeV}$. The CLAS 2000 energy binning was 600-MeV in E_γ while the current CLAS binning is 10-MeV-wide in \sqrt{s} .

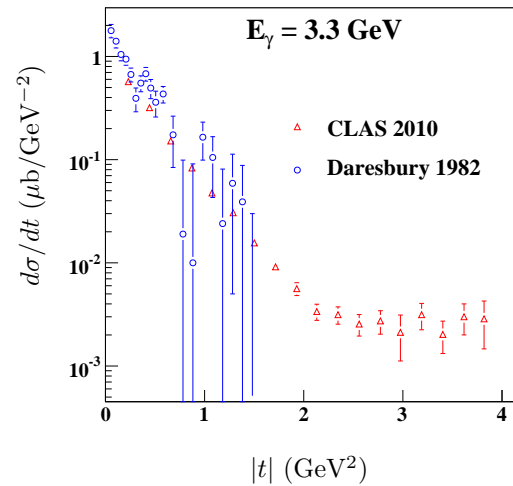


Figure 6.12: (Color On-line) Comparison between the current CLAS (red triangles) and 1982 Daresbury [62] (blue circles) results at the bin-center $E_\gamma = 3.3 \text{ GeV}$. The Daresbury energy bins were 1-GeV-wide in E_γ while the CLAS binning is 10-MeV-wide in \sqrt{s} .

6.3 Summary

In this chapter, we have presented differential cross section results for the ϕp channel. Comparison between the charged- and neutral-mode results show an interesting difference in the $\sqrt{s} \approx 2.2$ GeV region, most possibly due to the effect of a coupling between the ϕp charged-mode and $K^+ \Lambda(1520)$ channels. In the forward-most angular bin, $d\sigma/dt$ shows an approximately constant behavior with \sqrt{s} , the signature behavior of diffractive Pomeron exchange. Comparisons with the few existing previous world data is generally fair, thought most of these earlier results have wide energy binning, limited statistics and kinematic coverage.

Chapter 7

Spin Density Matrix Elements for ϕ

In this chapter we describe the extraction of the spin density matrix elements (SDME's) for the ϕ vector meson. We first describe the general formulation of the density matrix for a spin-1 particle and the connection between the different SDME's and physically meaningful observables. Similar to our approach for the $K^+\Sigma^0$ channel, we extract the polarization information using both an intensity distribution fit and by using the spin-projections of our PWA amplitudes. The two methods are found to be in excellent agreement. We also discuss the interpretation of our results at the amplitude level in terms of both s - and t -channel helicity conservation (SCHC and TCHC, respectively).

7.1 The Density Matrix of a Massive Vector Particle

In Sec ??, we showed that the spin density matrix of a massless vector particle (the photon) is given by the so-called Stokes parameters and the density matrix “lives” in the space spanned by the three Pauli matrices and $I_{2 \times 2}$. The reduced space results from the fact that the same gauge symmetry that makes the photon massless also renders the polarization component along its momentum unphysical. Thus, a real photon is always transverse. For the massive case, this is no longer necessary and a massive spin-1 particle is allowed to have a longitudinal spin component. The three spin-1 operators are

$$S_x = \frac{1}{\sqrt{2}} \begin{pmatrix} 0 & 1 & 0 \\ 1 & 0 & 1 \\ 0 & 1 & 0 \end{pmatrix}, \quad S_y = \frac{1}{\sqrt{2}} \begin{pmatrix} 0 & -i & 0 \\ i & 0 & -i \\ 0 & i & 0 \end{pmatrix}, \quad S_z = \begin{pmatrix} 1 & 0 & 0 \\ 0 & 0 & 0 \\ 0 & 0 & -1 \end{pmatrix}, \quad (7.1)$$

and a pure spin state $|\alpha\rangle$ is an eigenstate of the full \vec{S} operator. For a classical ensemble of states, the spin of the vector particle is described by the density matrix $\rho = \sum w_\alpha |\alpha\rangle\langle\alpha|$, where the sum is over a complete basis of state and w_α is the classical probability of finding the particle in the state $|\alpha\rangle$.

For the general case, however, ρ will not be diagonalizable and the different polarization states will be correlated. A general 3×3 complex matrix ρ has 2×3^2 real elements. Hermiticity constrains the diagonal elements to be all real (3 real elements) and the off-diagonal elements to be conjugate transpose of each other (3 complex elements or 6 real elements). The unit trace constraint further reduces the number of independent elements by 1. Therefore, in all, the most general 3×3 density matrix will have 8 real and independent elements. A convenient basis to expand the density matrix is given by three rank-1 tensors, S_i ($i = x, y, z$) and five rank-2 tensors τ_{ij} given by

$$\tau_{ij} = \frac{3}{2}(S_i S_j + S_j S_i) - 2\delta_{ij}. \quad (7.2)$$

Thus, by construction, in the tensorial space indexed by the two rank-1 tensors S_i and S_j , τ_{ij} is symmetric and traceless.

The above tensors were written in the Cartesian basis. Following Ref. [73], we switch to the helicity basis where the spin-1 operators are written as [?] $S_{1\pm 1} = \mp(S_x \pm iS_y)/\sqrt{2}$ and $S_{10} = S_z$. Explicitly, they are

$$S_{10} = \begin{pmatrix} 1 & 0 & 0 \\ 0 & 0 & 0 \\ 0 & 0 & -1 \end{pmatrix} \quad S_{11} = -\begin{pmatrix} 0 & 1 & 0 \\ 0 & 0 & 1 \\ 0 & 0 & 0 \end{pmatrix} \quad S_{1-1} = \begin{pmatrix} 0 & 0 & 0 \\ 1 & 0 & 0 \\ 0 & 1 & 0 \end{pmatrix}. \quad (7.3)$$

In the helicity basis, the rank-2 operators $\tau_{2\mu}$ are given by the tensor products $[S_1 \otimes S_1]_\mu$, $\mu = \{0, \pm 1, \pm 2\}$. Substituting the appropriate Clebsch-Gordan coefficients, the tensor polarization operators are

$$\tau_{22} = S_{11}S_{11} \quad (7.4a)$$

$$\tau_{2-2} = S_{1-1}S_{1-1} \quad (7.4b)$$

$$\tau_{21} = \frac{1}{\sqrt{2}}(S_{11}S_{10} + S_{10}S_{11}) \quad (7.4c)$$

$$\tau_{2-1} = \frac{1}{\sqrt{2}}(S_{1-1}S_{10} + S_{10}S_{1-1}), \text{ and} \quad (7.4d)$$

$$\tau_{20} = \frac{1}{\sqrt{6}}(S_{11}S_{1-1} + 4S_{10}S_{10} + S_{1-1}S_{11}). \quad (7.4e)$$

For the sake of completeness, we give the explicit form of these five matrices

$$\begin{aligned} \tau_{22} &= \begin{pmatrix} 0 & 0 & 1 \\ 0 & 0 & 0 \\ 0 & 0 & 0 \end{pmatrix} & \tau_{2-2} &= \begin{pmatrix} 0 & 0 & 0 \\ 0 & 0 & 0 \\ 1 & 0 & 0 \end{pmatrix} & \tau_{21} &= -\frac{1}{\sqrt{2}} \begin{pmatrix} 0 & 1 & 0 \\ 0 & 0 & -1 \\ 0 & 0 & 0 \end{pmatrix} \\ \tau_{2-1} &= -\frac{1}{\sqrt{2}} \begin{pmatrix} 0 & 0 & 0 \\ -1 & 0 & 0 \\ 0 & 1 & 0 \end{pmatrix} & \tau_{20} &= \frac{1}{\sqrt{6}} \begin{pmatrix} 1 & 0 & 0 \\ 0 & -2 & 0 \\ 0 & 0 & 1 \end{pmatrix}. \end{aligned} \quad (7.5)$$

The full expression of the density matrix is then given as

$$\rho = \frac{1}{3} \left[I + \frac{3}{2} \vec{S} \cdot \vec{P} + \sqrt{3} \tau \cdot T \right], \quad (7.6)$$

with the vector polarizations defined as

$$P_{1\pm 1} = \mp \frac{P_x \pm iP_y}{\sqrt{2}}, \quad P_{10} = P_z, \quad (7.7)$$

and the sum over the tensor polarizations defined as

$$\tau \cdot T = \sum_{\mu=0,\pm 1,\pm 2} (-1)^\mu \tau_{2-\mu} T_{2\mu}. \quad (7.8)$$

and the density matrix becomes

$$\rho_{\lambda\lambda'} = \begin{pmatrix} \rho_{-1-1} & \rho_{-10} & \rho_{-11} \\ \rho_{0-1} & \rho_{00} & \rho_{01} \\ \rho_{1-1} & \rho_{10} & \rho_{11} \end{pmatrix} \quad (7.9a)$$

$$= \frac{1}{3} \begin{pmatrix} 1 + \frac{3}{2}P_{10} + \sqrt{\frac{1}{2}}T_{20} & -\frac{3}{2}P_{11} + \sqrt{\frac{3}{2}}T_{2-1} & \sqrt{3}T_{2-2} \\ \frac{3}{2}P_{1-1} - \sqrt{\frac{3}{2}}T_{21} & 1 - \sqrt{2}T_{20} & -\frac{3}{2}P_{11} - \sqrt{\frac{3}{2}}T_{2-1} \\ \sqrt{3}T_{22} & +\frac{3}{2}P_{1-1} + \sqrt{\frac{3}{2}}T_{21} & 1 - \frac{3}{2}P_{10} + \sqrt{\frac{1}{2}}T_{20} \end{pmatrix}. \quad (7.9b)$$

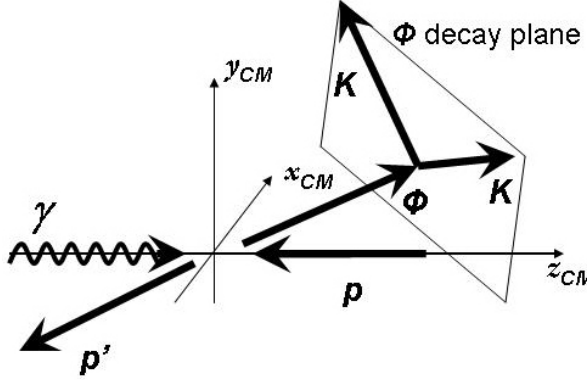


Figure 7.1: A schematic diagram of the reaction chain $\gamma p \rightarrow \phi p' \rightarrow KK p'$ in the overall center-of-mass frame. The beam direction is taken as the positive z -axis, and the y -axis is normal to the ϕ production plane.

For photoproduction with an unpolarized beam and unpolarized target, the parity constraint $\rho_{\lambda\lambda'}^V = (-1)^{\lambda-\lambda'} \rho_{-\lambda-\lambda'}^V$ requires $P_{11} = P_{1-1}$ ($P_x = 0$), $P_{10} = 0$ ($P_z = 0$), $T_{2-1} = -T_{21}$ and $T_{2-2} = T_{22}$, so that the density matrix becomes

$$\rho_{\lambda\lambda'} = \frac{1}{3} \begin{pmatrix} 1 + \sqrt{\frac{1}{2}}T_{20} & \frac{3}{2}\sqrt{\frac{1}{2}}(-iP_y) - \sqrt{\frac{3}{2}}T_{21} & \sqrt{3}T_{22} \\ \sqrt{\frac{1}{2}}(iP_y) - \sqrt{\frac{3}{2}}T_{21} & 1 - \sqrt{2}T_{20} & \sqrt{\frac{1}{2}}(-iP_y) + \sqrt{\frac{3}{2}}T_{21} \\ \sqrt{3}T_{22} & \sqrt{\frac{1}{2}}(iP_y) + \sqrt{\frac{3}{2}}T_{21} & 1 + \sqrt{\frac{1}{2}}T_{20} \end{pmatrix}. \quad (7.10)$$

Therefore, for the unpolarized case, instead of eight, the density matrix has only four non-zero independent variables given by $\rho_{00} = \frac{1}{3}(1 - \sqrt{2}T_{20})$, $\rho_{1-1} = T_{22}/\sqrt{3}$, $Re\rho_{10} = -1/\sqrt{6}T_{21}$ and $Im\rho_{10} = -1/(2\sqrt{2})P_y$. However, it turns out that for the decay of the vector meson through pseudoscalars ($\rho \rightarrow \pi\pi$, $\omega \rightarrow \pi\pi\pi$ or $\phi \rightarrow KK$), the element $Im\rho_{10}$ is also not a physically measurable. Kloet *et al.* [73] has shown that the only way to measure the vector-polarization P_y is through leptonic decay modes of the vector mesons, with the additional requirement that the daughter leptons be detected as well. Therefore, we come to the following conclusion: *for unpolarized photoproduction of vector mesons, and subsequent detection through pseudoscalar decay modes, only the three tensor polarization components T_{20} , T_{22} and T_{21} are non-zero and physically measurable. In particular, the vector polarization \vec{P} can not be measured at all.*

Fig. 7.1 shows the reaction $\gamma p \rightarrow \phi p$ with the subsequent decay of the ϕ into two kaons. This is a P -wave decay. The angular distribution of the daughter kaons is given by the Schilling's equation [75]

$$W(\zeta, \varphi) \sim \left(\frac{1}{2}(1 - \rho_{00}) + \frac{1}{2}(3\rho_{00} - 1) \cos^2 \zeta - \sqrt{2} Re\rho_{10} \sin 2\zeta \cos \varphi - \rho_{1-1} \sin^2 \zeta \cos 2\varphi \right), \quad (7.11)$$

where ζ and φ are the polar and azimuthal angles of the K^+ unit vector (for $\phi \rightarrow K^+K^-$). Note that the element $Im\rho_{10}$ does not feature in Eq.7.11, so that, as explained above, P_y remains unmeasurable.

7.2 Amplitude Level Construction of $\rho_{\lambda\lambda'}^V$

The discussion of the previous section was pertinent only to an unpolarized beam-target configuration. For the general reaction $\gamma p \rightarrow Vp'$, the density matrices of the beam and the target proton also have to be considered. The non-spin-correlated observable is the overall spin-averaged differential cross-section, with several single, double, triple and even quadrauple spin-observables possible. We start with the basic amplitude for vector meson photoproduction

$$\mathcal{A} = \langle \vec{q}\lambda_V\lambda_2 | T | \vec{k}\lambda_\gamma\lambda_1 \rangle, \quad (7.12)$$

where λ_γ , λ_1 , λ_V and λ_2 are the spin-components of the incoming photon, target proton, outgoing vector meson and outgoing proton respectively. The photon momentum is \vec{k} and the vector meson momentum is \vec{q} . In the helicity basis, the spin-quantization axes are along the direction of each particle momentum. Counting the number of helicity states possible for each incoming and outgoing particle, there are $2 \times 2 \times 3 \times 2 = 24$ such complex \mathcal{A} amplitudes. However, for parity conserving processes, we have the additional relation under parity-reversal

$$\langle \vec{q}\lambda_V\lambda_2 | T | \vec{k}\lambda_\gamma\lambda_1 \rangle = (-1)^{\lambda_{in} - \lambda_{out}} \langle \vec{q} - \lambda_V - \lambda_2 | T | \vec{k} - \lambda_\gamma - \lambda_1 \rangle, \quad (7.13)$$

where $\lambda_{in} = \lambda_\gamma - \lambda_1$ and $\lambda_{out} = \lambda_V - \lambda_2$ are the overall incoming- and outgoing-state helicities. Therefore there are only 12 independent complex amplitudes. Since the overall phase is irrelevant, there are 23 independent real observables to be measured. In the Pichowski-Savkli-Tabakin (PST) [74] formalism, these physical observables occur within the $12 \times 12 = 144$ bilinear products of the complex amplitudes. For a given beam helicity (the reverse helicity case is related by parity), the PST formalism breaks down the overall spin-space into a $\mathbf{4} = \mathbf{2} \otimes \mathbf{2}$ (enumerated by $a = \{1, 2, 3, 4\}$) space for the initial- and final-state spin- $\frac{1}{2}$ protons and a $\mathbf{3}$ space for the vector meson ($\lambda_V = \{\pm 1, 0\}$). The helicity amplitudes $H_{a\lambda_V}$ are written as

$$\begin{aligned} H_{1\lambda_V} &= \langle \lambda_V, \lambda_2 = +1/2 | T | \lambda_\gamma = 1, \lambda_1 = -1/2 \rangle \\ H_{2\lambda_V} &= \langle \lambda_V, \lambda_2 = +1/2 | T | \lambda_\gamma = 1, \lambda_1 = +1/2 \rangle \\ H_{3\lambda_V} &= \langle \lambda_V, \lambda_2 = -1/2 | T | \lambda_\gamma = 1, \lambda_1 = -1/2 \rangle \\ H_{4\lambda_V} &= \langle \lambda_V, \lambda_2 = -1/2 | T | \lambda_\gamma = 1, \lambda_1 = +1/2 \rangle \end{aligned} \quad (7.14)$$

In this “split” space, any general observable Ω can be written in the form

$$\Omega = \pm \frac{1}{2} \sum_{a,b,\lambda_V,\lambda'_V} H_{a\lambda_V}^* \Gamma_{ab}^\alpha \omega_{\lambda_V \lambda'_V}^\beta H_{b\lambda'_V}, \quad (7.15)$$

where the 16 Γ^α 's are the usual Dirac bilinears [20] and the 9 ω^β 's “live” in the vector meson spin-space spanned by the identity matrix the 3 vector polarizations and the 5 tensor polarizations. It turns out that there are 290 possible (single, double, triple and quadruple) polarization observables ???. Many of these observables include a similar set of bilinear $\Gamma^\alpha \omega^\beta$ observables leading to redundancies, and the question of what constitutes a “complete” set of measurements to determine the full 12 complex amplitude still remains to be answered.

7.3 Reference Frames and Helicity Conservation

The choice of the reference frame for the two decay angles in the intensity distribution of Eq. 7.11 depends on the production mechanism under examination. Three prevalent choices exist in the literature, the Adair frame, the Helicity frame, and the Gottfried-Jackson frame. We go over each of these below.

In the Adair (Ad) frame, the polarization axes from both the incoming and outgoing states are chosen as the z -axis (along the beam direction). With an unpolarized beam ($\rho^\gamma = \frac{1}{2}I$) and target, the vector meson density matrix elements are [75]

$$\begin{aligned}\rho_{m_\phi m'_\phi} &= \frac{\sum_{m_f m_\gamma m_i m'_\gamma} \mathcal{A}_{m_\phi m_f m_i m_\gamma} (\rho^\gamma)_{m_\gamma m'_\gamma} \mathcal{A}_{m'_\phi m_f m_i m'_\gamma}^*}{1/2 \sum_{m_\phi m_f m_\gamma m_i} |\mathcal{A}_{m_\phi m_f m_i m_\gamma}|^2} \\ &= \frac{\sum_{m_f m_\gamma m_i} \mathcal{A}_{m_\phi m_f m_i m_\gamma} \mathcal{A}_{m'_\phi m_f m_i m_\gamma}^*}{\sum_{m_\phi m_f m_\gamma m_i} |\mathcal{A}_{m_\phi m_f m_i m_\gamma}|^2},\end{aligned}\quad (7.16)$$

where $\mathcal{A}_{m_\phi m_f m_i m_\gamma}$ are the same amplitudes as in the Mother Fit in Sec. ???. In the “PWA” method of SDME extraction, we get the ρ elements in the Adair frame by directly employing Eq. 7.16. The Adair frame is convenient when the production mechanism conserves spin in the s -channel *c.m.* frame. The Helicity (Hel) frame has already been defined in the earlier sections of this chapter, *viz.* the vector meson direction in the *c.m.* frame defines the quantization axis. This is the preferred system for s -channel helicity conservation (SCHC). Under the assumptions of SCHC, $\rho_{00}^{Hel} = \rho_{10}^{Hel} = \rho_{1-1}^{Hel} = 0$ [76]. For the Gottfried-Jackson (GJ) frame, one makes a further boost to the vector meson rest-frame from the overall *c.m.* frame. The quantization axis is along the direction of the incoming photon, as seen in the vector meson rest-frame. For a t -channel exchange of X , the momentum of the incoming photon and X is collinear in the GJ frame. Therefore the ρ elements measure the degree of helicity flip due to the t -channel exchange of X in the GJ frame. For example, if the t -channel exchange particle is a 0^+ , then no helicity flip will occur (TCHC) and the vector meson will have the same helicity as the incoming photon. For this case $\rho_{00}^{GJ} = \rho_{10}^{GJ} = \rho_{1-1}^{GJ} = 0$ [76].

Note that for $m_\phi = m'_\phi = 0$, ignoring the initial and final proton spins (which are not measured)

$$\rho_{00} \sim |\mathcal{A}_{m_\phi=0, m_\gamma=1}|^2 + |\mathcal{A}_{m_\phi=0, m_\gamma=-1}|^2. \quad (7.17)$$

Therefore a non-zero value of ρ_{00} is a direct measurement of the helicity flip between the incoming photon and the outgoing vector meson.

7.3.1 Conversion between the Adair, Helicity and GJ frames

It is clear that knowing the ρ elements in one frame, one can immediately calculate them in any other frame by a Wigner rotation. The y -axis is always the normal to the vector meson production plane; $\vec{y} = \vec{k} \times \vec{q}$, where \vec{k} is the incoming photon direction and \vec{q} is the outgoing vector meson (ϕ) direction. The choice of the z -axis is frame dependent, as described above. For the Adair frame $\vec{z} = \vec{k}$, for the Helicity frame, $\vec{z} = \vec{q}$, and for the GJ frame, $\vec{z} = \vec{k}'$, where \vec{k}' points along the incoming photon direction in the vector meson rest frame. Once the y - and the z -axis has been fixed, $\vec{x} = \vec{y} \times \vec{z}$. Let $\hat{\pi}$ be the direction of the daughter K^+ (for $\phi \rightarrow K^+ K^-$) in the chosen reference frame. Then the angles ζ and φ in Eq. 7.11 are given as [75]:

$$\cos \zeta = \hat{\pi} \cdot \hat{z}, \quad \cos \varphi = \frac{\hat{y} \cdot (\hat{z} \times \hat{\pi})}{|\hat{z} \times \hat{\pi}|}, \quad \sin \varphi = -\frac{\hat{x} \cdot (\hat{z} \times \hat{\pi})}{|\hat{z} \times \hat{\pi}|}, \quad (7.18)$$

In the Rose convention of the signs for the Wigner matrices (this is followed by the Schilling paper [75]), the general form of the density matrix (after parity, Hermiticity and trace conditions

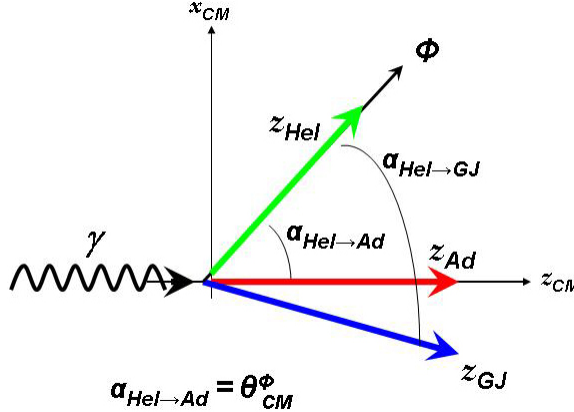


Figure 7.2: The spin-quantization axes for the Helicity (Hel, in green), Adair (Ad, in red) and Gottfried-Jackson (GJ, in blue) frames, in relation to the overall center-of-mass (*c.m.*) frame. The *z*-axis for the overall *c.m.* frame points along the beam direction and coincides with z_{Ad} . Since z_{Hel} points along the direction of the ϕ meson, the angle between the Helicity and Adair frames is just $\theta_{c.m.}^\phi$. The Gottfried-Jackson frame is defined as the direction of the incoming photon, as seen in the rest frame of the ϕ meson. The angle between the Helicity and Gottfried-Jackson frame is given by Eq. 7.22b.

have been placed) is

$$\rho = \begin{pmatrix} \frac{1}{2}(1 - \rho_{00}) & \rho_{10} & \rho_{1-1} \\ \rho_{10} & \rho_{00} & -\rho_{10} \\ \rho_{1-1} & -\rho_{10} & \frac{1}{2}(1 - \rho_{00}) \end{pmatrix}, \quad (7.19)$$

where we remind the reader that this is for unpolarized beam and unpolarized target. The Wigner rotation matrix for spin-1 is¹

$$d^1(\alpha) = \begin{pmatrix} \frac{1+\cos\alpha}{2} & -\frac{\sin\alpha}{\sqrt{2}} & \frac{1-\cos\alpha}{2} \\ \frac{\sin\alpha}{\sqrt{2}} & \cos\alpha & -\frac{\sin\alpha}{\sqrt{2}} \\ \frac{1-\cos\alpha}{2} & \frac{\sin\alpha}{\sqrt{2}} & \frac{1+\cos\alpha}{2} \end{pmatrix}. \quad (7.20)$$

To rotate the density matrix from reference frame *A* to *B*, the transformation is

$$\rho^B = d^1(-\alpha_{A \rightarrow B}) \rho^A d^1(\alpha_{A \rightarrow B}). \quad (7.21)$$

These rotation angles (counter-clockwise is positive) are given by

$$\alpha_{Ad \rightarrow Hel} = \theta_{c.m.}^\phi. \quad (7.22a)$$

$$\alpha_{Hel \rightarrow GJ} = -\cos^{-1} \left(\frac{\beta - \cos \theta_{c.m.}^\phi}{\beta \cos \theta_{c.m.}^\phi - 1} \right) \quad (7.22b)$$

$$\alpha_{Ad \rightarrow GJ} = \alpha_{Ad \rightarrow Hel} + \alpha_{Hel \rightarrow GJ}, \quad (7.22c)$$

where $\beta = \frac{|\vec{p}_K|}{E_K}$ is the velocity of the daughter kaon in the ϕ rest frame (for the $\phi \rightarrow KK$ decay).

¹In the Wigner convention, followed by the PDG [8] for example, the signs of α and ρ_{10} are reversed.

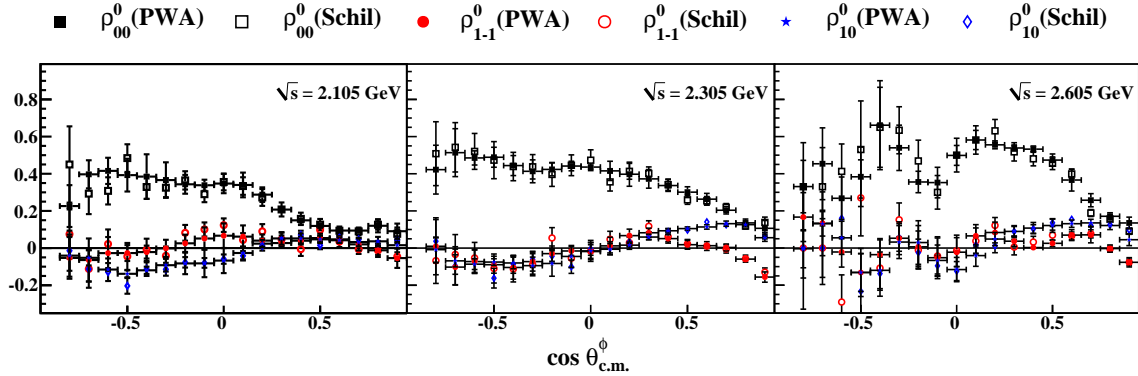


Figure 7.3: Comparison between SDME extraction using the PWA method and Schilling’s method in the Adair frame. Within the limitations of statistical uncertainties, the agreement is excellent.

7.4 Comparison of PWA and Schilling Methods

As mentioned earlier the density matrix in the Adair frame can be directly projected out using Eq. 7.16 and the PWA Mother Fit amplitudes. Equivalently, one can also employ the Schilling’s equation (Eq. 7.11). Fig. shows a comparison between the two methods of extraction using the charged-mode topology. Within the limitations of experimental uncertainties, the agreement is excellent.

7.5 Systematic Uncertainties

As for the $K^+\Sigma^0$ polarization results, there is no standardized method for calculating the systematic uncertainties for the SDME’s. We adopt the results obtained in a previous CLAS analysis for the ωp channel. This study [3] examined the maximal (or rather, the estimated maximal) effect of an incorrect acceptance calculation on the SDME’s. This would distort the acceptance corrected normalized intensity distribution given by Eq. 7.11 and would lead to incorrect values of the ρ elements. The deviation between the two results gave an estimation of the systematic uncertainties as

$$\sigma_{00} = 0.0175, \quad \sigma_{1-1} = 0.0125, \quad \text{and} \quad \sigma_{10} = 0.01. \quad (7.23)$$

Since the underlying assumption for this study was that the intensity distribution for the vector meson decay was given by the Schilling’s equation (Eq. 7.11) it is reasonable to adopt these results for the present analysis as well.

7.6 Final SDME results

Figs. 7.4-7.6 show the spin density matrix elements (SDME) for the charged-mode topology (including the $\Lambda(1520)$ hard cut) in the Adair frame. The most prominent feature is the large value of ρ_{00} , while ρ_{10} and ρ_{1-1} are small, but non-zero. There is a similarity with the corresponding results for the ωp channel [?] in the “hump-like” structure for ρ_{00} . At high \sqrt{s} , the ωp results had a distinct “dip” for ρ_{00} in the mid-forward angles. For the ϕp case, there are indications of a “dip” for ρ_{00} in the mid- to mid-backward angles, though the structure is much less well-defined due to statistical limitations at high \sqrt{s} and $\cos \theta_{c.m.}^\phi < 0$. Fig. 7.9 shows the SDME’s for the neutral-mode topology in the Adair frame. The energy bins are at least 30-MeV-wide in \sqrt{s} . Fig 7.10 shows comparisons between the charged- and neutral-mode SDME results for the ρ_{00} element.

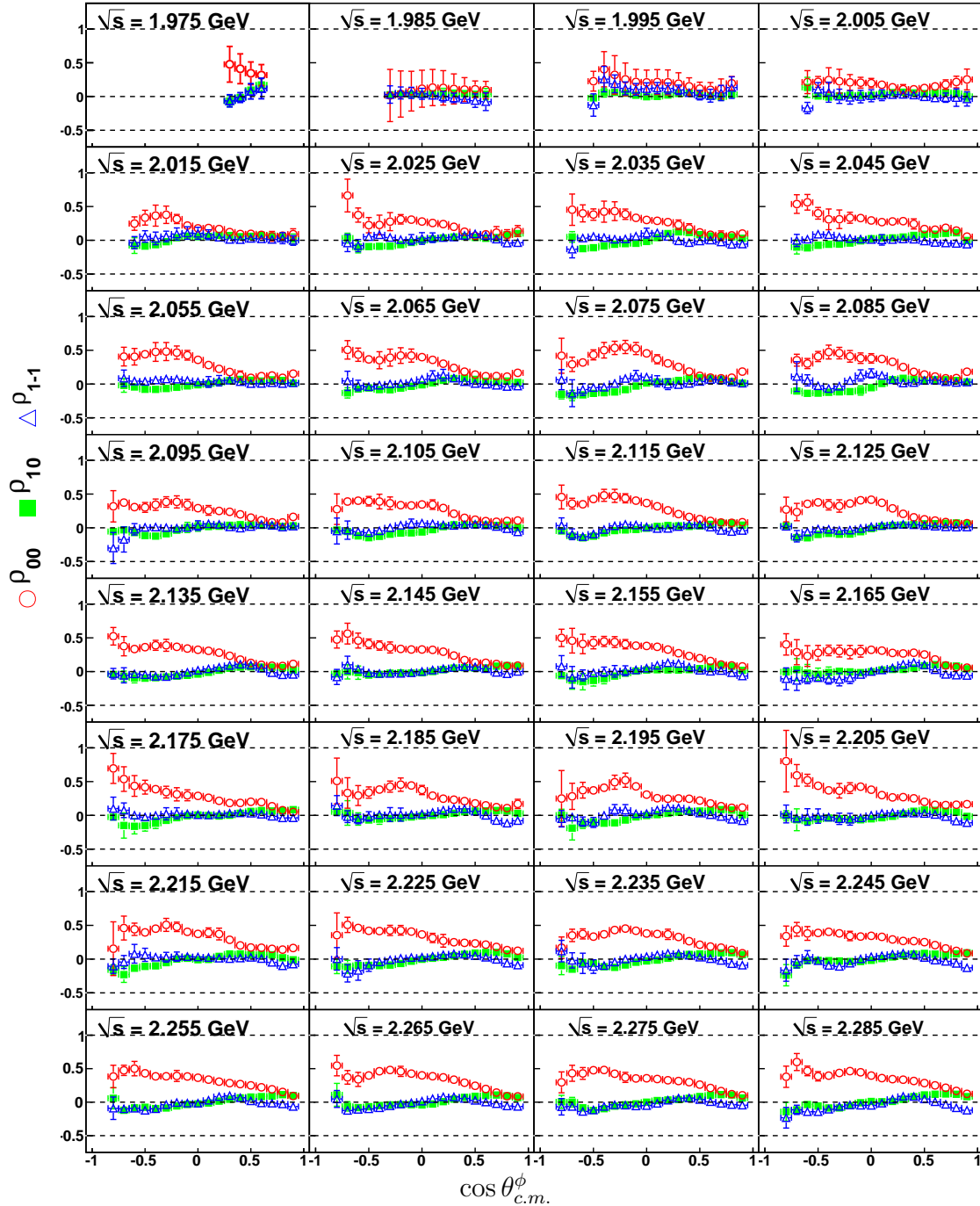


Figure 7.4: (Color On-line) SDME vs. $\cos \theta_{c.m.}^{\phi}$: spin density matrix elements in the Adair frame for the charged-mode topology (with $\Lambda(1520)$ hard cut) in the energy range $1.97 \text{ GeV} \leq \sqrt{s} < 2.29 \text{ GeV}$. The centroid of each 10-MeV-wide bin is printed on the plots. All error bars represent statistical uncertainties only.

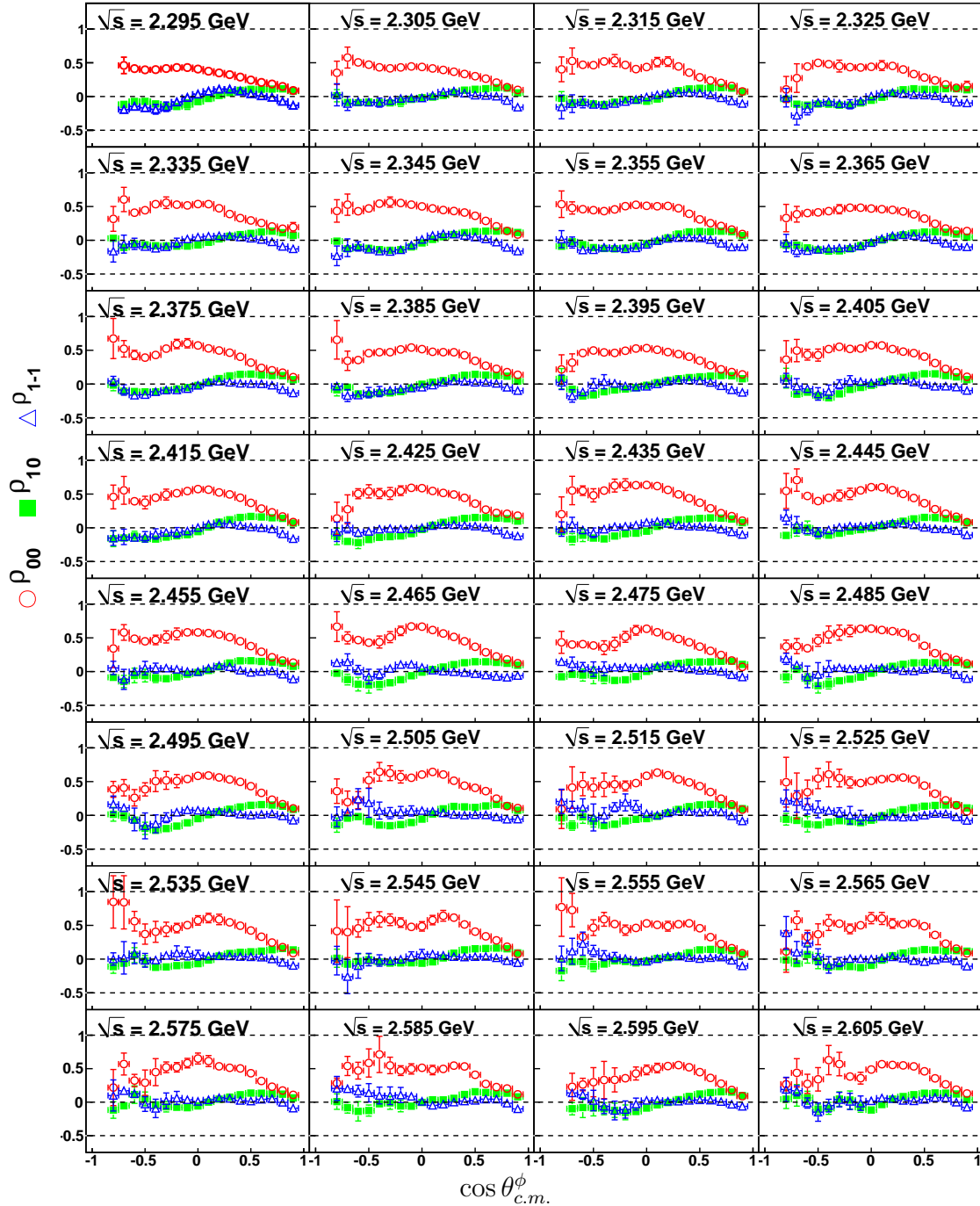


Figure 7.5: (Color On-line) SDME vs. $\cos \theta_{c.m.}^\phi$: spin density matrix elements in the Adair frame for the charged-mode topology with the $\Lambda(1520)$ hard cut in the energy range $2.29 \text{ GeV} \leq \sqrt{s} < 2.61 \text{ GeV}$. The centroid of each 10-MeV-wide bin is printed on the plots. All error bars represent statistical uncertainties only.

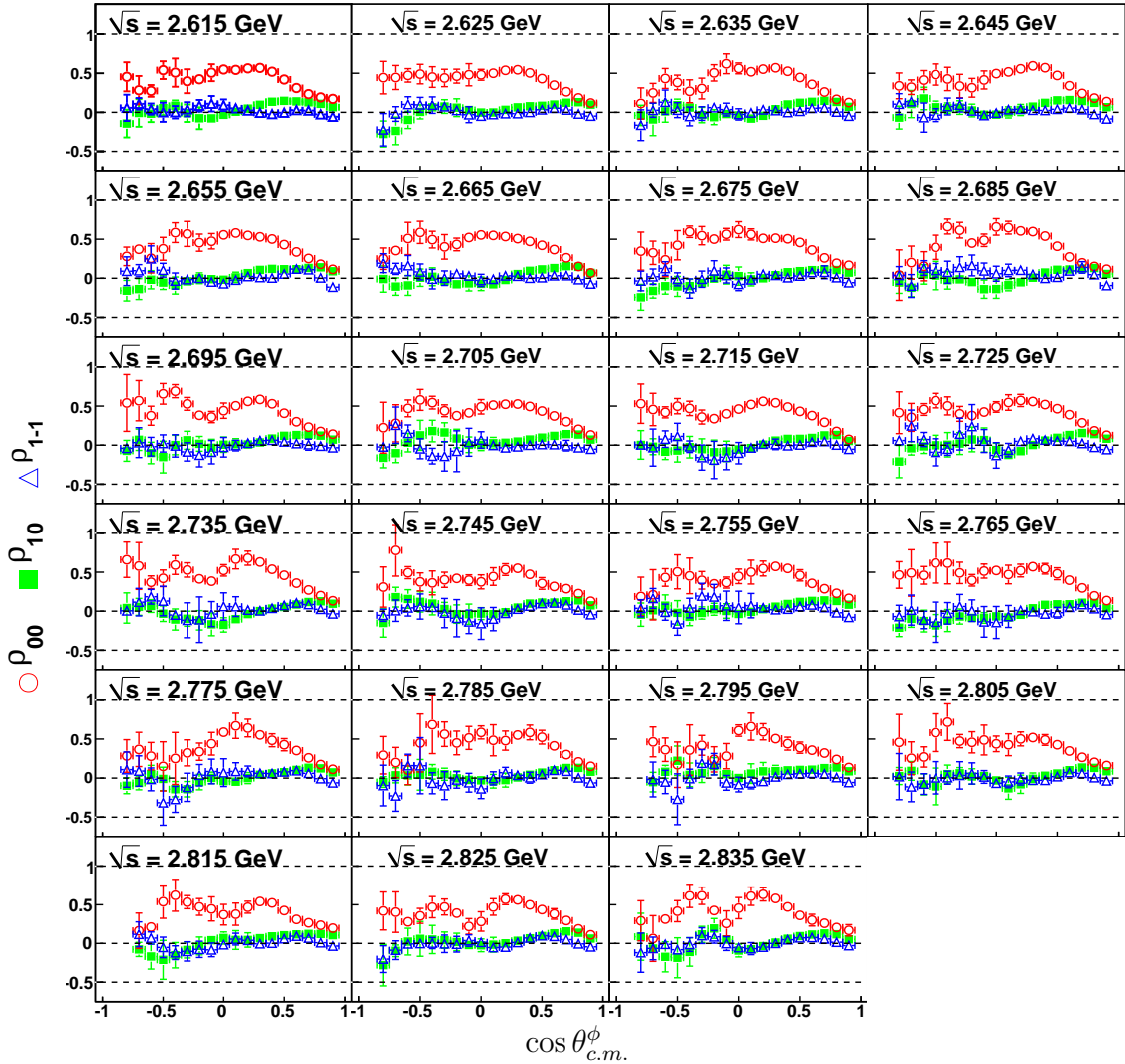


Figure 7.6: (Color On-line) SDME vs. $\cos \theta_{c.m.}^\phi$: spin density matrix elements in the Adair frame for the charged-mode topology with the $\Lambda(1520)$ hard cut in the energy range $2.61 \text{ GeV} \leq \sqrt{s} < 2.84 \text{ GeV}$. The centroid of each 10-MeV-wide bin is printed on the plots. All error bars represent statistical uncertainties only.

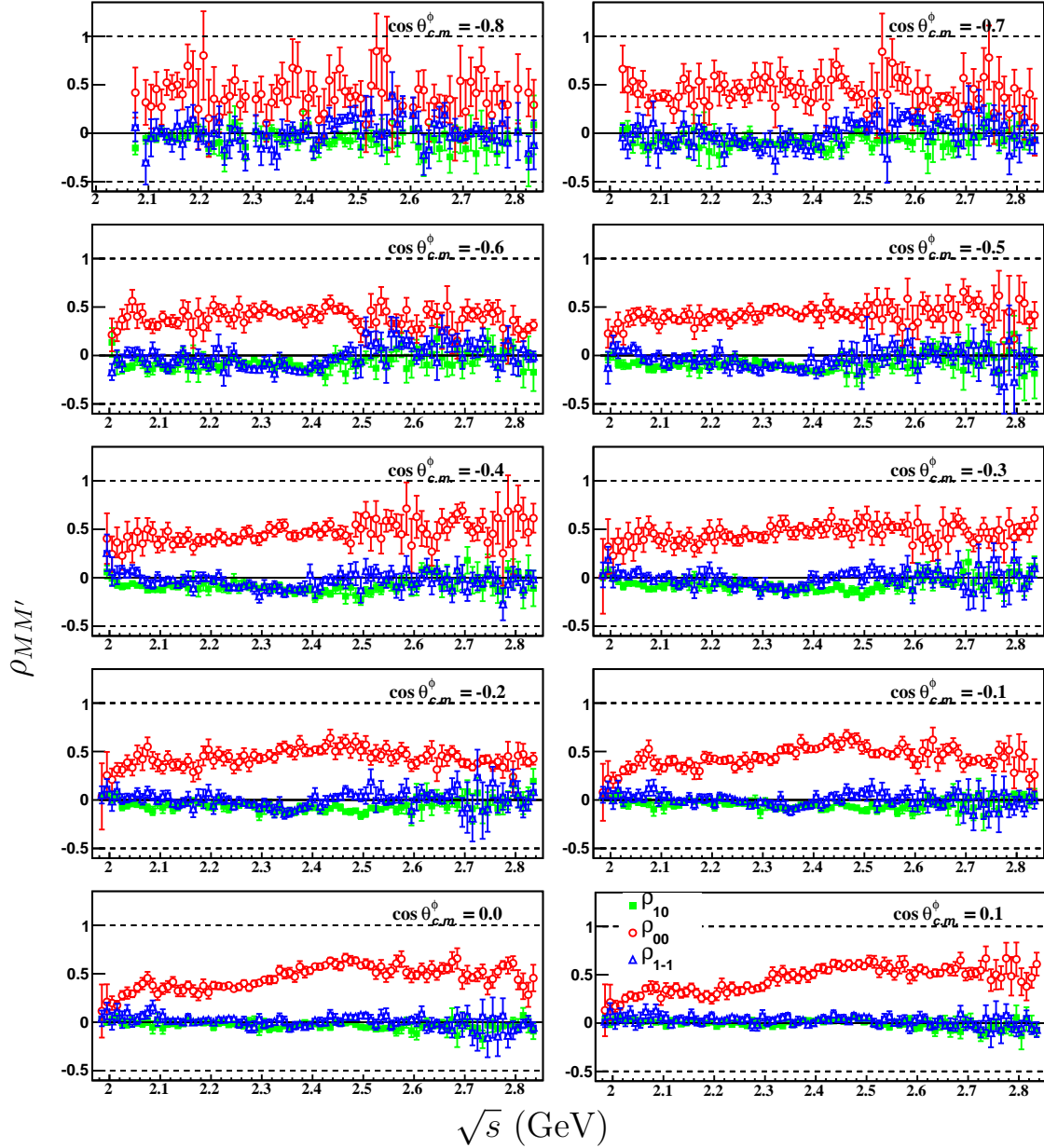


Figure 7.7: (Color On-line) The energy dependence of SDME's (Adair frame) in the backward-angle bins for the charged-mode topology. All error bars represent statistical uncertainties only.

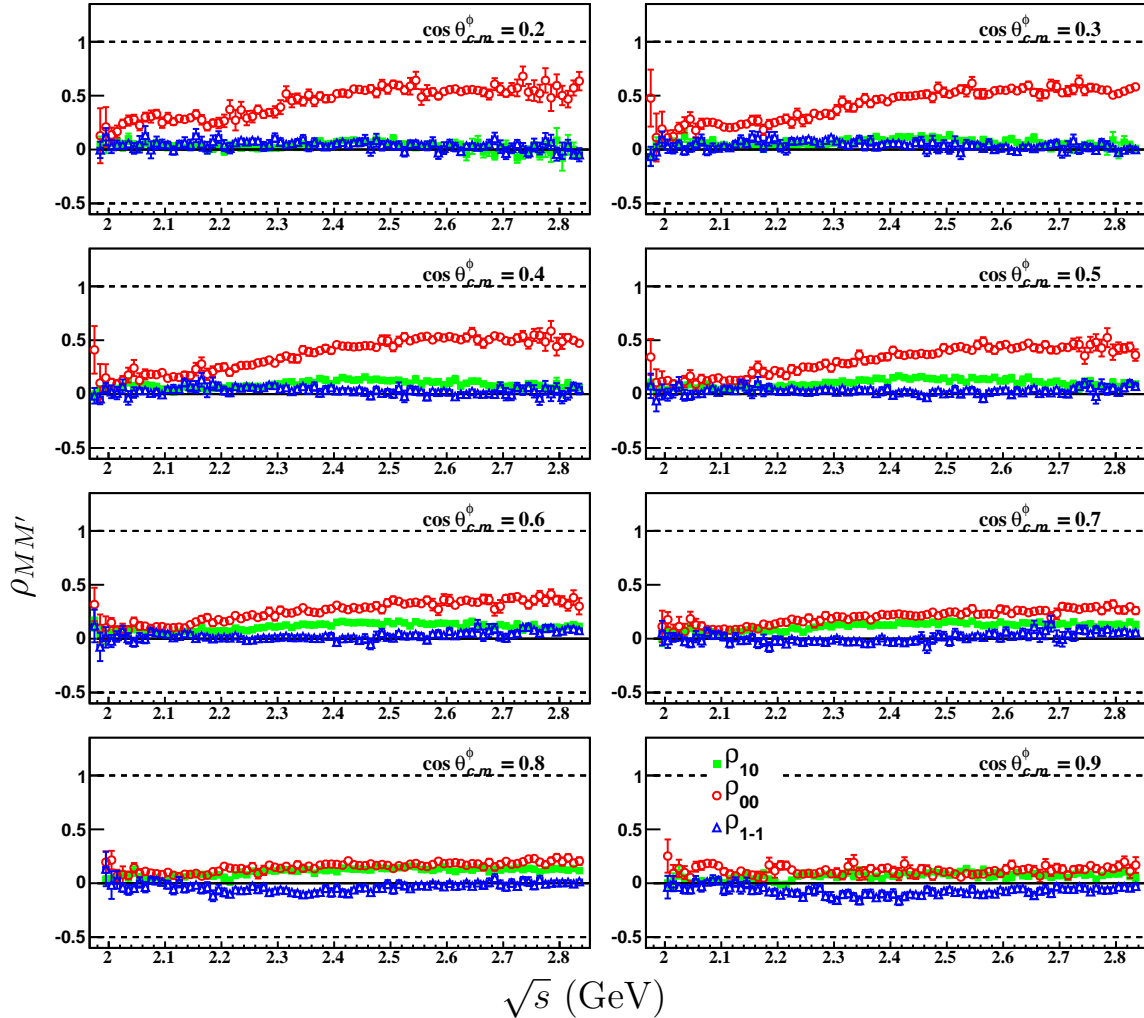


Figure 7.8: (Color On-line) The energy dependence of SDME's (Adair frame) in the mid- and forward-angle bins for the charged-mode topology. All error bars represent statistical uncertainties only.

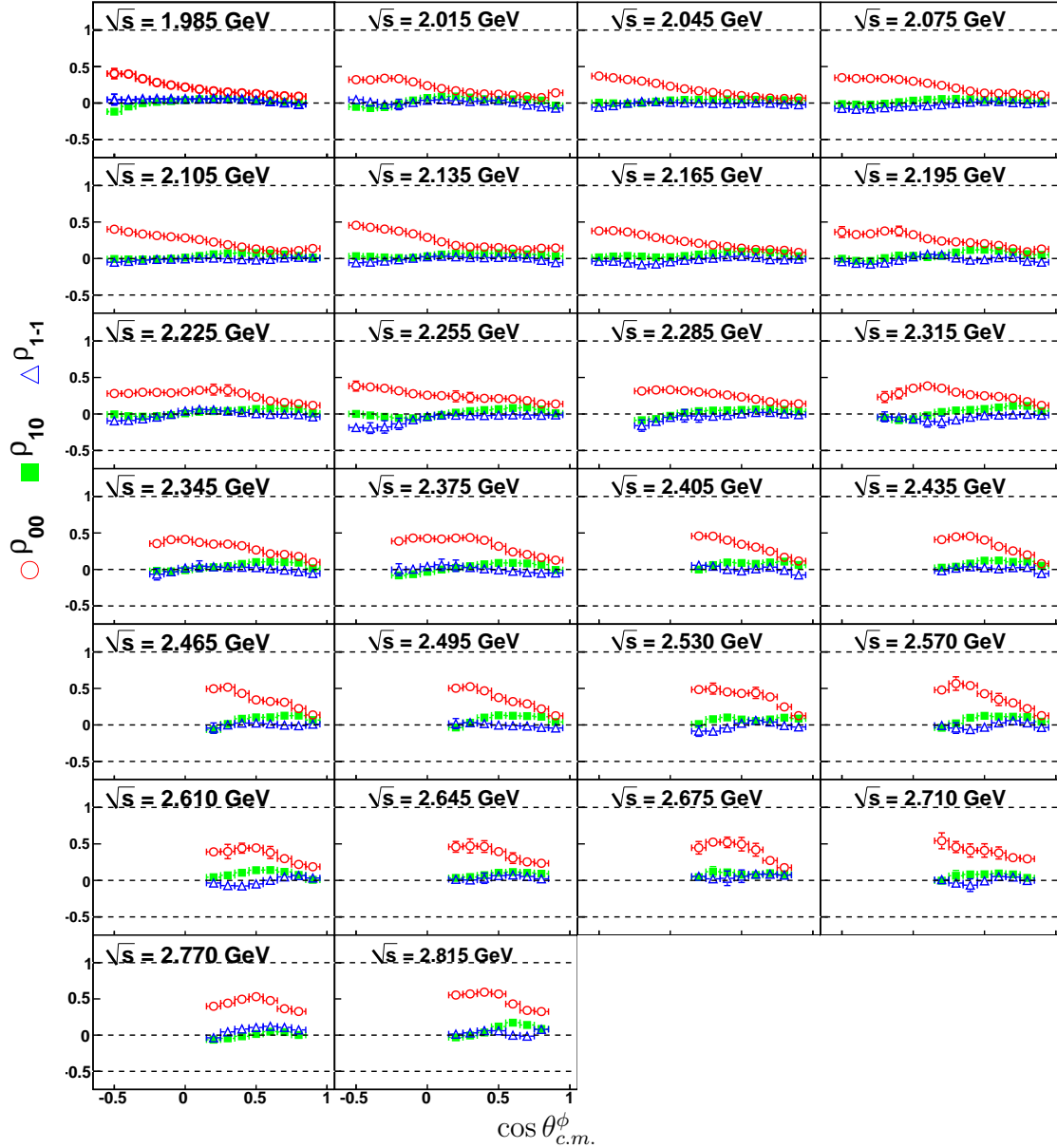


Figure 7.9: (Color On-line) SDME vs. $\cos \theta_{c.m.}$: spin density matrix elements in the Adair frame for the neutral-mode topology. The minimum bin-width is 30-MeV in \sqrt{s} and the centroid of each bin is printed on the plots. All error bars represent statistical uncertainties only.

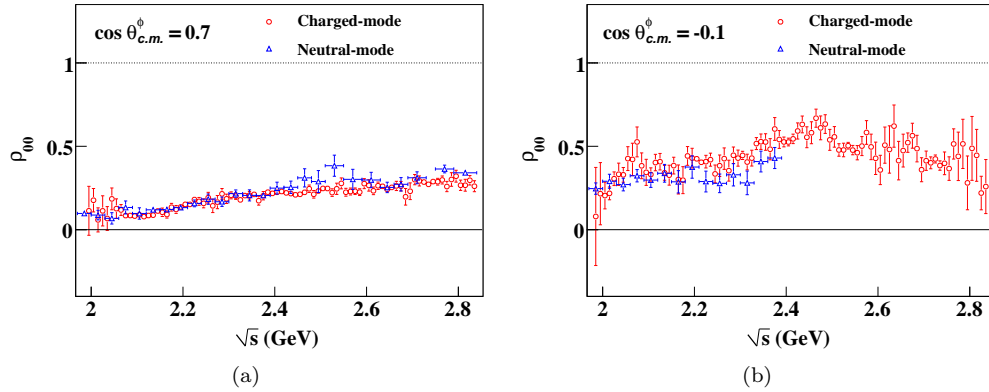


Figure 7.10: (Color On-line) Comparison between the charged- and neutral-mode ρ_{00} results in the Adair frame at (a) forward- and (b) mid-angle regions. While the agreement is generally good in most kinematic regimes, the charged-mode shows traces of a “structure” around $\sqrt{s} \approx 2.1$ GeV in the mid-angle regions. This is coincident with a similar feature for the differential cross sections, though the effect seems to be less prominent for the SDME’s.

Chapter 8

Systematic Studies of $g11a$

We now systematically address several issues either hinted at or touched upon in the earlier chapters. A chronological summary of our progress through this analysis would probably be useful here. We started off by analysing the three-track dataset. The kinematic fitter and the energy, momentum and tagger corrections, as well as the trigger efficiency maps for $g11a$ had already been scrupulously studied, well-established and applied to other channels [4, 5], which gave us confidence in using them. However, our preliminary differential cross sections showed significant discrepancies with Bob Bradford's CLAS $g1c$ results [37] over all energies and angles. Further investigation of $g11a$ [6] revealed that events where the Λ decays outside the start counter are not triggered in the data, something which was not being accounted for in the Monte Carlo. Fine-tuning the Λ decay vertex position reconstruction (from tracking and momentum information) took us a while. The vertexing package [10] being used had its own idiosyncrasies that had to be understood and at places, modified slightly. Note that the version of GSIM being employed at this time did not provide direct access to the decay vertices (see Section 2.1.2).

Including the correction for the Λ decay vertex pulled up our overall differential cross sections, but they were still lower than $g1c$ in a few places. We thus embarked upon a process of making various checks, as accounted in this chapter. This includes a scrutiny of our background subtraction procedure, an extensive TOF-paddle survey, effects of possible K^+ decays in the far interiors of the Drift Chamber regions, differential cross section extraction using unweighted acceptance calculations, amongst others. The gist, after all our corrections, was that, in a *couple of mid-energy, mid-angle bins*, $g11a$ was lower than $g1c$ by $\sim 10\%$. In every other region, including the forward-most angles, the agreement between the two was excellent.

One of the remaining aspects left to check was to abandon the approach of *reconstructing* the Λ decay vertex, but pull out the *actual* vertices directly from GSIM. GSIM was subsequently modified to churn out the Λ decay vertices directly and differential cross sections were extracted anew at five different center-of-mass energies – no systematic shift was noticed in the results. The silver lining however was that the updated version of GSIM enabled us to analyse the two-track dataset as well. The two-track analysis yielded measurements all the way into the backward angles, where the three-track had poor or no statistics at all.

The agreement between the two- and three-track analyses was found to be very good (Figure 4.10). It has to be kept in mind here, how distinct the two analyses really are. Even though both employ the $g11a$ dataset, the three-track analysis makes heavy use of the kinematic fitter, besides employing a physics-weighted acceptance calculation, while the two-track does neither. Given these circumstances, the overall consistency within $g11a$ is noteworthy indeed.

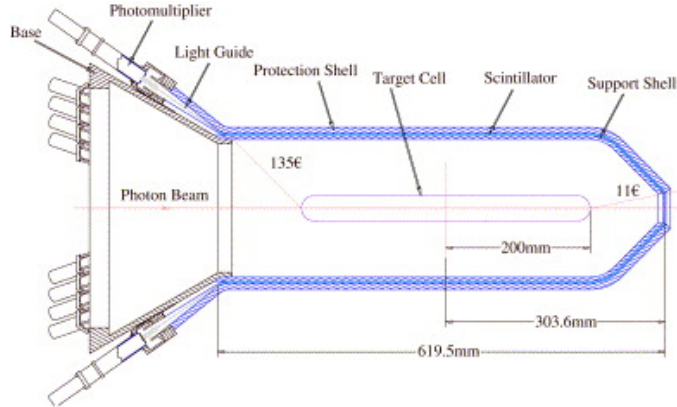


Figure 8.1: Cross-sectional view of the start counter for $g11a$ – it sits roughly 10 cms around the target, about the same as the Λ 's characteristic path-length. (Source: [77])

8.1 Trigger Correction for Λ Decay

Figure 8.1 shows a cross-sectional cutaway of the $g11a$ start counter. Recall that the $g11a$ trigger requires a coincidence between a start counter hit and a TOF paddle hit in the same sector for at least two charged tracks in two different sectors. In the $\gamma p \rightarrow K^+ \Sigma^0 \rightarrow K^+ \gamma \Lambda \rightarrow K^+ \gamma p \pi^-$ reaction chain, one of the hits has to come from the K^+ and the other from either the proton or the π^- , since the breakup momentum for the Λ decay is small and the proton and the π^- mostly go into the same sector, so that even if both the proton and the π^- triggers successfully, it still counts as a single sector-based hit.

Now, the start counter is triggered by charged tracks only, while the Λ is a neutral particle. Coupled with the fact that the Λ decay pathlength is $c\tau \sim 7.89$ cm [8] while the start counter is positioned about 10 cms around the target cell [77], this means that there is a finite chance that the Λ decays *outside* the start counter, the proton/ π^- (travelling radially outwards) miss hitting it, and the event does not trigger. Such an effect is not compensated for in the Monte Carlo however, as trigger information from the start counter is not included in GSIM. Figure 8.2 shows reconstructed Λ decay vertices for the data and the accepted Monte Carlo. The relative position of the start counter is marked by thick black lines. One can immediately spot the difference – for the data, there is a significant drop in occupancy whenever the Λ s decay outside the start counter, while the accepted Monte Carlo occupancy is smooth across the start counter boundary.

As apparent from Figure 8.2a, some “bleed through” occurs across the start counter boundary. This can be attributed to the fact that the opening angle between the proton and the π^- for the Λ decay is small, leading to resolution issues in our reconstruction of the position of closest approach between the two tracks using MVRT [10]. Because of this “bleed through”, instead of applying a hard-cut on both the data and the Monte Carlo based on the reconstructed secondary (Λ decay) vertex, we chose to apply a statistical based “trigger” cut only on the Monte Carlo, as explained below.

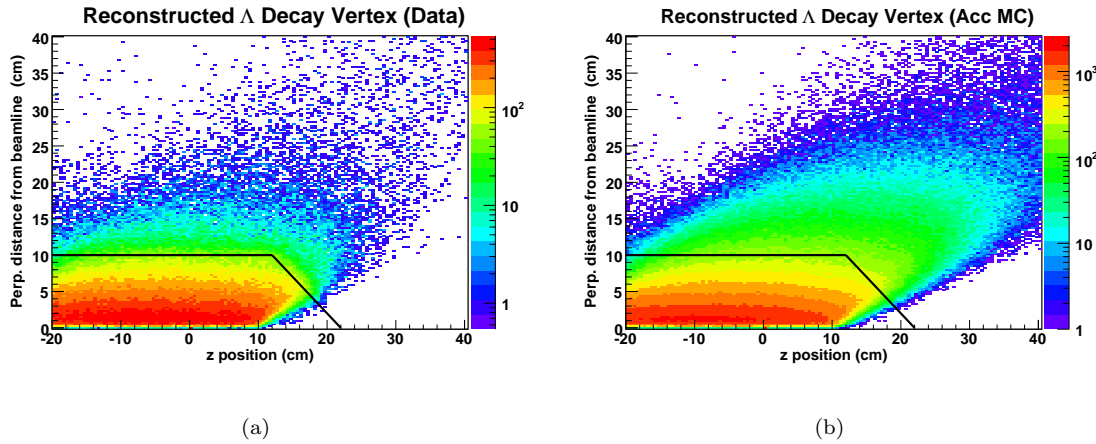


Figure 8.2: Perpendicular distance from beamline versus z position along beamline for the reconstructed Λ decay vertex: (a) data and (b) Monte Carlo. The outline of the start counter is marked by the thick black lines. Aside from the “bleedthrough” (due to resolution issues in the reconstruction fit), there is a sharp drop in occupancy across the start counter boundary for the data.

8.1.1 Simulated Λ Decay Start Counter Trigger

Our starting point is the primary/event vertex $\vec{r}_0 = (x_0, y_0, z_0)$ which is the position of closest approach between the K^+ track and an idealized beam along the center of the target cell, calculated using *MVRT* [10]. We also calculate the Λ momentum $\vec{p}_\Lambda = (p_\Lambda, \theta, \phi)$ as the sum of proton and π^- momenta. The interaction vertex where \vec{p}_Λ is projected to hit the start counter wall is denoted as $\vec{r}_{int} = (x_{int}, y_{int}, z_{int})$. If z_{int} lies prior to the “nose” of the start counter ($z_{nose} \sim 12$ cm), z_{int} and l (pathlength travelled by the Λ before it hits the start counter) are given by:

$$z_{int} = z_0 + \frac{d}{\tan \theta}, \quad \text{and} \quad (8.1a)$$

$$l = \frac{d}{\sin \theta \cos \phi'}, \quad (8.1b)$$

where $d \sim 10$ cm is the shortest radial distance between the beamline and the start counter and ϕ' is the azimuthal angle with respect to the azimuthal center of the CLAS sector in which \vec{p}_Λ belongs (i.e., $\phi' \in [-30^\circ, 30^\circ]$). However, if $z_0 + \frac{d}{\tan \theta} > z_{nose}$, this means that \vec{p}_Λ enters the “nose” region, and the expression for l changes to:

$$l = \frac{z_{nose} + d - z_0}{\cos \theta + \sin \theta \cos \phi'}. \quad (8.2)$$

Using the Λ 's characteristic lifetime $\tau = 2.63 \times 10^{-10}$ s, we can then calculate the characteristic lifetime of the Λ as observed in the laboratory frame to be

$$t = \gamma\tau = \frac{\tau}{\sqrt{1 - \beta^2}}, \quad (8.3)$$

where β is calculated from \vec{p}_Λ . We also calculate the distance d_Λ that the Λ would have traveled in time t to be

$$d_A = \beta c t. \quad (8.4)$$

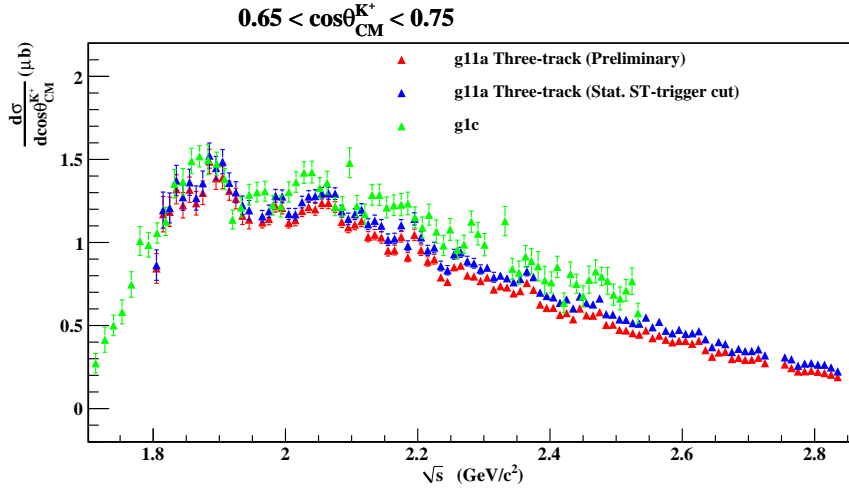


Figure 8.3: Effect of the simulated start counter trigger cut in one of the forward angle bins: in **red** are the preliminary cross-sections, in **blue** are the cross-section after including the cut, while in **green** are the *g1c* results for comparison. Similar results were obtained for other angles as well.

Finally, we consider the exponential nature of the Λ decay and construct the probability $P(l, \beta)$ that the given Λ will intersect the start counter before it decays:

$$P(l, \beta) = \exp\{-l/d_\Lambda\} = \exp\{-l/(\beta ct)\}. \quad (8.5)$$

We then use $P(l, \beta)$ to generate a start counter trigger efficiency along the same lines as we had generated the trigger maps in Section 2.2: a random number x is generated between 0 and 1; if $P(l, \beta)$ is greater than x , we cut the event. In this fashion, we treat the Λ decay effect for the Monte Carlo in a purely statistical fashion, as nature does for the data. Some resolution issues remain, pertaining to how well r_0 and the proton/ π^- momenta are known. To check for such effects we made slight variations in the parameters d and z_{nose} , but found minimal effect on the cross-sections.

The effect of the cut is ubiquitous and substantial. Figure 8.3 shows the comparison in one of the forward angle bins. Similar results are obtain in other angles as well – the cross-sections increase by 5-10% after the application of the cut.

8.1.2 Comparison With Hard Cut

To further check the credibility of the above cut, we generated Monte Carlo with a version of GSIM that provided direct access to the Λ vertices and placed a hard cut at the start counter limits. In cylindrical co-ordinates, let the secondary Λ decay vertex be $\vec{r}_{sec} = (\rho_{sec}, z_{sec}, \phi_{sec})$ and ϕ'_{sec} be the sector-based azimuthal angle. If $z_{sec} < z_{nose}$, we cut the event if

$$\rho_{sec} \cos \phi'_{sec} > d, \quad (8.6)$$

while if $z_{sec} > z_{nose}$, the event is cut if

$$\rho_{sec} \cos \phi'_{sec} > d - (z_{sec} - z_{nose}). \quad (8.7)$$

Instead of processing the entire dataset, we test-ran on five energy bins – $\sqrt{s} = 2.105, 2.135, 2.165, 2.205$ and 2.235 GeV, that is, bins which have substantial difference between the *g11a* and *g1c*

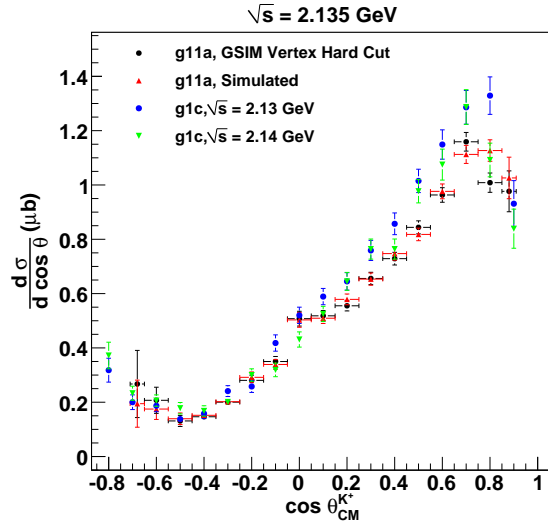


Figure 8.4: Comparison between the simulated trigger cut and a hard cut on GSIM secondary Λ decay vertices for $\sqrt{s} = 2.135 \text{ GeV}$. No systematic difference is apparent between the two. Checks were also done at four other energies yielding similar results. Two overlapping bins from $g1c$ are also shown for comparison.

results. Figure 8.4 compares the cross-sections between the simulated trigger and the hard cut, for the energy bin $\sqrt{s} = 2.135 \text{ GeV}$. The difference between is well within statistical and systematic error limits. This lends further credence to our usage of the simulated start counter trigger – all final $g11a$ results quoted for the three-track topology are obtained using the simulated trigger cut while the two-track results are using the hard cut.

8.2 Background Subtraction Systematics Check

After the application of all our cuts, the three-track $K^+\Sigma^0$ dataset is a pretty clean channel. Some 5-15% background remains, which is subsequently removed by our background subtraction method. Furthermore, no systematic shifts are noticed by the usage of different background shapes, which points towards the fact that we are not truncating events from any specific kinematic region. As an extreme case, consider the following: suppose our background subtraction scheme is completely inaccurate. We can instead apply a hard cut on the Σ^0 invariant mass, demanding $MM(K^+)$ to be within $1.192 \pm 0.02 \text{ GeV}$. This cut is applied on both the data and the Monte Carlo, but instead of weighing the data by Q -values from the background fits, we take all the Q 's to be unity. By doing this we are intentionally over-estimating our data yields because we know that our background levels are not completely null.

Figure 8.5 compares the cross-sections obtained by the above method to our original cross-sections as well as to $g1c$ results. From this plot we can conclude that everything else remaining the same, the discrepancy between $g1c$ and $g11a$ cannot be caused by our background subtraction method, since, even with the maximum over-estimated yield for the the data, $g11a$ is still lower than $g1c$.

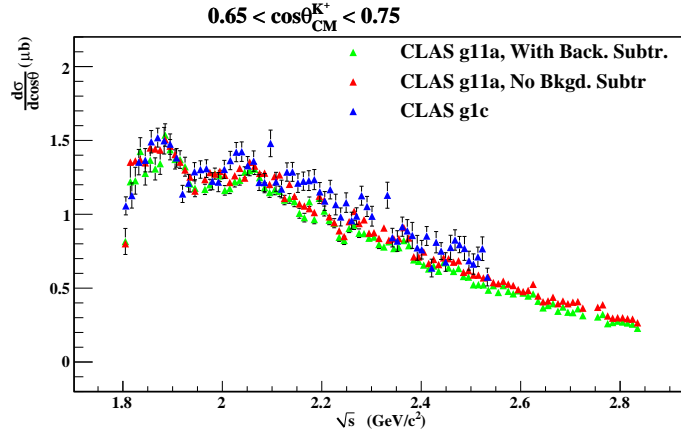


Figure 8.5: Cross-sections with $Q = 1$ for all events in red while original cross-sections are in green. Even after ignoring any background subtraction, the $g11a$ cross-sections are lower than $g1c$ (in blue)—the difference thus cannot be due to systematics in our background subtraction scheme.

8.3 Acceptance Calculation

One of the major differences between the (three-track) $g11a$ and (two-track) $g1c$ analyses is the way acceptance is calculated. Recall from Equation 4.37 that the three-track $g11a$ calculation invokes a physics-weighted acceptance calculation, while $g1c$ employed a less sophisticated unweighted calculation. To check how this difference can potentially affect our results, we re-extracted our cross-sections using the unweighted acceptance method. The results are shown in Figure 8.6. Though the cross-sections increase slightly with the unweighted acceptance, it cannot account for the larger difference between $g11a$ and $g1c$. Not that this was unexpected, but it serves as a confirmation on the fact that the physics model little impact on the cross-section calculation.

8.4 TOF Paddle Survey

A given value of \sqrt{s} and $\cos \theta_{CM}^{K^+}$ roughly maps on to a small “band” of TOF scintillator paddles that the K^+ s can hit in each sector. Since the difference between $g11a$ and $g1c$ cross-sections lies only in a few localized \sqrt{s} and $\cos \theta_{CM}^{K^+}$ bins (mid-energy, mid-angles), we carried out a careful survey of the TOF paddle hit occupancies in these kinematic regions. Note that at the time of this analysis, a detailed study of the systematic uncertainties for $g11a$ had already been carried out using the much higher-statistics $\gamma p \rightarrow p\pi^+\pi^-$ channel [13]. Problematic TOF paddles identified therein were already removed at the start of this analysis. However, these studies did not make any direct observation of TOF paddle efficiencies for the K^+ s.

Paddle 23 lies at the juncture of a discontinuity in the alignment of the scintillators giving rise to occasional physical overlaps between paddle 23 and 24. In this region, the tracking software cannot reliably decide on which of the two paddles a particular track passed through. On such occasions a default zero TOF paddle id is sometimes assigned to the track—to do away with these inconsistencies, we decided to remove paddle 23 altogether from this analysis.

Paddles 24 and 25 also seem questionable from the above point of view. However, removal of these paddles had almost no effect on the cross-sections, so we decided to keep them. Figure 8.7

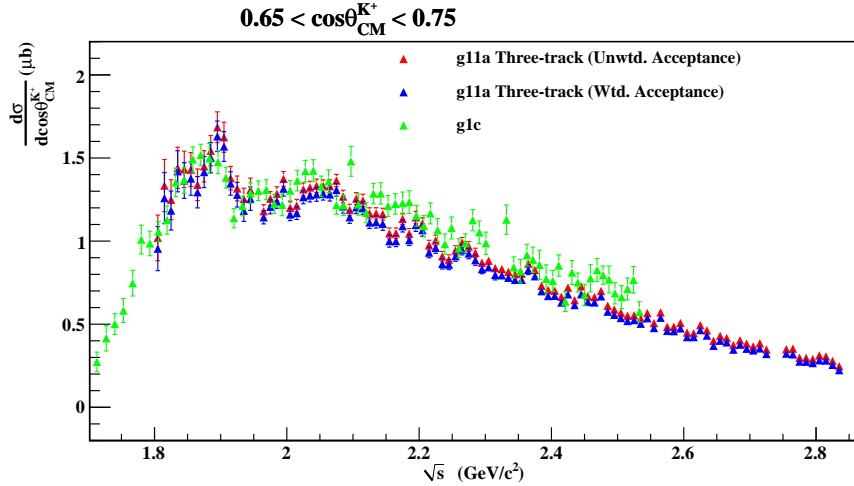


Figure 8.6: Effect of unweighted acceptance calculation as opposed to a physics-weighted acceptance, for the $g11a$ three-track dataset. The difference is small and cannot account for the $\sim 10\%$ difference between $g11a$ and $g1c$.

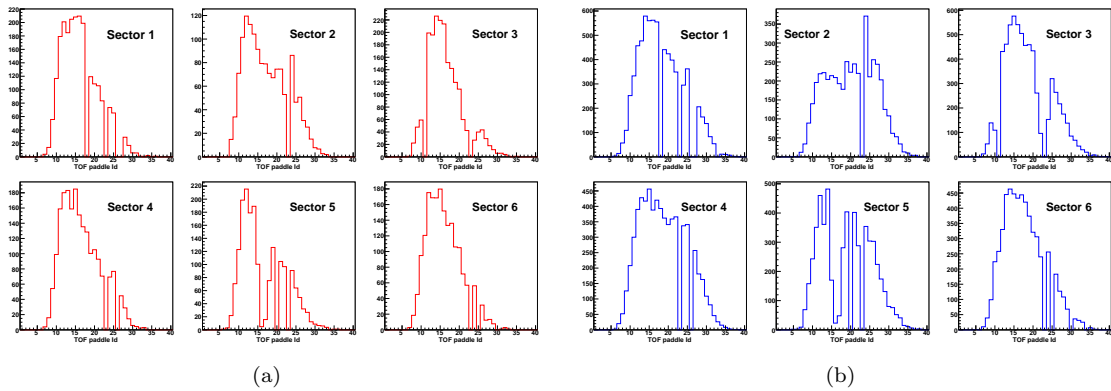


Figure 8.7: TOF paddle survey for (a) data (b) accepted Monte Carlo in the $\sqrt{s} = 2.135$ GeV bin. Paddle 23 is removed in all the sectors. Paddle 24 in sector 2 looks somewhat over-populated. This might be due to a spill-over from hits in Paddle 23. However, the effect occurs in both data and Monte Carlo. Cross-sections with this paddle removed over all sectors demonstrated no visible change either, so we chose to keep it.

shows a sector-wise comparison of TOF paddle occupancies between data and accepted Monte Carlo for the $\sqrt{s} = 2.135$ GeV bin. Overall, all the features present in the data are replicated in the Monte Carlo.

8.5 A Few Other Checks

8.5.1 Re-entry of proton/ π^- Into Start Counter Region

The trigger correction in Section 8.1 assumes that the proton or the π^- from the Λ decay does not re-enter the start counter region again. To check for the frequency of such events, we generated a “trigger bit” using Monte Carlo $\gamma p \rightarrow K^+ \Sigma^0 \rightarrow K^+ \gamma \Lambda \rightarrow K^+ \gamma p \pi^-$ events where the Λ was propagated in space and decayed by the event generator before submitting the event to GSIM. The propagation of the proton and the π^- from the Λ decay vertex onwards were then reconstructed using their individual momenta. In case any of the projected proton/ π^- trajectories re-entered the start counter region, their corresponding start counter sector id’s were noted. If the track satisfied the “Level 1” trigger condition (that is, the start counter sector id and the TOF paddle sector id matched) the trigger bit was set to 1 for the particular track. The event was cut unless at least two tracks “triggered” in this fashion (for the K^+ , the propagation vertex was simply the event vertex). In other words, the Level 1 trigger for $g11a$ was reconstructed “by hand”. Inclusion of the above cut was found to have almost zero influence on the differential cross sections. We therefore concluded that the frequency of events where the Λ decays outside the start counter but the proton/ π^- re-enters it and triggers the event, is very small.

8.5.2 Trigger Map For K^+

Recall from Section 2.2 that our trigger efficiency correction for K^+ uses the π^+ trigger map. This is justified on the account that K^+ ’s and π^+ ’s, having same the same charge and comparable masses, should have similar ionization properties. Given that the mass of K^+ lies mid-way between the proton and π^+ masses, the other possibility is to apply the p trigger map for the K^+ . The cross-sections obtained by applying the proton map (instead of the π^+ map) for the K^+ is shown in Figure 8.8 for one particular \sqrt{s} bin – no systematic shift is noticeable.

8.5.3 Additional $MM(K^+)$ Cuts (Three-track Topology)

Figure 8.9a shows the invariant (p, π^-) mass plotted versus the missing mass off K^+ ($MM(K^+)$) for the accepted Monte Carlo (three-track topology). The small “band” of events above $MM(K^+) = 1.24$ GeV passes all our event selection and PID cuts but seems to have an incorrect mass for the Σ^0 . However, the invariant (p, π^-) mass for these events seems to be around the correct Λ mass. Note that the (p, π^-) invariant mass reconstruction does not involve any K^+ momentum resolution (while $MM(K^+)$ obviously does). Furthermore, since only $K^+ \Sigma^0$ events were thrown in the Monte Carlo, we know that the only way a well-resolved Λ can arise is from a decaying Σ^0 . We thus conclude that these represent well-identified $K^+ \Sigma^0$ events after all, but where the K^+ decays somewhere deep inside the Drift Chamber regions. Since all the prominent K^+ decay modes produce a single positively charged track (along with other neutral tracks), the topology of the reaction is maintained; save that the reconstructed K^+ momentum gets affected in the process.

To avoid systematic errors due to such events, we place additional \sqrt{s} dependent $MM(K^+)$ cuts on both the data and the Monte Carlo as follows. Figure 8.9b shows the Q -value weighted (background subtracted) occupancy for the data for every \sqrt{s} bin. The $MM(K^+)$ cut limits are shown by the heavy red lines in this plot – they mark the $MM(K^+)$ values where the occupancy drops below 1% of the maximum on either side for that particular \sqrt{s} bin. The cut does not have a

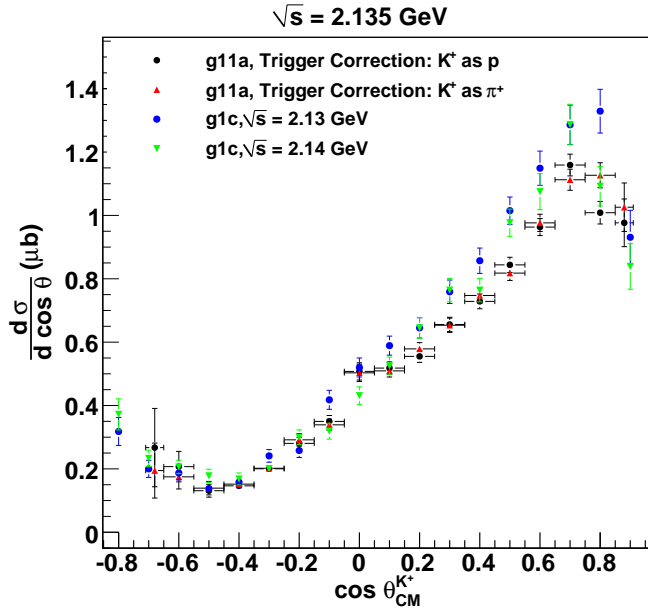


Figure 8.8: Effect of using the proton trigger efficiency map for K^+ instead of the π^+ map (used for rest of the analysis). No systematic shift is noticeable. Overlaid are the CLAS $g1c$ results for comparison.

significant effect on the cross-sections, but this study contributes towards a better understanding of some of the subtler aspects of this channel.

8.5.4 Additional $MM(K^+)$ Cuts (Two-track Topology)

Inkeeping with the discussion in the previous sub-section, we also make a similar cut for the 2-track dataset. The \sqrt{s} dependent $MM(K^+)$ limits in the cut are shown by the heavy red lines in Figure 8.10.

8.5.5 Additional Sector 5 Fiducial Cut

Sector-based studies of $g11a$ using the $\gamma p \rightarrow K^+ \Lambda$ channel by McCracken [6] indicated some additional inconsistencies in our understanding of certain regions of the CLAS detector pertaining to Sector 5. The effect seemed to be localized in $0.45 < \theta_{lab}^{K^+} < 0.55$ (Sector 5) but independent of the K^+ track momentum. McCracken *et al* thus chose to remove events that included *any* track (proton/ K^+/π^-) belonging to Sector 5 and satisfying $0.45 < \theta_{lab} < 0.55$. The effect of the cut on the overall dataset was small but it resulted in greater consistency in the $\gamma p \rightarrow K^+ \Lambda$ differential cross sections among the six sectors of CLAS. Our statistics for the $\gamma p \rightarrow K^+ \Sigma^0$ channel did not suffice for a similar sector based study of the differential cross sections, but given the similarity in kinematics between the two hyperon reactions, we found it prudent to include this cut in our present analysis too.

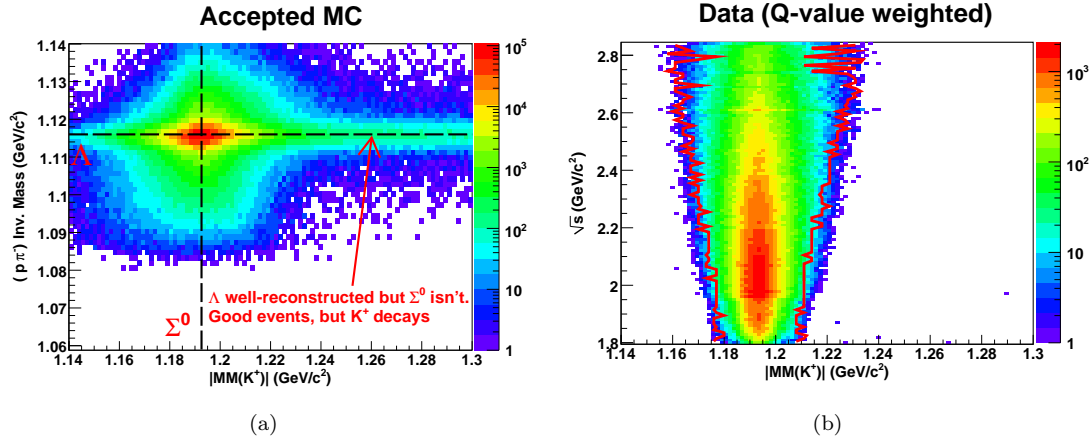


Figure 8.9: Three-track topology: (a) Possible K^+ decay inside CLAS during $K^+\Sigma^0$ photoproduction. The effect is explained in the text. (b) \sqrt{s} dependent $MM(K^+)$ cuts demarcated by the bold red lines – only events lying between these demarcations were accepted (both for data and Monte Carlo).

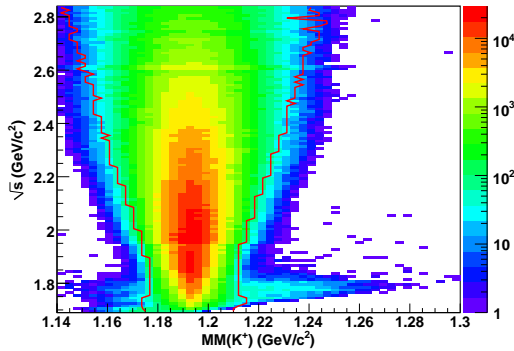


Figure 8.10: Two-track topology: Q -value weighted data events. The slightly long “tail” in $MM(K^+)$ near the threshold bins occurred at the very backward angles, due to extremely limited statistics for these kinematics. The \sqrt{s} dependent $MM(K^+)$ cuts limits are shown by the thick red lines, as for the 3-track case in Figure 8.9b.

8.6 Summary

We studied possible avenues for systematics issues in our analysis techniques and the $g11a$ dataset *per se*. Nuances in the kinematics of the $\gamma p \rightarrow K^+ \Sigma^0$ channel in conjugation with the $g11a$ trigger results in subtle issues in event triggering. We described in detail the resolution of this and some other minor effects. After all corrections, our final differential cross sections for $g11a$ is in fair to very good agreement with previous CLAS $g1c$ results (see also Section 4.9).

Bibliography

- [1] M. Ungaro, R. De Vita, and L. Elouadrhiri. *g11a data processing*. CLAS Analysis Note 2005-014 (2005).
- [2] M. Williams and C.A. Meyer. *Kinematic Fitting in CLAS*. CLAS Note 2003-017
- [3] M. Williams. *Measurement of Differential Cross Sections and Spin Density Matrix Elements along with a Partial Wave Analysis for $\gamma p \rightarrow p\omega$ using CLAS at Jefferson Lab*. Ph.D. Thesis, Carnegie Mellon University (2007).
- [4] M. Williams, et al. *Differential Cross Sections and Spin Density Matrix Elements for $\gamma p \rightarrow p\omega$* . submitted to Phys. Rev. C (2008).
- [5] M. Williams, et al. *Photoproduction of $p\eta$ using CLAS*. submitted to Phys. Rev. C (2008).
- [6] M. McCracken. *A Study of $K^+\Lambda$ Photoproduction in the CLAS g11a Dataset: Differential Cross Section, Recoil Polarization, and a Partial-Wave Analysis*. Ph.D. Thesis, Carnegie Mellon University (2008).
- [7] Robert K. Bradford *Measurement of differential cross sections and C_X and C_Z for $\gamma p \rightarrow K^+\Lambda$ and $\gamma p \rightarrow K^+\Sigma^0$ using CLAS at Jefferson Lab*. Ph.D. Thesis, Carnegie Mellon University (2005).
- [8] W.-M. Yao et al. *Review of Particle Physics*. J. Phys. G **33**, 1 (2006).
- [9] E. Pasyuk. *The CLAS ELOSS Package*. Software available via the CLAS CVS repository under `clas/utilities/packages/eloss`.
- [10] J. McNabb. *Photoproduction of Λ and Σ^0 Hyperons off Protons in the Nucleon Resonance Region using CLAS at Jefferson Lab*. Ph.D. Thesis, Carnegie Mellon University (2004).
- [11] M. Williams, D. Applegate, and C. A. Meyer. *Determining Momentum and Energy Corrections for g1c Using Kinematic Fitting*.
- [12] D. Sober, H. Crannell, and F. Klein. *The Tagger Energy Scale: Interpreting the CMU Kinematic Fit Results* CLAS Analysis Note 2004-019 (2004).
- [13] D. Applegate, M. Bellis, Z. Krahn, C. Meyer, and M. Williams. *A Detailed Study of the Sources of Systematic Errors in the CLAS g11 Data*. CLAS Analysis Note 2006-017 (2006).
- [14] M. Holtrop. *GSIM: CLAS GEANT Simulation*.
http://www.physics.unh.edu/maurik/Gsim/gsim_current_code_dev.shtml
- [15] M. Battaglieri and R. De Vita. *The g11 Triggers efficiency*. CLAS Internal Note/Private Communication. (2005).

- [16] R. Schumacher. *Photon Attenuation in the CLAS Beam Line*. CLAS Note 2001-010.
- [17] W. Rarita and J. Schwinger. *On a Theory of Particles with Half-Integral Spin*. Phys. Rev. **60**, 61 (1941).
- [18] Charles Zemach. *Three-Pion Decays of Unstable Particles*. Phys. Rev. B **133**, 1201-1220 (1964).
- [19] S. U. Chung. *Spin Formalisms*. BNL Preprint BNL-QGS-02-0900 (2004).
- [20] M. E. Peskin and D. V. Schroeder. *An Introduction to Quantum Field Theory*. Westview Press (1995).
- [21] S. Weinberg. *The Quantum Theory of Fields, Vol. 1: Foundations*. Cambridge University Press (1995).
- [22] C. Itzykson, J-B. Zuber. *Quantum Field Theory*. Dover Publications (2006).
- [23] A.V. Anisovich, E. Klempt, A.V. Sarantsev and U Thoma. *Partial-wave decomposition of pion and photoproduction amplitudes*. Eur. Phys. J. A **24**, 111-128 (2005).
- [24] J. D. Jackson. *Classical Electrodynamics*. Wiley 3 ed. (1998).
- [25] E. D. Commins and P. H. Bucksbaum. *Weak interactions of leptons and quarks*. Cambridge University Press (1983).
- [26] S. Janssen, J. Ryckebusch, D. Debruyne, and T. Van Cauteren. *Kaon photoproduction: Background contributions, form factors, and missing resonances*. Phys. Rev. C **65**, 015201 (2001).
- [27] H. Haberzettl, C. Bennhold, T. Mart, and T. Feuster. *Gauge-invariant tree-level photoproduction amplitudes with form factors*. Phys. Rev. C **58**, R40 - R44 (1998).
- [28] R. M. Davidson and R. Workman. *Form factors and photoproduction amplitudes* Phys. Rev. C **63**, 025210 (2001).
- [29] A. Usov and O. Scholten. *KLambda and KSigma photoproduction in a coupled-channels framework*. Phys. Rev. C **72**, 025205 (2005)
- [30] B. C. Pearce and B. K. Jennings. *A relativistic, meson exchange model of pion-nucleon scattering*. Nucl. Phys. A **528**, 655 (1991).
- [31] S. U. Chung. *Formulas for Partial Wave Analysis, Version II*. Brookhaven National Laboratory Preprint BNL-QGS-93-05 (1993).
- [32] F. James. *MINUIT: Function Minimization and Error Analysis, v. 94.1*. CERN Program Library D506.
- [33] S. Christo. *The g11a Target Cell*, http://www.jlab.org/~christo/g11a_target.html.
- [34] L. Lyons *et al.* *How to combine correlated estimates of a single physical quantity* Nucl. Instrum. Methods A **270**, 110 (1988).
- [35] A. Valassi. *Combining correlated measurements of several different physical quantities* Nucl. Instrum. Methods A **500**, 391 (2003).
- [36] T. Aaltonen, *et al.* (CDF collaboration), *Measurement of W-boson helicity fractions in top-quark decays using $\cos\theta^*$* Phys. Lett. B **674**, Issue 3, 160-167 (2009).
- [37] R. Bradford, *et al.* (CLAS Collaboration), *Differential cross sections for $\gamma p \rightarrow K^+ Y$ for Λ and Σ^0 hyperons*. Phys. Rev. C **73**, 035202 (2006).

- [38] K. H. Glander, *et al.* (SAPHIR Collaboration), *Measurement of $\gamma p \rightarrow K^+\Lambda$ and $\gamma p \rightarrow K^+\Sigma^0$ at photon energies up to 2.6 GeV*. Eur. Phys. J. A **19**, 2 (2004).
- [39] H. Kohri *et al.* (LEPS Collaboration), *Differential Cross Section and Photon-Beam Asymmetry for the gamma n->K+Sigma- Reaction at Egamma=1.52.4 GeV* Phys. Rev. Lett. **97**, 082003 (2006).
- [40] M. Sumihama, *et al.* (LEPS Collaboration), *The $\gamma p \rightarrow K^+\Lambda$ and $\gamma p \rightarrow K^+\Sigma^0$ reactions at forward angles with photon energies from 1.5 to 2.4 GeV*. Phys. Rev. C **73**, 035214 (2006).
- [41] G. Bunce *et al.*, *Hyperon Polarization in Inclusive Production by 300-GeV Protons on Beryllium*. Phys. Rev. Lett. **36**, 1113 - 1116 (1976).
- [42] H. -W. Siebert, *The challenge of polarizations in hadronic hyperon production*. Eur. Phys. J. Special Topics textbf{162}, 147 (2008)
- [43] W-T. Chiang and F. Tabakin, *Completeness rules for spin observables in pseudoscalar meson photoproduction*. Phys. Rev. C **55** 2054 (1997).
- [44] C.G. Fasano *et al.*, *Spin observables at threshold for meson photoproduction*. Phys. Rev. C **46** 2430 (1992).
- [45] G.F. Chew *et al.*, *Relativistic dispersion relation approach to photomeson production*. Phys. Rev. **106** 1345 (1957).
- [46] R. L. Walker, *Phenomenological analysis of single-pion photoproduction*. Phys. Rev. **182** 1729 (1969).
- [47] S. Barker *et al.*, *Complete experiments in pseudoscalar photoproduction*. Nucl. Phys. B **95** 347 (1975).
- [48] N. Levy *et al.*, *Kaon photoproduction*. Nucl. Phys. B **55** 493-512 (1973).
- [49] R. A. Adelseck and B. Saghai, *Kaon photoproduction: data consistency, coupling constants, and polarization observables*. Phys. Rev. C **42** 108-127 (1990)
- [50] P. Eugenio *et al.*, (CLAS Collaboration), *Search for Missing Nucleon Resonances in the Photoproduction of Hyperons Using A Polarized Photon Beam and A Polarized Target*. Jefferson Lab Experiment E02112.
- [51] R. Bradford. *Measurement of Differential Cross Sections and C_x and C_z for $\gamma p \rightarrow K^+\Lambda$ and $\gamma p \rightarrow K^+\Sigma^0$ Using CLAS at Jefferson Lab*. Ph.D. Thesis, Carnegie Mellon University (2004).
- [52] R. Gatto, *Relations between the Hyperon Polarizations in Associated Production*. Phys. Rev. **109**, 610 - 611 (1958).
- [53] *Determination of the relative $\Sigma - \Lambda$ parity*. G. Feldman and T. Fulton, Nucl. Phys. **8**, 106 (1958)
- [54] J. W. C. McNabb, *et al.* (CLAS Collaboration), *Hyperon photoproduction in the nucleon resonance region*. Phys. Rev. C **69**, 042201 (2004).
- [55] R. Bradford, *et al.* *First measurement of beam-recoil observables C_x and C_z in hyperon photoproduction*. Phys. Rev. C **75**, 035205 (2007).
- [56] A. Lleres, *et al.* (GRAAL Collaboration), *Polarization observable measurements for $\gamma p \rightarrow K^+\Lambda$ and $\gamma p \rightarrow K^+\Sigma^0$ for energies up to 1.5 GeV*. Eur. Phys. J. A **31**, 79 (2007).
- [57] J. J. Sakurai, *Currents and Mesons*, The University of Chicago Press (1969).

- [58] R. P. Feynman, *Photon-hadron Interactions*, W. A. Benjamin, Inc. (1972).
- [59] R. M. Egloff *et al.* Phys. Rev. Lett. **43**, 657660 (1979)
- [60] J. Ballam *et al.*, Phys. Rev. D **7**, 31503177 (1973).
- [61] H.-J. Behrend *et al.*, Nucl. Phys. **B144**, 22-60 (1978).
- [62] D. P. Barber *et al.*, Z. Phys. C **12**, 1 (1982).
- [63] M. Derrick *et al.* (ZEUS Collaboration) Phys. Lett. **B377** 259-272 (1996).
- [64] H. J. Besch *et al.*, Nucl. Phys. B **70**, 257 (1974).
- [65] J. Barth *et al.* (SAPHIR Collaboration), Eur. Phys. J. A **17**, 269 (2003).
- [66] T. Mibe *et al.* (LEPS Collaboration) Phys. Rev. Lett. **95**, **182001** (2005)
- [67] J. Breitweg *et al.* (ZEUS Collaboration), Eur. Phys. J. C **14**, 213-238 (2000).
- [68] E. Anciant *et al.* (CLAS Collaboration), Phys. Rev. Lett. **85** 4682 (2000).
- [69] T. Nakano and H. Toki, in *Proceedings of the International Workshop on Exciting Physics with New Accelerator Facilities*, SPring-8, Hyogo, 1997 (World Scientific, Singapore, 1998), p. 48.
- [70] A. I. Titov, T.-S. H. Lee, H. Toki, and O. Streltsova Phys. Rev. C **60**, 035205 (1999).
- [71] A. Sibirtsev, Ulf-G. Meißner, and A. W. Thomas, Phys. Rev. D **71**, 094011 (2005).
- [72] A. Donnachie and P.V. Landshoff, Phys. Lett. B **185**, 403 (1987); Nucl. Phys. **B244**, 322 (1984); **B267**, 690 (1986).
- [73] W. M. Kloet, W. -T. Chiang and F. Tabakin, *Spin information from vector-meson decay in photoproduction* Phys. Rev. C **58**, 1086 (1998).
- [74] M. Pichowsky, C. Savkli and F. Tabakin, *Polarization observables in vector meson photoproduction* Phys. Rev. C **53**, 593 (1995).
- [75] K. Schilling, P. Seyboth and G. Wolf, *On the analysis of vector-meson production by polarized photons*. Nucl. Phys. B **15**, 397 (1970).
- [76] F. J. Gilman, J. Pumplin, A. Schwimmer, and L. Stodolsky, *Helicity conservation in diffractive scattering*. Phys. Lett. B **31**, 387 (1970).
- [77] Y.G. Sharabian et al. *A new highly segmented start counter for the CLAS detector*. Nucl. Inst. Meth. A **556**, 246 (2006).